Observing Microphysical Properties of Atmospheric Water Using Polarization and Raman Lidar

by

Robert Andrew Stillwell

B.S., University of Colorado at Boulder, 2013

M.S., University of Colorado at Boulder, 2013

A thesis submitted to the

Faculty of the Graduate School of the

University of Colorado in partial fulfillment

of the requirements for the degree of

Doctor of Philosophy

Department of Aerospace Engineering Sciences

2017

This thesis entitled:
Observing Microphysical Properties of Atmospheric Water Using Polarization and Raman Lidar
written by Robert Andrew Stillwell
has been approved for the Department of Aerospace Engineering Sciences

_____
Prof. Jeffrey P. Thayer

_____
Prof. Peter Pilewskie

_____
Prof. Scott Palo

_____
Prof. Xinzhao Chu

_____
Dr. Ryan Neely III

Date _____

The final copy of this thesis has been examined by the signatories, and we find that both the content and the form meet acceptable presentation standards of scholarly work in the above mentioned discipline.

Stillwell, Robert Andrew (Ph.D., Aerospace Engineering Sciences)

Observing Microphysical Properties of Atmospheric Water Using Polarization and Raman Lidar

Thesis directed by Prof. Jeffrey P. Thayer

Signatures of climate change have been shown by observation and climate model studies to be most evident in the polar regions, so called polar amplification. However, the polar regions are among the least studied regions on Earth, limited largely due to harsh measurement environments and the logistical challenges of maintaining presence in such environments. A lack of high vertical and temporal resolution measurements of cloud properties and atmospheric state directly relates to uncertainty in climate model predictions inhibiting scientific understanding of the specific response of the polar regions within the context of global climate change.

This thesis focuses on measurements of water in the polar regions in its 3 thermodynamic phases, i.e. water vapor, liquid and ice. Uncertainty in water's 3-dimensional distribution and properties contributes to the uncertainty in specific response of the Arctic system to large-scale perturbations. By directly and indirectly modulating the surface energy and mass budgets of the region, water contributes to much of the fundamental uncertainty of model projections in the polar regions.

It is hypothesized that ground-based, active optical remote sensing measurements can contribute to the knowledge of atmospheric state and cloud properties by providing unmatched data resolution and quality to help identify and elucidate key cloud microphysical and cloud state properties. To address this hypothesis, 3 main questions are posed:

(1) How to accurately identify and distinguish liquid and ice water in Arctic clouds using polarimetric lidar?

(2) What unique signatures about Arctic cloud microphysical properties can be revealed using polarimetric and Raman lidar?

(3) How do we meet the needs of the next generation cloud and atmospheric state observations

in the Arctic using lidar?

This thesis addresses these questions using two lidar systems, the Clouds Aerosols Polarization and Backscatter Lidar (CAPABL) currently deployed to the top of the Greenland Ice Sheet at Summit, Greenland, and by developing a next-generation Arctic lidar, the Summit Polarized Raman Lidar (SuPR). Unique polarization processing of CAPABL data allows for separation of cloud thermodynamic phase and ice crystal orientation. Specific microphysical properties of these subclasses of cloud particle as well as uncertainties in lidar data are identified and linked directly to their impact on the surface radiation budget, using CAPABL data and ancillary sensors at Summit. First of their kind observations of radiative effects of the preferential orientation of ice crystals are demonstrated. These results from CAPABL inform the development of the design requirements of SuPR which is a first of its kind 3-phase water observing system designed specifically for the Arctic. The design and first measurements of the SuPR system are demonstrated.

Dedication

For my family and their never ending encouragement and support.

Acknowledgements

I wish to acknowledge and thank my advisor, Jeff Thayer, for his exceptionally patient help and dedication over the past several years. I also must thank my committee members for their critical insights and careful analysis, especially Ryan Neely for pushing me to challenge myself for the better. Additionally, this work would never have been completed without the help of many mentors including Matt Hayman and Mike O'Neill whose guidance and support were invaluable.

To my mother who taught me to follow my heart and that love is unconditional, my father who taught me the value of hard work and honesty, my brother who showed me the rewards of dedication, and Natalie who was always there for me when I needed anything, your love and encouragement have neither gone unnoticed nor unappreciated. Thank you so very much.

I also would like to thank the entire ICECAPS team especially Matt Shupe, Von Walden, and Dave Turner for their commitment to the success of its data, analysis, and students and the staff and science technicians at Summit as well as Polar Field Services for their support and dedication to help collect and maintain instrumentation, especially Hannah James and Sam Dorsi.

Finally, I would like to acknowledge Doug Philipp who finally pounded home the idea that school was not a punishment but an opportunity. I consider myself lucky to have spent time in his classroom learning the joy of learning.

Contents

Tables

Table

Figures

Figure

Chapter 1

Introduction

1.1   Water and the Atmosphere

It is difficult to overstate the importance of the atmosphere as it relates to the lives and evolution of humans. One author explains, "Our atmosphere is a delicate life-giving blanket of air that surrounds the fragile Earth. In one way or another, it influences everything we see and hear–it is intimately connected to our lives" [1]. This is hardly an overstatement as humans have evolved around atmospheric properties, to breath the gases that are present within it and adapted to be accustomed to the temperature that it maintains. We, therefore, have a vested interest in understanding the current and future state of the atmosphere because it will affect the manner in which we live within it.

In the loosest possible terms, the American Meteorological Society defines an atmosphere as an envelope of gases that is gravitationally bound to a celestial body. It further defines weather and climate as the state of the atmosphere on short time scales (minutes to days) and long time (much much longer than days) scales respectively [2]. On Earth, this layer is composed of many gases such as nitrogen, oxygen, argon, carbon dioxide, hydrocarbons, and water vapor. If the earth were the size of an apple, the atmosphere would be thinner than the apple's skin. Despite this apparent insignificance, much of our daily lives can be linked directly to the state of the atmosphere, its weather, and its climate.

The most important atmospheric constituent as it relates to weather is water, which is unique because it exists in all 3 phases, solid, liquid and gas, simultaneously at atmospheric temperatures

and pressures [3, 4]. In review of the link between climate and water vapor, Sherwood et al. notes, "Water vapor is the only radiatively important atmospheric constituent that is sufficiently short-lived and abundant in the atmosphere so as to be essentially under purely natural control," [5]. Water vapor accounts for about 60% of the natural greenhouse effect and approximately half of the energy transport from the equator to the poles, setting the temperature gradients upon which storms grow and intensify [5, 6, 7]. Water in the atmosphere has also been linked to much of the uncertainty in our future climate projections. The phase transitions of water from gas to liquid drives global circulation patterns and convection [3]. Understanding the 3-dimensional distribution of water vapor is critical for quantitative weather prediction of convection [8]. However, much of the uncertainty in future climate projections can be linked to the behavior of water in one of its three phases. The links between clouds, defined as "a visible aggregate of minute water droplets and/or ice particles in the atmosphere above the earth's surface" [2], and circulation and climate remain opaque [7, 9]. One study links as much as half of the variance in climate projections to the behavior and response of low clouds and a warming atmosphere [10], and it has been noted that inadequate representation of clouds and moist convection is the main limitation in current representations of the climate system [11]. The highly inhomogeneous nature of the distribution of water in Earth's atmosphere is both a complex problem and a visually stunning reminder of the beauty of the atmosphere. It was captured famously by NASA's Apollo 17 spacecraft photo, The Blue Marble, shown in Figure 1.1.

Water in its 3 phases strongly affect the way in which energy moves through and is stored within the atmosphere. Understanding the composition of the atmosphere as well as the sources and sinks of energy are important in understanding its temporal and spatial evolution. Stephens et al. note that climate change is controlled by the global energy budget [12], while Allen and Ingram note that the global hydrological cycle is tied to the availability of moisture to radiate energy [13]. Attempts to try to calculate the energy budget of the atmosphere have raised questions about the implications of imbalance [14, 15] and are challenged to a large degree by the inhomogeneity of the atmosphere and, especially, of atmospheric water. Two attempts to define earth's energy budget

Figure 1.1: View of the Earth as seen by Apollo 17 traveling towards the moon dubbed by NASA as "The Blue Marble". Visible on top is the horn of Africa and below Antarctica. Photo Credit: NASA.

have noted that the size and uncertainties of the energy terms involved are far in excess of the suspected net imbalance [12, 16]. The energy budget compiled by Stephens et al. is given in Figure 1.2. Furthermore, coupling of the atmosphere with the surface and oceans can mask the net energy imbalance via mixing and energy storage mechanisms of the oceans [15, 17]. When viewing the atmosphere on a shorter time scale, days to weeks, net radiative imbalances can cause or enhance major weather events such as the July 2012 melt event of the Greenland Ice Sheet (GrIS), which was enhanced by liquid baring cloud activity forced by an atmospheric river directing water vapor over the GrIS [18].

The sensitivity of weather and the climate system to water is profound. The state of the atmosphere and its temporal evolution, and by extension the state of atmospheric water, are critical to understand for the everyday lives of humans. Despite the major linkages between weather, climate, and water, much more work is required to better understand the subtle connections of the complicated system. Of particular concern in this thesis is the requirement for accurate measurements of water, which are used to validate and guide model predictions of weather and climate.

TOA imbalance 0.6±0.4

Incoming solar 340.2±0.1 Reflected solar 100.0±2

Clear-sky emission 266.4±3.3 Outgoing longwave radiation 239.7±3.3

Shortwave cloud effect 47.5±3

All-sky atmospheric window 20±4

Atmospheric absorption 75±10 5±5

Sensible heating Latent heating

Longwave cloud effect 26.7±4 3±5

All-sky longwave absorption -187.9±12.5

24±7 88±10

Clear-sky reflection 27.2±4.6

26.6±5 319±9 Clear-sky emission to surface

Surface shortwave absorption 165±6 23±3

398±5

345.6±9 All-sky emission to surface

Surface reflection Surface emission

Surface imbalance 0.6±17

Figure 1.2: Global energy budget as compiled by Stephens et al. [12]. Here, the yellow terms are "Shortwave" radiation defined as radiation occurring at less than 4 μm and pink is "Longwave" radiation defined as radiation occurring that is greater than 4 μm in wavelength. Atmospheric water is either directly or indirectly tied to many of the energy budget's terms including the cloud albedo forcing terms, cloud longwave emission, the clear sky absorption and emission from water vapor, and the latent heating due to precipitation. The terms here are global averages as compiled from independent satellite and ground based measurements from all over the world. Photo Credit: Stephens et al.

1.2   Regional Atmospheric Motions and the Arctic

The redistribution of energy in the atmosphere is given and described broadly by the Stephens et al. energy budget. Without an atmosphere, the temperature of the earth would be set by two competing energy sources and sinks. The Earth's surface absorbs radiation from the sun with energy concentrated primarily shorter than 4 μm, hereafter referred to as shortwave energy or shortwave radiation. The earth emits radiation with wavelengths primarily longer than 4 μm, hereafter referred to as longwave energy or longwave radiation. In the absence of intervening influences, the net balance of these two terms would determine the temperature of the earth. However, the existence of the atmosphere complicates this balance considerably.

Water, in its 3 phases, affects the energy budget in many ways. First, water vapor is a spectrally selective infrared (IR) active absorber [6, 19, 20]. Water vapor emits longwave energy

to the surface of the earth, which enhances the net amount of energy the surface receives, the greenhouse effect, which serves to warm the surface. Second, liquid and ice water in the form of fog and clouds also emit energy in the longwave further enhancing the net energy at the surface, further warming the surface. Third, liquid and ice water, in the form of fog and clouds, reflects shortwave energy by enhancing atmospheric optical depth, thereby cooling the earth. Fourth, changing the thermodynamic phase of water requires energy; the conversion from water vapor to liquid or ice and subsequent precipitation serves to warm the atmosphere by the release of latent heat. This also serves to redistribute energy via advection. Finally, the precipitation that falls as snow or freezes at the surface can enhance the overall reflection of shortwave energy from the surface. On global average, water vapor serves to warm the surface, and clouds as well as surface ice and snow serve to cool it [3, 5, 6, 11]. In all cases, the 3-dimensional distribution of water in its 3 phases, which is highly inhomogeneous as shown on the Blue Marble, affects the surface energy balance, but crucially, large regional differences appear. It is found that the surface energy balance is affected by the exact nature, altitude, and location on earth of the driving mechanisms indicating vastly different global effects based on regional behaviors [14].

Of particular interest on the regional scale are the polar regions. The Arctic has been warming at a rate more than twice as large as the rest of the earth [21, 22]. As temperatures rise, melt of the GrIS and sea ice cause dramatic systemic changes. The GrIS contains enough ice to cause global sea levels to rise by 7 m if melted [23], of which 25 mm has already been contributed since 1990 at increasing rate in recent years [24]. Combined with the Antarctic ice sheet, which contains enough water to cause sea levels to rise by approximately 57 m [25], a warming climate would cause a redistribution of coastlines across the world. Furthermore, the changing sea ice conditions are directly linked to changes in the Arctic ecosystems, with primary production increasing by 30% from 1998 to 2012 [26, 27, 28, 29, 30, 31].

The Arctic is unique in many respects. Due to its low temperature, the saturation vapor pressure, defined by the Clausius-Clapeyron relation, is much lower in the Arctic than the tropics or midlatitudes [4, 6, 32]. A result is that there is less water vapor in Arctic air than warmer regions

resulting in enhanced importance of clouds [33, 34, 35]. Arctic clouds, especially those containing liquid water, have been shown to enhance meltwater runnoff of the GrIS but have proven very difficult to understand via Earth system modeling [18, 36, 37, 38, 39]. The highly variable nature of clouds combined with the sparse measurements makes uncertainties in the radiation budget of the Arctic system very large [40, 33, 34, 41, 42].

Another complicating factor in the Arctic is the presence of many amplifying fast feedback mechanisms (here fast is on the order of days to years as opposed to slow feedbacks on the order of decades to millennia) such as the ice-albedo feedback, permafrost feedback, and water vapor feedback [26, 27, 28, 29, 30, 43, 44, 45]. The ice-albedo feedback occurs when highly reflective ice is replaced by less reflective ocean or ground surfaces. As the Arctic, and the Antarctic, warm, the ice begins to recede, which causes higher rates of absorption of solar energy that causes warming to occur faster due to higher rates of energy accumulation. The permafrost feedback is related to the emission of methane from melting permafrost. Microbial breakdown of the thawing permafrost releases methane, a known potent greenhouse gas, which serves to increase the IR emission of the atmosphere and thus the net surface longwave energy that causes further warming and faster rates of permafrost melting. Finally, as the Arctic warms, its saturation vapor pressure of water, described by the Clausius-Clapeyron relation, increases, which increase the overall amount of water vapor in the atmosphere that again serves to increase the net longwave energy at the surface further accelerating warming.

Because of the fast feedback mechanisms occurring in the Arctic, some of which have likely not been identified, and the relatively sparse availability of measurements, much of the variability in the Arctic is difficult to reproduce in model simulations of clouds and atmospheric state [36, 37, 46]. However, Shupe and Intrieri note that modeling is the most practical method to understand widespread climate change making predictions of future weather and climate difficult to assess in the Arctic [47].

1.3   Atmospheric Monitoring with Lidar

Measurements of the atmospheric state in the polar regions are sparse due to many factors. Measurements from satellite based passive sensors (sensors that do not actively transmit energy but simply observe available energy from the sun and earth) have difficulty in distinguishing the polar atmosphere from the surface below due to a lack of spectral or thermal contrast [33]. The lack of contrast between clouds or blowing snow and the bright polar surface is clearly visible on The Blue Marble, Figure 1.1, where it is easy to distinguish cloud cover from dark ocean and land but nearly impossible over Antarctica. Measurements from satellite based active sensors are not limited by spectral or thermal contrast, but are temporally sparse due to the design of orbital trajectories (also affecting passive satellite measurements)[48, 49]. Conversely, ground based active and passive sensors can solve the temporally sparse measurement problem from satellites, but the harshness of the environment and lack of support infrastructure make spatial characterization problematic [47]. Furthermore, as a practical matter, logistical challenges of maintaining a presence in an inhospitable environment requires much effort and is also exceptionally expensive. Making high quality ground based measurements in the polar regions is a substantial challenge. However, a synergistic approach of both methods shows promise in solving these temporal and spatial measurement issues. Measurements from the ground can be used to improve satellite retrievals by comparing measurements made in a common volume thus making it imperative to rise to the environmental challenges [33, 35].

Remote sensing leverages measurement of electromagnetic (EM) waves that have propagated through, and modified by, a medium of interest. In the case of active remote sensing, where the EM waves of interest are produced by a controlled system, one can retrieve information about a medium or volume of interest by measuring the final state of radiation after interaction with a medium. By knowing the starting state of the radiation and measuring the ending state, information about how the medium of interest modified the radiation can be retrieved. Furthermore, by measuring the time of flight from emission to measurement, range resolved measurements are possible based

on the rate of propagation of EM energy in a medium. The changes measured can be to any of the basic state variables of EM radiation such as amplitude, phase, direction, frequency, or polarization [50, 51, 52, 53].

Active remote sensing of the Atmosphere at optical wavelengths was first attempted with bright searchlight beams. This began with the investigations by Hulbert who used a continuous searchlight beam to study aerosol layers in the atmosphere [54]. This technique was pursued and advanced until the mid 1960's by Elterman who demonstrated advancements in accuracy, precision and range [55, 56, 57]. However, the major advances in optical remote sensing would follow a parallel but different track. Of note are contributions to quantum mechanics by Einstein, stimulated emission by gas discharge by Fabrikant, and co-developments with microwave amplification by stimulated emission of radiation (maser) and optical pumping by Townes [58]. This laid the groundwork for the use of stimulated emission, which in turn lead to the demonstration of the first light amplifications by the stimulated emission of radiation (laser) in 1960 by Maiman [58, 59].

Since the first demonstration of the ruby laser, active remote sensing in the form of lidar (light detection and ranging) systems have evolved in complexity. First attempts to sample the atmosphere with lidar started with simple clear-air and aerosol observing systems of the early 1960's [60, 61]. As laser and optical technology improved, more capable demonstrations of lidars observing other physical effects were shown. The use of Raman spectroscopy was demonstrated as early as 1968 by Cooney for vibrational transitions with a helium neon laser and later in 1971 for pure rotational transitions [62, 63]. The groundwork for observing atmospheric turbulence with polarization lidar was laid in the late 1960's but in 1969, Hoehn proposed that observations of depolarization might be affected by atmospheric scattering and required more attention [64]. Scotland discussed the shape of scatterers as a cause of the atmospheric depolarization values [65]. Boudreau noted that there might be an advantage to using certain wavelengths by trading scattering efficiency and transmission efficiency [66]. Over the next 20 years, technology improved allowing for system construction with more powerful and stable lasers and more precise optical elements [67, 68]. This advantage culminated in the conclusive demonstration of upper atmospheric elastic scattering

lidars that can observe polar mesospheric clouds in full solar background conditions, temperature, and gravity waves in the mesosphere and lower thermosphere [69, 70, 71] and the space-borne elastic lidar Cloud-Aerosol Lidar with Orthogonal Polarization (CALIOP) [72] . Further automation of tropospheric systems has allowed continuous monitoring leveraging both elastic and inelastic scattering [73, 74]. All of these advancements have increased the maturity and technical readiness of lidar to be applied to more extreme environments such as the Arctic.

1.4   Contributions to the State of Knowledge of Arctic Water

It is hypothesized that ground-based, active optical remote sensing measurements can contribute to the knowledge of atmospheric state and cloud properties by providing unmatched data resolution and quality to help identify and elucidate key cloud microphysical and atmospheric state properties to better understand the 3-dimensional distribution of water in the Arctic. To address this hypothesis, 3 main questions are posed:

(1) How to accurately identify and distinguish liquid and ice water in Arctic clouds using polarimetric lidar?

(2) What unique signatures about Arctic cloud microphysical properties can be revealed using polarimetric and Raman lidar?

(3) How do we meet the needs of the next generation cloud and atmospheric state observations in the Arctic using lidar?

The organization of this work used to answer the posed questions is as follows. Lidar theory required to understand lidar inversions and data products is presented in Chapter 2. Specification of the relevant scattering processes leveraged by lidar is presented in Chapter 3. A currently deployed polarization lidar, the Clouds Aerosols Polarization and Backscatter Lidar (CAPABL) is described in Chapter 4. Description of CAPABL's data products related to cloud water using the theory of Chapter 2 and Chapter 3 is given along with validation of the data products using multi-sensor

data retrievals. Observations of mixed-phase clouds and preferentially oriented ice crystals made by CAPABL are shown in Chapter 5. CAPABL's unique observational capabilities are combined with ancillary sensors to link microphysical properties to the local surface radiation budget. The design and initial data for the next generation Arctic lidar system, which adds the ability to measure water vapor and relative humidity to cloud properties, dubbed the Summit Polarized Raman Lidar (SuPR), is presented in Chapter 6. A discussion of the hardware design and analysis methods, especially analysis of laser safety, is presented. Finally, a summary of the major results of this thesis and how they address the questions posed and the hypothesis stated is given in Chapter 7 as well as a description of the author's vision for the future of observation of water in the Arctic.

Chapter 2

Lidar Theory

2.1   Lidar System Overview

Light Detection and Ranging (lidar) systems use light to probe the state of remote systems. Like other active remote sensing systems, lidars produce waves which propagate into a remote medium and observe the result. Typically waves are transverse EM waves, but systems using longitudinal waves such as sound detection and ranging (sodar) exist. By transmitting a known and stable EM wave and measuring any EM signal that reflects or scatters off of the medium of interest, one can quantify the change between the initial and measured EM waves. By measuring the change in the waves from start to finish, the properties of the scatterers or absorbers in the medium of interest can be inferred. In particular, lidars produce and observe EM waves near the visible portion of the EM spectrum which is given in Figure 2.1 for reference.

Lidar has matured rapidly from the first demonstration of the ruby laser in 1960 resulting in many sizes, shapes, specifications and observing vastly different physical effects. However, the basic components of an active remote sensing system, like lidars, have changed very little. All systems are broadly composed of a transmitter, a receiver, a medium in which EM waves propagate, and controlling and post processing software which collects and analyzes raw data. Beyond these basic pieces, many subclassifications of lidar system relate to how these pieces are assembled and configured. For example, systems can either be monostatic or bistatic, where the transmitter and receiver are co-located or not, respectively. Systems can further be co-axial or biaxial, where the receiver and transmitter and either aligned from the exit port of the system or not. Lidar systems
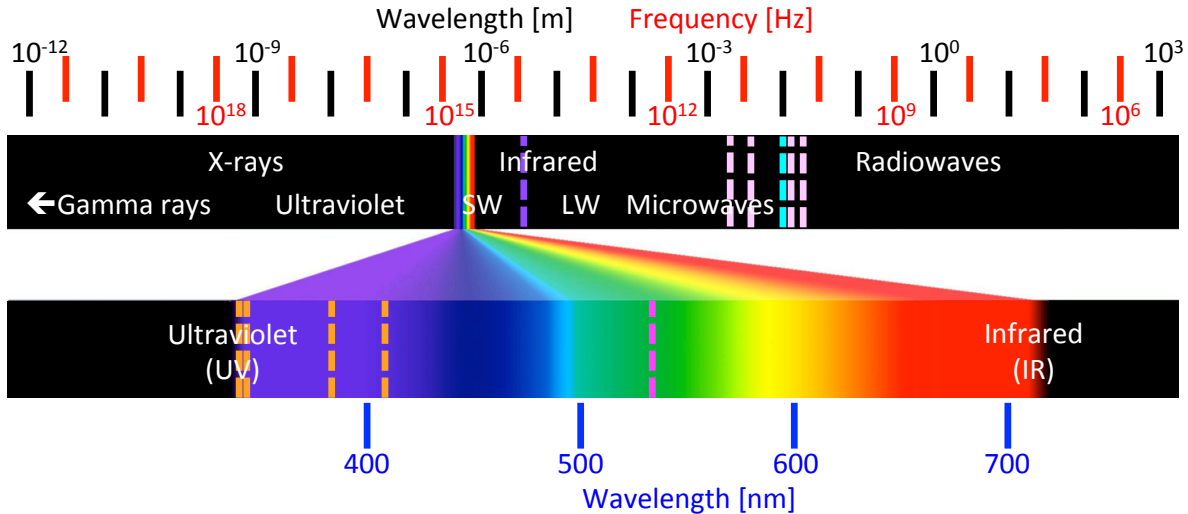
Figure 2.1: An illustration of the EM spectrum used for active remote sensing. Lidars use wavelengths near the visible portion of the spectrum roughly between the infrared and ultraviolet, which is broken out of the larger spectrum. The long and shortwave portions of the spectrum used in Figure 1.2 are also denoted with their separation line ($4\mu m$) given as the dashed dark purple. Other instruments used for this thesis, which are described in more detail in Chapter 4 and Chapter 6, are indicated for reference as additional dashed lines where they measure the EM spectrum. The color coding is as follows: light pink dashed = passive microwave radiometers, cyan dashed = active millimeter cloud radar, pink dashed = CAPABL and micropulse lidar, and orange dashed = SuPR.

can be classified by the physical effects that occur within the propagation medium, which are used to infer atmospheric properties.

For lidar, the transmitter is almost always a pulsed laser [60, 61, 66, 67, 68, 69, 70, 71, 73, 74, 75, 76, 77, 78, 79, 80, 81, 82, 83, 84, 85, 86, 87, 88, 89, 90, 91, 92]. The pulsed nature of the source allows for one to measure the time between transmitting a pulse and receiving a pulse, which allows for one to range resolve a scatterer based on the known speed of light in the medium of interest [50, 52, 51]. Some systems require extremely narrowband lasers [50, 51, 52, 69], on the order of MHz, while others can accommodate much wider wavelength bands [78, 89], on the order of tens of GHz. Some systems require short pulse lengths, possibly less than 1 ns [84], while others can accommodate much longer, on the order of μs [51, 91]. Finally some systems place stringent demands on the output polarization while others are completely agnostic to polarization. The ancillary components of a transmitter are used to refine the properties of the laser light to create a

stable and pure reference based on the requirements of the measurement of interest. Receivers are commonly telescopes with optics used to parse signals and separate noise and valid return signals. Receivers are analyzers to measure the change of the stable transmit beam with specifications again relating to the measurement of interest. Both the transmitter and receiver are designed and configured to measure some property of EM radiation, which can be uniquely attributed to a physical scattering effect of interest.

The most critical piece of a lidar system is the propagation medium at which the transmitter and receiver are aimed. An illustration of the propagation medium is given in Figure 2.2. Here a monostatic, co-axial lidar system consisting of a laser and a telescope serve to transmit and analyze light from the medium of interest. Light is directed into the medium of interest and will propagate indefinitely unless it interacts with some absorber or scatterer. The specifics of this interaction will be described in more detail in Chapter 3, but the interaction serves to change the properties of the EM wave, or photon, in some way and possibly redirect the wave, or photon. Only a small fraction of the original transmitted light will scatter back to the receiver and be collected. This perception angle is simply the solid angle the telescope area subtends on a sphere with a radius of the distance from the lidar system to the scatterer.

Only interactions which occur in the telescope's field of view and scatter back to the telescope are measurable but in principle multiple interactions can take place. The number of times light interacts with the medium of interest are related to the optical depth of the medium [93]. For lidar, single interactions are often observed for clear air due to its relatively small optical depth, but it is not uncommon for light to scatter multiple times in more optically thick media like clouds and thick aerosol layers [94]. One common interaction is a forward scattering event followed by a backscattering event [94].

The range resolution of the measurement is linked both to the length of the laser pulse in the medium of interest and the timing electronics used to measure the scattered light. The spatial resolution is linked to the size of the beam and telescope field of view at a particular radius. In Figure 2.2, the range resolution, ΔR, is exactly half of the laser pulse length but this is not

necessarily the case. The receiver resolution can be much smaller than the pulse length or much larger depending on the requirements and particular design of the system [69, 84].
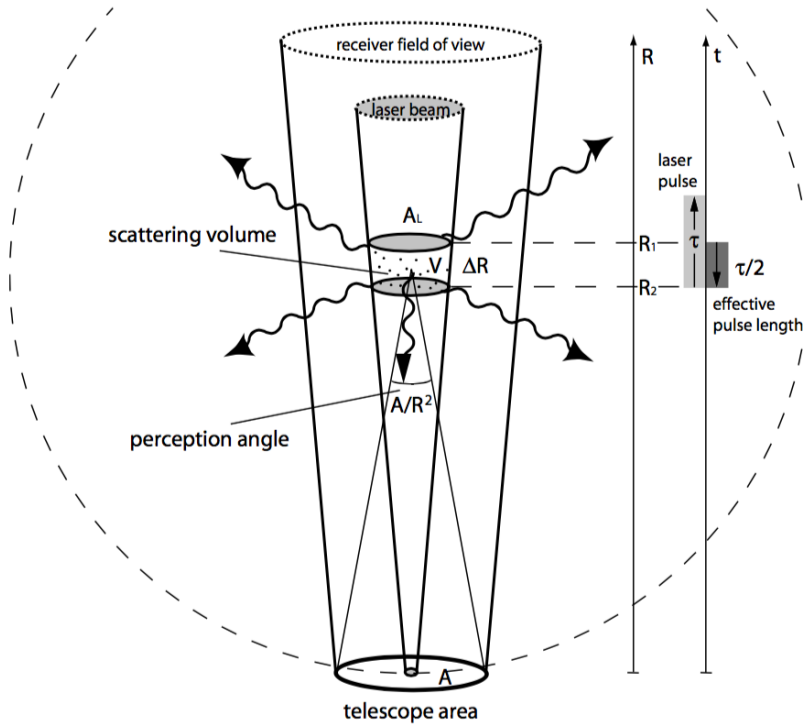
Figure 2.2: An illustration of the physical picture that is assumed in deriving the lidar equation taken from Weitkamp et al. [50]. This diagram shows a co-axial lidar setup where the beam and the receiver field of view always overlap. Furthermore, it assumes that the receiver field of view is larger than the beam at all times. This diagram is meant as a guide only as some designers choose other design parameters such as incomplete overlap and smaller receiver fields of view.

2.2   The Scalar Lidar Equation

The lidar equation is a useful tool to quantitatively analyze the measurements of a lidar system. Many versions exist but they are all based on the scattering picture described in Section 2.1. This thesis will leverage two versions, the first being a scalar version of the lidar equation, which simply describes the number of photons that result from any atmospheric interaction. The second version accounts for the vector nature of light and includes more physical effects, which serve to not only modify the number of photons observed, the measured intensity, but also the polarization state of the light. The scalar version is addressed first.

From the lidar picture presented in Figure 2.2, one can simply derive the lidar equation by describing the interactions a photon encounters during its propagation from laser to detector. The derivation of the scalar lidar equation often relies on two simplifying assumptions: first that independent scattering is occurring and second that single scattering is occurring. These assumptions will be addressed in more detail within the context of the full vector description of the lidar equation in Section 2.3. Independent scattering effectively assumes that there is no structure on the scale of the wavelength of the scatterer that would cause constructive or destructive interference. This statement relies on the stochastic nature of atmospheric scatterers and is not found by any work, to the author's knowledge, to be violated for optical wavelengths in the atmosphere [50, 51, 52]. The single scattering assumption is, however, found to be incorrect on multiple occasions based on the optical depth of the scattering target. This will be addressed in greater detail in Section 2.3 and Chapter 3.

The number of photons observed at the detector is a function of the following system parameters and propagation medium properties. These terms can be combined into an equation, which explicitly links the transmitter parameters, receiver parameters, and propagation medium characteristics to the number of photons observed by the system. This equation, referred to as the scalar lidar equation is given in Equation 2.1.

(1) The number of photons emitted from the laser. The number of photons that are emitted by the laser is simply a function of the laser's energy output at the wavelength of interest, λ_{T_x}. The energy can be specified either by the laser's average power, $P_L(\lambda_{T_x})$, and its pulse width, Δt, or by the energy per pulse. The number of photons per shot is the transmitted energy per shot divided by the energy per photon, given as $\frac{hc}{\lambda_{T_x}}$ where h is the Planck's constant and c is the speed of light in the medium of interest. Note that the wavelength and speed of light need to be specified in the same medium, which is usually air for atmospheric lidar.

(2) The optical efficiency of the transmitter. Most transmitters are composed of optical el-

ements such as mirrors, lenses, and windows which do not have 100% efficiency due to reflection from mismatch indices of refraction or by design to do, for example, diagonsitics of the transmitter system. This efficiency scales the number of output photons and is represented as η_{T_X}.

(3) The optical efficiency of the transmission from the transmitter exit port to the scatterer. As the scalar lidar equation assumes single scattering only, this term is a pure extinction term which is composed of absorption of photons and scattering of photons out of the main beam. Scattering and absorption are a strict function of the transmitted wavelength and the range at which the interaction is occurring, R, and is given as $T_{T_x}(\lambda_{T_x}, R)$.

(4) The backscattering efficiency of the scatterer of interest. This scattering efficiency can be modeled in many ways, but is often simplified as a cross section of an equivalent sphere, which would scatter photons. Multiplying this cross section, represented as $\sigma(\lambda_{T_x}, \lambda_{R_x})$, by the number density of scatterers, $N_D(R)$, and the width of the observed region, ΔR, yields a probability of scattering. The number density of scatterers is a function of range. The scattering cross section is discussed in greater detail in Chapter 3, but is not limited to scattering that occurs at a similar wavelength as the incident wavelength. If the scatterer causes a shift in wavelength, this is known as inelastic scattering, and if not it is referred to as elastic scattering. Therefore, the scattering cross section is a function of both transmit, λ_{T_x}, and receive, λ_{R_x}, wavelengths and so too is the observed number of photons by the receiver.

(5) The optical efficiency of the transmission from the scatterer to the receiver entrance port. This is a second path transmission much like the first from transmitter to scatterer except the transmission efficiency in this case is a function of the scattered wavelength and is given as $T_{R_x}(\lambda_{R_x}, R)$. Again a photon can be extinguished at this point as for the transmit leg by scattering or absorption but can not be scattered again and still received as a valid signal photon by the single scattering assumption made for this form of the lidar equation.

(6) The solid angle of observation of the receiver. The solid angle is a function of the area of the telescope, A, and the range of observation. This is also referred to as the perception angle in Figure 2.2.

(7) The physical overlap in space of the transmitter beam and receiver field of view, given as a function of range as $G(R)$. This term arrises due to the focusing and field of view of the receiver as well as the physical overlap of the system, especially for bi-axial systems. Because the depth of field of the receiver system is not the length of the measurement in general, there will be some ranges at which the system is in a non-optimal configuration. Often times, though not always, the telescope for a lidar system is focused at infinity, which causes light in the telescope near field to be imaged improperly onto the detector. Additionally for co-axial systems like the one illustrated in Figure 2.2, there is a near field shading effect due to secondary mirrors in the telescope system.

(8) The optical efficiency of the receiver and detectors. This is similar to the optical efficiency of the transmitter but again is a function of the scattered wavelength, given as η_{R_x}. Values for optical efficiency can be optimized for many features but usually include filtering of portions of the spectrum other than the desired receive portion. For example, many lidar systems specify solar blocking filters to remove unwanted light for daytime operations or may choose to block the transmitted wavelength if the received wavelength is not the same. In either case, the efficiency for the lidar equation is usually only specified at the observation wavelength of interest but is always a function of wavelength in general.

(9) Any background light or noise which exists in or near the frequency band of interest. The source of this noise can be any light pollution for bright lights in and around the lidar system or sunlight. Additionally, there are systematic detector and electrical noise characteristics that can appear as photon noise sources. All noise sources are lumped together into a number of photons $N_B\left(\lambda_{R_x}\right)$.

$$N_{R_x} = \left[\frac{P_L\left(\lambda_{T_x}\right)\Delta t}{\frac{hc}{\lambda_{T_x}}}\right][\sigma(\lambda_{T_x},\lambda_{R_x})N_D(R)\Delta R]\left[\frac{A}{R^2}\right]\left[T_{T_x}\left(\lambda_{T_x},R\right)T_{R_x}\left(\lambda_{R_x},R\right)\right]\left[\eta_{T_x}\eta_{R_x}G(R)\right]+N_B\left(\lambda_{R_x}\right)$$

$$(2.1)$$

One way to consider the terms of the lidar equation is as efficiency terms. The terms presented in Equation 2.1 all have units of photons or are unitless. The terms in brackets on the right side of the equation except the first term, $\left[\frac{P_L(\lambda_{T_x})\Delta t}{\frac{hc}{\lambda_{T_x}}}\right]$, which is the transmitted number of photons and $N_B\left(\lambda_{R_x}\right)$ which is the number of noise photons, can all be considered efficiency terms. The second term, $[\sigma(\lambda_{T_x},\lambda_{R_x})N_D(R)\Delta R]$, can be thought of as the efficiency of scattering. The third term, $\left[\frac{A}{R^2}\right]$, can be considered the efficiency of collection of scattered light. The fourth term, $[T_{T_x}\left(\lambda_{T_x},R\right)T_{R_x}\left(\lambda_{R_x},R\right)]$, is the transmission efficiency to and from the scatterer from the lidar system. The fifth term, $[\eta_{T_x}\eta_{R_x}G(R)]$, can be thought of as the optical system's efficiency. These efficiency terms are all unitless and have values less than or equal to unity.

Equation 2.1 is useful for linking all the known parameters of the system together. In normal operations, the number of received photons is measured and elements on the right hand side of the equation are inferred. Typically, the lidar system values such as η_{T_x}, η_{R_x}, $G(R)$, A, ΔR, $P_L\left(\lambda_{T_x}\right)$, Δt, λ_{T_x}, and λ_{R_x} are known in advance of the measurement through system calibration and design. That leaves parameters like $\sigma(\lambda_{T_x},\lambda_{R_x})$, $N_D(R)$, $T_{T_x}\left(\lambda_{T_x},R\right)$, $T_{R_x}\left(\lambda_{R_x},R\right)$, $N_B\left(\lambda_{R_x}\right)$, and R to be determined from measurements. Range is readily determined from the time of flight of the photons knowing that the photons must have taken a single straight line path to and from the system given the single scattering assumption. The other terms are less easy to measure operationally.

The first measurement to consider before being able to retrieve atmospheric properties is characterizing noise. Broadly, one can lump noise either into range resolved or not range resolved noise. Noise which is not correlated with range can be measured simply by making a measurement outside the time period where one expects to be receiving signal photons. For example for a lower tropospheric lidar system, one does not expect to receive signal much higher than the troposphere, effectively saying that the efficiency terms multiplied by the transmitted photons is much less than

one. Therefore, measuring for longer than the light takes to propagate into and back from the troposphere will effectively zero out the transmitter photons in the lidar equation and just yield noise. If the noise is range-correlated, it is much more difficult to remove and can not typically be measured as non range-correlated signal and must often be modeled.

It is worth noting that lidars can measure both extensive and intensive properties. Extensive properties are properties that change as the sample size changes such as scatterer number density and volume [95]. Intensive properties are properties that do not change with the sample size such as temperature or scattering cross section [95]. One can often cancel out extensive properties by taking ratios of signals taken in common volume or comparing neighboring altitude ranges. For example, comparing two measurements made in common volume at the same altitude will cause transmission and number density to be constant and cancel. Strictly, it also cancels out properties that are common to both measurements, for example transmitter efficiency and laser power. This technique is leveraged extensively in describing polarization retrievals in Sections 2.3.1 and 2.3.2.

2.3   The Stokes Vector Lidar Equation

One major simplification of the scalar lidar equation is that it does not account for the vector nature of light. Two major classes of vector representations of the orientation of the electric field of light, or polarization, are Jones vectors and Stokes vectors [96, 97]. Jones vectors are 2 element complex vectors and Stokes vectors are 4 element real vectors. One major difference lies in their ability to handle photon aggregates. While there is no such thing as an unpolarized photon, large groups of photons can have zero net polarization, i.e. they have a uniform distribution of polarizations with no dominant mode. Jones vectors are useful for coherent polarized sources or large groups of photons with similar polarization. Stokes vectors are more flexible because they can handle sets of photons that have no net polarization, even though the individual photons are polarized, but are not useful for modeling interference effects [96, 97]. For atmospheric lidar, Jones vectors are useful for the analysis of coherent systems like wind lidar systems but are severely limited in other respects. As such, this thesis will use Stokes vectors exclusively.

Stokes vectors are 4 element row vectors. The first element is used to describe the intensity of the beam or set of photons. The other 3 terms are used to describe any net polarized properties that the beam or set of photons has. They are given generally by Hayman and Thayer [98] in Equation 2.2.

$$\bar{S} = \begin{bmatrix} S_0 \\ S_1 \\ S_2 \\ S_3 \end{bmatrix} = S_0 \begin{bmatrix} 1 \\ p\cos(2\psi_{PC})\cos(2\chi_{PC}) \\ p\sin(2\psi_{PC})\cos(2\chi_{PC}) \\ p\sin(2\chi_{PC}) \end{bmatrix} \tag{2.2}$$

p is the degree of polarization given in Equation 2.3.

$$p = \frac{\sqrt{S_1^2 + S_2^2 + S_3^2}}{S_0}. \tag{2.3}$$

The description of the Stokes vector as given in Equation 2.2 is convenient because it can be easily linked to spherical coordinates. Here, the angles correspond to the angles in Poincaré space and are thus tagged with a subscript PC. The S_0 term relates to the size of a sphere in Poincaré space relating to the overall light intensity and p to the length of the polarization vector in Poincaré space.

By expressing light by its Stokes vector instead of simply by the number of photons, more complete and descriptive derivations of optical properties can be performed. One complication of describing the full vector nature of light is that altering the state must be done via matrix instead of scalar efficiency terms as presented in Equation 2.1. These matrix transformations are given as Mueller matrices. In Poincaré space, these matrices serve to rotate, translate, and change the length of the Stokes vector. One elegant way of describing general Mueller matrices is through polar decomposition. While the decomposition is not unique, the method used here follows the definitions of Lu and Chipman and Hayman and Thayer [98, 99]. Mueller matrices are decomposed into a depolarizing element, $\bar{\bar{M}}_\Delta$, and retarding element, $\bar{\bar{M}}_R$, and a diattenuating element, $\bar{\bar{M}}_D$. This decomposition is given in Equation 2.4 and it is noted that matrix multiplications do not commute in general.

$$\bar{\bar{M}} = \bar{\bar{M}}_\Delta \bar{\bar{M}}_R \bar{\bar{M}}_D \qquad (2.4)$$

Addressing the elements of this polar decomposition in order of their effect on an incident Stokes vector allows one to analyze the effect on that vector in general and its representation in Poincaré space.

A diattenuator preferentially attenuates one component of an incident stokes vector having the effect of projecting an incident Stokes vector onto the diattenuation vector, $\bar{D}$. This is given in Equation 2.5 where D is the magnitude of the diattenuation vector and $\bar{\bar{I}}$ is the identity matrix.

$$\bar{\bar{M}}_D = \begin{bmatrix} 1 & \bar{D}^T \\ \bar{D} & \bar{\bar{m}}_d \end{bmatrix}, \qquad \bar{\bar{m}}_d = \sqrt{1-D^2}\bar{\bar{I}} + \left(1 - \sqrt{1-D^2}\right)\bar{D}\bar{D}^T \qquad (2.5)$$

A retarder simply alters the phase of the components of an input electric field and is modeled in Poincaré space as a rotation of angle Γ about a retarding axis, $\bar{R} = \begin{bmatrix} R_i & R_j & R_k \end{bmatrix}^T$. The Mueller matrix definition of a retarder is given in Equation 2.6 where δ_{ij} and ϵ_{ijk} are the Kronecker delta and Levi-Civitá permutation symbol respectively.

$$\bar{\bar{M}}_R = \begin{bmatrix} 1 & \bar{0}^T \\ \bar{0} & \bar{\bar{m}}_r \end{bmatrix}, \qquad \bar{\bar{m}}_r = \delta_{ij}\cos\left(\Gamma\right) + \epsilon_{ijk}R_k\sin\left(\Gamma\right) + R_iR_j\left(1 - \cos\left(\Gamma\right)\right) \qquad (2.6)$$

Combining just these two elements results in non-depolarizing Mueller matrices. The final element, the depolarizer, serves to shorten an incident Stokes vector frequently but, given non zero polarizance vector, $\bar{R}$ can actually act as a weak polarizer [99]. The most general form of a pure depolarizer is given in Equation 2.7.

$$\bar{\bar{M}}_\Delta = \begin{bmatrix} 1 & \bar{0}^T \\ \bar{P} & \bar{\bar{m}}_\Delta \end{bmatrix}, \qquad \bar{\bar{m}}_\Delta = \bar{\bar{T}}^{-1}\begin{bmatrix} 1-d_1 & 0 & 0 \\ 0 & 1-d_2 & 0 \\ 0 & 0 & 1-d_3 \end{bmatrix}\bar{\bar{T}} \qquad (2.7)$$

The matrix $\bar{\bar{T}}$ is a 3-dimensional rotation matrix between the conventional Poincaré coordinates S_1, S_2, and S_3 to the eigen polarization states of the depolarizer. If the eigen polarizations of

the depolarizer align with the Poincaré coordinates and there is zero polarizance, the form of the depolarizer is a diagonal matrix given in Equation 2.8.

$$\bar{\bar{M}}_\Delta = \begin{bmatrix} 1 & 0 & 0 & 0 \\ 0 & a & 0 & 0 \\ 0 & 0 & b & 0 \\ 0 & 0 & 0 & c \end{bmatrix}, \qquad |a|, |b|, |c| \leq 1 \tag{2.8}$$

With this general decomposition method, the 16 elements of a general Mueller matrix can be recast by 16 degrees of freedom from the decomposition. The diattenuator carries 3 degrees of freedom, the direction of the diatenuation vector. The retarder carries four, three for the direction of the retardance vector and one for the angle of retardance. Finally, the depolarization matrix carries 9 degrees of freedom, where 3 terms define the direction of the polarizance vector, 3 terms define the eigenvector of $\bar{\bar{m}}_\Delta$, and the final 3 define the eigenvalues of the submatrix $\bar{\bar{m}}_\Delta$ [98, 99, 100].

By stacking many instances of diattenuation, retardance, and depolarization in series, the state of light from the lidar transmitter to the receiver are tracked in a similar way as in the scalar lidar equation. The Stokes vector lidar equation (SVLE) is given in Equation 2.9 with the terms described in more detail below. Unlike the scalar lidar equation which had terms grouped for convenience into efficiency terms, the SVLE's terms are matrices and do not commute so their terms are stacked in order of occurrence. Note here that the SVLE also assumes independent scattering as with the scalar lidar equation, but the multiple scattering representation has been included via a product of all propagation and scattering events.

$$N = \bar{O}\bar{\bar{M}}_{R_x}\left(\bar{k}_s\right)\left[\left(G(R)\frac{A}{R^2}\Delta R\right)\left[\prod_{j=1}^{i}\bar{\bar{T}}_{j_{atm}}\left(\bar{k}_{j_s}, R\right)\bar{\bar{F}}_j\left(\bar{k}_{i_j}, \bar{k}_{s_j}, R\right)\right]\bar{\bar{T}}_{atm}\left(\bar{k}_i, R\right)\bar{\bar{M}}_{T_x}\bar{S}_{T_x} + \bar{S}_B(\lambda_{R_x})\right] \tag{2.9}$$

The terms are similarly described as for the scalar lidar equation as follows. Note that the scalar terms lumped in the parenthesis are exactly as they are in the scalar lidar equation except this development assumes they are multiplied by the identity matrix.

(1) The state of light at the exit of the laser is given by $\bar{S}_{T_x}$. This vector is typically normalized for convenience.

(2) The transmitter system is described by any or all of the polar decomposition terms, diattenuation, retardance, or depolarization and is given as $\bar{\bar{M}}_{T_x}\left(\bar{k}_i\right) = \bar{\bar{M}}_{\Delta_{T_x}} \bar{\bar{M}}_{R_{T_x}} \bar{\bar{M}}_{D_{T_x}}$. This term, though technically a function of the transmitter wavelength through the transmitter wave vector, $\bar{k}_i$, is not given as such in Equation 2.9 because of the typically monochromatic nature of lidar transmitters.

(3) The transmission of light from the output of the lidar transmitter to the first scattering event is given by $\bar{\bar{T}}_{atm}\left(\bar{k}_i, R\right) = \bar{\bar{T}}_{\Delta_{atm}} \bar{\bar{T}}_{R_{atm}} \bar{\bar{T}}_{D_{atm}}$ which is a function of the transmit wave vector and range. This terms is often taken as a scaled identity matrix, $\bar{\bar{T}}_{atm}\left(\bar{k}_i, R\right) = T_{T_x}\left(\lambda_{T_x}, R\right)\bar{\bar{I}}$, directly linking the terms in the scalar lidar equation and SVLE.

(4) The scattering phase matrix is given as $\bar{\bar{F}}_j\left(\bar{k}_{i_j}, \bar{k}_{s_j}, R\right) = \bar{\bar{F}}_\Delta \bar{\bar{F}}_R \bar{\bar{F}}_D$. It can be subscripted with a j indicating a multiple scattering model. The representation of this matrix is complicated to a large degree by its dependence on the transmitted and scattered wave vectors. Additionally, its form can be simplified using a number of assumptions about the scatterers including axial symmetry or random orientation, but these simplifications are not always valid. More detail is provided on the scattering phase matrix in Chapter 3.

(5) The second and subsequent transmission matrices are the same as the first transmission matrix except the wave vector through the medium is likely changed. It can be given with or without a subscripted j indicating multiple scattering or single scattering respectively as $\bar{\bar{T}}_{j_{atm}}\left(\bar{k}_{j_s}, R\right) = \bar{\bar{T}}_{\Delta_{atm}} \bar{\bar{T}}_{R_{atm}} \bar{\bar{T}}_{D_{atm}}$. The final transmission matrix must include the path from any arbitrary point within the telescope's field of view to the receiver system.

(6) The Mueller matrix of the receiver system is given as $\bar{\bar{M}}_{R_x}\left(\bar{k}_s\right) = \bar{\bar{M}}_{\Delta_{R_x}} \bar{\bar{M}}_{R_{R_x}} \bar{\bar{M}}_{D_{R_x}}$. The receiver system contains all of the signal Stokes vectors as well as the noise Stokes vectors from sources like light pollution. This term is given in Equation 2.9 as a function of its

incident wave vector as noise is often broadband and scattered signal need not be the same wavelength as the original transmitted wavelength. This element often serves as a polarization analyzer for polarization sensitive systems.

(7) One term that appears only in the SVLE is the observation vector $\bar{O} = \begin{bmatrix} \eta_R & 0 & 0 & 0 \end{bmatrix}$. This is necessary because the polarization of light can not be directly measured, but rather intensity is measured. This vector can either be given as here or as a matrix of polarization vectors. The matrix approach allows for a slightly more compact representation but requires all previous terms of the matrix be block diagonal terms. In either case, the observations of polarization come from the combinations of the observation vector and different configurations of the analyzer.

The two representations of the lidar equation, Equation 2.1 and Equation 2.9, are derived in the same manner and contain similar information, with the SVLE containing more information on the polarization state of light. As such, use of Equation 2.1 is possible for polarization lidar but it requires careful bookkeeping of polarization coupling terms. The utility of both equations is their generality, no scattering effects have yet been specified, but it is a major caveat that most terms in Equation 2.1 and Equation 2.9 can be expanded to include more realistic physical models especially pertaining to scattering.

2.3.1   Nonorthogonal Polarization Retrievals, General Principles

With active remote sensing systems like lidars, the elements of interest are not the elements measured. In Equation 2.9 and throughout this thesis, the elements of interest are contained within the scattering phase matrix, $\bar{\bar{F}}_j \left(\bar{k}_{i_j}, \bar{k}_{s_j}, R \right)$. The inversion of those parameters from measured parameters is of vital importance to the observing capability of lidar systems. General inversions are given by [98, 100, 101, 102], but one critical example is shown here restricting Equation 2.9 to linear polarization transmission and linear polarization retrievers. This is the case for many polarization sensitive lidar systems such as those described by [65, 72, 73, 84, 85, 87, 89, 92, 101, 103, 104, 105].

The number of photons to be observed can be derived in each polarization channel, given in Eq. 2.12, assuming that an arbitrary system emits a linear polarization at angle ϕ from the tilt axis, yielding the simplification $\bar{\bar{M}}_{T_x}\left(\bar{k}_i\right)\bar{S}_{T_x} = \begin{bmatrix} 1 & \cos\left(2\phi\right) & \sin\left(2\phi\right) & 0 \end{bmatrix}^T$, and consists of a linear polarization analyzer, which is a polarizer at angle θ from the reference transmit polarization, specifying that $\bar{\bar{M}}_{R_x}\left(\bar{k}_s\right) = \bar{\bar{R}}\left(\theta\right)\bar{\bar{P}}\bar{\bar{R}}\left(-\theta\right)$. Here $\bar{\bar{R}}\left(\theta\right)$ is the Poincaré space linear rotation matrix given in Equation 2.10 and $\bar{\bar{P}}$ is a general linear polarizer given in Equation 2.11.

$$\bar{\bar{R}}\left(\theta\right) = \begin{bmatrix} 1 & 0 & 0 & 0 \\ 0 & \cos\left(2\theta\right) & -\sin\left(2\theta\right) & 0 \\ 0 & \sin\left(2\theta\right) & \cos\left(2\theta\right) & 0 \\ 0 & 0 & 0 & 1 \end{bmatrix} \qquad (2.10)$$

$$\bar{\bar{P}}\left(\theta\right) = \frac{1}{2}\begin{bmatrix} 1 & 1 & 0 & 0 \\ 1 & 1 & 0 & 0 \\ 0 & 0 & 0 & 0 \\ 0 & 0 & 0 & 0 \end{bmatrix} \qquad (2.11)$$

$$N_M\left(R\right) = \xi\left(R\right)\left[F_{11}\left(R\right) + \cos\left(2\theta\right)F_{12}\left(R\right) + \cos\left(2\phi\right)\left(F_{12}\left(R\right) + \cos\left(2\theta\right)F_{22}\left(R\right)\right) + \sin\left(2\theta\right)\sin\left(2\phi\right)F_{33}\left(R\right)\right]$$

$$(2.12)$$

Here, the number of measured photons incident upon the photodetector, $N_M\left(R\right)$, is a function of transmitted and received polarization angle ϕ and θ, respectively, and is related to the backscattering phase matrix terms, $F_{11}\left(R\right)$, $F_{12}\left(R\right)$, $F_{22}\left(R\right)$, and $F_{33}\left(R\right)$, which are all functions of range. Note that all constant terms of Equation 2.9 which will cancel when taking signal ratios to convert properties to intensive rather than extensive properties are lumped into the term $\xi\left(R\right)$ in Equation 2.12 such as the measurement solid angle, geometric overlap, range resolution, and atmospheric transmission. To invert Equation 2.12 to solve for the backscattering phase matrix elements $F_{11}\left(R\right)$, $F_{12}\left(R\right)$, $F_{22}\left(R\right)$, and $F_{33}\left(R\right)$ would require four unique combinations of transmitter and analyzer angles. The CAPABL lidar system, which will be discussed in greater detail

in Chapter 4, uses $\phi = 45^o$ resulting in the complete cancellation of the dependency of the $F_{22}(R)$ from Eq. 2.12. If then three unique analyzer angles are chosen, a system of three equations and three unknowns can be explicitly stated as given in Equation 2.13.

$$
\begin{bmatrix} N_1(R) \\ N_2(R) \\ N_3(R) \end{bmatrix} = \xi(R) \begin{bmatrix} 1 & \cos(2\theta_1) & \sin(2\theta_1) \\ 1 & \cos(2\theta_2) & \sin(2\theta_2) \\ 1 & \cos(2\theta_3) & \sin(2\theta_3) \end{bmatrix} \begin{bmatrix} F_{11}(R) \\ F_{12}(R) \\ F_{33}(R) \end{bmatrix} \to \bar{N} = \bar{\bar{A}}\bar{F} \tag{2.13}
$$

The general matrix inverse of $\bar{\bar{A}}$ is given in Eq. 2.14, which is not a function of range but only receive polarizations. The term ζ is introduced in Eq. 2.15 as a constraint on the validity of the inversion where $\zeta = 0$ results in a degenerate inversion because of receiver polarization selection.

$$
\bar{\bar{A}}^{-1} = \frac{1}{\zeta} \begin{bmatrix} \sin(2\theta_2 - 2\theta_3) & \sin(2\theta_3 - 2\theta_1) & \sin(2\theta_1 - 2\theta_2) \\ \sin(2\theta_3) - \sin(2\theta_2) & \sin(2\theta_1) - \sin(2\theta_3) & \sin(2\theta_2) - \sin(2\theta_1) \\ \cos(2\theta_2) - \cos(2\theta_3) & \cos(2\theta_3) - \cos(2\theta_1) & \cos(2\theta_1) - \cos(2\theta_2) \end{bmatrix} \tag{2.14}
$$

$$
\zeta = \cos(2\theta_3)(\sin(2\theta_2) - \sin(2\theta_1)) + \cos(2\theta_1)(\sin(2\theta_3) - \sin(2\theta_2)) + \cos(2\theta_2)(\sin(2\theta_1) - \sin(2\theta_3)) \tag{2.15}
$$

A general form of depolarization and diattenuation for CAPABL can be expressed in terms of arbitrary observation angles as given in Eq. 2.16 and Eq. 2.17, respectively, assuming the condition $\zeta \neq 0$. Note that the range dependency of depolarization (d), diattenuation (D), $F_{\#\#}$, and $N_{\#}$ are dropped to simplify the expressions.

$$
\begin{aligned}
d - 1 &= \frac{F_{33}}{F_{11}} = \frac{(\cos(2\theta_3) - \cos(2\theta_2))N_1 + (\cos(2\theta_1) - \cos(2\theta_3))N_2 + (\cos(2\theta_2) - \cos(2\theta_1))N_3}{\sin(2\theta_2 - 2\theta_3)N_1 + \sin(2\theta_3 - 2\theta_1)N_2 + \sin(2\theta_1 - 2\theta_2)N_3} \\
&= \left[\sum_{i,j,k=1}^{3} \frac{|\epsilon_{ijk}| - \epsilon_{ijk}}{2}(\cos(2\theta_i) - \cos(2\theta_j))N_k \right] \left[\sum_{i,j,k=1}^{3} \frac{\epsilon_{ijk} + |\epsilon_{ijk}|}{2}(\sin(2\theta_i - 2\theta_j))N_k \right]^{-1}
\end{aligned} \tag{2.16}
$$

$$D = \frac{F_{12}}{F_{11}} = \frac{(\sin(2\theta_3) - \sin(2\theta_2))\,N_1 + (\sin(2\theta_1) - \sin(2\theta_3))\,N_2 + (\sin(2\theta_2) - \sin(2\theta_1))\,N_3}{\sin(2\theta_2 - 2\theta_3)\,N_1 + \sin(2\theta_3 - 2\theta_1)\,N_2 + \sin(2\theta_1 - 2\theta_2)\,N_3}$$

$$= \left[\sum_{i,j,k=1}^{3} \frac{|\epsilon_{ijk}| - \epsilon_{ijk}}{2} \left(\sin(2\theta_i) - \sin(2\theta_j) \right) N_k \right] \left[\sum_{i,j,k=1}^{3} \frac{\epsilon_{ijk} + |\epsilon_{ijk}|}{2} \left(\sin(2\theta_i - 2\theta_j) \right) N_k \right]^{-1} \quad (2.17)$$

An error analysis of the non-orthogonal polarization retrieval equations for both depolarization d and diattenuation D is also performed for this thesis using a propagation of error. This propagation of error takes the form of a Taylor expansion of each equation assuming each error is not covariant. The depolarization d error bound is given in Equation 2.18 with the partial derivatives explicitly stated given in Equations 2.19-2.20. The diattenuation D error bound is given in Equation 2.21 with the partial derivatives explicitly stated given in Equations 2.22-2.23.

$$\sigma_d = \sqrt{ \sum_{i=1}^{3} \left[\left(\frac{\partial d}{\partial N_i} \right)^2 \sigma_{N_i}^2 + \left(\frac{\partial d}{\partial \theta_i} \right)^2 \sigma_{\theta_i}^2 \right] } \quad (2.18)$$

$$\frac{\partial d}{\partial N_K} = \left[\sum_{i,j=1}^{3} \frac{|\epsilon_{ijK}| - \epsilon_{ijK}}{2} \left(\cos(2\theta_i) - \cos(2\theta_j) \right) N_K^0 \right] \left[\sum_{i,j,k=1}^{3} \frac{\epsilon_{ijk} + |\epsilon_{ijk}|}{2} \left(\sin(2\theta_i - 2\theta_j) \right) N_k \right]^{-1}$$

$$- \left[\sum_{i,j,k=1}^{3} \frac{|\epsilon_{ijk}| - \epsilon_{ijk}}{2} \left(\cos(2\theta_i) - \cos(2\theta_j) \right) N_k \right] \left[\sum_{i,j=1}^{3} \frac{\epsilon_{ijK} + |\epsilon_{ijK}|}{2} \left(\sin(2\theta_i - 2\theta_j) \right) N_K^0 \right]$$

$$\left[\sum_{i,j,k=1}^{3} \frac{\epsilon_{ijk} + |\epsilon_{ijk}|}{2} \left(\sin(2\theta_i - 2\theta_j) \right) N_k \right]^{-2} \quad (2.19)$$

$$\frac{\partial d}{\partial \theta_I} = \left[\sum_{j,k=1}^{3} \left(\epsilon_{Ijk} - |\epsilon_{Ijk}| \right) \sin(2\theta_I) \left(N_j - N_k \right) \right] \left[\sum_{i,j,k=1}^{3} \frac{\epsilon_{ijk} + |\epsilon_{ijk}|}{2} \left(\sin(2\theta_i - 2\theta_j) \right) N_k \right]^{-1}$$

$$- \left[\sum_{i,j,k=1}^{3} \frac{|\epsilon_{ijk}| - \epsilon_{ijk}}{2} \left(\cos(2\theta_i) - \cos(2\theta_j) \right) N_k \right] \left[\sum_{j,k=1}^{3} \left(\epsilon_{Ijk} + |\epsilon_{Ijk}| \right) \left(\cos(2\theta_I - 2\theta_j) \right) N_k \right]$$

$$\left[\sum_{i,j,k=1}^{3} \frac{\epsilon_{ijk} + |\epsilon_{ijk}|}{2} \left(\sin(2\theta_i - 2\theta_j) \right) N_k \right]^{-2} \quad (2.20)$$

$$\sigma_D = \sqrt{\sum_{i=1}^{3}\left[\left(\frac{\partial D}{\partial N_i}\right)^2\sigma_{N_i}^2 + \left(\frac{\partial D}{\partial \theta_i}\right)^2\sigma_{\theta_i}^2\right]} \tag{2.21}$$

$$\begin{aligned}
\frac{\partial D}{\partial N_K} =& \left[\sum_{i,j=1}^{3}\frac{|\epsilon_{ijK}|-\epsilon_{ijK}}{2}\left(\sin(2\theta_i)-\sin\left(2\theta_j\right)\right)N_K^0\right]\left[\sum_{i,j,k=1}^{3}\frac{\epsilon_{ijk}+|\epsilon_{ijk}|}{2}\left(\sin\left(2\theta_i-2\theta_j\right)\right)N_k\right]^{-1}\\
&-\left[\sum_{i,j,k=1}^{3}\frac{|\epsilon_{ijk}|-\epsilon_{ijk}}{2}\left(\sin(2\theta_i)-\sin\left(2\theta_j\right)\right)N_k\right]\left[\sum_{i,j=1}^{3}\frac{\epsilon_{ijK}+|\epsilon_{ijK}|}{2}\left(\sin\left(2\theta_i-2\theta_j\right)\right)N_K^0\right]\\
&\left[\sum_{i,j,k=1}^{3}\frac{\epsilon_{ijk}+|\epsilon_{ijk}|}{2}\left(\sin\left(2\theta_i-2\theta_j\right)\right)N_k\right]^{-2} \tag{2.22}
\end{aligned}$$

$$\begin{aligned}
\frac{\partial D}{\partial \theta_I} =& \left[\sum_{j,k=1}^{3}\left(|\epsilon_{Ijk}|+\epsilon_{Ijk}\right)\cos(2\theta_I)\left(N_j-N_k\right)\right]\left[\sum_{i,j,k=1}^{3}\frac{\epsilon_{ijk}+|\epsilon_{ijk}|}{2}\left(\sin\left(2\theta_i-2\theta_j\right)\right)N_k\right]^{-1}\\
&-\left[\sum_{i,j,k=1}^{3}\frac{|\epsilon_{ijk}|-\epsilon_{ijk}}{2}\left(\sin(2\theta_i)-\sin\left(2\theta_j\right)\right)N_k\right]\left[\sum_{j,k=1}^{3}\left(\epsilon_{Ijk}+|\epsilon_{Ijk}|\right)\left(\cos\left(2\theta_I-2\theta_j\right)\right)N_k\right]\\
&\left[\sum_{i,j,k=1}^{3}\frac{\epsilon_{ijk}+|\epsilon_{ijk}|}{2}\left(\sin\left(2\theta_i-2\theta_j\right)\right)N_k\right]^{-2} \tag{2.23}
\end{aligned}$$

This example inversion, based on the SVLE can be used to determine the components of the scattering phase matrix and an error estimate in terms of its polar decomposition elements depolarization and diattenuation. Note that the restriction of linear polarization observation and linear receive polarizations masks the retardance element of the phase matrix polar decomposition, which are all contained within the circular polarizations.

2.3.2 Orthogonal Polarization Retrievals, A Special Case

Retrieval of phase matrix elements must be rooted in physical scattering effects. It is of no use to measure the elements of the phase matrix of the atmosphere or clouds if they can not be uniquely tied to micro or macrophysical properties of the atmosphere and clouds. The first known attempt to relate the terms of these polar decomposition matrices in Equation 2.4 was by Höhn

who tried to relate depolarization to atmospheric turbulence [64]. Shortly thereafter, Schotland et al. linked depolarization to the shape of a scatterer [65]. More details on this attempt will be given in Chapter 3, but broadly speaking small spherical particles like cloud water droplets do not depolarize a laser beam when singularly scattered while irregular particles like ice crystals depolarize a laser beam significantly. Many subsequent operational lidar systems use this effect to parse cloud water thermodynamic phase and aerosol types based on their shape [50, 51, 52, 82, 85, 101, 104, 106, 107]. Further advancement has been undertaken by combining measurements of depolarization ratios at many wavelengths leveraging different electrical sizes of scatterer [69, 108, 109]. To the author's knowledge, one attempt has been made to add diattenuation measurements to depolarization measurements, which is related to particle orientation [89, 100, 105]. There have been, to the author's knowledge, two further attempts to characterize full scattering phase matrices with the depolarization, diattenuation and retarding terms [110, 111].

Most polarization lidar systems that are currently in operation today measure depolarization using orthogonal polarizations [71, 82, 101, 102, 103, 104]. With the notable exception of Flynn et al. [82] and the works of Kaul et al. [110] and Hayman et al. [111], depolarization is frequently measured with linear transmit and receiver polarizations. Flynn et al. uses orthogonal polarization states but chooses circular and linear. The derivation of depolarization given in Equation 2.16 can easily be simplified to orthogonal polarization states. In general, diattenuation and retardance are assumed to be zero by assuming random orientation, i.e. Equation 2.17 equals zero. This simplifies the expression for returned photon counts in terms of Mueller matrix elements, Equation 2.12, to a simple function of two terms: $F_{11}(R)$ and $F_{22}(R)$, $F_{33}(R)$, or $F_{44}(R)$.

Chapter 3

Atmospheric Scattering

3.1   Elastic Scattering

Much of the complexity of lidar represented in the lidar equation is related to the specification and understanding of the exact way light interacts with the medium through which it propagates and by which it is scattered or absorbed. Only by precisely understanding the interaction of light with this medium can one hope to retrieve properties of the medium from measurements of radiation. In particular, an understanding of scattering is required in the specification of the backscattering efficiency or the scattering phase matrix, the transmission efficiency or transmission Mueller matrices, and the background photons or background Stokes vector. These represent absorption, scattering, and emission processes that need to be understood to uniquely retrieve properties of the medium of interest from the possible measurements.

Many models exist to quantitatively describe the interaction of light with matter, which incorporate different physical scattering effects, but they vary in their assumptions and physical realism. Elastic scattering, or scattering that occurs without an apparent change in wavelength, is one common interaction which occurs for lidar systems. Elastic scattering can occur by particles both large and small compared to the wavelength of light and by axially symmetric or irregular shaped particles in general, but the behavior of light is tightly linked to the size and shape of the scatterers. The size of the wavelength of light with respect to the scatterer is easily compared using the electrical size of the scatterer, x, given in Equation 3.1, where a is the diameter of the scatterer and λ is the wavelength of interest [93, 112, 113]. For small scatterers like molecular oxygen and

nitrogen, the diameter is difficult to visualize but is often taken to be the bond length between atoms. For values of $x \ll 1$, the Rayleigh scattering model is useful which is not dependent on the scatterer shape [114, 53, 112, 113, 115, 116, 117]. For values approximately $0.1 \leq x \leq 100$, resonant effects dominate the scattering cross section [112]. For spherical particles, Mie theory is developed. For non-spherical particles more sophisticated methods like T-matrix codes or non-spherical basis functions are used [118, 119, 120]. For particles $x \gg 1$, geometric optics can be used [96].

$$x = \frac{2\pi a}{\lambda} \tag{3.1}$$

3.1.1   Rayleigh Scattering

One problem of practical importance within elastic scattering is Rayleigh scattering, which is the interaction of light with a particle much smaller than the wavelength of light. This occurs frequently at optical wavelengths for atmospheric gases like diatomic nitrogen, diatomic oxygen, water vapor, and many others. The bond length of such molecules are often on the order of angstroms (0.1 nm) with interactions of light on the order of hundreds of nm [20]. Therefore, light's interaction with much of the atmospheric gases can be well modeled as Rayleigh scattering.

From the perspective of classical mechanics, Rayleigh scattering can be modeled as a wave impinging on a dipole driving the molecule to oscillate which in turn radiates a field [114, 115]. The field incident and resulting from the dipole oscillation are at the same frequency. The direction and overall magnitude of the radiated field is a function of the incident wave's polarization, or orientation, as dipoles can not radiate in the direction they oscillate. From the perspective of quantum mechanics, Rayleigh scattering is a two photon instantaneous process. A photon is absorbed and a second photon emitted simultaneously. If the photons are at the same frequency, the particle maintains its overall energy [114, 115]. Both pictures are valid and allow for quantitative prediction of the state of the scattered light based on the state of the incoming light.

One method for determining the scattering cross section of a scatterer was introduced by Placzek with his polarizability theory [115]. By distilling all of the information contained within

a scatterer into a polarizability tensor, one could describe the scattering cross section in terms of the mean polarizability, α, and the anisotropy of the polarizability tensor, γ. From the scattering tensor alone, the backscattering cross section can be calculated as given in Equation 3.2.

$$\sigma_{Ray} = \left(\frac{\pi^2}{\epsilon_o^2}\right)\tilde{\nu}^4\left(\alpha^2 + \frac{7}{180}\gamma^2\right) = (2\pi\tilde{\nu})^4\left(\frac{\alpha^2}{(4\pi\epsilon_o)^2} + \frac{7}{180}\frac{\gamma^2}{(4\pi\epsilon_o)^2}\right) \qquad (3.2)$$

Here, ϵ_o is the permittivity of vacuum and $\tilde{\nu}$ is the incident frequency. The spectroscopic constants for oxygen and nitrogen to calculate Rayleigh backscattering cross sections of air are given in Table 3.1 [50, 114].

Table 3.1: Spectroscopic constants for nitrogen and oxygen to calculate the Rayleigh backscattering cross section of air [50, 114]. Note that the second piece of Equation 3.2 is given to clarify the constants and units provided by Weitkamp et al. [50]. The derivative of the polarizability and anisotropy of the polarizability tensor are also given used in Section 3.2.2.

Gas	$\alpha^2/(4\pi\epsilon_o)^2$	$\gamma^2/(4\pi\epsilon_o)^2$	$\alpha'^2/(4\pi\epsilon_o)^2$	$\gamma'^2/(4\pi\epsilon_o)^2$
Nitrogen	$3.17\times10^{-60}\ m^6$	$0.52\times10^{-60}\ m^6$	$2.62\times10^{-14}\ m^4/kg$	$4.23\times10^{-14}\ m^4/kg$
Oxygen	$2.66\times10^{-60}\ m^6$	$1.26\times10^{-60}\ m^6$	$1.63\times10^{-14}\ m^4/kg$	$6.46\times10^{-14}\ m^4/kg$

3.1.2   Mie Theory

Rayleigh scattering can be derived in a number of ways including the small particle solution of the sphere problem. The sphere problem considers the interaction of a field with a sphere of arbitrary size [112]. Many solutions have been given but it is often attributed to Gustov Mie who solved the problem by expressing the interaction of a spherical surface with uniform plane waves in spherical coordinates. Specifically, Mie performed a separation of variables on the vector Helmholtz equations expanding the incident, internal, and scattered electric field from a sphere in vector spherical harmonics. The result are three seperated equations which can be solved by harmonic functions, Legendre functions, and spherical Bessel functions. In terms of atmospheric scattering, Mie theory can predict the scattering cross section and angular distribution of scattering from small particles like diatomic molecules and from larger spherical particles like liquid water droplets in clouds exactly. It does not solve for scattering in large asymmetric particles like ice

crystals but is often considered as a starting point for such problems.

Mie's solution can describe both the scattering cross section of the sphere as well as the angular distribution of light scattered. The theory expands the incident, internal, and scattered waves in terms of spherical harmonics and represents all in terms of an infinite series of coefficients, referred to as the Mie a and b coefficients. The Mie a and b coefficients are computed by matching boundary conditions for the incident, internal, and scattered waves on the boundary of the sphere. These coefficients are given in Equation 3.3 and Equation 3.4 where m is the complex index of refraction, x the electrical size of a scatterer as given in Equation 3.1, j_n is a spherical Bessel function of the first kind of order n, and h_n is a spherical Hankel function, which is a combination of spherical Bessel functions of the first and second kind, of order n.

$$a_n^s(m, x) = -\frac{j_n(mx)[xj_n(x)]' - j_n(x)[mxj_n(mx)]'}{j_n(mx)[xh_n^{(2)}(x)]' - h_n^{(2)}(x)[mxj_n(mx)]'} \tag{3.3}$$

$$b_n^s(m, x) = -\frac{j_n(x)[mxj_n(mx)]' - m^2 j_n(x)[xj_n(x)]'}{h_n^{(2)}(x)[mxj_n(mx)]' - m^2 j_n(mx)[xh_n^{(2)}(x)]'} \tag{3.4}$$

Figure 3.1 shows the absolute value of the first 40 Mie a and b coefficients for scatterers of electrical size $x = 0.1$, $x = 1$, $x = 10$, and $x = 20$. Take for example the scatterer with $x = 20$, one can see that the terms are not negligible but decrease precipitously after approximately the 23rd index. As a practical matter, a Mie infinite series expansion can be truncated to just a few terms as a function of the electrical size of the scatterer [112, 121].

The total scattering and backscattering efficiencies can be given in terms of the scattered field Mie a and b coefficients as an infinite series in Equation 3.5 and Equation 3.6, respectively. The total scattered field is an average over all scattering angles whereas backscattered refers to scattering at $\Theta = 180°$. Figure 3.2 shows the shape of both total scattering and backscattering efficiency curves as a function of electrical size, x.

$$\eta_s = \frac{\sigma_s}{\pi a^2} = \frac{2}{x^2} \sum_{n=1}^{\infty} (2n+1) \left(|a_n^s|^2 + |b_n^s|^2 \right) \tag{3.5}$$
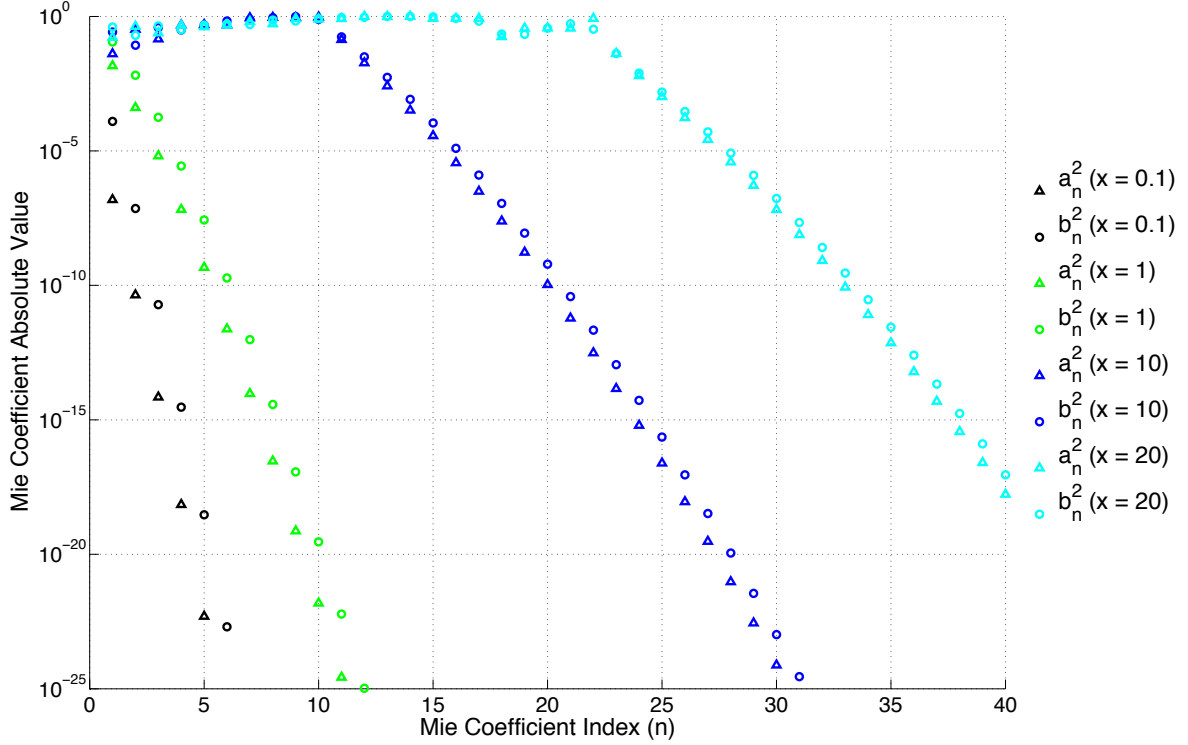
Figure 3.1: The absolute value of the first 40 Mie a and b scattered field coefficients for 4 different electrical size parameters: $x = 0.1$, $x = 1$, $x = 10$, and $x = 20$. The subsequent terms of the expansion fall off precipitously indicating that an approximation, that a full summation including the Mie a and b coefficients can be well expressed with its first few terms, is reasonable.

$$\eta_b = \frac{\sigma_b}{\pi a^2} = \frac{1}{x^2} \left| \sum_{n=1}^{\infty} (-1)^n (2n+1)(a_n^s - b_n^s) \right|^2 \tag{3.6}$$

The angular dependence of the scattering can also be calculated via Mie theory. The angular building blocks are the recursively defined Legendre polynomials divided by $\sin(\theta)$ and the derivative of the Legendre polaynomials given in Equation 3.7 and Equation 3.8, respectively. These functions are a direct result of the separation of variables used to derive Mie theory.

$$\pi_0 = 0$$
$$\pi_1 = 1 \tag{3.7}$$
$$\pi_n = \frac{2n-1}{n-1} \cos(\theta) \pi_{n-1} - \frac{n}{n-1} \pi_{n-2}$$
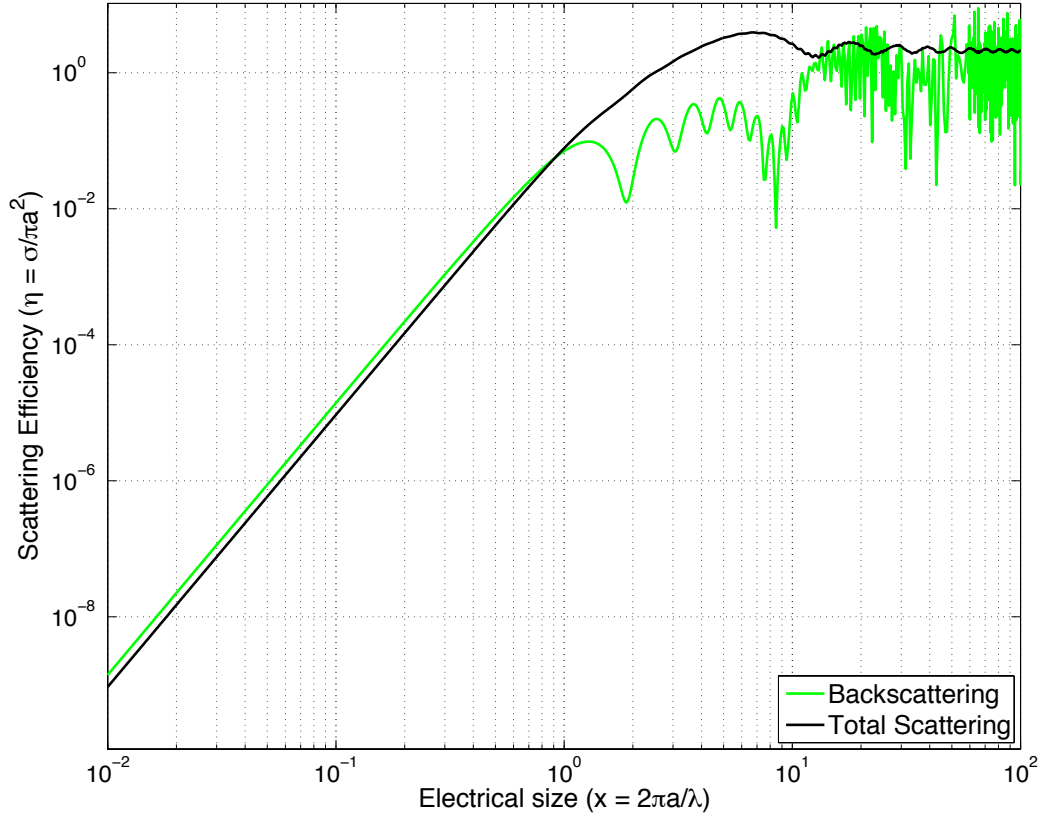
Figure 3.2: The Mie scattering efficiency for both back scattering and total scattering as a function of electrical size. The λ^{-4} behavior of Rayleigh scattering can be seen for electrical sizes approximately $x \leq 0.1$.

$$\tau_0 = 0$$

$$\tau_1 = \cos(\theta) \tag{3.8}$$

$$\tau_n = n \cos(\theta)\, \pi_n - (n+1)\, \pi_{n-1}$$

Combining the Mie a and b coefficients and the Legendre polynomials yields a pair of scattering functions, $S_1(\Theta)$ given in Equation 3.9 and $S_2(\Theta)$ given in Equation 3.10, which are functions of the scattering elevation angle, Θ. From these functions, the backscattering phase matrix of a spherical scatterer of any arbitrary size can be written explicitly.

$$S_1(\Theta) = \sum_{n=1}^{\infty} \frac{(2n+1)}{n(n+1)} \left[a_n \pi_n(cos\Theta) + b_n \tau_n(cos\Theta) \right] \tag{3.9}$$

$$S_2(\Theta) = \sum_{n=1}^{\infty} \frac{(2n+1)}{n(n+1)} \left[b_n \pi_n(cos\Theta) + a_n \tau_n(cos\Theta) \right] \tag{3.10}$$

The entries of the backscattering phase matrix are given in Equations 3.11, 3.12, 3.13, and 3.14 with the full scattering phase matrix given in Equation 3.15. Here the * symbol is the complex conjugate. Note that all the terms, $S_{11}(\Theta)$, $S_{12}(\Theta)$, $S_{33}(\Theta)$, and $S_{34}(\Theta)$, are strictly real by the definition of the Mueller matrices.

$$S_{11}(\Theta) = \frac{1}{2} \left[|S_2(\Theta)|^2 + |S_1(\Theta)|^2 \right] \tag{3.11}$$

$$S_{12}(\Theta) = \frac{1}{2} \left[|S_2(\Theta)|^2 - |S_1(\Theta)|^2 \right] \tag{3.12}$$

$$S_{33}(\Theta) = \frac{1}{2} \left[S_2^*(\Theta) S_1(\Theta) + S_2(\Theta) S_1^*(\Theta) \right] \tag{3.13}$$

$$S_{34}(\Theta) = \frac{1}{2} \left[S_2^*(\Theta) S_1(\Theta) - S_2(\Theta) S_1^*(\Theta) \right] \tag{3.14}$$

$$\bar{\bar{M}}_{Mie}(\Theta) = \begin{bmatrix} S_{11}(\Theta) & S_{12}(\Theta) & 0 & 0 \\ S_{12}(\Theta) & S_{11}(\Theta) & 0 & 0 \\ 0 & 0 & S_{33}(\Theta) & S_{34}(\Theta) \\ 0 & 0 & S_{34}(\Theta) & S_{33}(\Theta) \end{bmatrix} \tag{3.15}$$

An example of the scattering phase matrix terms as a function of angle is given in Figure 3.3 for the 4 electrical sizes presented in Figure 3.1. Figure 3.3 contains some exceptionally important conclusions as they relate to lidar retrievals. Foremost, for spheres in the backscattering direction, the values of $S_{12}(\Theta = 180°)$ and $S_{34}(\Theta = 180°)$ are strictly equal to 0 and the normalized value of $S_{33}/S_{11}(\Theta = 180°)$ is strictly equal to -1. This result is not dependent on the electrical size of the scatterer as long as it is spherical. This means that the Mueller matrix of any spherical or small atmospheric scatterer, in the backscattering direction, is a diagonal matrix with values of either 1 or -1 on the diagonal, given in Equation 3.16. In terms of the Mueller matrix decomposition given in Chapter 2, Mie scatterers have zero net depolarization term in the backscattering direction, no polarizance, and no diattenuation. Mie scatterers can be modeled as attenuating half wave retarders with their fast axis along the S_1 Stokes direction.
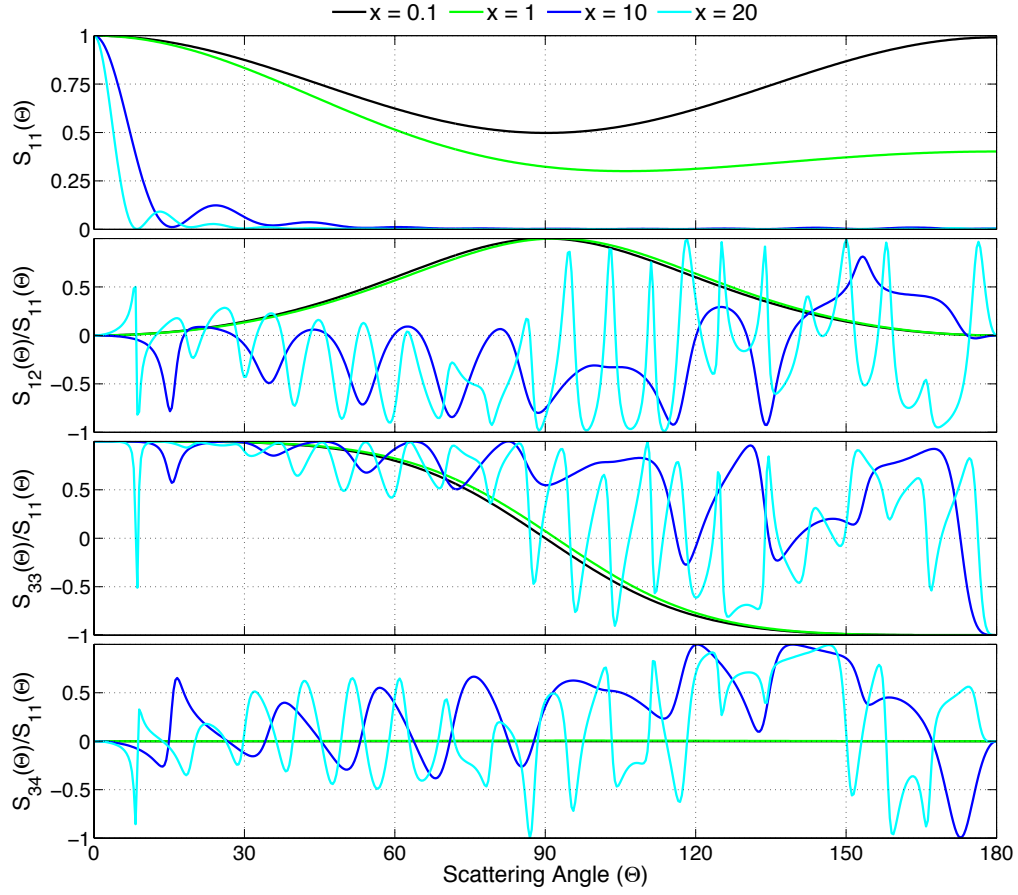
Figure 3.3: Angular dependent elements of the Mie scattering phase matrix as a function of angle, Θ, between the incident and scattered polarization. The color codes and electrical sizes correspond to the Mie coefficients given in Figure 3.1. The S_{11} terms are normalized to their $\Theta = 0$ element. The other 3 terms, S_{12}, S_{33}, and S_{34} are normalized to $S_{11}(\Theta)$ at the corresponding angle. Note that the highly resonant behavior modeled is typically smoothed to a large degree by the polydisperse nature of atmospheric scatterers. For a size distribution of scatterers, the overall phase function is the integral of the phase functions with respect to size as a function of scattering angle.

$$\bar{\bar{M}}_{Mie}(\Theta = 180^\circ) = S_{11}(\Theta = 180^\circ) \begin{bmatrix} 1 & 0 & 0 & 0 \\ 0 & 1 & 0 & 0 \\ 0 & 0 & -1 & 0 \\ 0 & 0 & 0 & -1 \end{bmatrix} \tag{3.16}$$

One other important result to take from Figure 3.3 is that the nondepolarization of spheres is strictly only in the backscattering direction. If more than one scattering event takes place,

Mie scatterers can depolarize, retard, and diattenuate. Multiple scattering from liquid clouds and single scattering from ice clouds can have the similar effects on the polarization signatures if multiple scattering is not considered or isolated.

3.2   Inelastic Scattering

Inelastic scattering, or Raman scattering, is defined as scattering of light where the incident and scattered frequencies are not the same. This phenomenon was named for Chandrasekhara Venkata Raman who discovered the effect in liquids in 1928. It is quantitatively best described in the photon picture of light, though vibrational Raman can be described qualitatively in the wave picture of light. Strictly, Raman scattering is a two photon process where the incident and scattered photons are at different frequencies where the frequency change is related to the energy structure of the atomic or molecular scatterer [114, 19]. Because no two atoms or molecules have the same energy structure, their full Raman spectra are unique (though some atoms share similar transition energies) and can be used to identify a constituent. The frequency shift and magnitude of the scattering cross section of a scatterer are the critical pieces of information required by the lidar equation to fully describe the scattering phase matrix, $\bar{\bar{F}}\left(\bar{k}_i, \bar{k}_s, R\right)$.

3.2.1   Rotational and Vibrational Transitions

Some molecules have Raman spectra that can be solved analytically using reasonable physical models. Others must be solved numerically. Some molecules have modes that are not Raman active at all. The starting point for all calculations of Raman spectra is the definition of the Hamiltonian. For molecules like diatomic oxygen or nitrogen, the Hamiltonian is straightforward to calculate and can be solved within the time-independent Schrödinger equation using methods originally used to solve for the energy structure of the hydrogen atom [50, 114, 19, 20]. Other molecules, such as water, have Hamiltonians that can only be solved within the time-independent Schrödinger equation numerically due to mixing of energy modes resulting in effects like Fermi resonance [122, 123, 124].

For diatomic molecules a trick is used where the two atoms are condensed into one by using

spherical coordinates and a reduced mass. Effectively, the Hamiltonian of two atoms can be simplified into a Hamiltonian, which is of the form of the hydrogen atom. The fully time-dependent Schrödinger's equation can be separated into time-dependent and time-independent equations. The time-independent equation takes the form of an eigenvalue problem, which can be cast into spherical coordinates with the radial and angular components separated via a separation of variables method. The result is that one can separate rotational and vibrational motions of diatomic molecules. The full derivation of this procedure is shown in Appendix 8.3.1 for completeness with the results used here with no further proof. One can then assume a physical model of a diatomic molecule to determine the exact energy structure. Two common models are a rigid rotor and a harmonic oscillator.

The quantization of the energy levels for a rigid rotor is demonstrated in Appendix 8.3.2. The quantization is given in Equation 3.17 where E is the energy level, h, $\hbar$, and c are Planck's constant, the reduced Planck's constant, and the speed of light, respectively, I is the moment of inertia of the diatomic molecule about the spin axis, and J is the quantum number, which is an element of the integers.

$$\frac{E}{hc} = \frac{\hbar}{2I} J(J+1) = B_o J(J+1) \tag{3.17}$$

This model can be extended to model non-rigid rotations by expanding Equation 3.17 in a power series. This work will take on higher order term, which results in a final rotational quantization condition given in Equation 3.18. The physical reason for the necessity of the extension is that rotating molecules tend to deform slightly due to centrifugal forces. This distortion is more pronounced for rotations with higher energy. As such, it is a second order consideration and for rotational levels of interest will yield a minimal correction. Note that it is not possible to calculate this energy quantization relation from classical theory as there is no reason in classical theory that rotational motions should be quantized [114].

$$\frac{E}{hc} = B_o J \left(J + 1\right) - D_o J^2 \left(J + 1\right)^2 \tag{3.18}$$

The vibrational quantization condition is given in Equation 3.19 with no anharmonic correction as derived in Appendix 8.3.3. Here, K is the diatomic molecule harmonic oscillator restoring force, μ is the reduced mass of the molecule, $\hbar$ is the reduced Planck's constant, and v is the vibrational quantum number, which is an element of the integers. The constant terms can be condensed into a single constant, $\tilde{\nu}_{vib}$, which is the ground diatomic vibration constant for a molecule. This relation can be attained from classical theory considering the Raman vibrational scattering modes as beat frequencies of the incident wave and the vibrational motion of the molecule.

$$\frac{E}{hc} = \left(v + \frac{1}{2}\right) \hbar \sqrt{\frac{K}{\mu}} = \tilde{\nu}_{vib} \left(v + \frac{1}{2}\right) \tag{3.19}$$

The utility of the separate quantization conditions is based on the condition that the energies of both rotation and vibration are additive. This is a form of Born-Oppenheimer approximation which strictly assumes that nuclear and electronic motion are decoupled. Within this approximation, the total energy of an atom or molecule can be separated into electronic, vibrational, and rotational energies [20]. The results of Equation 3.18 and Equation 3.19 are thus combined into the ro-vibrational energy of a molecular scatterer, given in Equation 3.20.

$$E_{ro/vib} = hc_o \left[\tilde{\nu}_{vib} \left(v + \frac{1}{2}\right) + B_v J(J + 1) - D_v \left(J(J + 1)\right)^2 \right] \tag{3.20}$$

The energies presented in Equation 3.20 are the states in which a diatomic molecular scatterer can exist and are also the eigenvalues of the time-independent Schrödinger's equation for diatomic molecules, like nitrogen and oxygen. The transition between these states during scattering is the reason for the shift in scattered photon frequency from incident photon frequency. This transition energy calculated in Equation 3.21 directly relates to the observed Raman spectrum and is useful to calculate the energy shift of scattered photons for pure rotational, pure vibrational, and ro-vibrational molecular transitions.

$$\frac{\Delta E}{hc_o} = \tilde{\nu}_{vib} (v_2 - v_1) + [B_{v_2} J_2(J_2 + 1) - B_{v_1} J_1(J_1 + 1)] - \left[D_{v_2} \left(J_2(J_2 + 1) \right)^2 - D_{v_1} \left(J_1(J_1 + 1) \right)^2 \right]$$

(3.21)

The major caveat that is needed to understand Raman spectra are the selection rules that define how an atom or molecule can transition from one quantum state to another. There are limitations on the relations between rotational quantum numbers J_1 and J_2 in Equation 3.21. Considering that photons are bosonic with spin equal to one, the selection rules can be determined knowing they can only change total spin by one. As Raman scattering is a two photon process and each photon can change the total spin, the selection rule is $\Delta J = 0, \pm 2$. If one photon serves to increase and the other to decrease the overall spin, then $\Delta J = 0$ is observed. If both photons serve to reduce or increase the overall spin, then $\Delta J = \pm 2$ is observed.

As a practical concern for atmospheric scattering, not all Raman transitions are readily observable based on atmospheric temperatures. To have a Raman transition from one energy level to another, a molecule must exist on that energy level to initiate a transition. Knowledge of the population of molecules at each energy level is required. The occupation of energy levels is thermal, a function of temperature by the factor $k_B T$ where k_B is the Boltzmann constant and T is temperature on an absolute temperature scale. The probability of a photon existing in a thermal state is given in Equation 3.22 [20]. Note that the denominator of Equation 3.22 is referred to as the partition function.

$$p_i = \frac{e^{-\frac{E_i}{k_B T}}}{\sum_{j=1}^{M} e^{-\frac{E_j}{k_B T}}}$$

(3.22)

The ratio of state probabilities follows the Boltzmann distribution given in Equation 3.23. In this case, the thermally available energy in wave numbers is $\frac{k_B T}{hc}$, which at terrestrial temperatures is approximately $208 \, cm^{-1}$. Rotational energy level spacing is on the order of $10^1 \, cm^{-1}$ to $10^2 \, cm^{-1}$; vibrational energy level spacing is on the order of $10^3 \, cm^{-1}$; electronic energy level spacing even greater. Therefore at terrestrial temperatures, only the ground electronic and vibrational states are

occupied but many rotational levels can be occupied. As a side note, this makes the above assumed harmonic oscillator model for vibrational quantization a good approximation without needing to add correction terms in the form of a power series for anharmonic stretching.

$$\frac{P_i}{P_j} = \frac{\exp\left(\frac{-E_i}{k_B T}\right)}{\exp\left(\frac{-E_j}{k_B T}\right)} = \exp\left(-\frac{E_i - E_j}{k_B T}\right) \tag{3.23}$$

With all of this in mind, the Raman spectrum for major atmospheric constituents can be produced. First, the energy levels for nitrogen are calculated with constants B_0, B_1 and $\tilde{\nu}_{vib}$ from Equation 3.18 and Equation 3.19 given in Table 3.2 from Weitkamp et al. [50]. Next, all the possible transitions from the ground and first vibrationally excited energy state are given superimposed upon the energy level diagram. This includes both Stokes and anti-Stokes transitions where Stokes transitions result in scattered photons with lower energy than incident photons and molecules with higher rotational or vibrational quantum numbers than before scattering. Anti-Stokes is the opposite with scattered photons having higher energy than incident photons resulting from a drop in quantum numbers. These transitions are named for George Stokes who showed that fluorescence from atoms and molecules will always yield photons of lower frequency than incident photons due to intersystem crossings resulting in some energy description due to non-radiative transitions. This energy level structure and Raman transition set is given in Figure 3.4.

Table 3.2: Spectroscopic constants to calculate rotational and vibrational energy level offsets for the ground state for both oxygen and nitrogen copied from Weitkamp et al. [50]. Note that the constants are given in units of cm^{-1}. To convert to energy, one simply needs to multiply by hc_o (Planck's constant times the speed of light in vacuum). This is already done in Equation 3.21. It is however important to note that the speed of light must be given in the units of cm/s instead of the more common m/s. The units are given in inverse wave numbers in cm typically by spectroscopists because the numbers look more reasonable. Energy numbers are given in the thousands instead of $\times 10^{-20}$.

Gas	$\tilde{\nu}_{vib}$	B_0	B_1	D_0
Nitrogen	$2330.7 \; cm^{-1}$	$1.98957 \; cm^{-1}$	$1.97219 \; cm^{-1}$	$5.76 \times 10^{-6} \; cm^{-1}$
Oxygen	$1556.4 \; cm^{-1}$	$1.42768 \; cm^{-1}$	$1.42188 \; cm^{-1}$	$4.85 \times 10^{-6} \; cm^{-1}$

Considering all these effects given above, the Raman transitions that are observable in the
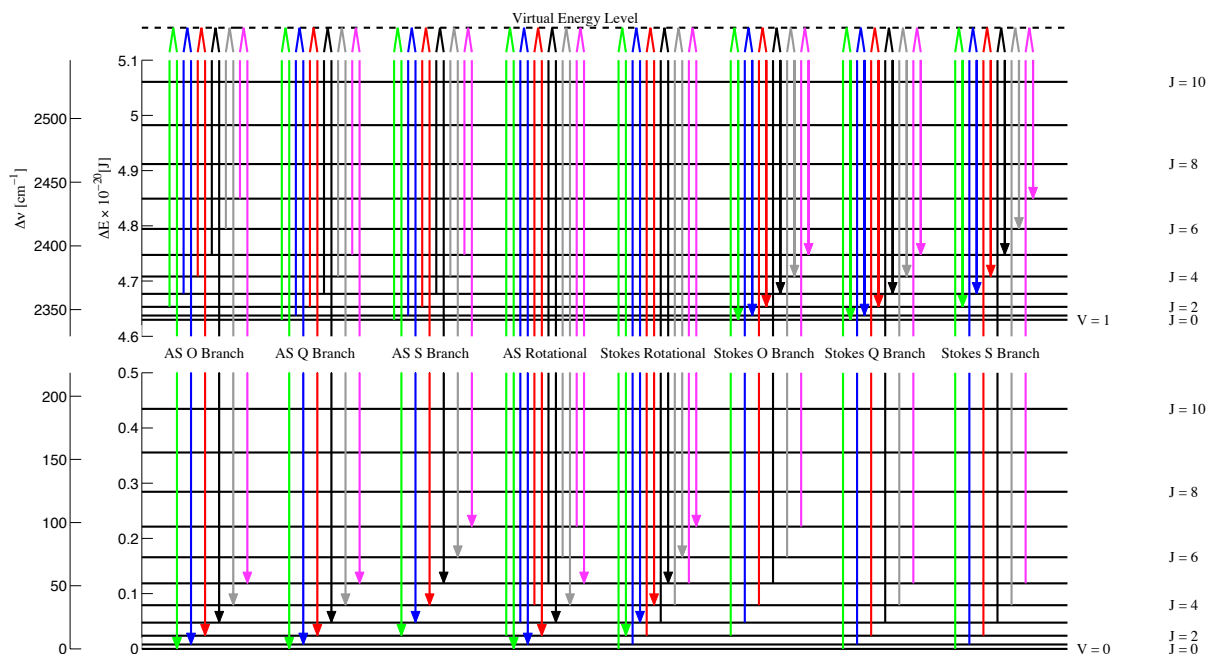
Figure 3.4: An energy level diagram for diatomic nitrogen. The quantum numbers for each energy state are given to the right where the vibrational quantum number is v and the rotational quantum number is J. In standard spectroscopic notation, O, Q, and S branches are linked to $\Delta J = -2$, $\Delta J = 0$, and $\Delta J = 2$ respectively. Here AS is "anti-Stokes". Only the first two vibrational levels are shown because at terrestrial temperatures the thermally available energy is approximately 208 cm^{-1} indicating only the ground vibrational state will be occupied significantly. Finally, the y-axis is given in energy in units of J; to convert to cm^{-1}, one needs to divide that unit by hc where the speed of light is given in cm/s.

atmosphere are Stokes vibrational Raman, and Stokes and anti-Stokes rotational Raman transitions. Anti-Stokes vibrational Raman causes exceptionally weak signals because of extremely limited thermal population of scatterers in the atmosphere.

3.2.2 Raman Scattering Cross Section

The scattering cross sections of Raman scattering transitions can be calculated as was first discussed by Placzek [115]. If a photon comes within the area, which is defined by the scattering cross section, the photon will be scattered. This area can be multiplied by a number density to determine the interactions per meter that one would expect due to scattering from a particular molecule.

General equations for the transitions between quantum states are given both by Placzek and Long in terms of the polarizability tensor [114, 115]. The equations presented in these works are very general but not particularly tractable. The reason for this is that the transition probability relates to the summation of probabilities over all the possible paths from one energy level to the second. Pending all the complications that one is willing to accept, these apply to very general transition situations but are fairly opaque. However, if systems are confined by a few approximations, the complexity can be greatly reduced. The set of approximations, which Long refers to as "radical approximations", allows for one to define the Placzek transition polarizability. The approximations required are:

(1) The frequency of incident radiation is very much larger than the frequency of any ro-vibrational transition and the frequency of incident radiation is very much less than any electronic transition of a molecule.

(2) The ground electron state is non-degenerate.

These equations limit the number of transitional states that are considered because there is no transition between electronic levels. Furthermore, resonance phenomena may be ignored because the incident photons are far from transitions peaks.

The validity of these assumptions should be carefully considered because they are the basis for defining the scattering cross sections and by extension how one remotely perceives atoms or molecules. At terrestrial temperatures, as has been previously mentioned, the thermally available energy is approximately $208 \ cm^{-1}$. There is little chance that a molecule will be found in the first excited vibrational state. As vibrational spacing is smaller than electronic spacing, this is reasonable assuming the scatterers are in thermodynamic equilibrium. In the troposphere, due to the pressure of the atmosphere and the frequent collisions, non-equilibrium states are very short lived and are negligible. Finally, the major atmospheric constituents absorb energy in the vacuum UV, wavelengths less than approximately $200 \ nm$. Therefore, probing wavelengths from the IR, visible, and UVA portions of the spectrum do not cause electronic transitions.

The degeneracy of the ground state is important to consider because summations over intermediate states to non-degenerate ground states are often zero. In special cases degenerate ground states can cause the summation of the paths between intermediate and ground to be non-zero on the strict condition that the transition is infrared active and that the transition is associated with a change in permanent electric dipole moment [114]. This contributes to the symmetric portion of the scattering tensor, which is typically completely negligible in non-resonant Raman cases. Diatomic molecules like nitrogen and oxygen do not have permanent electric dipole moments and are thus not infrared active. In this case, using laser sources in the IR, visible, and UVA portions of the spectrum for observing terrestrial diatomic molecules meets both assumptions relatively easily. Note that water vapor does have a permanent electric dipole moment and is infrared active. Therefore, Raman cross section calculations of water need to consider the latter assumption more carefully.

With these conditions met, the cross section of Raman scatterers can be given, originally stated by Placzek [115], reformulated by Long [114], and summarized by Wandinger [50]. The backscattering cross section for a single ro-vibrational transition, from rotational level J_1 and the ground vibrational state, is given in Equation 3.24.

$$\sigma_{B_{J_1}} = \left(\frac{\pi^2}{\epsilon_o^2}\right)(\tilde{\nu}_1 \mp |\Delta\tilde{\nu}|)^4 \left(\frac{g_N \Phi_{J_1}}{\frac{k_B T}{2hcB_0}}\right)\exp\left[-\frac{B_{J_1}hcJ_1(J_1+1)}{k_B T}\right] \tag{3.24}$$

In Equation 3.24, the first term are electrical constants resultant of the units chosen. The second term is the frequency shift for Stokes and anti-Stokes Raman, respectively, calculated from the Raman spectra in Section 3.2.1. The third term contains the nuclear spin statistical weight, g_N, and the denominator is the partition function in an approximate form. Finally, the fourth term is the Boltzmann distribution of populated rotational states. This leaves the definition of the Φ_j term which contains all of the polarizability terms, rotational degeneracy terms, and observation geometry assumptions. This is given in by Wandinger as three separate equations, one for each spectroscopic branch: O, Q, and S [50]. For reference, this set of equations is given in Appendix 8.4

Equation 8.84. These equations can all be derived from a single equation with the application of the appropriate selection rules for each spectroscopic branch. The base equation can be retrieved though it is not given in any of the references to the author's knowledge. This is given in Equation 3.25 for the ro-vibrational transitions and Equation 3.26 for pure rotational transitions. Note that here J_1 is the rotational quantum number of the initial state and J_2 is the rotational quantum number of the final state. This equation can be misused because, for example, O-Branch Raman transitions require a starting rotational quantum number of at least 2. One must make sure that the starting and final quantum numbers obey the selection rules and are positive or zero value integers.

$$\Phi_J = \frac{\frac{h}{8\pi^2 c\tilde{\nu}_{vib}}}{1 - \exp\left[\frac{-hc\tilde{\nu}_{vib}}{k_B T}\right]} \left[\frac{2 - |J_1 - J_2|}{2}\alpha'^2 + \frac{7\left(\frac{|J_1 - J_2|}{2} + 2\right)\left(\frac{J_1 + J_2}{2}\right)\left(\frac{J_1 + J_2 + 2}{2}\right)(3J_1 - J_2 + 1)}{90\left(2J_1 + 3\right)\left(2J_1 - 1\right)}\gamma'^2\right]$$

(3.25)

$$\Phi_J = \frac{2 - |J_1 - J_2|}{2}\alpha^2 + \frac{7\left(\frac{|J_1 - J_2|}{2} + 2\right)\left(\frac{J_1 + J_2}{2}\right)\left(\frac{J_1 + J_2 + 2}{2}\right)(3J_1 - J_2 + 1)}{90\left(2J_1 + 3\right)\left(2J_1 - 1\right)}\gamma^2$$

(3.26)

Note that the α and γ terms from Equation 3.26 are the mean polarizability and anisotropy of the polarizability where those in Equation 3.25 are derivatives of the mean polarizability and anisotropy with respect to the normal coordinate of vibration. The constants for nitrogen and oxygen are given in Table 3.1.

With all the pieces in place, one can calculate the Raman scattering cross section for any set of energy levels. This is shown in Figure 3.5 for diatomic nitrogen and oxygen. Furthermore, the Raman scattering cross sections for water vapor can be found in the recent literature compiled by Avila et al. [122, 123, 124]. Note that the complexity associated with Fermi resonance and the lack of simplification from the assumptions listed above are handled in the model by Avila then tested by laboratory measurement.
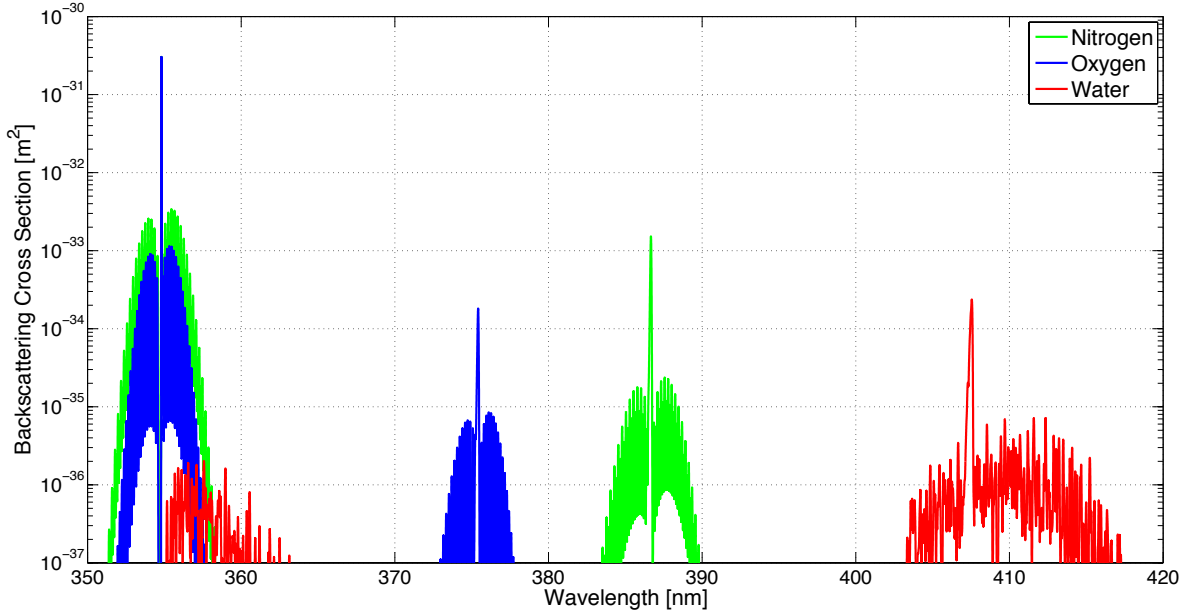
Figure 3.5: Raman cross section for diatomic nitrogen, diatomic oxygen and water vapor at a temperature of 300 K. Both the pure rotational and ro-vibrational spectra are calculated for the diatomic species but only the Stokes Raman scattering is for the water vapor. The base wavelength for this analysis is the that of a tripled Nd:YAG laser, 354.71 nm in air. The profiles plotted are Gaussian profiles with a full width half maximum corresponding to the unseeded line width of the Continuum 9030 laser which is discussed later. The asymmetry of the O and S branches is a direct result of the Φ term combined with the Boltzmann term. Φ_{S_J} is equal to $\Phi_{O_{J+2}}$ combined with a smaller Boltzmann factor causes the O branch to be slightly weaker.

3.3   The Polarization of Scattered Light

The cross sections and frequency shifts given in Sections 3.1 and 3.2 allow for a partial statement of how light interacts with scatterers. The final piece of information is the polarization state of the scattered light. This has been addressed for the limited case of spheres in Equation 3.15 for a general scattering direction and in Equation 3.16 for backscattering. For shapes other than spheres, such simplifications are invalid and result in a slightly different formulation for the backscattering phase matrix.

It is possible to define the scattering phase matrix in a number of ways which vary only in the assumptions that are made to compute them [116]. Two are useful for the work presented in this thesis. The first assumes axially symmetric randomly oriented scatterers and the second as-

sumes axially symmetric scatterers with preferential horizontal orientation. These assumptions are limiting to an extent but a good starting place for ice particles as will be noted further below. The most general phase matrix is given as a Mueller matrix in Equation 3.27. The common assumption of axial symmetry reduces the unknown elements of the Mueller matrix from 16 independent parameters as presented in Equation 2.4 for a full polar matrix decomposition to 6 independent parameters (recall assuming spherical scatterers for Mie theory results in 4 independent parameters). This matrix still consists of retarding, diattenuating, and depolarizing elements, but the unknowns reduce to one retarding element ($f_{34}(\Theta, \Phi)$ is a retarding element about the horizontal), one diattenuating element ($f_{12}(\Theta, \Phi)$ is a diattenuating term about the horizontal), and 4 which are a mix of all 3 polar decomposition components. It is important to note that the general phase matrix is a function of incoming and outgoing wave vectors, but the matrix terms are often written in terms of the angle from zenith, Θ, and azimuth angles, Φ, of the outgoing wave vector with respect to the incoming.

$$\bar{\bar{F}}\left(\bar{k}_i, \bar{k}_s, R\right) = \begin{bmatrix} F_{11}(\Theta, \Phi) & F_{12}(\Theta, \Phi) & 0 & 0 \\ F_{12}(\Theta, \Phi) & F_{22}(\Theta, \Phi) & 0 & 0 \\ 0 & 0 & F_{33}(\Theta, \Phi) & F_{34}(\Theta, \Phi) \\ 0 & 0 & -F_{34}(\Theta, \Phi) & F_{44}(\Theta, \Phi) \end{bmatrix} \tag{3.27}$$

In the case of axially symmetric and randomly oriented particles, relations exist between some of the matrix elements in the backscattering direction [98, 100, 116]. In that case, the phase matrix becomes a function not of 6 independent elements but 2: a backscattering efficiency, β, and a depolarization term, d. This is given in Equation 3.28 where backscattering is also assumed. In the case of backscattering, $\Theta = \pi$ and the azimuth angle is unimportant. For clarity, the backscattering wave vector is given as the inverse of the incident wave vector $-\bar{k}_i$.

$$\bar{\bar{F}}\left(\bar{k}_i, -\bar{k}_i, R\right) = \beta \begin{bmatrix} 1 & 0 & 0 & 0 \\ 0 & 1-d & 0 & 0 \\ 0 & 0 & d-1 & 0 \\ 0 & 0 & 0 & 2d-1 \end{bmatrix} \tag{3.28}$$

One point to clarify is the apparent doubling of depolarization in the circular polarizations compared to the linear polarizations. This is a result of a subtle definitional detail of the construction of the matrix and depolarization term. For linear polarizations, d is defined such that totally depolarized light would result in transmission of half of the incident intensity of an unpolarized beam through a linear analyzer. For circular polarizations, depolarization is defined with opposite handedness. As such, totally depolarized light has some portion of energy in the parallel orientation while circular does not [125]. Examining the end cases for backscattering, if $d = 0$, horizontal and vertical polarizations are preserved where ±45 and circular are flipped, shown in Equation 3.29. For $d = 1$ cases, linear polarizations should be nullified and scattered circular polarizations flip their sign relative to the non-depolarizing case, given in Equation 3.30.

$$\bar{\bar{F}}\left(\bar{k}_i, -\bar{k}_i, R, d = 0\right) = \beta \begin{bmatrix} 1 & 0 & 0 & 0 \\ 0 & 1 & 0 & 0 \\ 0 & 0 & -1 & 0 \\ 0 & 0 & 0 & -1 \end{bmatrix} \tag{3.29}$$

$$\bar{\bar{F}}\left(\bar{k}_i, -\bar{k}_i, R, d = 1\right) = \beta \begin{bmatrix} 1 & 0 & 0 & 0 \\ 0 & 0 & 0 & 0 \\ 0 & 0 & 0 & 0 \\ 0 & 0 & 0 & 1 \end{bmatrix} \tag{3.30}$$

If instead of randomly oriented particles, preferential orientation is allowed, the scattering phase matrix does not simplify as completely. As ice falls, it can preferentially orient horizontally, referred to throughout this thesis as horizontally oriented ice crystals or HOIC, as a result of

aerodynamic forces in the atmosphere [126]. HOIC are observed in clouds by many, but a complete picture of how it occurs and the driving processes remains illusive [127, 128, 129, 111, 130, 131, 132, 133]. The preferential nature of falling ice crystals invalidates some of the simplifications used to simplify Equation 3.27. In particular, the backscattering phase matrix retains all 6 independent elements, unlike Equation 3.28, at all orientations including backscattering. The backscattering phase matrix for HOIC is given in Equation 3.31.

$$\bar{\bar{F}}\left(\bar{k}_i, -\bar{k}_i, R\right) = \begin{bmatrix} F_{11} & F_{12} & 0 & 0 \\ F_{12} & F_{22} & 0 & 0 \\ 0 & 0 & F_{33} & F_{34} \\ 0 & 0 & -F_{34} & F_{44} \end{bmatrix} \tag{3.31}$$

3.4   Monte Carlo Methods for Modeling Scattered Light

If simplified scattering models, such as the single scattering typically assumed for the lidar equation, are not sufficient for the applications of interest, more sophisticated methods may be implemented. The only such method used by this thesis will be Monte Carlo analysis, which is leveraged for this thesis to analyze laser safety [134] but is not limited to this narrow focus. The results of the laser safety analysis completed as part of this thesis are presented with more details given in Chapter 6. However, the method used for this analysis is based completely on representing scattering effects in a statistical manner and as such is described here.

Transfer of radiation in complicated multi-scattering media is solved by the Monte Carlo method in a statistical manner to produce solutions that converge to exact solutions given large numbers of modeled events. In the case of radiation propagation in the atmosphere, statistical methods can be used to model absorption and scattering especially considering multiple scattering [93]. The Monte Carlo technique is a statistical method that leverages random sampling techniques to understand problems containing multiple probabilistic events [135]. The Monte Carlo method is well equipped for applications within the atmosphere because it can robustly handle optically thick

media, multiple scattering media, without a priori constraint on the number of scattering events [93, 136, 137, 138, 139, 140].

3.4.1   Weighted Random Numbers for Monte Carlo Applications

Many working pieces are needed to implement Monte Carlo simulations. One critical element of implementing a Monte Carlo simulation is developing a method to produce weighted random numbers. For this work weighted random numbers are needed in the initialization and propagation of photons. The starting location of a photon within the beam, the photon ray angle, the propagation distance before interaction, the probability of scattering versus absorption, and the scattering angle are all needed. A general method is to constrain the probability density of a function such that it obeys Equation 3.32 [93, 135]. Here, μ is any variable for which a weighted random number is desired, ξ is a randomly generated number from a uniform probability distribution, and p is the continuous probability density of the desired variable. For functions that can be easily integrated and inverted, optical depth being one example, this method is straightforward and robust. The integration yields the functional dependence; all that is needed is the specification of boundary conditions.

$$\int p\left(\mu\right)\,d\mu = \int 1\,d\xi \tag{3.32}$$

An example of the utility of Equation 3.32 is producing weighted random numbers which represent optical depth. The probability density of a photon propagating at an optical depth, τ, before scattering can be given in Equation 3.33.

$$p\left(\tau\right) = \exp\left(\tau\right) \tag{3.33}$$

Integrating Equation 3.33 using Equation 3.32 and matching the boundary conditions, $\xi = 0$ where $\tau = 0$ yields a weighting function of optical depth. This is given in Equation 3.34. Using Equation 3.34, a number derived from a uniform probability distribution can be converted to a probability

distribution for optical depth.

$$\tau(\xi) = -\ln(1 - \xi) \tag{3.34}$$

One can verify Equation 3.34 by plotting the theoretical probability density along with the Monte Carlo simulations of the optical depth weighted random number. In the style of Bohren and Clothiaux, the values of τ are discretized into a set number of bins, which are incremented by one each time a Monte Carlo event produces a value in that bin [93]. A large number of random trials are run producing weighted random numbers and the percent error between the Monte Carlo predicted probability density and the known probability density are calculated. The results of this process are given in Figure 3.6 with 5 different numbers of photons with 500 bin discretization over the range $0 \leq \tau \leq 5$.

For functions that do not possess a simple closed form to this integral, this method is impractical. An example of such a function is a phase function, the $(1, 1)$ element of the scattering phase matrix, calculated directly from Mie theory. A second is a phase function calculated from an improved geometric optics method [120], which does not have a closed form representation. Furthermore, simple functions, which can be integrated but result in equations that can not be inverted to yield a μ dependence as a function of ξ are also problematic. An example of this is the Rayleigh scattering phase function, which when solved using Equation 3.32 yields an equation of the form $\mu + \sin(\mu) = \xi$ which can not be simplified to μ as a function of ξ.

One method to solve this problem is to approximate the scattering phase function with analytic functions that match some of the general characteristics. For the phase functions mentioned, the Henyey-Greenstein function is commonly used [93, 139, 140, 141, 142, 143]. It can be exactly integrated and a weighted random number can be specified as a function of the random number generated, ξ. The Henyey-Greenstein phase function cannot match several of the characteristics exhibited in real scattering phase functions, such as the forward and backward peaks, or the rainbow, so numerical solutions are required for improved accuracy. These numerical solutions are
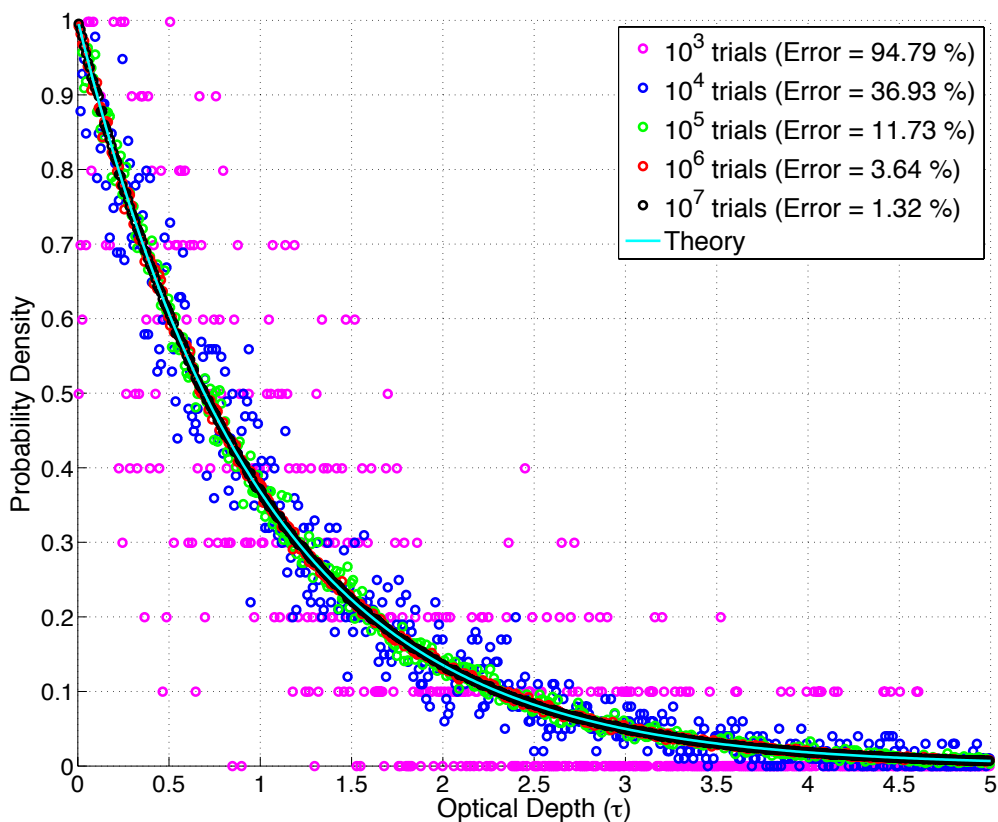
Figure 3.6: The continuous probability distribution function $p = \exp(-\tau)$, Equation 3.33, and its weighted random number Monte Carlo representation in the style of Bohren and Clothiaux [93]. The Monte Carlo representation is computed from calculating weighted random numbers. The axis from $\tau = 0$ to $\tau = 5$ is discretized into 500 equal sized bins. The five different approximations yield a given number of weighted random numbers which are lumped into the bin which contains it. The average percent error for each of the 500 bins compared to the known probability distribution is given in the legend.

described in Section 3.4.3. Furthermore, the results shown in Chapter 6 will demonstrate that exact treatment of the phase function, and in particular the representation of the prominent forward scattering peak, is critical to laser safety applications.

3.4.2 Coordinate Representations of Photon Propagation for Monte Carlo Applications

A crucial need to implement a Monte Carlo scattering simulation after the generation of weighted random numbers is a method to track the motion of a photon through a layer of interest. The scattering phenomena described in this thesis can be expressed in spherical coordinates. The angle from zenith, θ, for a scattering event can be directly calculated from the phase function of the scatterer, with details given in Section 3.4.3, and the azimuth angle, ϕ, is defined as a uniform probability distribution when scattering is azimuthally symmetric, as it is for spheres and most atmospheric ice particles. With these two angles, the direction of propagation of the ith propagation is defined in Equation 3.35. Note that in the development to this point, Θ and Φ have been used as general angles but the nomenclature switches to θ and ϕ as the angles required for Monte Carlo developments are actual numbers and not general symbols.

$$
\bar{\Omega}_i = \begin{bmatrix} \sin{(\theta_i)}\cos{(\phi_i)} \\ \sin{(\theta_i)}\sin{(\phi_i)} \\ \cos{(\theta_i)} \end{bmatrix}
\tag{3.35}
$$

Using Equation 3.35, each scattering event for multiple scattering media is referenced to a unique reference frame. It is noted that vectors referenced to different frames cannot be simply added. The z-axis of each frame is determined by the previous scattering vector. A definition of the vector in terms of a common coordinate system is required to track the photon after multiple scattering events. To link the vectors, a system of rotation matrices is used. This system can be derived from general Cartesian rotation matrices, which is generated from two of the three basic 3 dimensional rotations, rotation about the y-axis and rotation about the z-axis, given in Equation 3.36 [144].

$$R_y\left(\beta\right) = \begin{bmatrix} \cos\left(\beta\right) & 0 & -\sin\left(\beta\right) \\ 0 & 1 & 0 \\ \sin\left(\beta\right) & 0 & \cos\left(\beta\right) \end{bmatrix} \quad R_z\left(\delta\right) = \begin{bmatrix} \cos\left(\delta\right) & \sin\left(\delta\right) & 0 \\ -\sin\left(\delta\right) & \cos\left(\delta\right) & 0 \\ 0 & 0 & 1 \end{bmatrix} \tag{3.36}$$

Combining a rotation about the y-axis with a rotation about the z-axis is sufficient to define the scattering events. This combination is given in Equation 3.37 and shown in Figure 3.7. This matrix is used to link the propagation vector before and after scattering. It is useful to construct this matrix relationship from basic rotations because the basic rotations are orthonormal matrices. This implies that the matrix is invertible and that the inverse of the matrix can be expressed as the transpose of the matrix [144].

$$\bar{\bar{M}}_i = R_y\left(\theta_i\right)R_z\left(\phi_i\right) = \begin{bmatrix} \cos\left(\theta_i\right)\cos\left(\phi_i\right) & \cos\left(\theta_i\right)\sin\left(\phi_i\right) & -\sin\left(\theta_i\right) \\ -\sin\left(\phi_i\right) & \cos\left(\phi_i\right) & 0 \\ \sin\left(\theta_i\right)\cos\left(\phi_i\right) & \sin\left(\theta_i\right)\sin\left(\phi_i\right) & \cos\left(\theta_i\right) \end{bmatrix} \tag{3.37}$$

In this way, the location of the photon within the layer of interest, ζ, can always be linked back to some specified coordinate system by performing rotations back to the original reference frame. Furthermore, the vector defined in Equation 3.35 is simply the z-direction before and after scattering. The general transformation is given in Equation 3.38.

$$\begin{aligned} \zeta_n &= \bar{\bar{M}}_{n-1}\left(\theta_{n-1}, \phi_{n-1}\right)\zeta_{n-1} \ or \\ \bar{\bar{M}}_{n-1}^{-1}\left(\theta_{n-1}, \phi_{n-1}\right)\zeta_n &= \zeta_{n-1} \end{aligned} \tag{3.38}$$

After coordinate system transformations, the location of a photon within a layer is simply the vectorial addition of all of the individual propagation legs. Note that the matrix given in Equation 3.37 connects the old coordinate system to the new so to map a vector in the newest scattering system into an original system, the matrix inverse, or transpose since it is orthonormal, is required. The total path traveled after n scattering events is then given in Equation 3.39 where τ is the distance traveled on each leg calculated from randomly sampling Equation 3.34 and $\bar{\bar{M}}$
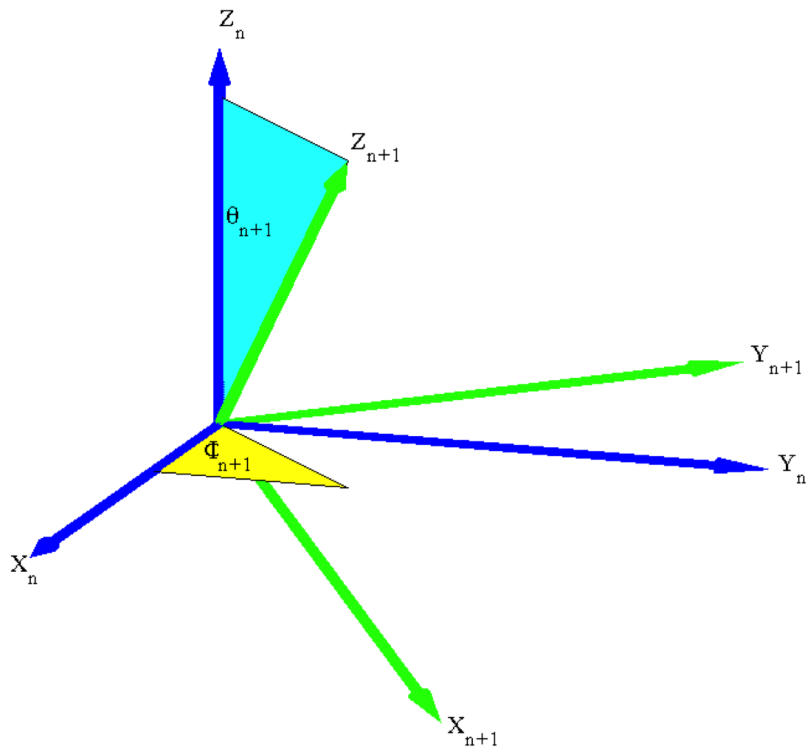
Figure 3.7: A representation of the scattering angles needed to define the propagation orientation after scattering. The original coordinates are taken with the propagation direction along the z-axis. These angles are used to define scattering and to rotate new propagation vectors back to a standard coordinate system.

is the rotation matrix defined in Equation 3.37 with sampling defined by randomly sampling the scattering phase function, described in Section 3.4.3.

$$\bar{\tau} = \tau_1 \bar{\bar{M}}_1^{-1} \bar{\Omega} + \tau_2 \bar{\bar{M}}_1^{-1} \bar{\bar{M}}_2^{-1} \bar{\Omega} + ... + \tau_n \bar{\bar{M}}_1^{-1} \bar{\bar{M}}_2^{-1} \bar{\bar{M}}_3^{-1} ... \bar{\bar{M}}_n^{-1} \bar{\Omega} \tag{3.39}$$

Equation 3.39 is generalized in Equation 3.40. It is of note that the vector $\bar{\Omega} = \begin{bmatrix} 0 & 0 & 1 \end{bmatrix}^T$ and the angles θ_1 and ϕ_1 are the angles at which the photon enters the layer of interest. Note also that $\bar{\Omega}_1$ given in Equation 3.35 is simply calculated as $\bar{\Omega}_1 = \bar{\bar{M}}_1^{-1}(\theta_1, \phi_1) \bar{\Omega}$. In Equation 3.40 the matrix multiplications are defined to be right multiplications and are not commutative, as indicated in Equation 3.39.

$$\bar{\tau} = \sum_{i=1}^{n} \tau_i \left[\prod_{j=1}^{i} \bar{\bar{M}}_j^{-1}(\theta_j, \phi_j) \right] \bar{\Omega} \tag{3.40}$$

Note that the above allows for one to track a photon within the layer of interest. It does not, however, track the polarization state of light. This can be done as, for example, presented by the theses of Hayman or Gisler [100, 145]. The results of the laser safety analysis provided in Chapter 6 for this thesis does not require the complexity.

3.4.3 Representations of Phase Functions for Monte Carlo Applications

The final piece that is required for realistic Monte Carlo simulations of scattering is a weighted random number representation of scattering phase functions. Commonly, the scattering phase function is approximated by simple phase functions, which can be directly integrated in Equation 3.32. One such phase function is the Henyey-Greenstein phase function [53, 143]. While it has no physical basis, it broadly resembles the phase functions calculated from Mie theory for spheres and geometric ray tracing codes or T-Matrix algorithms for non-spherical large particles. The forward scattering peak is approximate for small size parameters but more importantly, the function has a simple integral, which can be inverted. The drawback of this function is that it poorly captures forward and backscattering for large size parameters or other features such as the rainbow from

spherical droplets and halos from hexagonal ice. Modifications such as a double Henyey-Greenstein phase function have been suggested but the system becomes impossible to invert to a function of a random variable. A further modification is proposed by Cornette and Shanks [142] that captures more reasonable forward and backscattering behavior especially for smaller particles. Even this more complicated function fails to capture some of the prominent features like the rainbow angle for spheres or the halo in hexagonal ice crystals.

One method for handling real phase functions is defined by Toublanc [143] where the normalized cumulative distribution function is used to create weighted random numbers and Equation 3.32 is solved numerically. The method can be used to capture all the features of arbitrarily complicated phase functions calculated via Mie theory or ray tracing. The cumulative distribution becomes a lookup table to convert a random number to a scattering direction. This method is more computationally expensive than the method used for the optical depth but is simple and robust to implement and has the advantage that the continuous scattering function can be arbitrarily complicated. Additionally, the phase function has no requirements on the angular resolution, it can be coarse or fine depending on the features within the phase function, or closed form representation making it very flexible.

Three phase functions are used for the analysis of laser safety in Chapter 6 given in Figure 3.8. The first function is the Rayleigh scattering phase function. It is known analytically but it cannot be inverted like the Henyey-Greenstein phase function or optical depth probability distribution. It is calculated at 500 evenly spaced points. Note that there exists a unique relationship between cumulative probability (right ordinate), and scattering angle (top abscissa), yielding a procedure for deriving the latter with a random number. The second phase function is one calculated directly from Mie theory. The phase function is calculated using the Mie development given in Section 3.1.2 assuming a gamma distribution of spherical particles with an average size of 10 μm. The wavelength of interest is 355 nm and the optical properties of water at that wavelength are used as compiled by Warren [146]. The axis from $\theta = 0°$ to $\theta = 180°$ is discretized into 500 equal sized bins. The final phase function is calculated for a collection of roughened ice crystals by Yang et al.

[120]. This phase function has no closed form representation and is given only in tabulated form by Yang et al. The roughened ice phase function is calculated using a wavelength of light of 355 nm with a mean size of 30 μm. The axis from $\theta = 0°$ to $\theta = 180°$ is discretized into non-equal sized bins. The axis of the cumulative distribution function is given in steps of $0.01°$ for $0° \leq \theta \leq 2°$, $0.05°$ for $2° < \theta \leq 5°$, $0.1°$ for $5° < \theta \leq 10°$, $0.5°$ for $10° < \theta \leq 15°$, $1°$ for $15° < \theta \leq 176°$, and $0.25°$ for $176° < \theta \leq 180°$. The Monte Carlo representation is computed from calculating weighted random numbers and compared to all 3 phase functions.
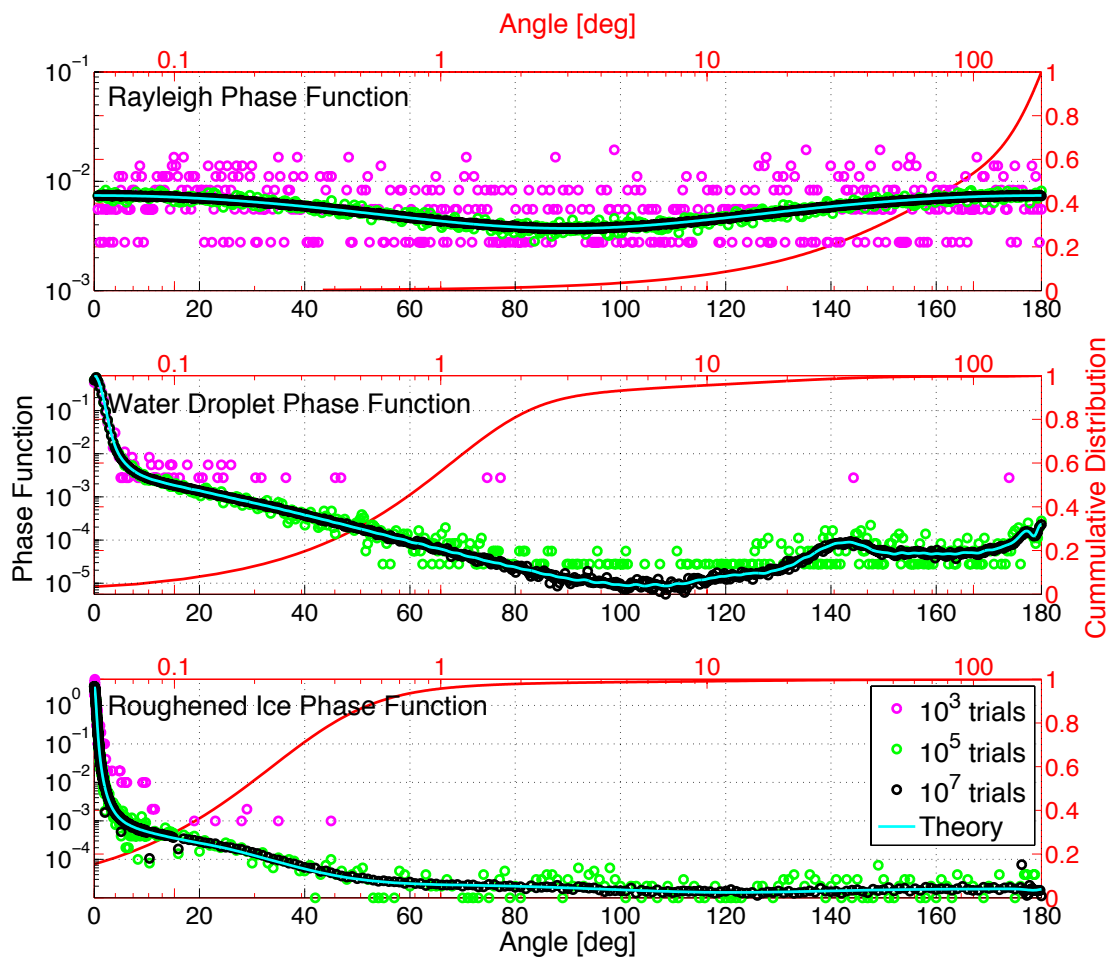
Figure 3.8: The phase functions for three major scattering types encountered in the high Arctic: clear air, liquid water, and roughened ice, used to calculate laser safety parameters of an Arctic lidar system. The cumulative distribution function of the continuous phase function is given on the red axes as calculated from numerical integration of the phase function. Note that the red x-axis is logarithmic to highlight the forward scattering peak of the phase function. The cumulative distribution function is used to create weighted random numbers to retrieve the phase functions using the Monte Carlo method described in Equation 3.32 with 10^3, 10^5, and 10^7 trials in the circles. Note that the red axes are consistent but that the black y-axis changes range to show the required detail in the phase function.

<div align="center">

Chapter 4

The Clouds Aerosols Polarization and Backscatter Lidar

</div>

The lidar theory and atmospheric scattering described in Chapter 2 and Chapter 3 are used in this thesis as they relate to observing water in the atmosphere in the polar regions. The observations are contained within a larger currently running National Science Foundation (NSF) funded observational program based at Summit, Greenland ($72°35'46.4"N$, $38°25'19.1"W$, $3212\ m\ asl$) called the Integrated Characterization of Energy, Clouds, Atmospheric State, and Precipitation at Summit (ICECAPS). An overview of the ICECAPS program and the ancillary sensors contained within it are given as well as a description of the Clouds Aerosols Polarization and Backscatter Lidar (CAPABL), which is one major contribution of this thesis work to ICECAPS and Arctic observing more generally.

4.1   The Integrated Characterization of Energy, Clouds, Atmospheric State, and Precipitation at Summit

The instruments for the ICECAPS program were installed at Summit in the summer of 2010 and the project is currently funded through the summer of 2018. The ICECAPS program consists of many active and passive remote sensors as well as in-situ measurements used to try to understand the atmospheric state and cloud properties above the GrIS. Its two major goals are to provide a first detailed look at cloud and precipitation properties over the GrIS and to extend atmospheric measurements across the Arctic. Similar measurements have been made based on the Atmospheric Radiation Measurement (ARM) program sites at coastal locations such as Barrow, Alaska and

Eureka, Canada [42, 147] and in sea ice for the Surface Heat Budget of the Arctic (SHEBA) Experiment, but none before ICECAPS had been made at an Arctic high altitude location.

The ICECAPS sensor suite consists of many active remote sensing instruments including lidars, radars, and sodar and several passive remote sensing instruments including an infrared spectrometer, microwave radiometers, all sky imagery, and snowflake imagery and in situ probes such as radiosondes. This aggregate of sensors is used because they observe different phenomena like falling snow or clear air from different perspectives and thus have more information content than single sensors [18, 33, 35, 41]. The entire suite of instruments is described by Shupe et al. [35]. ICECAPS instruments will be described in this thesis as they relate to evaluating and enhancing the performance of CAPABL.

An outline of the program and a requirements traceability matrix are given in Figure 4.1, which describes the design of the ICECAPS instrument suite and links instrument requirements to the scientific requirements of the program. This traceability matrix focuses on the contributions of lidar to measurements of moisture and cloud properties. Note that the Summit Polarized Raman Lidar (SuPR) is included in this traceability matrix. It is currently under construction and not a part of the ICECAPS suite but would add significantly to the ICECAPS observational capacity. SuPR is described in Chapter 6.

The CAPABL instrument was originally deployed within the ICECAPS suite in 2010 with the specific goal of distinguishing horizontally oriented ice crystals (HOIC) from randomly oriented ice crystals (ROIC) and distinguishing cloud thermodynamic phase [35, 89] but was removed from the field in 2014 for repairs. The original instrument, described by Neely et al. [89], consisted of a large telescope (35.6 cm aperture) and micropulse laser (0.05 W with 2 kHz rep rate). It was limited to a large degree by the power aperture product it could maintain and the signal to noise ratio (SNR) especially in the polar summer where the sun never sets at Summit. In the winter, signals were observed from clouds as high as 3 km, but in the summer signals were limited to just a few hundred meters. Shupe et al. have shown that the clouds of interest at Summit occur from near the surface up to approximately 8 km above the surface making CAPABL's sampling very limited

Figure 4.1: A requirements traceability matrix for the ICECAPS program.

[35]. In winter of 2013, the instrument's primary and secondary laser heads failed necessitating a complete replacement. This thesis will focus almost entirely on the redeployed Version 2 of the instrument. A photo of the CAPABL system in its housing at Summit is given in Figure 4.2 taken in the winter of 2015.

Figure 4.2: A photo of CAPABL's beam taken under bright aurora taken on December 12, 2015. The building housing the CAPABL system also houses most of the ICECAPS sensor suite. Photo taken by Mike Finnegan.

4.1.1   The Clouds Aerosols Polarization and Backscatter Lidar Instrument and Data Processing Description

4.1.1.1   Lidar Hardware and Baseline Performance

The CAPABL system has been deployed to Summit, Greenland within the ICECAPS sensor suite since 2010 [35, 89]. The basic operation and measurement principle is well described by Neely at al. [89] based on polarization theory, the SVLE given in Equation 2.9, developed by Hayman and Thayer [98]. The basic measurement principle and resulting raw data products were originally described by Neely et al. [89], but have been extended and generalized by this thesis, described in Section 2.3.1. This thesis work also includes several lidar hardware modifications that have improved the system's overall observational capacity. These hardware modifications were completed in June 2015. These modifications are described with an emphasis on how they allow the CAPABL system to better observe clouds via enhancement of counting system dynamic range.

After several years of data collection, the original Nd:YLF laser described by Neely et al. [89] was replaced by a more powerful Nd:YAG laser. This changed the laser wavelength from 523 nm to 532 nm. The optical components were accordingly changed and shrunk. Of particular need were the transmit mirrors, which were not rated for the new laser's power, and a narrowband optical filter. In addition, the telescope was replaced by a smaller Schmidt Cassegrain telescope to allow the system to be more easily tilted. The original system, Version 1, was approximately the size of a refrigerator and was limited therefore in its achievable tilt angle. Version 2 has a tilt angle of 32° from vertical and the overall size is approximately 1 m long and 20 cm wide. The photo multiplier tube (PMT) was upgraded from the original PMT, a Thorn EMI 9863B/100, to a Hamamatsu R7400U-03.

The major change for CAPABL from Version 1 to Version 2 was an upgrade of the receiver counting system from a purely photon counting system to a combined analog and photon counting system. It is critical to note that it is implicit in the polarization retrievals using the lidar equation, Equation 2.1, or the SVLE, Equation 2.9, that the incident intensity is linearly proportional to

the signals measured. Photon counting systems are capable of measuring weak light signals, while analog systems sacrifice sensitivity to measure stronger signals. In photon counting, detector signals are discriminated with a fixed voltage threshold. This threshold is set to remove much of the electrical noise resulting from using single-photon, high-gain PMTs. When a voltage signal is observed in excess of the threshold, a photo-electron is counted and its time of flight is assigned to a particular time bin. The intensity is presumed to be linearly related to the total number of counts in that bin over some integration period. Error can arise with this technique, however, if photons arrive at the counting system in close succession. It is possible that pulses can pileup in such a way that two or more pulses either overlap in time or pass through the system faster than the counting system can reset itself [68, 105, 148, 149, 150]. In either case, the intensity observed by the optical system is not linearly proportional to the number of photo-electrons counted because some photo-electrons have not been counted. In analog detection, the discrimination threshold is removed and the voltage produced by the detector is passed through an analog-to-digital converter with its amplitude providing the relative intensity of the collected backscattered signal. This method requires much higher signal-to-noise ratio than photon counting. By using a counting system that combines photon counting and analog detection, saturation is mitigated for high count rates using analog detection, approximately $> 10 \; MHz$, while maintaining sensitivity to low count rates, approximately $< 1 \; MHz$, using photon counting detection. More about this type of counting system can be found in Newsom et al. [150].

The current system specifications, Version 2, are given in Table 4.2, which can be compared to the original specifications, Version 1, from Neely et al. and reproduced in Table 4.1 [89].

One optical element, which is added in Version 2, is a neutral density filter in the receiver. As Version 2 of CAPABL's hardware has enhanced power aperture product over Version 1, the signal strength observed is well in excess of the counting system's ability to measure. In particular, the analog counting system uses a 12-bit monopolar analog-to-digital converter. The bounds are set from 5 mV to -495 mV by instrument default with negative tending PMT pulses. If the signal intensity at the PMT is too strong, the PMT pulses do not exist within this valid voltage range.

Table 4.1: CAPABL Version 1 system specifications.

Version 1

Transmitter	Receiver	Signal Processing
Spectra-Physics EL2-523Q Nd:YLF	Dall-Kirkham Cassegrain Telescope	Photon Counting Data Acquisition
Wavelength: 523.5 nm	Receiver Aperture: 35.6 cm	Data System:
Pulse Energy: 25 μJ	Filter bandwidth: 0.3 nm	Fast Comtec P7882
Pulse Rate: 2000 Hz	Channels: 2 (High, Low)	Range Bin Size: 30 m
2 Single Heads	Field of View: .3 $mrad$, .7 $mrad$	Integration time: 5 sec
		PMTs (2): EMI 9863B/100
	Polarizations Observed: 4	

Table 4.2: CAPABL Version 2 system specifications. Polarization purity and polarization rejection are measured quantities. Polarization purity is measured with a 100,000:1 Glan-Taylor polarizer.

Version 2

Transmitter	Receiver	Signal Processing
Big Sky Laser Ultra Nd:YAG	Schmidt Cassegrain Telescope	Combined Analog and Photon Counting acquisition
Wavelength: 532.2 nm	Receiver Aperture: 20.8 cm	Data system:
Pulse Energy: 60 mJ	Filter Bandwidth: 0.3 nm	Licel Transient Recorder TR20
Pulse Rate: 15 Hz	Channels: 1	Range Bin Size: 7.5 m
Twin Head	Field of View: 1.4 $mrad$	Integration time: 5 sec
Pol. Purity: $> 123 : 1$	Pol. Rejection: $> 800 : 1$	PMT: Hamamatsu R7400U-03
	Polarizations Observed: 4	

This can either happen via too many photons striking the cathode at once or as the cathode recharges from strong signals, there is often a positive overshoot. In either case, the summation of the digitized PMT pulses is not linearly proportional to the incident intensity at the cathode. This data is flagged by the counting system as having clipped the bounds of the analog-to-digital converter. To prevent this clipping, attenuation is added to reduce the overall intensity of the measured light at the PMT cathode. The neutral density filter could be placed in either the transmitter or the receiver to attenuate the lidar beam power, but by placing the neutral density filter in the receiver the background light is also attenuated. Especially in the Arctic summer, this extra noise attenuation improves system performance dramatically (this will be quantified with a direct comparison to a co-located micro-pulse lidar without receiver attenuation in Section 4.2).

In the summer of 2016, automatic steering motors were added to the system to alleviate some of the difficulty with performing alignments in the summer and to facilitate remote realignment. The completed system is given as a block diagram in Figure 4.3.

Given the specifications in Table 4.2, the SVLE given in Equation 2.9 can be used to model the ideal system performance. Using optical efficiency values provided by manufacturers of the optical elements shown in Figure 4.3 and measured laser power, the number of photons in each polarization to be expected can be modeled as a function of range. Data is taken from the ICE-CAPS radiosonde program to represent the number density of scatterers as a function temperature and pressure, which are themselves functions of height. Solar background counts are taken from irradiance measurements by an ultra-violet and visible spectrometer located at Summit. The total irradiance measured by the spectrometer is converted to background using the receiver system optical properties, field of view, and detector area.

In addition to the SVLE modeling, two theoretical saturation models are considered, a paralyzable and non-paralyzable model [68, 105, 148, 149, 150]. The paralyzable model is given in Equation 4.1 where S_{obs} is the observed signal count rate by the lidar system and S_0 is the ideal signal count rate at the cathode. This model assumes that it takes some finite time for the system to reset itself after counting a photon before a subsequent photon can be counted. This model

Figure 4.3: A block diagram of the CAPABL system indicating its major optical and data acquisition hardware. Here LCVR stands for Liquid Crystal Variable Retarder and PMT for Photo Multiplier Tube.

allows for the system to be paralyzed by high count rates where the photon arrival time is less than the dead time, τ_P. The non-paralyzable model is given in Equation 4.2, which assumes that the system needs some finite reseting time after counting a photon before a subsequent photon can be measured. The non-paralyzable dead time, τ_{NP}, is not dependent on the arrival of photons and is not paralyzed by high count rates.

$$S_{obs} = S_0 \exp\left(\tau_P S_0\right) \tag{4.1}$$

$$S_{obs} = \frac{S_0}{1 + \tau_{NP} S_0} \tag{4.2}$$

Comparing that ideal performance to observed performance yields a benchmark on the overall system alignment and operation. Sample data were taken on May 27, 2015 during a clear air period at Summit. Before the test started, CAPABL was measuring depolarization values on the order of 1-2% indicating no sub-visible ice was present. The operational receiver neutral density filter was removed from the counting system and the full laser power was emitted. This test provided two major system verifications, the first verifying overall performance and alignment compared to the model and the second was a quantification of the photon counting system's saturation behavior. One representative profile of the calibration data is given in Figure 4.4.

Figure 4.4 indicates that the observed signals are 71% of the modeled signals, i.e. the SVLE with all CAPABL operational inputs needs to be reduced to 71% of the predicted photon count rates to match the data. Though the system efficiency is not 100%, this simple data reveals that the CAPABL system is well aligned and operating reasonably. The loss of light is almost certainly related to the specified optical efficiency of the narrowband filter. The filters central wavelength is approximately 532 nm but the laser outputs approximately 532.1-532.2 nm. This slight shift results in a lower optical efficiency than expected.

Saturation models are also fit to these calibration data. Analog and photon counting data were combined based on the work of Newsom et al. [150] with the main difference being that profiles were background subtracted before analysis. This has the effect of multiplying the analog signal by a non-unity factor to convert its measured data, mV, into virtual count number. Both data streams are converted to count rate from count number using Equation 4.3 where N_{obs} is the number of observed counts, S_{PP} is the shots per profile of data taken, and T_{PB} is the time it takes for light to propagate in the bin of interest. From these data, the analog profile is taken as the
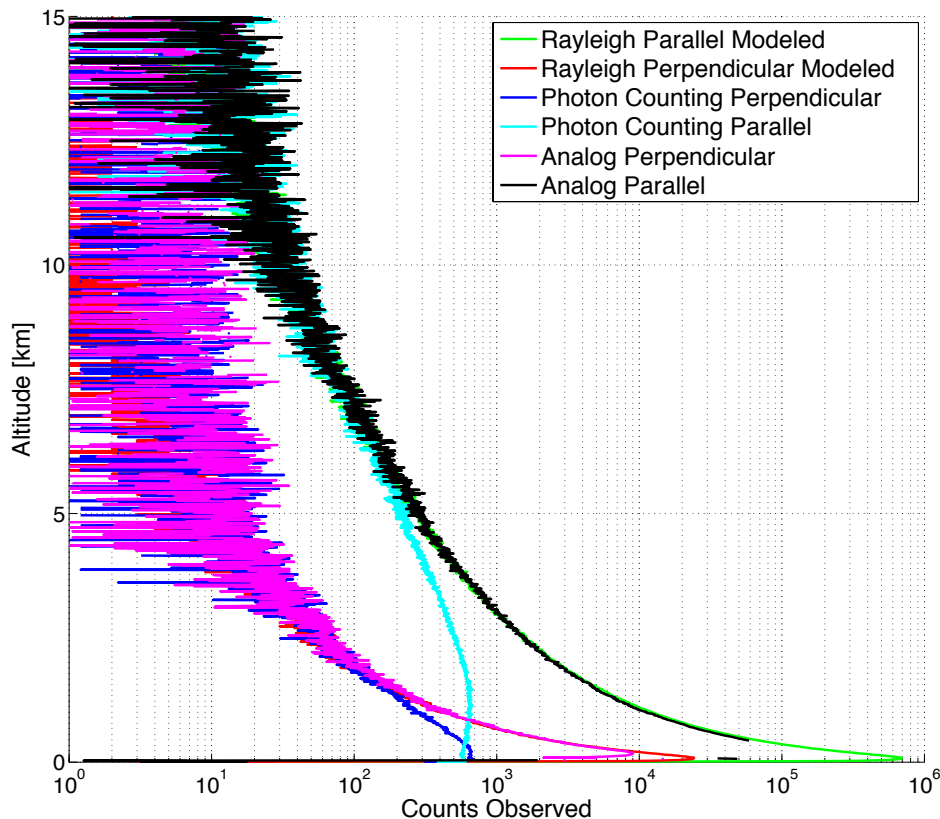
Figure 4.4: CAPABL polarization signals from measurements and also modeling the system using the full SVLE. Two polarizations are given, parallel and perpendicular to the transmit polarization. The results from analog and photon counting acquisition for each signal is given as well as the modeled signals with only Rayleigh scattering from nitrogen and oxygen. Background counts are modeled using data from an ultra-violet and visible spectrometer located at Summit and the system overlap via ray tracing code. The number density of scatterers is taken via ICECAPS radiosonde measurements. The system here represents 5 *sec* of integration at 7.5 *m* resolution. The clipping described can be seen clearly by the data removed from the black analog parallel profile. Saturation is seen in the underrepresentation of parallel data to approximately 6 *km* and in perpendicular data to approximately 2 *km*. The ideal signals are multiplied by a factor of 71% to match the measured data. Note that the overlap function predicted is slightly different than observed due to signal clipping for the perpendicular channel. Predicted overlap occurs at approximately 50 *m* whereas observed occurs near 80 *m*. Clipping is observed in the perpendicular channel to approximately 200 *m* and in the parallel channel to approximately 500 *m*.

ideal count rate and compared to the observed count rate in the photon counting channel. These data are plotted in Figure 4.5 with both paralyzable and non-paralyzable models fit to the data using a Levenberg-Marquardt nonlinear least squares solver.

$$N_{obs} = S_{obs} \times S_{PP} \times T_{PB} \tag{4.3}$$
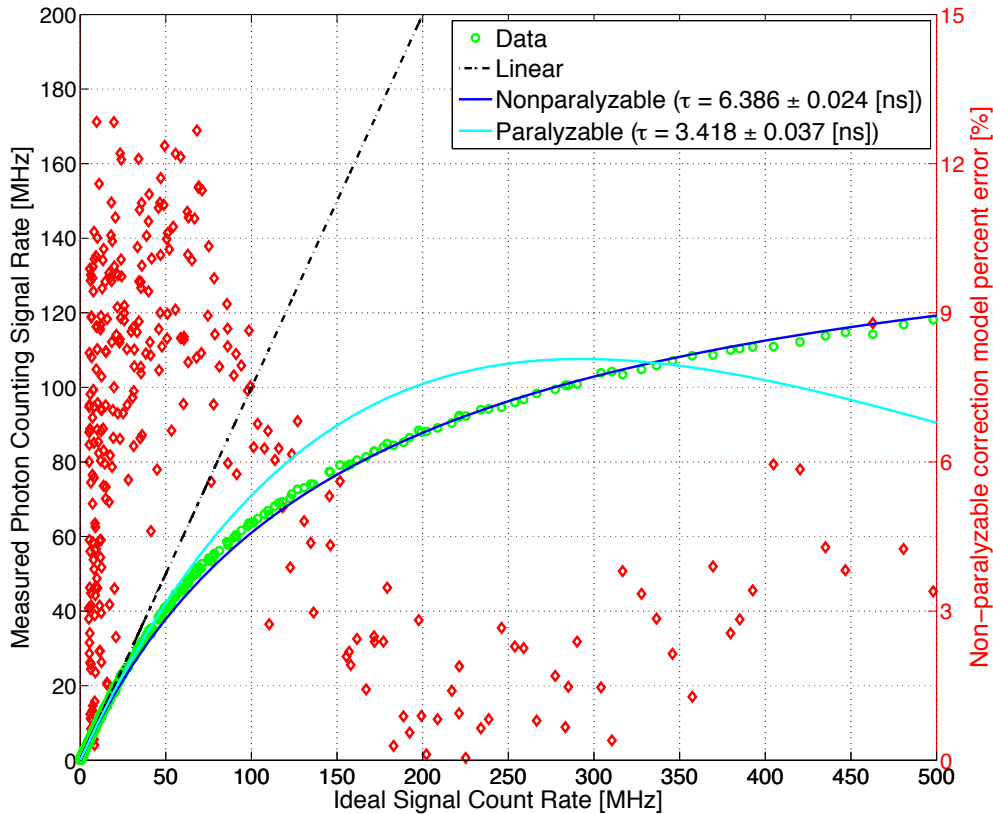
Figure 4.5: CAPABL saturation characteristics. Green dots are the measured pairs of count rates from the analog and photon counting calibration data. The black line is the 1:1 line. Cyan and blue lines are paralyzable and non-paralyzable modes respectively with the dead time fit parameter estimated using a Levenberg-Marquardt nonlinear least squares solver. The percent error of each individual point from the non-paralyzable model is given on the right axis. The legend specifies the 1σ error estimate taken from the fitting confidence bounds.

Figure 4.5 indicates that saturation is a severe problem for high count rates. At least 5% underrepresentation in count rate from photon counting acquisition due to saturation results from

ideal count rates above 8.24 MHz . Count rates below 1 MHz result in an error less than 0.63%. This saturation effect results in misclassification of cloud phase by causing a depolarization measurement bias by photon counting acquisition using count rates in excess of approximately 1 MHz. Theoretical errors in depolarization δ measurements related to this underrepresentation of signal strength are given in Figure 4.6. These theoretical errors are calculated as follows. Parallel count rates are specified then the accompanying count rates for other polarization orientations are calculated based on Equation 2.12 and specified ideal depolarization values d. The non-paralyzable model is then assumed and all count rates are modified according to Equation 4.2. Simulated non-orthogonal depolarization d_O observations are calculated using Equation 2.16. Depolarization d is converted to depolarization δ (d to δ and d_O to δ_O) via Equation 4.4 reproduced from Flynn et al. and Hayman and Thayer [82, 101]. The errors in observed depolarization δ_O from the known ideal depolarization δ is plotted in Figure 4.6 for the 6 possible depolarization measurements types for CAPABL's receiver hardware. Note that Figure 4.6 is given with a colorbar from 0 to 0.11. The value of $\delta = 0.11$ is used as the differentiation point between liquid and ice indicating values at or above this level must be observed as ice regardless of the actual target due to saturation effects.

$$\delta(R) = \frac{S_{0_\perp}(R)}{S_{0_{||}}(R)} = \frac{d(R)}{2 - d(R)} \tag{4.4}$$

Finally, as CAPABL uses a liquid crystal variable retarder (LCVR) to perform its polarization control, calibration of voltage input to the LCVR is required. Specifically, the voltages of the LCVR corresponding to the 4 channel polarization angles is desired. The voltage of the LCVR is scanned during a clear air period at Summit with each of CAPABL's laser heads. Received signal is integrated in space for several altitude ranges. Data is examined at 1-2 km, 3-4 km, and 8-9 km and compared. The maximum signal throughput and the minimum signal throughput indicate the locations of the parallel and perpendicular channels for the receiver, respectively. As the CAPABL lasers are cross polarized, the minimum signal throughput of one laser is the maximum signal throughput of the other. This is useful because minimizing the signal is far easier than maximizing.
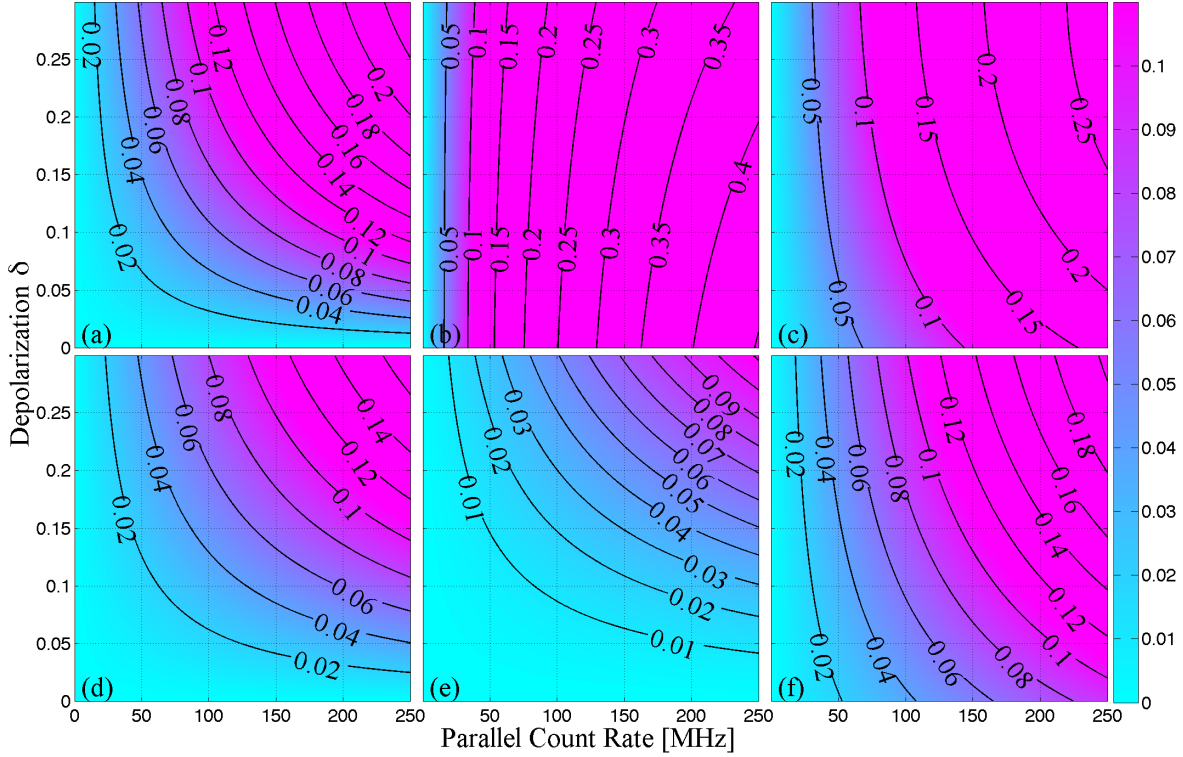
Figure 4.6: Theoretical deviation of the observed depolarization and the true depolarization $(\delta_O - \delta)$ as a function of the parallel count rate and the depolarization ratio (δ). The count rates for all CAPABL channel is calculated using Equation 2.12 and the depolarization using Equation 2.16. Assuming zero diattenuation, only two channels are required for the inversion. The channels used to calculated each contour are: a) $\theta_1 = 0°$ and $\theta_2 = 90°$ (traditional), b) $\theta_1 = 0°$ and $\theta_2 = 45°$, c) $\theta_1 = 0°$ and $\theta_2 = 110°$, d) $\theta_1 = 90°$ and $\theta_2 = 45°$, e) $\theta_1 = 90°$ and $\theta_2 = 110°$, and f) $\theta_1 = 45°$ and $\theta_2 = 110°$. The color bar is scaled to match the adopted thresholds for liquid water, $\delta = 0.11$ as defined by [151, 40].

The 45° channel is found where the throughput of the lasers crosses. The CAPABL channels are set based on these voltage scans given in Figure 4.7. The locations of the ideal polarization signals are marked on Figure 4.7. Operationally, the 45° channel is operated with lower signal intensity and not at exactly 45°. This allows for more spacing of the signal strengths of the 4 polarization channels. The minimum measurable depolarization can be calculated from this data and is approximately 1-1.5% for CAPABL. This procedure is automated for CAPABL and operational via a software option in the main operational software.
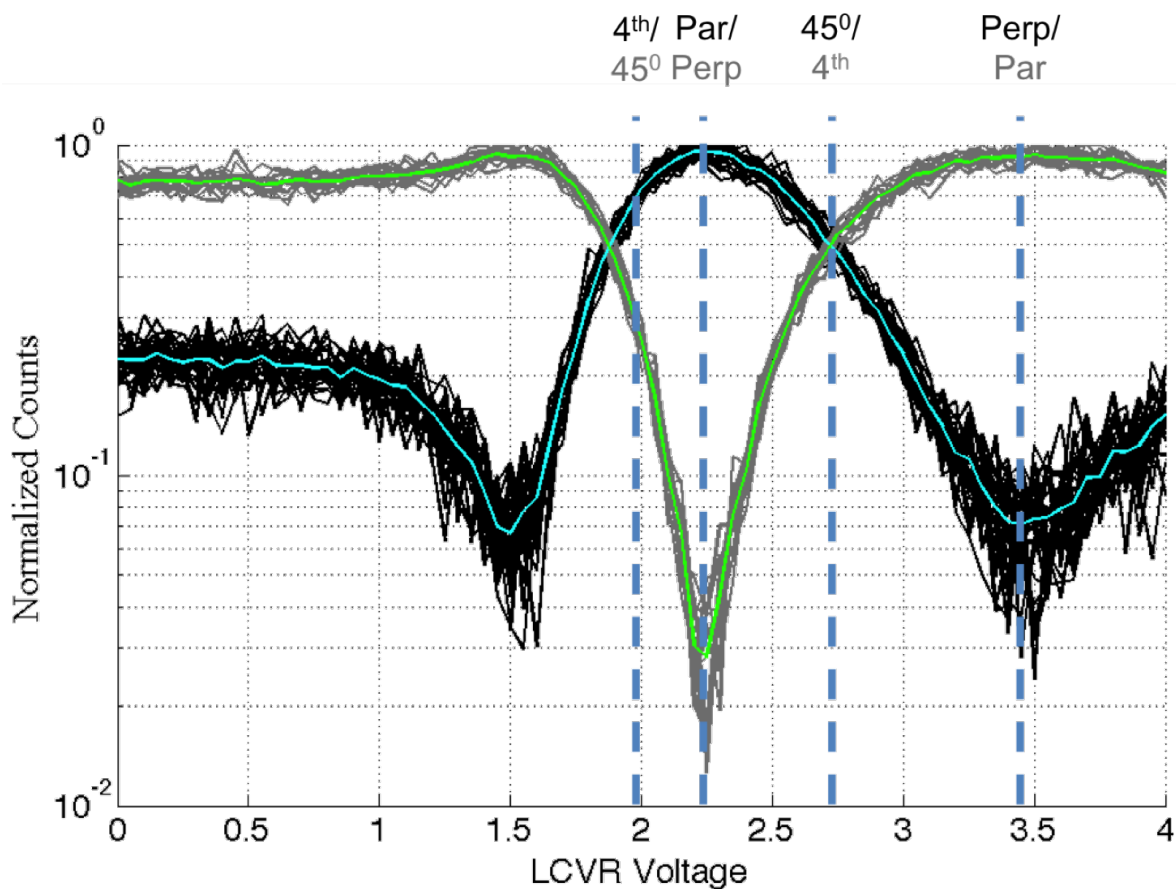
Figure 4.7: Voltage scan of the CAPABL LCVR in clear air (gray) and during a slight diamond dust event (black). The gray lines are analog data taken for laser 1 and the black for laser 2 from May 2015. The green line is the average of all gray lines and the cyan line is the average of all black lines. There are 16 complete data scans for the laser 1 and 34 complete data scans for laser 2. The channels identified by these scans are marked by the bold dashed blue lines.

4.1.1.2   Lidar Operational Software and Base Postprocessing

The CAPABL system is designed to run autonomously with only periodic checks by an onsite technician at Summit. The Version 2 hardware described in Section 4.1.1.1 necessitated creation of new controlling and processing software, which was completed for this thesis. The main acquisition scripts are written by the author in Labview and the main processing is done in multiple steps via Matlab, also written by the author. This section provides a brief description of the software stream used to control and process CAPABL data and relates the lidar theory developed in Chapter 2 and Chapter 3 to the operational implementation.

Raw photon counting and analog lidar profile data is taken every 5 *sec* and saved in a subfile approximately every 4 *min* all day. Profiles are taken at 7.5 *m* resolution to approximately 18 *km* above the surface. The last 8 *km* are used to measure noise. Each night at midnight UTC, the day's data is compiled and zipped for automatic transfer to NOAA Physical Sciences Division (PSD) servers. The data from the entire ICECAPS suite takes approximately 12 *hrs* to transfer in the winter and 5-6 in the summer. Once transferred, the data is automatically loaded and processed by PSD for basic polarization properties. Daily quicklook files as well as loadable Matlab and NetCDF files are written automatically every day. These basic variables are calculated with the SVLE non-orthogonal polarization retrievals given in Section 2.3.1. This data is then copied manually from NOAA PSD with radiosonde data to perform further processing; data is saved in a highly redundant way. A flow diagram for the data processing is given in Figure 4.8.

Once raw data is available at NOAA PSD, a manual script is run that ingests and can process all data from CAPABL's redeployment to the present. Table 4.3 gives the processing steps that are taken. Raw CAPABL and ICECAPS radiosonde data is required for this processing level. CAPABL makes observations with 5 *sec* resolution per polarization angle and scans through 4 polarization angles before returning to the original polarization, taking a total of 20 *sec* before returning to the first polarization angle. These polarizations are all linear and were oriented parallel to the outgoing polarization, 0°, (referred to as par), perpendicular to the outgoing polarization, 90° (referred to as perp), approximately 45° between parallel and perpendicular polarization (referred to as 3rd channel), and approximately 110° from parallel (or 20° from perpendicular) polarization (referred to as 4th channel). The outgoing polarization is 45° rotated from the tilt axis. These scans are parsed by like-polarizations and time integrated to 20 *sec* per polarization and spatially integrated to the resolution of 30 *m*. Saturation corrections are applied assuming CAPABL is a non-paralyzable system (shown in Figure 4.5) using Equation 4.2 and Equation 4.3 [105, 153]. It is important to note that the variance of saturation-corrected photon counting is not simply the variance from Poisson statistics, but when saturation correcting, the error introduced by an inexact model fit is also included that increases the variance. A propagation of error is performed
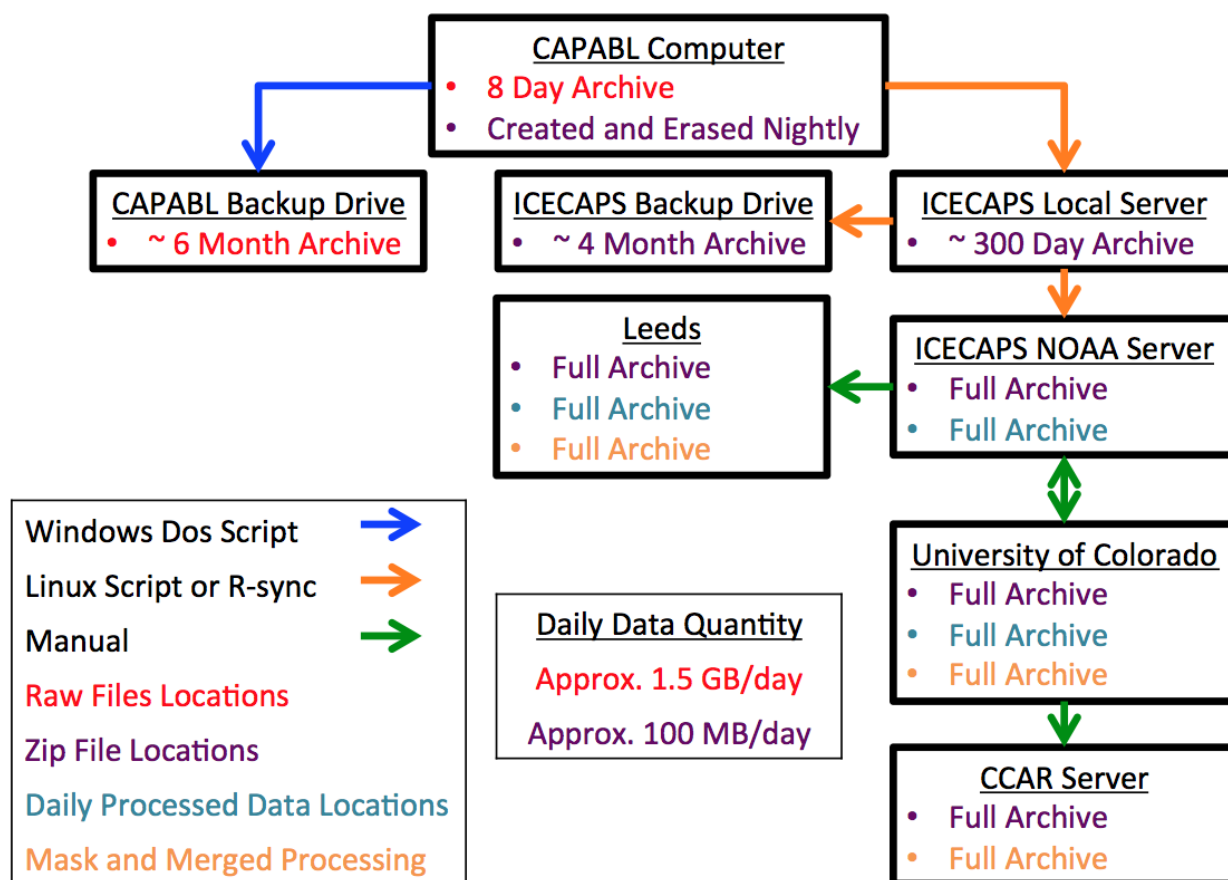
Figure 4.8: Data flow diagram of the raw and processed CAPABL data. Data is saved in a highly redundant manner via the ICECAPS backup server on site at Summit, backup drive local to the CAPABL controlling computer, and servers at NOAA, the University of Colorado, and the University of Leeds.

Table 4.3: A summary of the data processing steps taken to create the data masks desired for CAPABL. The processing for each data type: Analog (A), Photon Counting (PC), and Saturation Corrected Photon Counting (SCPC), is constant except where noted. Note that the diattenuation error equation is calculated per standard propagation of error techniques taking a Taylor series expansion of Equation 2.17 given in Equation 2.21 with partial derivatives defined in Equation 2.22 and Equation 2.23.

	Processing Step	Channels	Details
1)	Time integration	A/PC	To a constant 20 second resolution
2)	Spacial integration	A/PC	To a constant 30 meter resolution
3)	Saturation correction	PC	Creates SCPC level per Figure 4.5
4)	Background subtraction	All	Removes measured noise data
5)	SNR filter	All	
6)	Speckle filter	All	5×5 surrounding box
			$> 75\%$ data already removed = bad
			$> 25\%$ data available = good
7)	Calculate polarization properties	All	Depolarization and depolarization ratio
			and accompanying error estimates
			Diattenuation and diattenuation error
			Backscatter ratio (R) per [152, 89]
8)	Remove non-physical values	All	Values outside $0 \leq \delta \leq 1$
			Values outside $0 \leq \sigma_\delta \leq 0.4$
			Values outside $-1 \leq D \leq 1$
			Values outside $0 \leq \sigma_D \leq 0.2$
9)	Calculate base voxel type	All	Clear: $1 \leq R < 2.6$
			Aerosol: $2.6 \leq R < 6.5$
			Cloud: $R \geq 6.5$
10)	Calculate phase voxel type	All	Liquid: cloud voxels with $0 \leq \delta \leq 0.11$
			Ice: cloud voxels with $\delta > 0.11$
11)	Calculate orientation voxel type	All	Random: ice with $0 \leq D_1 D_2 \leq 0.01$
			HOIC: ice with $D_1 D_2 \geq 0.01$
			and $\sigma_D \leq 0.005$

with Poisson error and the inexact model fit error, which is given in Equation 4.5. Here S_{PP} is the number of shots per profile, T_{PB} is the time per bin for light to travel, N_{obs} is the number of observed photons in the photon counting channel, $\sigma_{\tau_{NP}}$ is the error in the model fit from the 1σ confidence bounds from the Levenberg-Marquardt nonlinear least squares solver, $\sigma_{N_{obs}}$ is the Poisson error from the photon counting process, and τ_{NP} is the non-paralyzable dead time for CAPABL. To the author's knowledge, this formulation is not presented elsewhere. This propagation of error is taken into account for all error analyses [105].

$$\sigma_N = S_{PP}T_{PB}\sqrt{\frac{N_{obs}^4\sigma_{\tau_{NP}}^2 + S_{PP}^2T_{PB}^2\sigma_{N_{obs}}^2}{(S_{PP}T_{PB} - \tau_{NP}N_{obs})^4}} \tag{4.5}$$

All data is then background subtracted and subject to an SNR filter. The filter bounds are as follows: photon counting data with less than one photon count per bin after background subtraction and analog voltages less than 1 mV per bin after background subtraction (SNR ratio of approximately -5 dB) are removed. This background subtracted and SNR filtered data is then passed to a speckle filter, which interrogates a 5 by 5 voxel region around all observations. Measurements where more than 75% of the surrounding data is removed by the SNR filter are also removed. This yields three sets of quality controlled data referred to as analog, photon counting (PC), and saturation corrected photon counting (SCPC).

Polarization properties are then calculated for each analog, PC, and SCPC dataset by using the non-orthogonal polarization retrievals from Section 2.3.1. One deviation from the original analysis presented for CAPABL hardware Version 1 by Neely et al. [89] used here is the removal of the feedback loop for the 3rd and 4th channels; instead an atmospheric calibration range is used in post processing, which performs the same function as the feedback loop on a measurement by measurement basis. The original feedback loop described by Neely et al. [89] was designed to accommodate slight retardance changes in the LCVR as a function of ambient temperature. However, in rapidly changing atmospheric scenes, the original feedback loop, designed to eliminate slow systematic effects, was observed by the author to become unstable based on fast atmospheric effects.

Using post processing calibration removes the instability by calculating LCVR retardance for each measurement independently. This has been observed to be more stable than the original feedback loop especially in quickly changing cloud scenes and when clouds occupy the pre-determined calibration altitude. This stability has been especially noted when observing low-lying, liquid-only or mixed-phase clouds because of the rapidly changing scene and flexibility of altering the calibration altitude to avoid cloud scenes in post processing.

Depolarization, depolarization ratio, and diattenuation as well as their error estimates are calculated using the standard orthogonal polarization approach presented by in Section 2.3.2 [89], and also using the non-orthogonal approach described in Section 2.3.1. The non-orthogonal approach uses all the same steps as the original presentation by Neely et al. but with the following exception. Instead of assuming the observations are made at exactly 1) parallel, $0°$, 2) perpendicular, $90°$, and 3) $45°$, the angle of the third channel is carried through the analysis as a variable and the retrieved angle from atmospheric calibration is used. For the depolarization retrieval in areas that lack oriented scatterers, the depolarization can be calculated with any set of measurements of the 6 presented in Figure 4.6, but for this analysis the strongest 2 signals (par and 3rd channels) were used to demonstrate the range enhancement possible. Orientation is identified by non-zero diattenuation, D, for those voxels identified as ice. Diattenuation is calculated in two ways, 1) using par, perp, and the 3rd channel referred to as D_1 and 2) using par, perp, and the 4th channel referred to as D_2. These channels are chosen because of their opposite sensitivity to saturation for the PC retrievals. By multiplying the two measurements together, negative values indicate D_1 and D_2 are tending in opposite directions indicating a saturation event. Conversely, positive values of D_1D_2 indicate the two measurements are tending together and that the non-zero diattenuation is physical.

Data is removed outside of the allowable ranges: $0 \leq d \leq 1$, $0 \leq \sigma_d \leq 0.4$, $-1 \leq D \leq 1$, and $0 \leq \sigma_D \leq 0.2$, as these represent non-physical conditions. The error analysis procedure for PC described by Neely et al. [89] assumes Poisson statistics where the data is assumed shot noise limited. The same procedure for PC is carried through the analysis shown here. The analog signal is

not governed by Poisson statistics however. The analog uses the variance of the background voltages for its error estimates. Additionally, as mentioned above, the variance for SCPC is modified to reflect the correction procedure and the variance introduced via inexact model fitting, Equation 4.5. Finally the backscattering ratio is calculated using temperature and pressure information collected from the ICECAPS twice daily radiosonde program, interpolating between launches, and using the inversion technique of Klett [152] with a lidar ratio, the ratio of extinction to backscattering, of 10 following the results of Nott and Duck [154]. A derivation of the Klett inversion is given in Appendix 8.3.4.

Using all of this information, the identification of data is performed in the following manner. Clear air is found as any time and altitude bin, referred to here as a voxel, with a backscattering ratio less than 2.6. Sub-visible clouds and aerosols are any voxel with a backscattering ratio between 2.6 and 6.5. Clouds are tagged as voxels with backscattering ratio greater than 6.5 (for comparison, Cesana et al. use a backscattering ratio threshold of 5 to define clouds [155]). Within cloud voxels, the depolarization ratio threshold, originally defined by Intrieri et al. [151] of $\delta \geq 0.11$ was used to define ice and $\delta < 0.11$ as water. As the most common aerosol at Summit is ice, any voxels tagged as aerosol that displays a depolarization $\delta \geq 0.11$ is reset as ice. Finally, preferentially oriented ice crystals are identified by $D_1 D_2 > 0.01$ with $\sigma_{D_1} \sigma_{D_2} \leq 0.0025$.

The depolarization threshold is a subject of much discussion within the lidar community. Here, the threshold of $\delta = 0.11$ is taken from both literature and by analyzing CAPABL's first 4 months of available data. The cloud phase fractional occurrence (FO) is calculated for these 4 months of data varying the depolarization ratio threshold from 0.05 to 0.3, given in Figure 4.9. The FO of liquid and ice rapidly changes from thresholds from $\delta = 0.05$ to $\delta = 0.11$ for all months then stabilizes until approximately $\delta = 0.2$. This indicates thresholds from $\delta = 0.11$ to $\delta = 0.2$ result in similar FO values but that a threshold of $\delta = 0.11$ is a reasonable threshold for CAPABL.

Sample data from this procedure is given in Figure 4.10 for analog and in Figure 4.11 for PC detection. Time-height contours of raw signal and polarization processed data are given. Total backscattering is simply the addition of the parallel and perpendicular channels per the
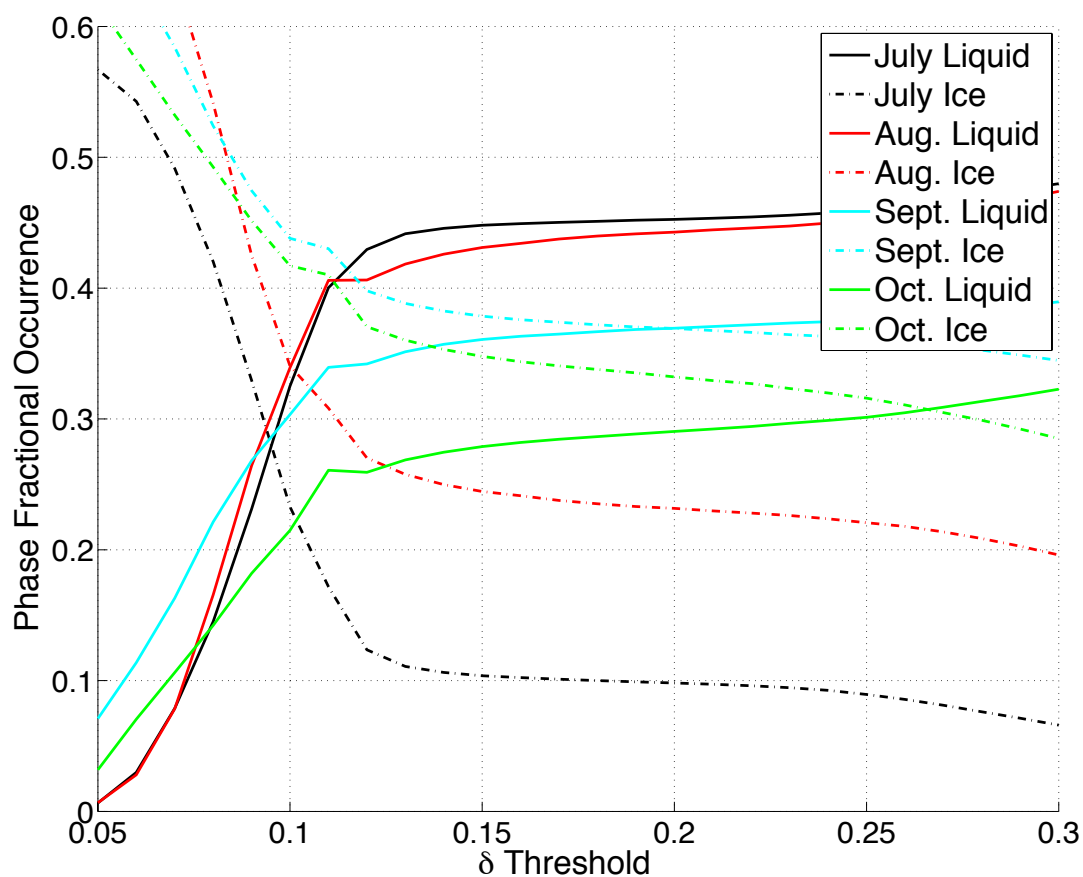
Figure 4.9: Fractional occurrence (FO) of cloud phase for the first 4 months of available CAPABL data. The FO of liquid and ice rapidly changes from thresholds from $\delta = 0.05$ to $\delta = 0.11$ for all months then stabilizes until approximately $\delta = 0.2$. This indicates thresholds from $\delta = 0.11$ to $\delta = 0.2$ result in similar fractional occurrence values but that a threshold of $\delta = 0.11$ is a reasonable threshold for CAPABL.
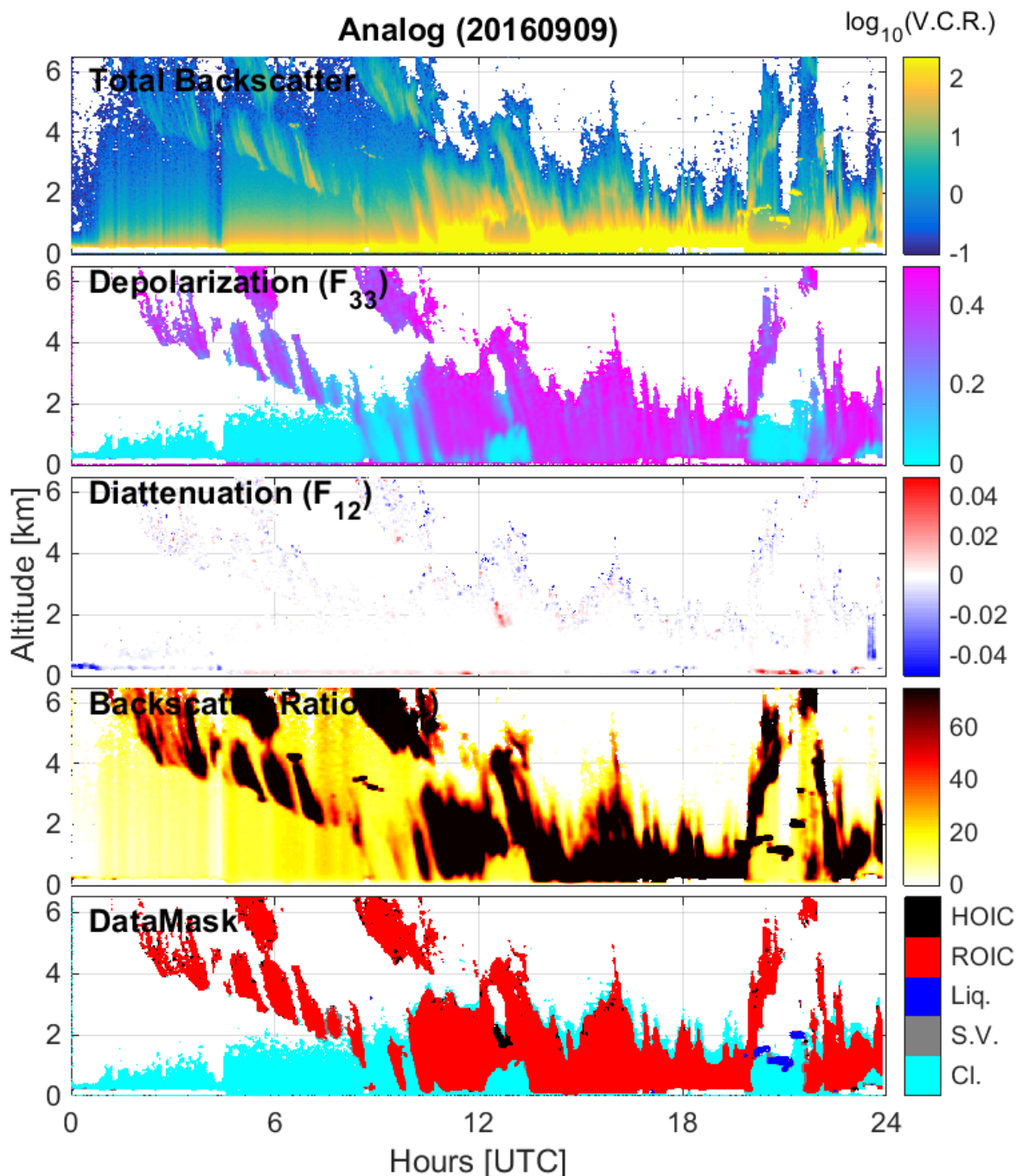
Figure 4.10: Analog data from the CAPABL system for September 9, 2016. Total Backscatter is the summation of background subtracted par and perp voltages converted to a virtual count rate (V.C.R.) using a data gluing procedure in MHz. The total backscatter color bar is given from $100\ kHz$ to $250\ MHz$ on a logarithmic scale. Depolarization is calculated as given in Equation 2.16. Diattenuation is calculated as given in Equation 2.17 and Table 4.3 . Backscatter ratio is calculated by performing a Klett inversion and using ICECAPS radiosonde data (launched at 2400 UTC and 1200 UTC daily) to calculate a molecular extinction component [152]. Liq., S.V., and Cl. stand for liquid, sub-visible, and clear, respectively.
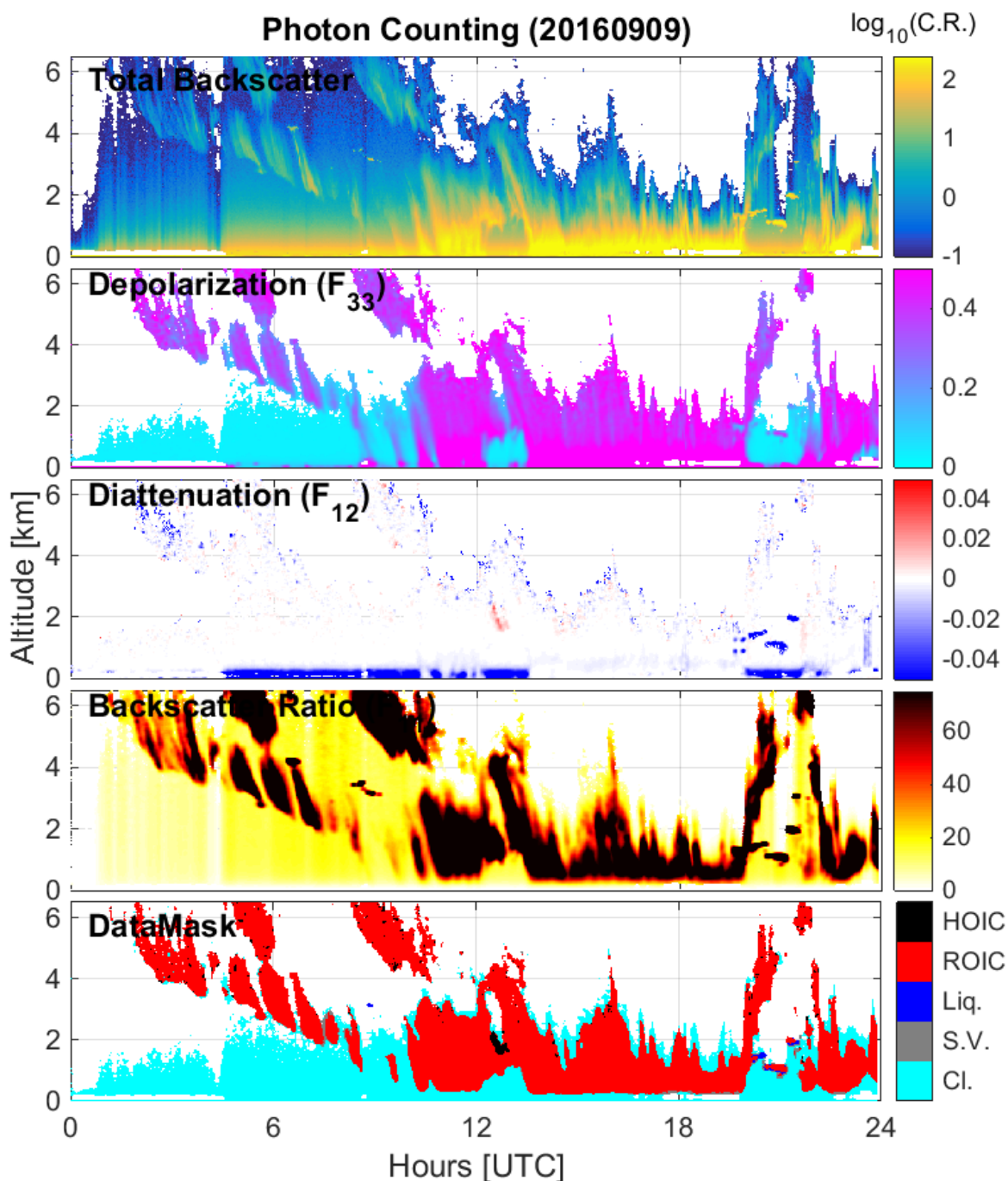
Figure 4.11: Photon counting data from the CAPABL system for September 9, 2016. Total Backscatter is the summation of background subtracted par and perp counts (C.R.) in MHz. The total backscatter color bar is given from 100 kHz to 250 MHz on a logarithmic scale. Depolarization is calculated as given in Equation 2.16. Diattenuation is calculated as given in Equation 2.17 and Table 4.3 . Backscatter ratio is calculated by performing a Klett inversion and using ICECAPS radiosonde data (launched at 2400 UTC and 1200 UTC daily) to calculate a molecular extinction component [152]. Liq., S.V., and Cl. stand for liquid, sub-visible, and clear, respectively.

general inversion of the measurement matrix given in Equation 2.14. The depolarization plotted is depolarization d not depolarization ratio δ. On the day given, both measurement types show a descending cloud layer in the morning from approximately 2 to 8 UTC and then low ice clouds until approximately 20 UTC where the air clears and a liquid cloud passes through the field of view. On this day, and most days where CAPABL observed ice clouds, some small sections of HOIC are visible with a much less common large section around 1230 UTC. These identifications of HOIC are common throughout the data set and are discussed more in Section 5.1. One note that will be expanded in Section 5.1 is that diattenuation is observed to be a sensitive measure of saturation effects. Dark blue sections of diattenuation are caused by the 2 calculation types tending in opposite directions indicating non-physical diattenuation measurements.

One measure of success of the operational software and hardware created for CAPABL for this thesis is the total amount of data collected by CAPABL. Some analysis is performed but much more is possible with a large data set. After its deployment and testing in May and June 2015, CAPABL Version 2 was declared operational on July 2, 2015. Since that day, CAPABL has run nearly continuously. The analysis for this thesis is truncated at February 28, 2017. In that 608 day span, CAPABL has achieved an uptime (time spent taking measurements as opposed to being repaired or experiencing software errors) of 97.8%. This is approximately 14,200 hrs. For the 608 days of interest, a combined total of only 13.2 days is missed. This 20 month period constitutes the longest continuous record of HOIC measurements known to the author and also contains valuable polarization data useful within the context of the ICECAPS sensor suite. The following sections describe combination and validation of this data set, and the scientific results obtained from evaluating CAPABL's data are shown in Chapter 5.

4.1.2   Lidar Data Merging and Best Estimate Data Product

A single combination of all of the CAPABL data products into a best estimate cloud product leverages all of the advantages of analog and PC as well as non-orthogonal retrievals to extend the dynamic range of the counting system [105]. This section describes the broad rules used to

merge all of the possible data collected into a single best estimate profile. This merging is done on the basis of signal counting regimes. Here valid signal ranges are defined where the measured signal count rate is linearly proportional to incident intensity at the detector. For analog detection, the range is fixed by the analog noise in the detector circuit on the low end and by the width of the analog-to-digital converter (ADC) bounds on the high end. For PC, the range is fixed by the discriminator threshold and pulse height distribution on the low end and detector and counting system dead time on the high end.

The SNR filter and the speckle filter defined by Section 4.1.1.2 and Table 4.3 are designed to remove data lacking signal strength of one or more of the polarization signals. These filters are applied to all data streams individually (to each polarization and counting type) and provide a lower limit of acceptable count rates for all channels. This limit is much higher for analog detection (approximately 1 MHz) and much lower for PC detection (approximately 10-100 kHz). The upper limit of count rate is enforced via bounds set on the receiver ADC. The analog counting system is able to track PMT signals that exceed the ADC bounds. This occurs either with a PMT pulse that is too large or with multiple PMT pulses piling up in succession or with a pulse that has too large of a voltage rebound. The ADC bounds are set from -495 mV to 5 mV with negative tending detector signals which are nominally set to result in PMT pulses of approximately 10-15 mV. In all cases, if any shot results in any altitude bin signal on any polarization outside the valid ADC range, that altitude bin is removed from the data stream (hereafter referred to as clipping). Such clipped signals are removed from both analog and PC detection data streams as they represent counting data which are no longer linearly proportional to incident intensity.

Applying the filters defined in Table 4.3 to analog and PC raw data forces the data outside the valid counting range to be removed. For the analog signal, the data above the valid counting range is removed by the clipping filter and that data below the valid count range by the SNR and speckle filters directly. For the PC signal, the data below the valid count range is also removed by the SNR and speckle filters. The upper range of PC signal is however not necessarily limited by the clipping filter, in fact it is still poorly constrained due to possible pulse pileup. To specify

the upper bound of the valid signal range for PC signals, the combination of analog and PC is considered. Implicit in the combined detection of analog and PC data is the assumption that there exists a range of counting signals, in the range of approximately 1- 5 MHz, where both signals are acting linearly, i.e. that both measurement values reported are linearly proportional to the incident intensity at the detector. By this assumption, all data measured by the analog channel will be an upper bound on the PC detection. Practically speaking, this means that data removed from the analog detection scheme by the SNR and speckle filters is potentially valid PC data and any data still present in the analog detection data denotes invalid PC data. SCPC is not needed.

There exists another way of viewing analog, PC, and SCPC data which is presented by Newsom et al. [150]. The Newsom et al. [150] method effectively combines all signals into one raw merged signal and then produces data products from pre-merged data. Here it is chosen not to merge the data in this manner for a few reasons. Foremost, the method used by Newsom et al. [150], which includes frequent calculation of gluing coefficients, is not practical at Summit because of the limited systematic access throughout the year. It has been found that the easiest way to perform this calibration for CAPABL is in clear skies with no receiver optical attenuation. This allows for the largest possible range of signals and a smooth clear transition between analog and PC signals. However, at Summit given the height of most clouds is confined to below 8 km above the ground and most strong liquid only and mixed phase clouds are below 3 km, optical attenuation is critically needed operationally. Therefore, the system optical setup is sub-optimal for such calibrations. Additionally, it is not clear how to combine analog and PC signals at a single height to adequately account for error introduced by temporal variation of gluing coefficients. Newsom et al. [150] highlights PMT relaxation as a source of error in the gluing coefficients, which make them vary in time. While this should at least in theory be less significant at Summit given the long periods of sun-up or sun-down, the observed signal count rates at Summit are more often linked to cloud properties, such as base height and optical thickness, which are far less predictable. Finally, it is not clear how the Klett inversion method is affected by the gluing procedure. The Klett inversion requires range correlation of signals, which for a glued profile is affected to some

unquantified degree by the thresholds and gluing procedure itself.

In contrast to these issues with data gluing, the method described for this thesis addresses these problems in the following ways. Primarily, there is no need to track the temporal variation of gluing coefficients. By performing polarization retrievals as described by Stillwell et al. [105], the time dependence of the detector is effectively canceled by ratio values of the polarization measurements. This method effectively reduces the assumption of a time variance in the detector from hours to the time it takes to make a complete polarization measurement set, which for CAPABL is 20 sec. Additionally, the range correlation required by the Klett inversion is preserved by considering each type of profile individually. Moreover, by systematically verifying each detector signal is within the counting system's observable and valid dynamic range, polarization retrievals can track Poisson or Gaussian errors (associated with PC and analog detection respectively) in a more accountable way. Finally, as a practical matter, access to CAPABL occurs approximately once per year. The method used allows the optical attenuation in the receiver to be set once and left untouched for the year.

An example of the merged data product is given in Figure 4.12 for February 17th, 2016 and in Figure 4.13 for August 22nd, 2016. Figure 4.12 shows the levels of data merging. In Figure 4.13, the raw analog signals are provided in the top panel, the merged data in the middle panel, and the origin of the data for each mask in the lower panel. This procedure takes most of its data from analog detection during daytime and low cloud scenes, much more data from PC during nighttime, and in the upper clear air and cloud scenes from non-orthogonal retrievals.

The data volume of interest is from 0 km to 8 km above the surface where most of the clouds exist at Summit [35]. Performing the above data merging and examining the effect for a 6 month period from July to December 2016, CAPABL has data available at 34.2% of the data volume of interest from 0 km to 8 km above ground level. This overlaps 75.3% of all filtered co-located millimeter cloud radar observations (described in more detail in Section 4.1.3) during this time. Other data is removed due to filtering or instrument downtime. In comparison, retrievals performed with just orthogonal polarizations result in data availability at 24.7% of the volume of interest. The
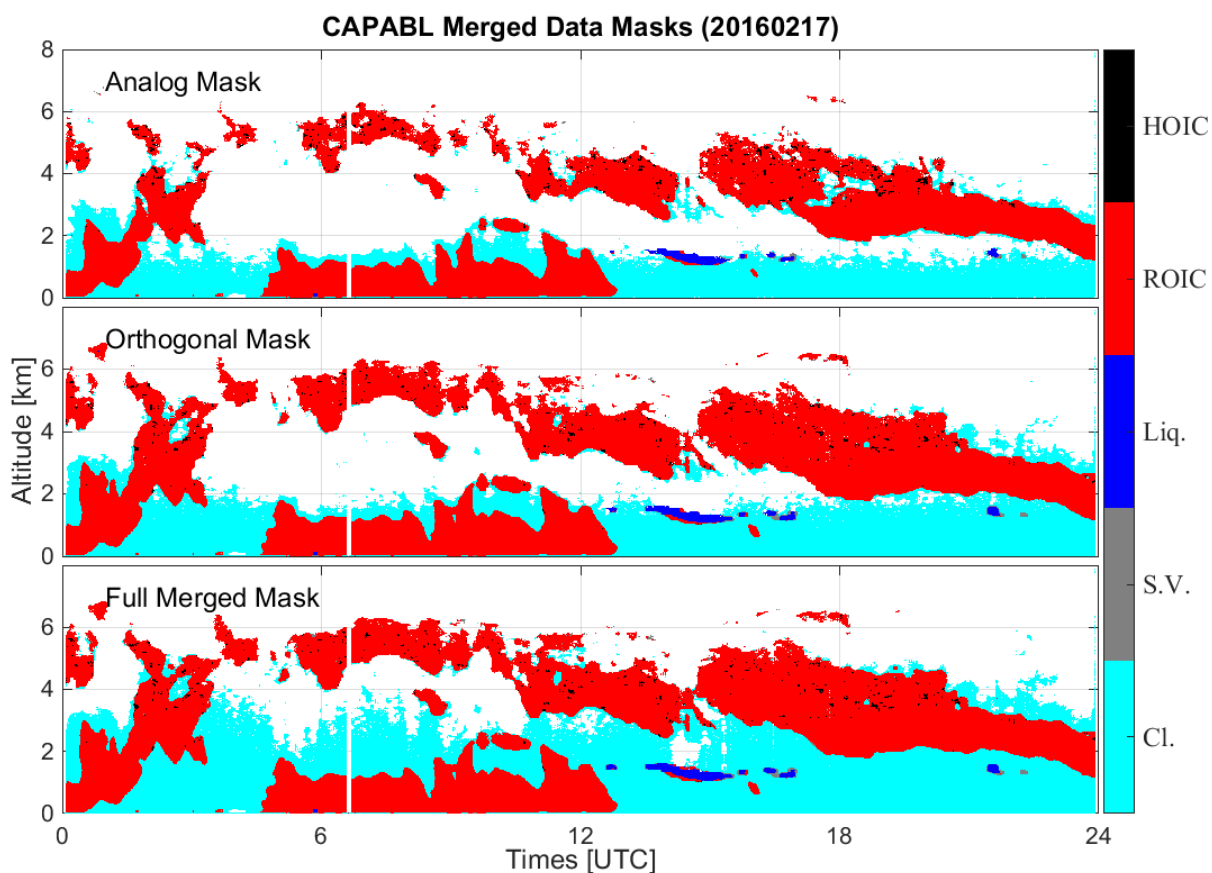
Figure 4.12: Merged data product for the CAPABL system for February 17, 2016. Analog Mask is the base analog data product. The Orthogonal Mask is a combination of analog and PC data products. The Full Merged Mask includes both orthogonal and non-orthogonal data for analog and PC. Liq., S.V., and Cl. stand for liquid, sub-visible, and clear, respectively.
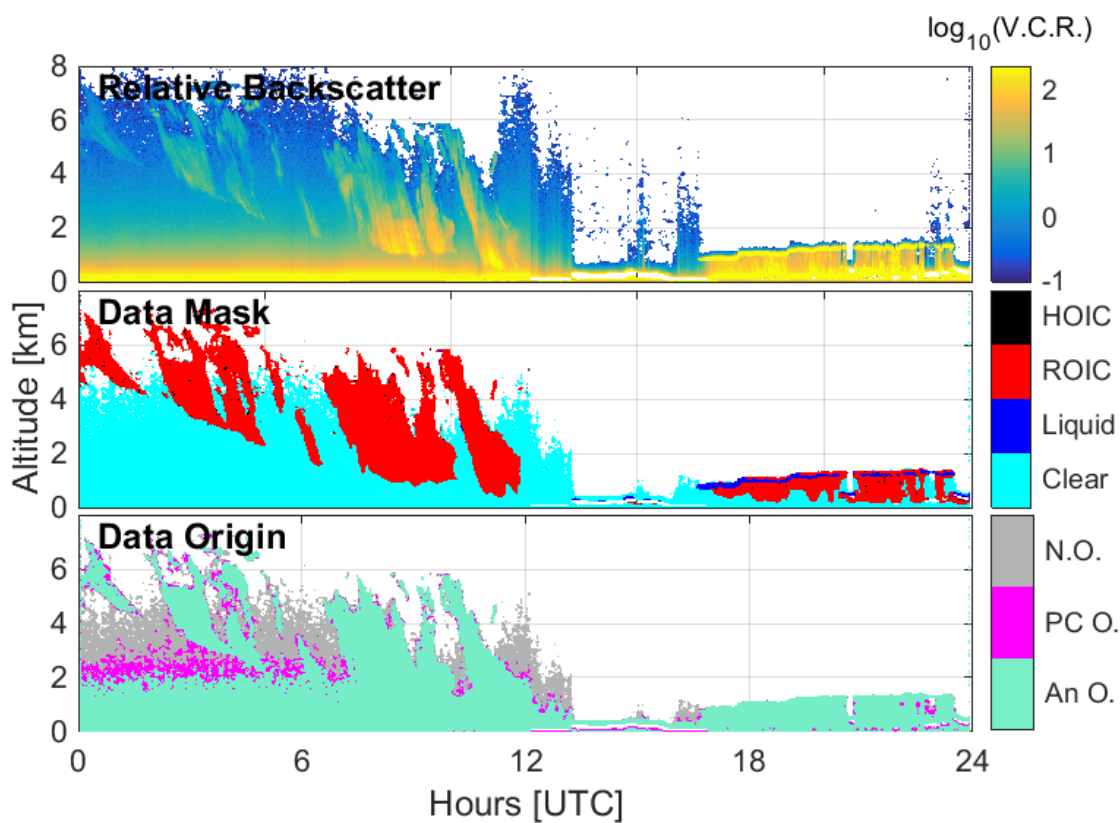
Figure 4.13: A sample of the CAPABL merged data product from August 22, 2016. The top panel shows total analog backscatter for the whole day in log base 10 signal intensity. The middle panel shows the merged data product. The bottom panel shows the origin of each voxel. An O. indicates orthogonal processing with analog data, PC O. indicates orthogonal processing with photon counting data, and all non-orthogonal types are lumped together.

improvement due to non-orthogonal polarization retrievals is either 9.5% of the entire data volume or 27.7% of the total valid data output from CAPABL.

4.1.3   ICECAPS Ancillary Data Sources

As the CAPABL system is a new lidar system and much of the operational software and hardware were developed for this thesis, validation of its data products is of major concern. In particular, the novel measurements of HOIC that it makes must be considered carefully. Validation of the data products produced, specifically of the voxel identifications for the analog and PC as well as the merging procedure described in Section 4.1.2 is provided by comparison to the co-located ICECAPS instrumentation. The instrumentation is described in this section and the results of the validation study are presented in Section 4.2.

4.1.3.1   Micro-Pulse Lidar

The micro-pulse lidar (MPL) used in this work is a Sigma Space V4 polarization sensitive system using a frequency doubled Nd:YAG laser at 532 nm. The system hardware design is well described by Campbell et al. [78] and the polarization hardware and retrievals by Flynn et al. [82]. The system at Summit has been changed twice during the duration of the ICECAPS experiment; both times due to a malfunctioning liquid crystal variable retarder. The validation study presented in this thesis will use only data from the third system for consistency.

MPL raw data (photon counts) is time and space integrated as close as possible to CAPABL's data grid. Calibrations as described by Campbell et al. [78] are performed monthly to remove signal induced noise (SIN) resulting from the strong light signals from the shared telescope transceiver design. The SIN calibration corrections applied are linear interpolations between subsequent SIN calibrations. The calibration data is taken at 30 m resolution, which sets the lidar range resolution of the validation study. This SIN corrected raw data is then linearly interpolated from the MPL grid directly to the CAPABL grid. The polarization properties are calculated as in Flynn et al. [82] with no modification to the method presented. Note that the MPL measures depolarization

using both linear and circular polarizations while CAPABL measures only linear polarizations. The methods derived from the SVLE compensate for this discrepancy.

A Klett inversion of the MPL data is also performed using the original development by Klett [152] to calculate total (aerosol plus molecular) backscattering efficiency, β. As no high spectral resolution lidar or Raman lidar is available at the site as a direct measurement of molecular scattering, the molecular backscattering efficiency is calculated from radiosonde thermodynamic data. Data are linearly interpolated from the ICECAPS twice daily radiosonde program to the common CAPABL and MPL data grid. Scatterer number density are derived from radiosonde pressure and temperature measurements and then multiplied by the backscattering cross section described in Equation 3.2 [50, 115]. The Klett inversion, assuming again a lidar ratio of 10, results in combination with the molecular backscattering efficiency result in an estimate of the backscattering ratio, $R = (\beta_a + \beta_m)/\beta_m$.

MPL data is classified by the method given in Table 4.3 [105] as for CAPABL. Note that CAPABL has the unique ability to measure the F_{12} element of the scattering matrix upon which the diattenuation measurement is based; the MPL does not make this extra measurement. Filtering steps based on diattenuation and classification for HOIC are not performed for the MPL. For this validation study, MPL data results in voxel classifications that are either clear air, cloud ice, cloud liquid, or removed due to data filtering.

4.1.3.2   Millimeter Cloud Radar

The Millimeter Cloud Radar (MMCR) used in this validation study was originally developed for the ARM Program and deployed in the SHEBA experiment [151]. The MMCR is a zenith-pointing 35 GHz single-polarization Doppler radar. A general hardware description is given by Moran et al. [156] and its software and operational measurement modes documented by Clothiaux et al. [157]. Data products available are based on observed Doppler spectra. Specifically, the system reports reflectivity (the integral of power in the Doppler spectrum), Doppler shift (the first moment of the Doppler spectrum), and Doppler spectral width (the second moment of the Doppler

Table 4.4: Radar operational mode configuration settings. The radar cycles between 4 modes of which only the cirrus and general modes are used in this work. The modes are cycled such that the general mode is every 4th measurement and the cirrus mode is every 8th at a cadence of approximately 0.5 sec per mode.

Radar Mode	General	Cirrus
Average power [W]	0.5353	7.146
Intra-pulse period [ms]	96	115
Pulse width [ns]	583	583
Number of code bits	0	16
Number of coherent averages	5	6
Range resolution [m]	87.5	87.5

spectrum). The zenith-pointing system occupies space in the same building as CAPABL and is carefully leveled by an onsite technician as needed to within approximately $0.2°$ as the snow on which the building sits settles.

Data used for this study are from the radar general mode and radar cirrus mode, with some operational settings given in Table 4.4. Radar data is generally taken at higher temporal resolution and lower spatial resolution than CAPABL. To push the radar data onto a similar grid as CAPABL and the MPL, radar data is incoherently averaged in time to as close to the CAPABL grid as possible. Then as with the MPL, data is linearly interpolated, in time and space to the CAPABL grid. Data is typically filtered with a signal-to-noise ratio (SNR) of less than -14 dBZ but is done only selectively in this work due to the preferential filtering of clear air data. Data which is filtered for its SNR is referred to as filtered radar data and data not including the filtering is referred to as raw radar data.

4.1.3.3   Microwave Radiometer

Column moisture measurements are calculated using two co-located microwave radiometers (MWR) manufactured by Radiometer Physics GmbH (RPG). The first radiometer, an RPG Humidity and Temperature Profiler (HATPRO), samples 14 channels from 22.2 GHz to 60 GHz of which 23.8 GHz and 31.4 GHz are used to observed liquid water while the second radiometer,

an RPG LWP-90-150, samples at 90 GHz and 150 GHz. From microwave brightness temperature observations, the column liquid water path (LWP) is retrieved using physical retrievals and optimal estimation [158]. Using both radiometers and optimal estimation is specifically designed to reduce the retrieval error from the dry Arctic environment by approximately a factor of 5 from approximately 25 g/m^2 to approximately 5 g/m^2 for LWP. Similar steps, incoherent averaging in time then linear interpolation, are performed as with the radar to push MWR data onto CAPABL's grid. MWR data is a column measurement so averaging and interpolation are only performed in time and are compared to the CAPABL column data product.

4.1.3.4   Radiation

Broadband radiation measurements are made at Summit by a pair of heated aspirated Kipp and Zonen CM22 pyranometers with spectral sensitivity from 200 nm to 3600 μm and a pair of aspirated Eppley Precision Infrared Radiometers (PIR) pyrgeometers, sensitive to the spectral range from 3.5 μm to 50 μm [159]. These instruments were originally installed in August 2013 by and are operated by NOAA's Global Monitoring Division. The instruments are maintained by an onsite technician at Summit. Raw data is reported as 1 min averages

The pyranometers are calibrated every 2 years at NOAA's Solar Radiation Calibration Facility. The raw data is manually quality controlled by NOAA's Global Monitoring Division Radiation Group. A dome correction factor for the longwave PIR is applied similar to that of Albrecht and Cox [160]. More information about the available radiation measurements at Summit is given by Miller et al. [159].

4.1.3.5   Rapid Radiative Transfer Model Inputs

The radiation data described in Section 4.1.3.4 will be used in this validation study to interpret the CAPABL data merging procedure in terms of known radiation relationships of cloud phase in the Arctic [33, 34, 159, 161]. Two methods will be performed: 1) considering the radiation data as measured without modification and 2) calculation of cloud radiative effect (CRE) by considering

radiation measurements with a radiative transfer model. To calculate CRE, knowledge of the state of the atmosphere is required to separate the contributions in the long and shortwave due to the clouds and due to the atmosphere. The Rapid Radiative Transfer Model (RRTM) is used to model clear sky longwave and shortwave irradiances [162]. The model requires temperature, moisture, and chemical composition inputs from which emission and absorption are calculated at model layers between the surface altitude, 3212 m, and the stratopause, approximately 58255 m. Data input for the RRTM model runs are presented where all data is pushed to 1 min resolution with 75 non-evenly spaced altitude bins ranging from 20 m to 2000 m vertical resolution between 3212 m to 58255 m as done by Miller et al. [159].

Temperature   Temperature profiles are a blend of two major data sources. Temperature profiles of the troposphere and lower stratosphere are taken from the ICECAPS twice daily radiosonde launches. Radiosondes launched from Summit are Vaisala RS-92GP sondes. As the radiosondes burst altitude is well below the top layer needed by the RRTM model, additional temperature data is required. Model data is taken from the Naval Research Labs's Mass Spectrometer and Incoherent Scatter Radar model (MSIS). Data is blended for approximately 3 km on each side of the radiosonde balloon burst height to provide a smooth transition from data to model. A simple weighting scheme is used, which over the merging altitude averages radiosonde and model data with a linear data weight. This scheme changes weights in altitude from 0% model and 100% radiosonde 3 km below burst height to 50% radiosonde and 50% model at burst height and uses the last radiosonde measurement at burst height in a linearly decreasing weight to 0% radiosonde and 100% model 3 km above burst height.

Trace Gases   Active emission and absorption from chemical species like ozone (O_3), oxygen (O_2), nitrous oxide (N_2O), carbon monoxide (CO), carbon dioxide (CO_2), methane (CH_4), and water vapor (H_2O) are considered in the clear sky emission and absorption model by the RRTM. Default standard arctic winter (SAW) profile from the RRTM model are used as model data except for the following: profiles of ozone are taken from weekly launched ozonesondes, Environmental Science type 2Z-V7 sondes, at Summit and SAW modeled data. Moisture profiles are taken from

the ICECAPS twice daily radiosonde launches and SAW modeled data. Surface measurements of CO_2 are taken from NOAA at Summit and used to scale the SAW CO_2 vertical profile. All data, like temperature, is merged above the balloon burst height for each profile with model data then linearly interpolated to 1 min resolution.

4.2   Multi-Sensor Validation of CAPABL Observations

The period of comparison for this validation study is from July to December 2016. Data uptime for this period is given in Figure 4.14 and is one major reason for the selection based on the simultaneous measurement of much of the ICECAPS suite. This period also covers both day and night and is composed of several hundred thousand individual profiles for each system.

4.2.1   Direct Lidar Comparisons

The first comparison performed is between CAPABL and the MPL. This is the simplest comparison to make because the data products of the MPL and CAPABL are very similar and both systems use the same operational principles. Relevant system characteristics are given in Table 4.5 where it is noted that CAPABL uses receiver optical attenuation to tune the irradiance from the backscattered signal on the detector. This attenuation is OD 3 or a factor of 1,000. This attenuation gives CAPABL an effective power aperture product smaller than that of the MPL. Because both instruments are lidars and have similar data streams, the results can be compared directly. As such, CAPABL's voxel identifications are compared directly to the MPL's voxel identifications. Data for CAPABL and the MPL are calculated for three separate time periods: July 2016, December 2016, and July-December 2016. This data comparison is given in a matrix of confusion, Table 4.6, where ROIC and HOIC voxels are both combined for this comparison into CAPABL Ice.

The time periods given in Table 4.6 are selected due to the solar background conditions. During the summer, July, the sun is always above the horizon at Summit. During the winter, December, the sun is always below the horizon at Summit. These two cases are highlighted to show the difference solar background makes on the data and, in particular, the effect on the MPL signals,
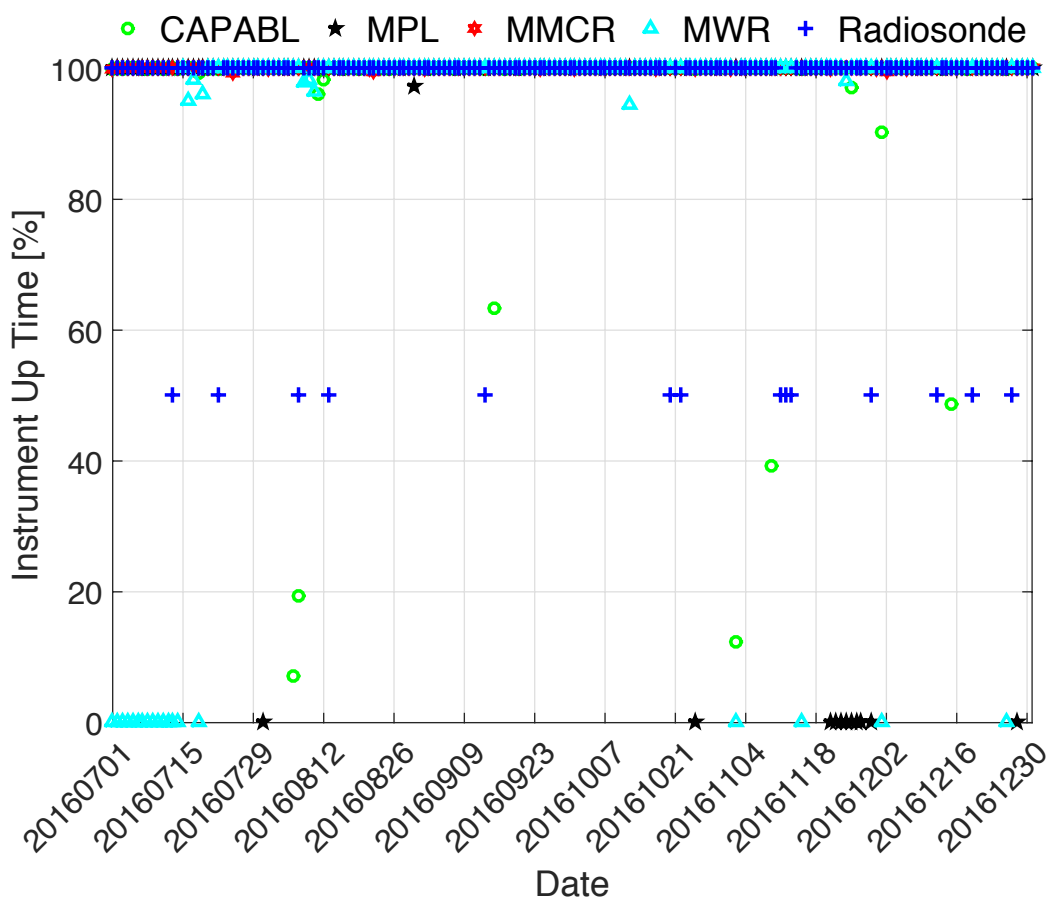
Figure 4.14: Instrument uptime over the validation study period from July to December 2016. Over this time period, CAPABL measures approximately 34.2% of the data column above Summit from 0 to 8 km with its full merged data product, and has data available at 75.3% of the voxels where the MMCR has data available. Using only analog retrievals results in 21.7% data availability and merged analog and photon counting orthogonal polarization retrievals results in 24.7% data coverage; non-orthogonal polarizations retrievals increase the data availability by 27.7%. The total uptime over the study period for CAPABL, MPL, MMCR, MWR, and radiosonde are 97.2%, 94.0%, 100%, 89.5%, and 96.2% respectively.

Table 4.5: Hardware comparison of relevant CAPABL and MPL lidar specifications. The resolutions quoted are limited in range by the MPL afterpulse calibration data and in time by the CAPABL scan rate. The resolutions presented are as close as the data can be processed before linear interpolation of MPL data to CAPABL's data grid.

Specification	CAPABL	MPL
Laser Power $[W]$	0.3	0.02
Receiver Attenuation $[OD]$	3	0
Telescope Diameter $[mm]$	208	178
Effective Power/Aperture Product $[W \cdot mm^2]$	10.2	497
Polarizations	4	2
Range Resolution $[m]$	25.98	30
Polarization Scan Resolution $[s]$	$\approx$82	80

Table 4.6: Matrix of confusion of CAPABL and MPL processed data. The diagonal shows agreement, highlighted by bold text. The last row and last column indicates one instrument had data removed by quality control steps, also highlighted in italics. The cells colored blue indicate enhanced sensitivity by CAPABL processing and cells colored red indicate enhanced sensitivity by the MPL processing. The bottom right cell, highlighted by both bold and italics, indicates both instruments lack data implying that much of the data missed by CAPABL is in a regime not reachable via lidar (i.e. large optical depth). Three sets of data are given in each cell. The first line of each cell covers the time period July 1st - July 31st, 2016. The second line of each cell covers December 1st - December 31st, 2016. The final row of each cell covers July 1st - December 31st, 2016.

	CAPABL Clear	CAPABL Liquid	CAPABL Ice	CAPABL Filtered	
MPL Clear	A) **69.7%**	B) 37.0%	C) 62.2%	D) *3.4%*	July
	97.7%	64.9%	78.9%	*74.5%*	December
	83.2%	41.8%	63.9%	*35.1%*	All
MPL Liquid	E) 0.3%	F) **56.3%**	G) 5.5%	H) *0.1%*	July
	0.0%	**26.3%**	0.2%	*0.0%*	December
	0.4%	**47.9%**	2.0%	*0.2%*	All
MPL Ice	I) 0.2%	J) 3.7%	K) **29.4%**	L) *0.5%*	July
	0.2%	8.2%	**20.2%**	*0.3%*	December
	1.4%	8.9%	**31.7%**	*1.1%*	All
MPL Filtered	M) *29.9%*	N) *3.0%*	O) *3.0%*	P) ***96.0%***	July
	2.1%	*0.5%*	*0.6%*	***25.2%***	December
	15.1%	*2.5%*	*2.4%*	***63.7%***	All

which are affected strongly by solar background. CAPABL is less affected by solar background because of the receiver attenuation.

An examination of Table 4.6 highlights some striking sensitivity improvements of CAPABL's merged data product for daytime operations. In the clear column for example, in approximately 98% of the time that CAPABL observes clear air, the MPL either agrees or lacks data to refute the CAPABL measurements over the entire study period (seen in Table 4.6 cells A, E, I, and M). This increases to 99.5% for daylight measurements. Likewise, 96% of the data in daylight that fails the CAPABL filtering process also fails the MPL's filtering process indicating a limit of penetrable optical depth that is a theoretical limit of all lidars. In many cases, highlighted in blue in Table 4.6 given in boxes B and C, the MPL observes clear air while CAPABL observed clouds of some sort. This is linked directly to the Klett inversion technique requiring a strong signal derivative to highlight large backscattering ratios, approximately > 5.0. In the case of many high clouds, the signal derivative is not strong due to noise in the perpendicular observation channel of the MPL. In comparison, the red values highlighted in Table 4.6 in boxes E and I are more than two orders of magnitude smaller because the strength of the perpendicular signal does not limit detection range for CAPABL as it does for the MPL due to CAPABL's non-orthogonal polarization retrievals.

The data presented in Table 4.6 for December observations show a major jump where CAPABL data fails QC filtering but MPL data shows clear air (seen in Table 4.6 cell D). The filtering performed after SNR and speckle filtering by CAPABL is mostly done via the unique diattenuation measurement and diattenuation error bounds. As a result, the depolarization filters are set fairly wide as they are practically unneeded. However, for the MPL, the same bounds for the filter do not tag similar low SNR cases. As a result, CAPABL data is filtered more conservatively than the MPL given the same filtering bounds on depolarization based on the diattenuation filter that can not be applied to the MPL.

The MPL and CAPABL rarely miss detecting cloud cases when they are observable by lidar, i.e. one system observes clouds while the other has data filtered. For each background condition and for the entire length of the study, not more than 3% of data is missed by one instrument where

the other instrument sees cloud activity, indicated in boxes H, L, N and O. However, the MPL frequently mischaracterizes clouds as clear, as highlighted in blue in Table 4.6. This is attributed as above to the signal in high background cases being hard to determine and the Klett inversion often misses thin cloud layers.

4.2.2   Comparisons with Other ICECAPS Data Sources

Comparisons of CAPABL data to ancillary, non-lidar, instrumentation is less straightforward than the comparison presented in Section 4.2.1. Instead of a direct comparison such as presented in Table 4.6, arguments about data consistency must be made. For example, within a mixed-phase cloud, both phases of water will have large electrical size (the radius of the particle, r relative to the wavelength, λ, given as $2\pi r/\lambda$), likely greater than 50-100 when observed by lidar, whereas relative to the radar wavelength will have small electrical size, much less than 1. In this regime, the lidar will see a scatterer well into the resonant and geometric optics regime of elastic scattering whereas the radar will see a Rayleigh scattering target. As such, it is unreasonable to expect to see exactly the same thing between unlike sensors and is one major benefit for having multiple sensors, which are not sensitive to the same effects.

The broad expectations of multi-sensor comparisons are as follows. At 35 GHz, the MMCR is more sensitive to ice than liquid water droplets via a diameter to the sixth scaling because liquid water drops are much smaller in diameter than ice in the Arctic [35, 41, 163]. Liquid water is on the order of 10^{-5} m while ice is on the order of 10^{-4} m to 10^{-3} m. By extension, the MMCR is more sensitive to liquid water droplets than clear air. One expects therefore, to see higher radar reflectivity for ice than liquid and less still for clear air. Furthermore, as ice is much larger at Summit than liquid water drops one expects to see higher Doppler velocities for ice as liquid water drops are too small to be effectively precipitated [127, 164]. Additionally, given liquid water's colloidal instability at supercooled temperatures, one expects to find higher Doppler spectrum widths accompanying liquid water due to cloud top cooling and turbulence that is required to maintain the liquid phase [34, 41, 164]. For comparison of CAPABL's data to column

measurements of liquid water path, one expects CAPABL to identify liquid overhead while the MWR observes non-zero liquid water path. Likewise, one expects to have little to no liquid water path measured for ice or clear air columns observed by CAPABL.

In light of these expectations based on observed geophysical properties, the multi-sensor comparisons are performed as follows. MWR data is processed and pushed to the CAPABL time grid as described in Section 4.1.3.3. CAPABL data is then collapsed to a column measurement based on the most radiatively important voxel type. The MWR LWP data is then assigned to one of the 4 possible column types: clear, ice (with or without HOIC), or liquid defined by CAPABL. The probability density function of the MWR LWP characteristics are calculated from all available data. The cumulative distribution function is then calculated and presented in Figure 4.15. The data that has been filtered by lidar is removed. Raw radar data, that is pushed to CAPABL's data grid as described in Section 4.1.3.2, is assigned using CAPABL's data identifiers. The 5 data types (clear air, cloud liquid, ROIC, HOIC, and filtered) are parsed. The probability density function of the radar Doppler characteristics and the cumulative distribution function are also calculated from all available data. The data that has been filtered by lidar is removed. The cumulative distribution function of the remaining 4 variables are shown in Figure 4.15 for the three Doppler moments the radar reports and its SNR. CAPABL has data available for 75.3% of the locations where there is filtered MMCR data available. Note that though they contain and represent the same data, this thesis will choose to represent instrument comparisons in terms of their cumulative distribution functions as opposed to the probability density function. Both facilitate comparisons of large quantities of data but cumulative distribution functions allow simple comparisons of differences of shape and median whereas the probability density function allows for investigations of modes and biases.

It can be seen in Figure 4.15 that the expected relationships between the lidar, MMCR, and MWR hold very well. Comparisons of lidar column data to LWP are also consistent with the stated expectations. 70% of all columns tagged as liquid columns have non-zero LWP (here zero and non-zero are taken below and above the error bounds of the measurement respectively). 91% of
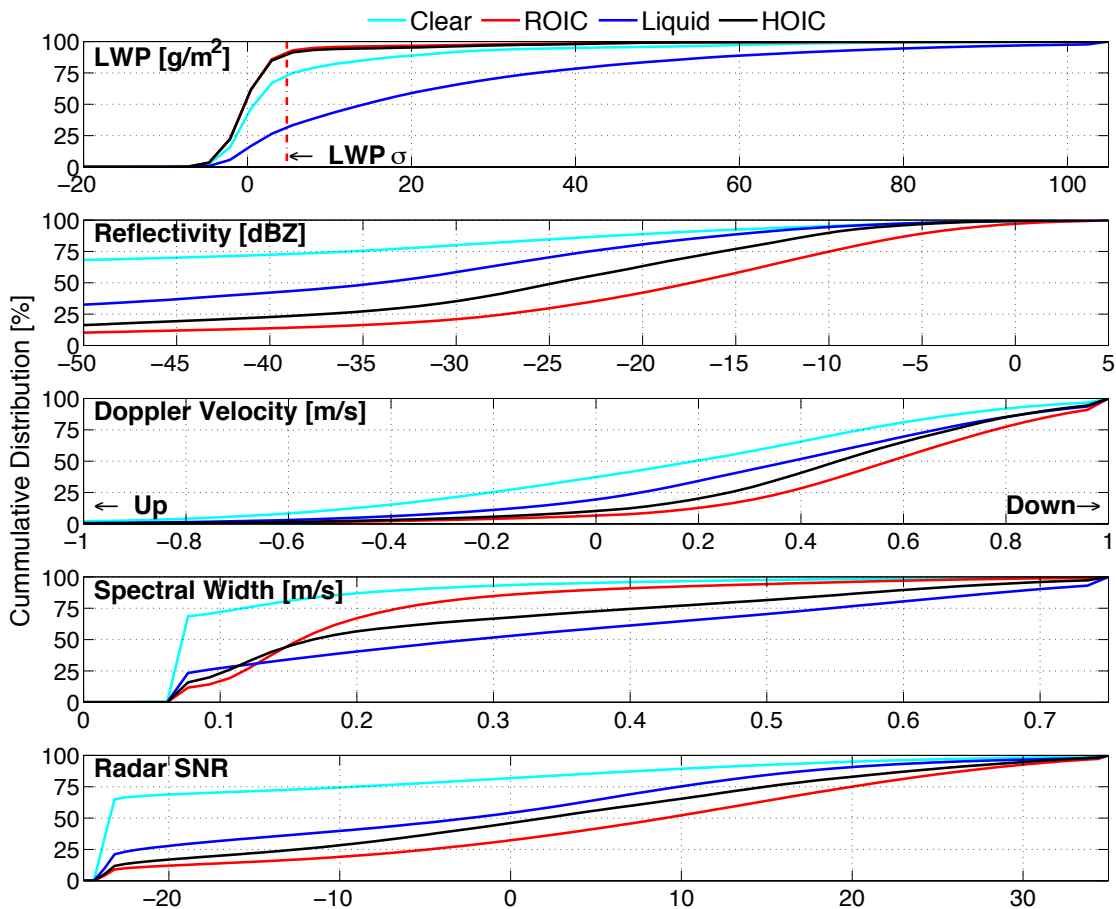
Figure 4.15: Cumulative distribution functions of co-located ICECAPS data parsed by CAPABL data. All data over the 6 month validation study period, approximately 54 million radar measurements for each Doppler moment type and 148,000 MWR column measurements, is collected and identified. Note that the average LWP uncertainty is given for the entire study period and that here a positive Doppler velocity is defined towards the zenith pointing radar system or downwards.

columns tagged as ROIC and 90% of columns tagged with HOIC do not have LWPs above the error bounds of the MWR measurement. One interesting note is that 72% of columns tagged as clear air have zero LWP. This value, being less than the ice columns, is initially puzzling. The explanation for this is related to CAPABL's non-zero overlap range, about 45 m in altitude from the system. CAPABL's measurements are completely insensitive to cloud properties to this range. Additionally, given very low cloud cover, it is possible for CAPABL's polarization signals to be discarded resulting in additional data loss, due to the post-processing clipping filter, up to approximately 200 m to 300 m. However, CAPABL's beam is not insensitive to low cloud cover and is rapidly attenuated in this relatively high optical depth environment. As a result, CAPABL can mis-identify very low cloud and precipitation, below approximately 200 m, as clear air columns because there is no cloud data in the lower range in the instrument field of view or passing the clipping filter and no data passing the SNR and speckle filtering. In terms of comparison to radar, this is not a problem as no mask is returned and is thus not considered, but in terms of column measurements this will yield an error in identification. This error is considered and times of very low visibility are flagged and removed manually. This results in an increase in the percent of columns tagged as clear air which have a zero LWP from 72% to 87%, tagged as ice from 91% to 93%, and tagged with HOIC from 90% to 94%.

The reflectivity of clear air voxels is much lower than that of ice and liquid water. 90% of all voxels identified by CAPABL as clear fall below -20 dBZ whereas only 43% of radar voxels for ice fall below the same threshold. This is confirmed with radar SNR cumulative distribution functions where 69% of all clear air data falls below the SNR threshold of -20 dBZ (this value is 72% for the threshold of -14 dBZ used by Shupe et al. [35]). Similarly, the largest scatterers, ROIC and HOIC, have higher SNR. It is worth noting that HOIC have a lower median reflectivity than ROIC in Figure 4.15. This is not true in the more sensitive radar cirrus mode above 3 km. The cumulative distributions for the radar cirrus mode have reflectivity values for ROIC and HOIC that almost overlap. This change in reflectivity and inconsistency between radar modes could indicate two things: first that HOIC are possibly occurring in thinner more tenuous clouds on average

than ROIC, or second that ground based measurements have a sampling bias which only allows observations of HOIC in thinner clouds. A combination of both is likely. This effect is examined in greater detail in Section 5.1.

ROIC has the highest Doppler velocity, with HOIC and liquid falling slower. ROIC has a median Doppler velocity of approximately 0.57 m/s downward, while HOIC and liquid are 0.47 m/s and 0.35 m/s respectively both in the downward direction. The slight skewness of the clear air identifier to downward Doppler velocity, indicated by the non-zero median, indicates some ice is being tagged as clear air by CAPABL, which is known to occur at the very top of clouds due to the Klett inversion (the inversion requires a non-negligible amount of optical depth before the initial seed optical depth is no longer influencing the overall optical depth integral), and is especially prominent as mentioned with the MWR results where low (below approximately 100-200 m) thick clouds are observed. The reduced Doppler velocity of HOIC is anticipated due to the aerodynamic drag associated with their orientation [126]. This is a clear verification that HOIC identification by CAPABL based on the novel diattenuation technique of Neely et al. and Stillwell et al. are physical [89, 105].

Comparisons of Doppler spectral width are likewise consistent with CAPABL's cloud identifiers. Relatively higher spectral width is expected in liquid phase and mixed phase clouds based partially on feedback mechanisms related to turbulence [164]. Here liquid has the highest median spectral width of 0.29 m/s with HOIC and ROIC following at approximately 0.17 m/s and 0.16 m/s respectively. It is of note that the spectral width of preferentially HOIC is slightly broader than ROIC. This phenomenon would be interesting to investigate in more detail but one possible mechanism for this behavior is suggested as follows. Spectral width is the combination of air motion (turbulence), and microphysics (differential fall velocity). As HOIC are observed to have lower Doppler velocity and are thought to fall slower than ROIC, this suggests that HOIC comprise a non-constant subpopulation of crystals. This subpopulation of HOIC, if falling slower than ROIC, would increase the spectral width of the measurement and simultaneously lower the average Doppler velocity of the profile regardless of the turbulence conditions. The spectral width

differences could thus be related to the quantity of overall orientation with lower spectral width values occurring in areas with more preferential orientation and high values occurring during less significant orientation populations.

4.3 Relevance to Posed Thesis Questions

The design and validation of the CAPABL system directly addresses two of the thesis questions posed. A bulleted summarizing list of relevant findings is given for each question.

(1) How to accurately identify and distinguish liquid and ice water in Arctic clouds using polarimetric lidar?

   (a) The SVLE developed by Hayman and Thayer [98] shows how instrument effects like diattenuation and retardance affect depolarization measurements. The measurements of the CAPABL system illustrate further how depolarization measurements can be affected by system dynamic range and cloud macrophysical properties. The results from CAPABL include both effects to further identify and distinguish instrument and measurement related effects from cloud microphysical effects.

   (b) The non-orthogonal polarization retrieval methods of Stillwell et al. [105] provide a flexible means of mitigating dynamic range effects on depolarization measurements to both limit systematic biases and enhance overall sampling and cloud identification.

   (c) Observations of HOIC in non-zenith directions removes their confounding low depolarization effects to enable unique identifications of water by depolarization and at the same time HOIC's are identified by diattenuation. These separation methods are compared and found consistent with other remote sensing hardware indicating their validity.

(3) How do we meet the needs of the next generation cloud and atmospheric state observations in the Arctic using lidar?

(a) Many of the technologies for next generation systems are tested via modifications to the CAPABL system. Specifically, the software design, counting system, alignment procedures, steering motor hardware, and data processing developed for CAPABL are considered for SuPR. Additionally, all of the data results of CAPABL are considered in the design of SuPR especially the removal of systematic polarization errors.

Chapter 5

Arctic Observations

5.1   Lidar Observations of Polar Mixed Phase and Ice Clouds and Their Radiative Effect

Having produced a near continuous validated lidar data set, its first observations are summarized here. In particular, comparisons of lidar data types: analog, PC, SCPC, orthogonal, and non-orthogonal data to the merged data product are given. These comparisons quantify the effect that each measuring system has on quantities of scientific interest to the ICECAPS program such as cloud fractional occurrence (FO) and CRE.

Using the cloud and phase masks described, monthly statistics are compiled for CAPABL observations at Summit. A single month example is given then multiple months are summarized. Voxels are separated by cloud phase and clear air. Voxels are integrated over the month-long period for each altitude and time bin. These altitude profiles are presented in Figure 5.1 for July 2015, the first month of data available since the deployment of CAPABL hardware Version 2. There is general disagreement in liquid identifications despite the data coming from the same photodetector. The only difference is the method used to handle the electrical signals within the lidar receiver and it is exactly this choice that affects geophysical interpretation. The channel sensitivity can be seen in the ice panel where all lines trend together and with similar slope; analog detection is less sensitive than PC resulting in an offset of the profile values. Profiles for non-orthogonal and orthogonal data as well as PC and SCPC overlap well for clear air above approximately 3 km. Saturation correction at low count rates is akin to multiplying by unity thus resulting in overlapping values of PC and

SCPC.

There is a dramatic underestimate of liquid water by CAPABL's PC acquisition, which worsens with decreasing altitude, shown in Figure 5.1. At 1000 m, PC and analog differ by 94% (PC observes 34 voxels of water over the month and analog observes 544). This difference is attributed to liquid voxels being mistaken for ice due to saturation in the PC par channel causing erroneously high depolarization ratio values. Below 2.5 km orthogonal and non-orthogonal results are nearly identical but above that altitude non-orthogonal polarization retrievals see more clear air and ice and have higher rates of effective sampling due to the stronger signals used. Recall the par, 3rd, and 4th channel measurements are used in the non-orthogonal calculation, which is stronger than perp measurements and reduces the detector-induced dynamic range between the measurement and the par measurement allowing for greater range-induced dynamic range and, by extension, signal range.

To demonstrate that July data is not anomalous, four months of available data from July 2, 2015 to October 31, 2015 are presented in Figure 5.2. Over this time, the CAPABL system had an uptime of $> 99\%$ (this equates to approximately 5 minutes of missed data per day, which occurs at midnight UTC each day to perform system diagnostics and housekeeping). This figure illustrates any altitude biases in classifying the type of cloud or clear air while Figure 5.2 illustrated the occurrence frequencies with height for each identifier. These data are compiled into box-and-whisker plots based on the profiles calculated for each month similar to those presented in Figure 5.1. The median altitude of all voxels for each identifier: ice, liquid, and clear, is given as a line through the center of the box, which is completed by the 25th and 75 percentile of all monthly data. The whiskers extend to the 5th and 95th percentiles. The other data values are considered outliers.

Figure 5.2 indicates 3 prominent features. First, the median altitude of liquid voxels is not constant between analog, PC, and SCPC. There is a clear 1 km to 2 km offset in the medians between analog and PC (1.72 km, 1.43 km, 0.75 km, and 0.91 km offsets for July, August, September, and October, respectively). This offset in mean voxel height indicates that low-level, liquid clouds
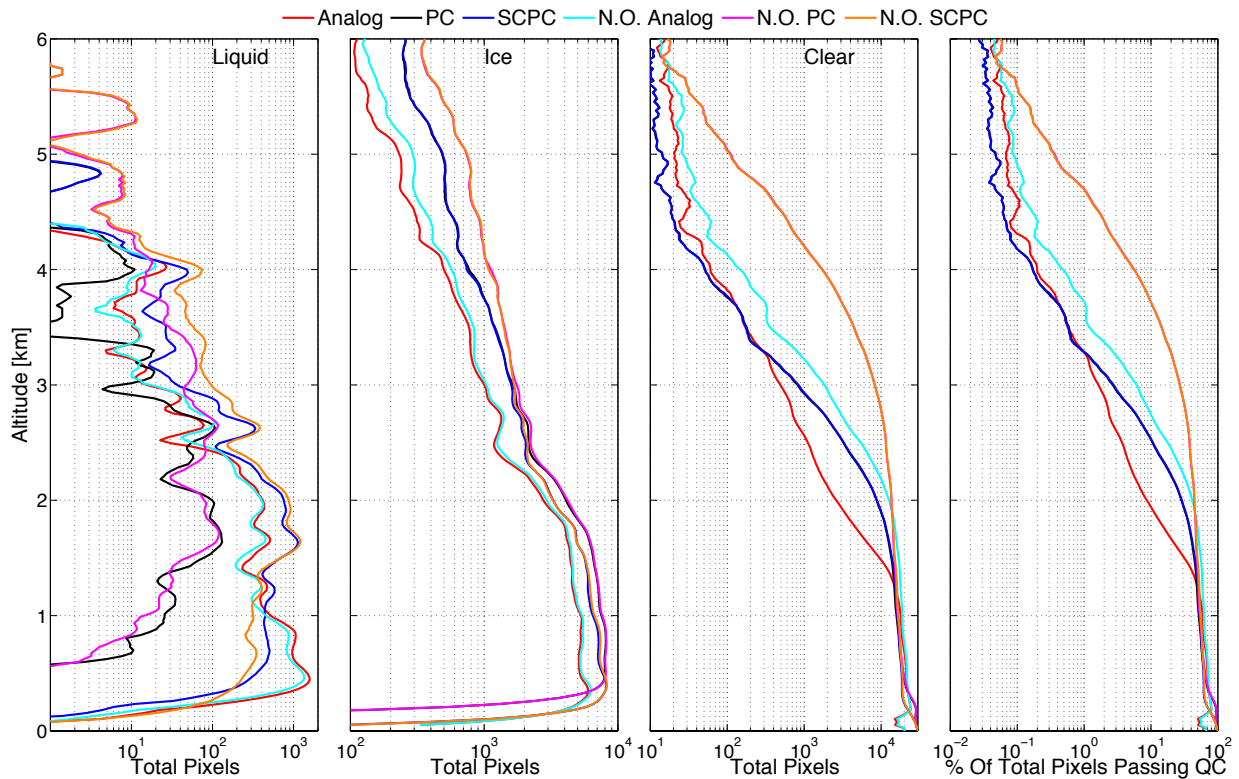
Figure 5.1: Histograms of all the monthly data collected in July, 2015. All voxels observed which pass the criteria described in Table 4.3 are included. The panels labeled Liquid, Ice, and Clear are summed voxels and the final panel without a labels is the percent of possible voxels observed. The legend descriptor N.O. indicates non-orthogonal calculation of polarization properties and those without indicate standard orthogonal calculation procedures. Note that the sensitivity of the channel is given quantitatively by how often measurements at a given height pass the criteria defined in Table 4.3. At altitudes above approximately 4 km, most voxels fail the SNR filter except cloud scenes and at altitudes below approximately 200 m, some data is filtered because the analog detector signals exceed the range set for the analog to digital converter.
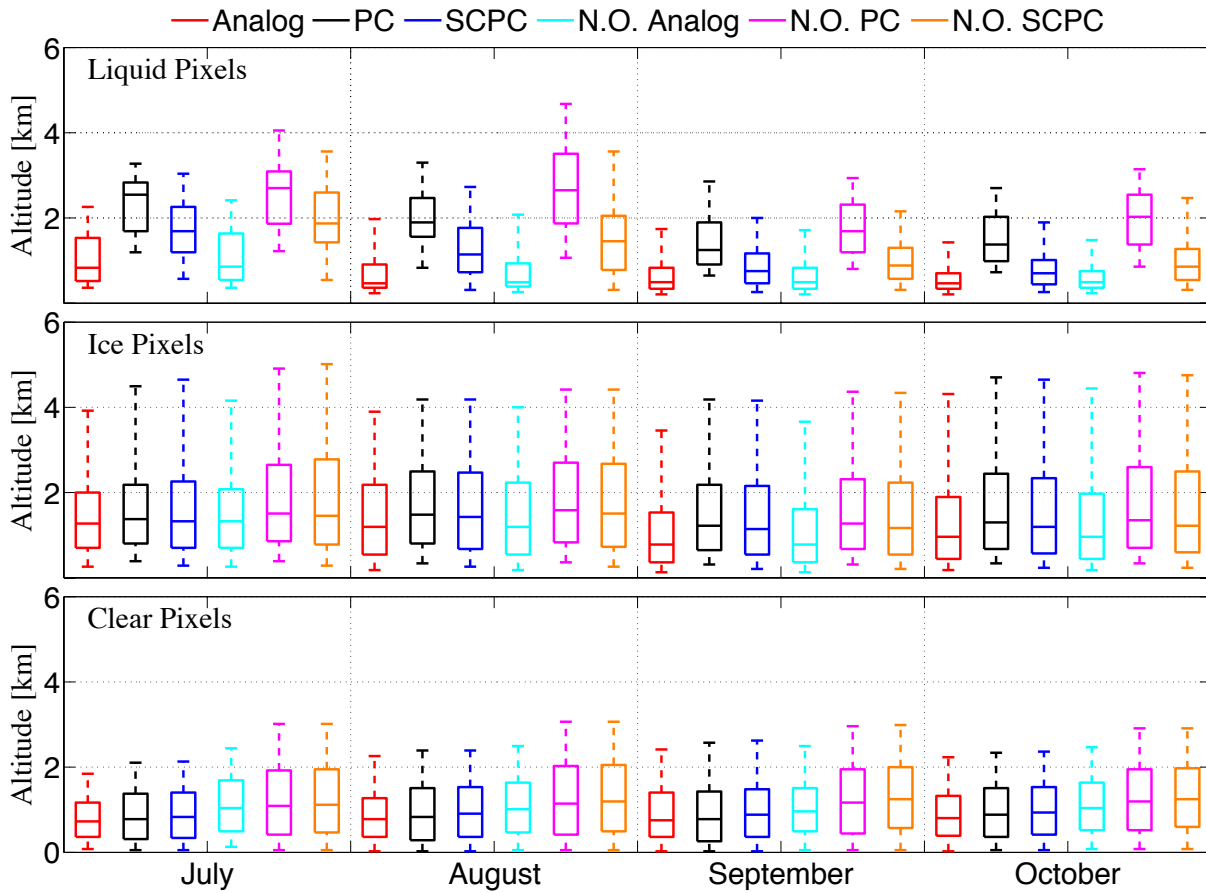
Figure 5.2: 4 months of CAPABL data binned into liquid, ice, or clear air. The median is indicated by a line through the box, the 25th to 75th percentile ranges complete the box and the whiskers extend to the 5th and 95th percentiles. The channel sensitivity can be seen looking at the clear voxels where analog is expected to be less sensitive than PC and orthogonal less sensitive than non-orthogonal. Note also that there is a significant deviation in the median altitude for liquid water observed via PC and via analog detection.

are often misclassified by the PC channel. This is shown for a single case as indicated by Figure 5.3 and Figure 5.4, clearly demonstrating that saturation can change the geophysical interpretation of the polarimetric lidar signals and must be considered when detector-induced dynamic range is high, for CAPABL this occurs approximately when $\delta \leq 0.1$. The second feature is seen in the clear sky data where there is increased sensitivity of the PC channel over the analog channel and increased sensitivity of the non-orthogonal polarization retrievals over the orthogonal versions, as noted for the July histogram. This increased sensitivity is seen by the increase in whisker range of approximately 1 km (0.96 km, 0.70 km, 0.34 km, and 0.55 km for July, August, September, and October for SCPC to the 95th percentile, respectively, or 1.17 km, 1.12 km, 0.99 km, and 0.83 km to the inner fence) indicating the presence of more high altitude clear air voxels that pass the quality control standards specified in Table 4.3. As a result of the increased sensitivity, the median of the data shifts upwards as well (0.29 km, 0.29 km, 0.36 km, and 0.31 km for July, August, September, and October for SCPC, respectively). The final feature is the relative consistency of the occurrence of ice for all methods. The median altitude of the data shifts slightly upwards again due to increased sensitivity between analog and photon counting (0.05 km, 0.23 km, 0.36 km, and 0.23 km for July, August, September, and October for SCPC and analog, respectively) but the boxes cover similar altitude ranges, especially for July. Comparing the whiskers for the non orthogonal and orthogonal polarization retrievals within a month indicates that the increased sensitivity gained by using non orthogonal polarization retrievals does not change the geophysical interpretation of the data when saturation is of little concern (shifts of 0.26 km, 0.08 km, 0.21 km, and 0.10 km for July, August, September, and October for A to the 95th percentile, respectively, or 0.18 km, 0.13 km, 0.21 km, and 0.18 km to the inner fence are observed), i.e. when signals are of similar strength or when signal rates are less than approximately 1 MHz.

One clear example of a day when saturation changes the geophysical interpretation of CAPABL data is given for February 29, 2016. Analog data from this day is given in Figure 5.3 and PC data is given in Figure 5.4. On this day, there is a low liquid cloud layer at approximately 1.5 km altitude for the first half of the day. There are secondary liquid layers below the consistent layer

below 1 km. Later in the day, there is ice in the air and HOIC observed throughout the second half of the day. Examining the PC data, the liquid layers are almost completely missed for the first half of the day while the ice layers and HOIC are observed. Analog clearly shows these liquid layers as it is better equipped to handle the high count rate of scattering off of liquid clouds. One clear indication of saturation is negative values of the diattenuation product $D_1 D_2$ in Figure 5.4. Throughout the CAPABL data set, diattenuation is shown to be a sensitive measure of saturation and is the reason for introducing the diattenuation product for data quality assurance.

Given the results of Figure 5.2 and the example of saturation causing geophysical differences in retrievals, as shown in Figure 5.3 and Figure 5.4, one major question to ask is to what extent is saturation affecting the entire data set. To determine the effect, FO of cloud phase and clear air are calculated using the CAPABL column data product for each of the 6 types of calculations possible and for the merged data product for the 4 month period from July to October 2015 presented in Figure 5.2. Results are given in Figure 5.5 where it can be seen that saturation causes errors in FO of liquid and ice on the order of 30%. Within the context of surface radiation or trying to attribute CRE, this 30% difference in FO is an untenable issue.

The CAPABL measurements and cloud voxel type merging procedure presented in Section 4.1.2 is designed to extend the measurements and enhance the overall value of the lidar data product and to fix the error in FO observed in Figure 5.5. The identification procedure can be evaluated in many ways, one of which is the affect it has on the quantitative analysis of the surface radiation budget (SRB). In particular, at Summit measurements of downwelling and upwelling radiation are measured in both the longwave and shortwave regions. Attribution of the radiative energy measured is important to give an understanding of what types of clouds strongly or weakly affect the overall SRB. This thesis will use lidar measurements and radiation measurements in two ways to understand the effect of clouds and atmospheric state on the SRB.

The first method, by which this thesis examines radiation, is using the lidar column phase identifier to attribute raw radiation measurements to liquid and ice phase, with or without HOIC, of clouds as well as clear air, in a similar way as LWP in Section 4.2.2. This method allows one to
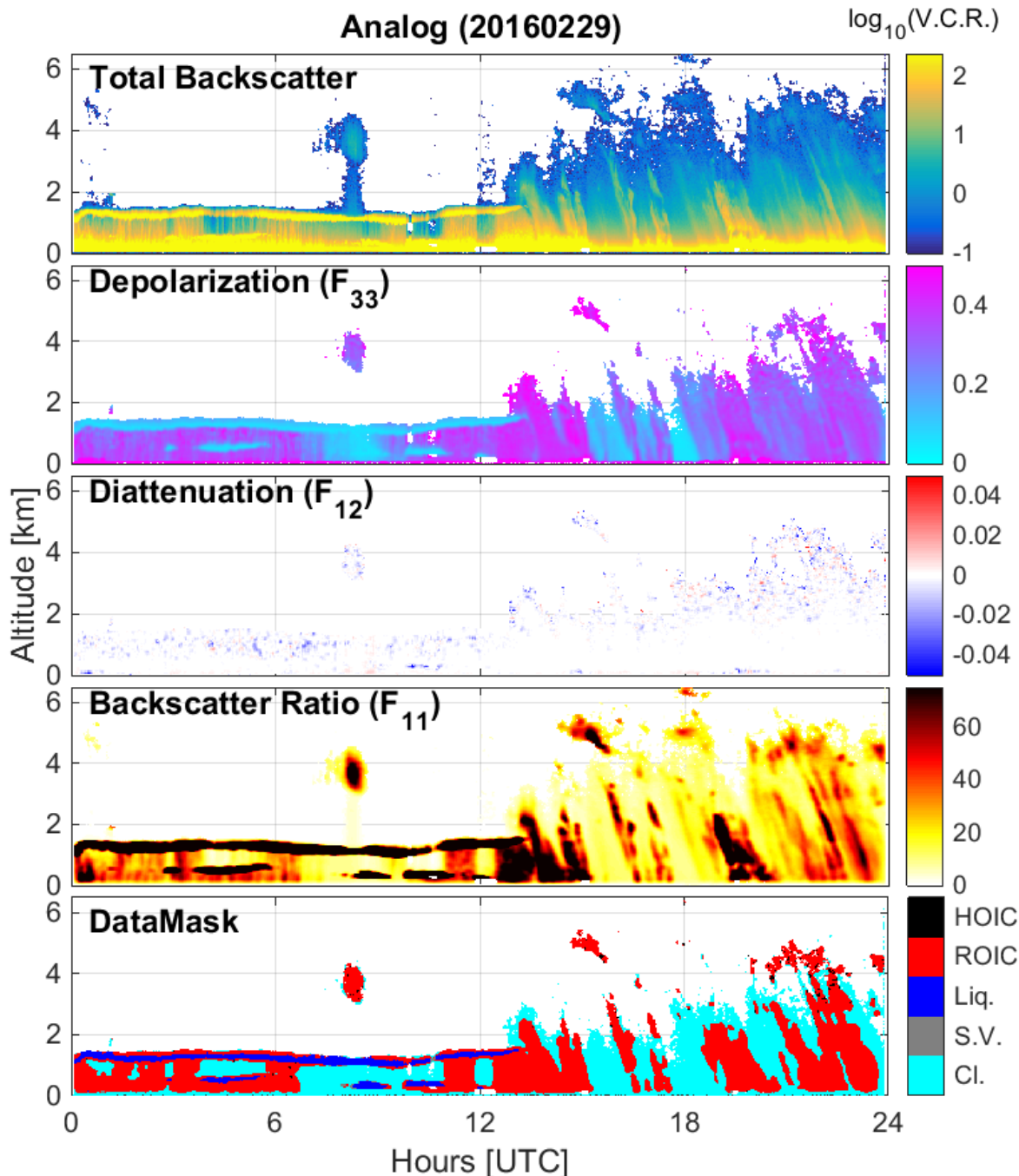
Figure 5.3: Analog data from the CAPABL system for February 29, 2016. Total Backscatter is the summation of background subtracted parallel and perpendicular voltages converted to a virtual count rate (V.C.R.) using a data gluing procedure in MHz. The total backscatter color bar is given from 100 kHz to 250 MHz on a logarithmic scale. Depolarization is calculated as given in Equation 2.16. Diattenuation is calculated as given in Equation 2.17 and Table 4.3 . Backscatter ratio is calculated by performing a Klett inversion and using ICECAPS radiosonde data (launched at 2400 UTC and 1200 UTC daily) to calculate a molecular extinction component [152]. Liq., S.V., and Cl. stand for liquid, sub-visible, and clear, respectively.
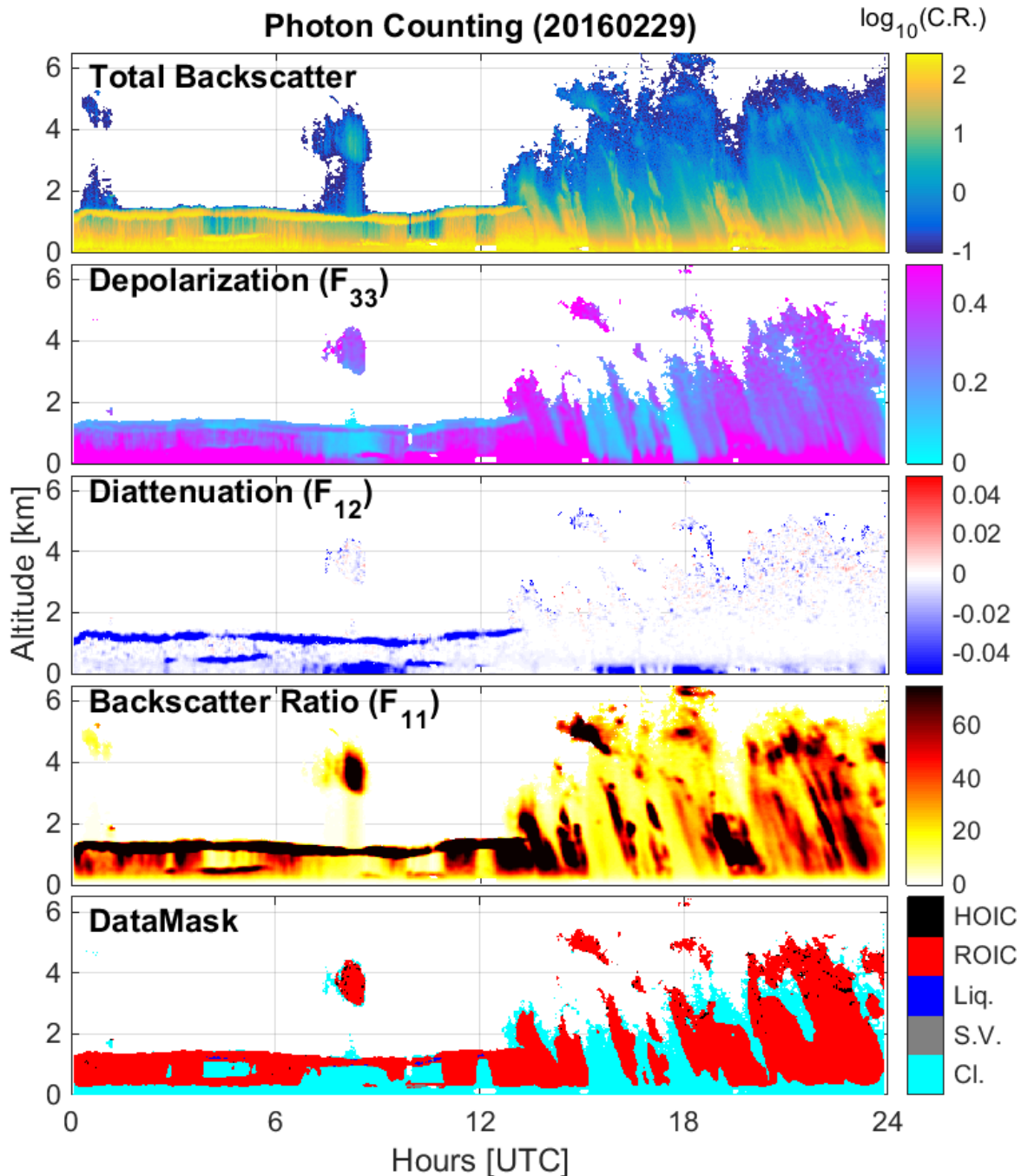
Figure 5.4: Photon counting data from the CAPABL system for February 9, 2016. Total Backscatter is the summation of background subtracted parallel and perpendicular counts (C.R.) in MHz. The total backscatter color bar is given from 100 kHz to 250 MHz on a logarithmic scale. Depolarization is calculated as given in Equation 2.16. Diattenuation is calculated as given in Equation 2.17 and Table 4.3 . Backscatter ratio is calculated by performing a Klett inversion and using ICECAPS radiosonde data (launched at 2400 UTC and 1200 UTC daily) to calculate a molecular extinction component [152]. Liq., S.V., and Cl. stand for liquid, sub-visible, and clear, respectively.
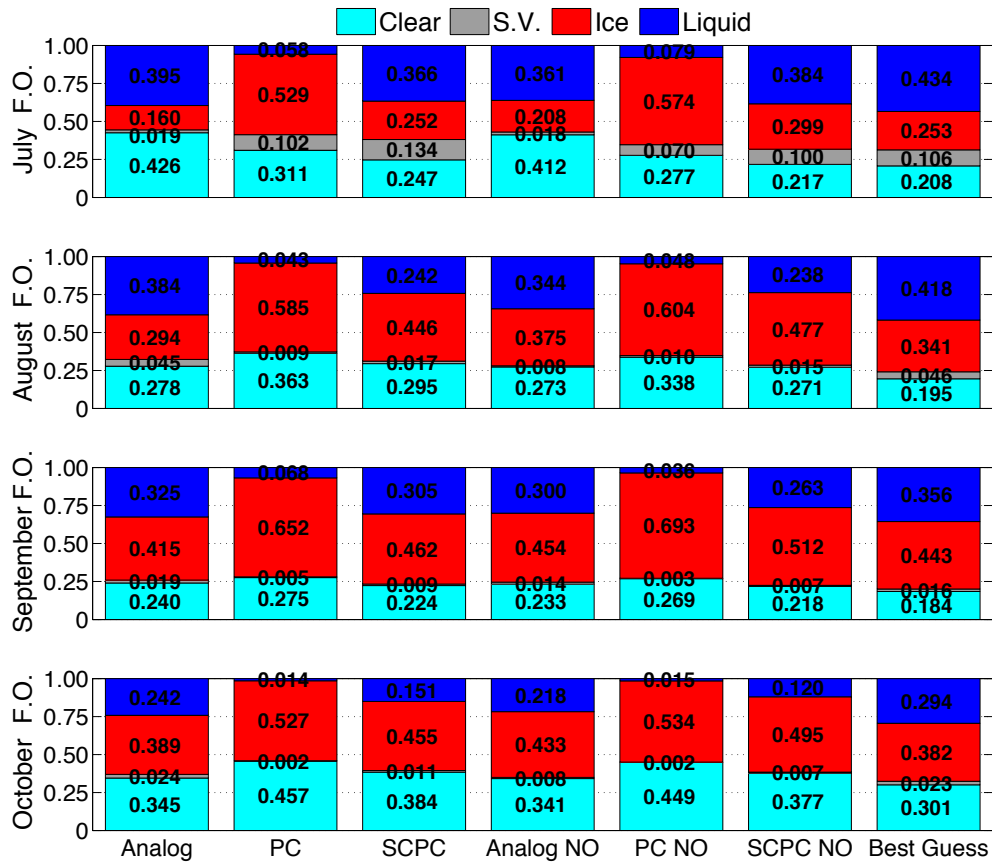
Figure 5.5: Fractional occurrence (FO) of each voxel type in the column for each month. To be labeled clear, the column must lack all sub-visible, ice, and water voxels. To be labeled sub-visible, the column must lack ice or water voxels. To be labeled as ice, a column must lack water voxels. If a column contains a water voxel, the column is labeled as liquid. The FO is given for each bar rounded to the nearest thousandth.

understand the distribution of energy measurements based on cloud phase. The advantage of this method is that one only requires the measurements provided by the lidar identification procedure and the radiation measurements. The disadvantage of this procedure is that it fails to account for confounding effects like atmospheric temperature and composition. The second method for examining the radiative effect of the clouds, and by extension the classification of clouds, is to perform full CRE calculations. CRE is defined here as the total radiative effect of the entire atmosphere (measured quantity) minus all other contributions other than clouds following Miller et al. [159] (modeled quantity). This allows one to isolate the effect that clear air and cloud phase have on the SRB. To perform this analysis, much more information on the atmosphere is required to remove confounding atmospheric effects from the radiation measurements. Here, as discussed in Section 4.1.3.5, measurements of absolute moisture and temperature are required as well as quantities of active gasses such as N_2O, CO, CO_2, CH_4, O_3, and O_2. The advantage of using more measurements to parse atmospheric contributions to the SRB is that the major biases in the radiation measurements such as atmospheric temperature and moisture are removed, but the disadvantage is they require more information, which can often be difficult to obtain, and introduce more assumptions and uncertainty attributed to the additional measurements and models. The first method is considered here while the second method is considered in Section 5.2.

Performing the first method using the lidar identification product described in Section 4.1.2, the cumulative distribution functions of down and upwelling shortwave and longwave radiation measurements are given in Figure 5.6, parsed into column types: clear air, ice (with HOIC labeled HOIC and without labeled ROIC), and liquid bearing. Figure 5.6 shows some simple relationships which are examined for consistency with previous studies. The median value of downwelling longwave radiation is higher for liquid clouds than it is for ice clouds. Ice is higher still than for clear air. This is expected based on many previous results including those of Curry et al., Shupe and Intrieri, and Miller et al. [33, 34, 159]. Likewise, the downwelling shortwave energy is highest for clear air and reduced for ice clouds, which is further reduced for liquid clouds. This shows the albedo effect of clouds which is well described by Shupe and Intrieri, Stevens and Bony, and Miller
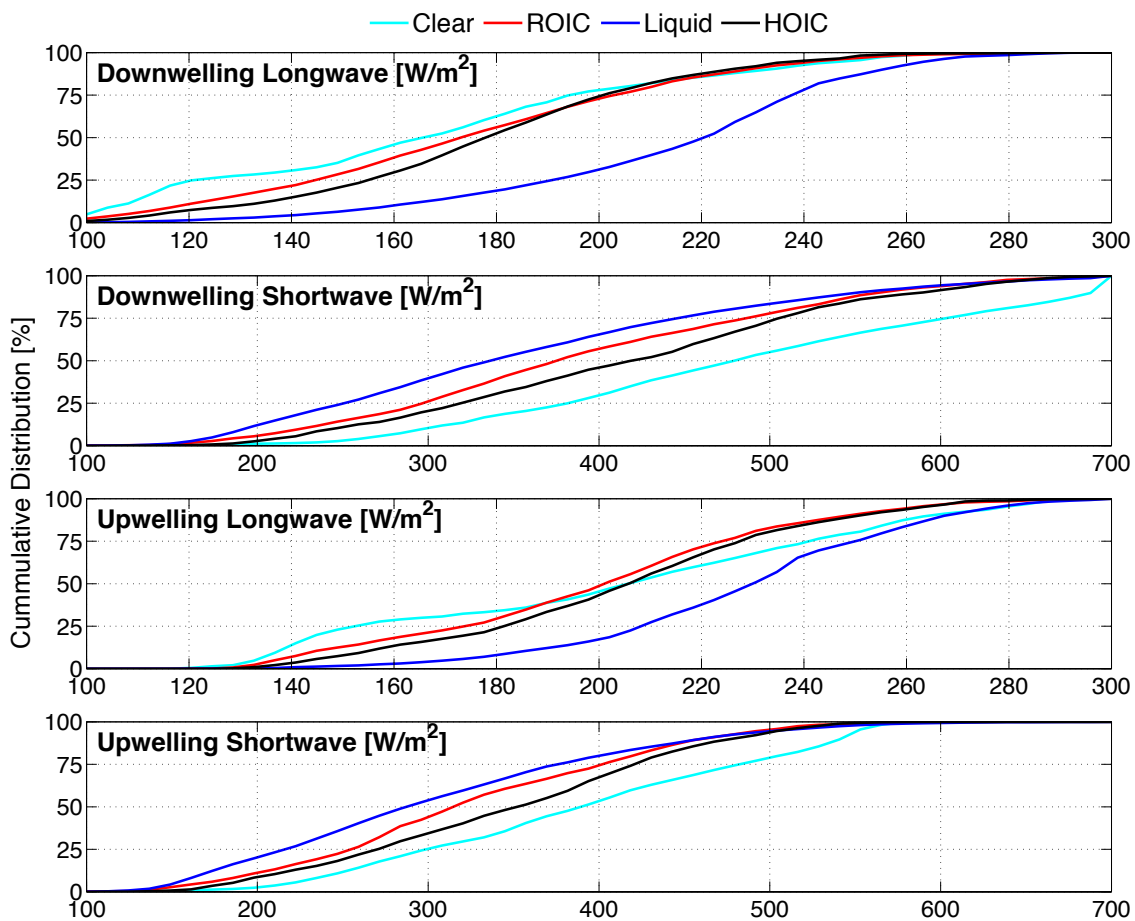
Figure 5.6: Cumulative distribution function of NOAA downwelling and upwelling radiation data parsed by CAPABL column data product. Columns with liquid are expected and show larger longwave downwelling flux and reduced downwelling shortwave flux. Clear air shows the highest upwelling and downwelling radiation values as there is no cloud shading of the surface.

et al. [11, 34, 159]. The upwelling longwave measurements are highest for liquid cloud scenes, which can be understood based on the enhanced downwelling longwave radiation [161]. Finally, upwelling shortwave is simply the scaled version of the downwelling shortwave given the high surface albedo at Summit again demonstrating the albedo effect of clouds. These results are all expected and provide further validation that the CAPABL cloud identification procedure is acting as expected. However, the effect that the identification procedure has on the radiation interpretation and parsing the effects of ROIC and HOIC is not expected. The shapes of the cumulative distribution functions for the ROIC and HOIC are similar for all radiation types but downwelling longwave radiation. The medians are not the same between ROIC and HOIC. More on this effect is given in Section 5.2.

A further analysis of CAPABL voxel identifications is presented in Figure 5.7 and Figure 5.8 for longwave and shortwave respectively. In both cases, similar steps as done for Figure 5.6 are performed but for the merging procedure as well as orthogonal analog and orthogonal photon counting voxel identifications. There are observable differences in the cumulative distribution functions of each set of voxel type. For example, it was noted above that it was possible to misclassify liquid as ice by lidar due to saturation and dynamic range limitations of the lidar counting system [105]. The manifestation in the longwave data presented in Figure 5.7 is that the photon counting data shows much less contrast between the liquid and ice phase due to falsely classifying liquid clouds as ice clouds. This biases the radiative effect of ice high and biases liquid low by removing the more optically thick clouds. It is clear from examining the liquid profiles of the merged data product and analog that there is almost no difference between the two indicating that strong signals are to blame confirming the photon counting dynamic range limitation. Further lidar limitations are seen in Figure 5.8 when examining the clear sky voxels. Analog and PC underestimate downwelling shortwave radiation from ice clouds because high ice clouds are not visible due to the weak signals that are only visible to non-orthogonal retrievals in the merged data product.

The median values of all distributions for all three classification types for all four radiation types are listed in Table 5.1. The results of this table suggest a shift in median values on the order

of 6 W/m^2 to 20 W/m^2 for ice clouds in the longwave due to difficulty measuring the whole column of ice especially in the polar summer with just orthogonal polarization retrievals. The results in Table 5.1 also strongly suggests that the nature of liquid baring clouds in the polar regions being low and thick causes lidar classification errors resulting in longwave radiative biases on the order of 20 W/m^2 for PC detection. The shortwave biases are higher than that for the longwave, in error by as much as 30 W/m^2 to 35 W/m^2. These results suggest the necessity of the merged classification of lidar data that extends the system dynamic range and overall measurement quality.

5.2   First Observations of Preferentially Oriented Ice Crystals

One of the major scientific results of this thesis is the ability to reliably measure and beginning to characterize the nature of HOIC. The observations by CAPABL that can parse ROIC and HOIC are truly unique because of the length of the data set produced, the spatial resolution attainable, and the extensive suite of instruments used for verification of HOIC identifications. The merged data product created for this thesis was used extensively by Cole et al. to announce the first 11 months of data on HOIC and to begin to develop a climatology of HOIC at Summit. Additionally, the ability to parse ROIC from HOIC was used by Stillwell et al. in a first attempt to attribute radiative effects of HOIC [165].

This first major finding was the nature of HOIC observed at Summit. From the observational results of the CALIOP lidar, HOIC are expected primarily within cirrus clouds [129, 131, 132, 133]. However, the measurements from CAPABL suggest a completely different possibility. A histogram of the number of days HOIC were observed in cirrus clouds, stratiform clouds, and falling as snow at Summit is given from Cole et al. in Figure 5.9 [127]. CAPABL observes most HOIC in stratiform clouds and as precipitation. Additionally, in contrast to the first reported HOIC event at Summit by Neely et al. [89], HOIC are observed to exist in very small patches within clouds. Neely et al. observed an event that lasted nearly 3 hours with a major section of the clouds above Summit having HOIC [89]. This event reported by Neely et al. is by far the longest HOIC event in the CAPABL record since 2010. There are only 2 other events to the authors knowledge that last
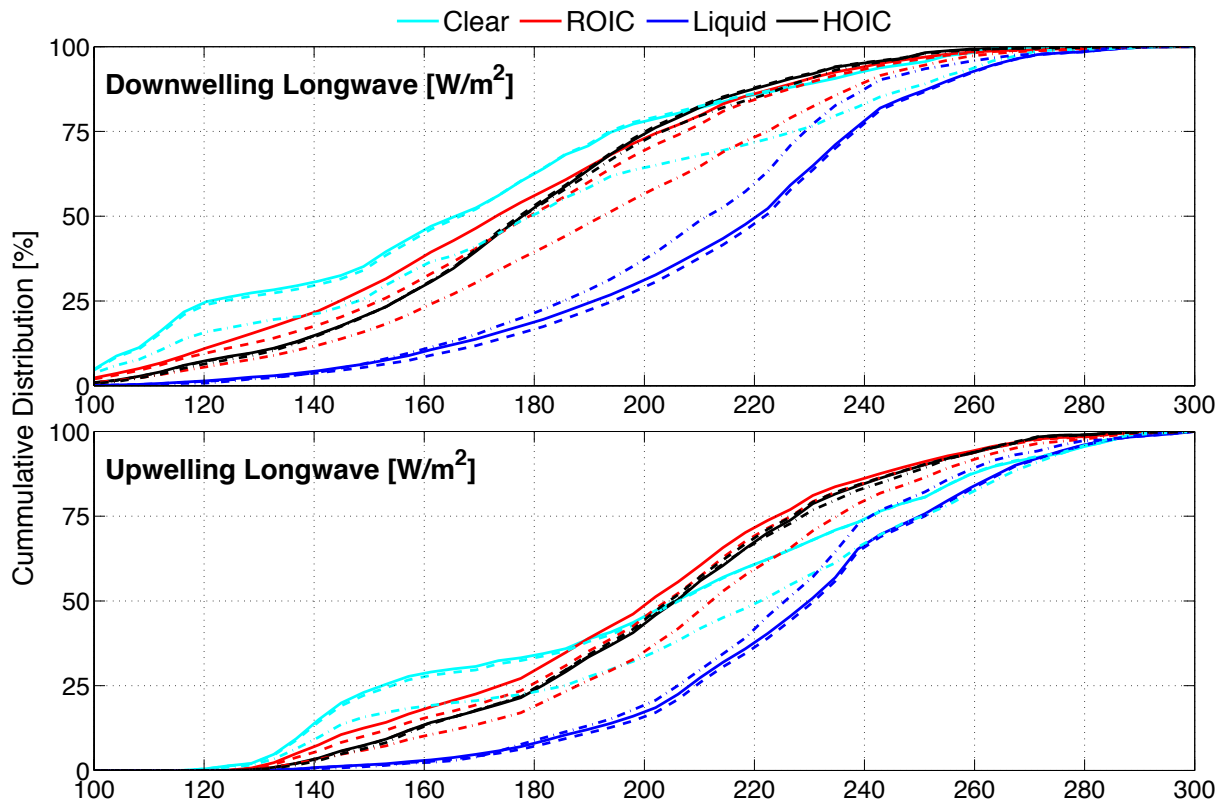
Figure 5.7: Cumulative distribution functions of NOAA longwave radiation measurements for all three processing methods: A (dashed), PC (dash dot), and merged (solid). Compared to the results of the data merging procedure, PC and A detection show smaller contrast between liquid and ice which indicates systematic misidentification of those clouds which is rectified via the data merging procedure.
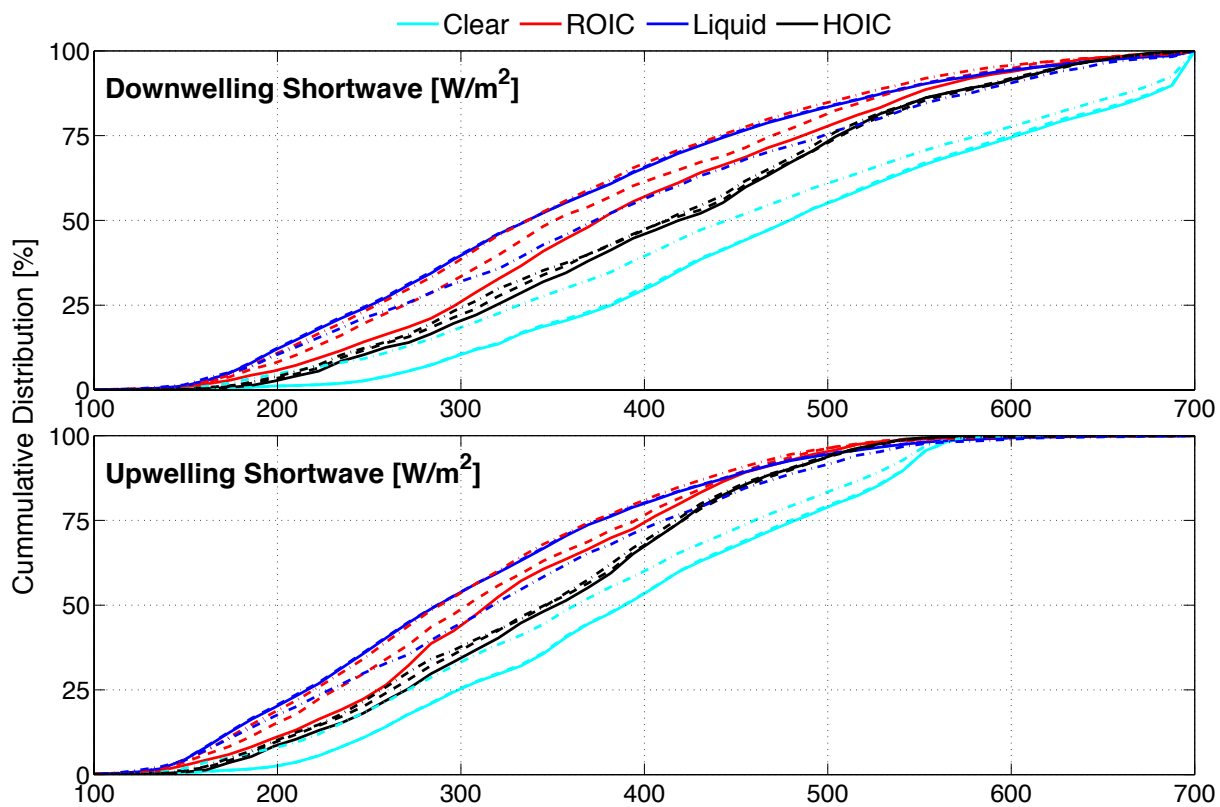
Figure 5.8: Cumulative distribution functions of NOAA shortwave radiation measurements for all three processing methods: A (dashed), PC (dash dot), and merged (solid).

Table 5.1: Median values, in W/m^2, of the probability density function for each data processing type for each radiation component.

	Type	Merged	Analog	PC	Merged - Analog	Merged - PC
Downwelling Longwave						
	Clear	167.48	168.12	180.58	-0.63	-13.10
	Ice	175.15	181.25	194.90	-6.11	-19.75
	Water	222.86	224.08	213.50	-1.21	9.36
Downwelling Shortwave						
	Clear	485.79	485.78	454.22	0.01	31.57
	Ice	391.77	386.52	360.19	5.25	31.57
	Water	342.48	342.41	379.16	0.07	-36.68
Upwelling Longwave						
	Clear	207.41	207.72	222.50	-0.31	-15.09
	Ice	203.23	206.06	214.60	-2.83	-11.37
	Water	232.05	232.92	227.56	-0.87	4.45
Upwelling Shortwave						
	Clear	395.66	395.07	370.75	0.59	24.92
	Ice	329.64	328.26	308.86	1.38	20.78
	Water	293.33	293.04	323.81	0.29	-30.48

more than about 10-20 minutes. Most other events, as shown in the CAPABL data sample Figures 4.10, 4.11, 4.12, 5.3, and 5.4, are almost noise-like in nature. They occur quickly and sporadically within the data set. This sporadic nature of HOIC was only highlighted with the automatic tagging procedure and processing given in Table 4.3.

One other significant contribution to HOIC study at Summit was the result by Cole et al. that HOIC occur at statistically significantly higher temperatures for all cloud types and statistically significantly higher relative humidities for stratiform clouds. Cole et al. used the analog voxel identification to conclude that HOIC and ROIC have statistically different properties, especially occurrence temperature. The histogram of temperature is given in Figure 5.10.

Finally, one other major contribution of this thesis work to characterizing HOIC is enabling characterization of the CRE of HOIC versus ROIC. The results of the full CRE analysis is found to be similar to the simplified analysis of Section 5.1 in a number of key respects. CRE is calculated and combined for both the downwelling longwave and shortwave and examined for the CAPABL cloud classifications. Instead of cumulative distributions, the normalized probability distribution of CRE is presented to facilitate a more direct comparison with other work on the polar radiation budget such as Shupe and Intreiri and Miller et al. [34, 159]. The downwelling longwave CRE is given in Figure 5.11 and downwelling shortwave CRE is given in Figure 5.12.

The conclusions about liquid water dominating the downwelling longwave effect of clouds from Section 5.1 is clearly visible in Figure 5.11. This conclusion provides confidence to lidar identifications. The expected bimodal nature of the downwelling longwave with clear air, ROIC, and liquid water are clearly visible in the merged best estimate product. Furthermore, the conclusion indicating liquid water can be misrepresented as ice given invalid lidar detector signals is clearly seen here as a major CRE peak in the PC data for ROIC [105, 165]. The analog data shows quantitatively similar data to the merged best estimate product. As the analog signals measure the lower 0 km to 2 km of the lidar signal well, this indicates that the major longwave forcing of the surface at Summit occurs in the lowest altitude bands. It is unexpected however that HOIC would defy this bimodel nature and exist with a median and mode in between the liquid water
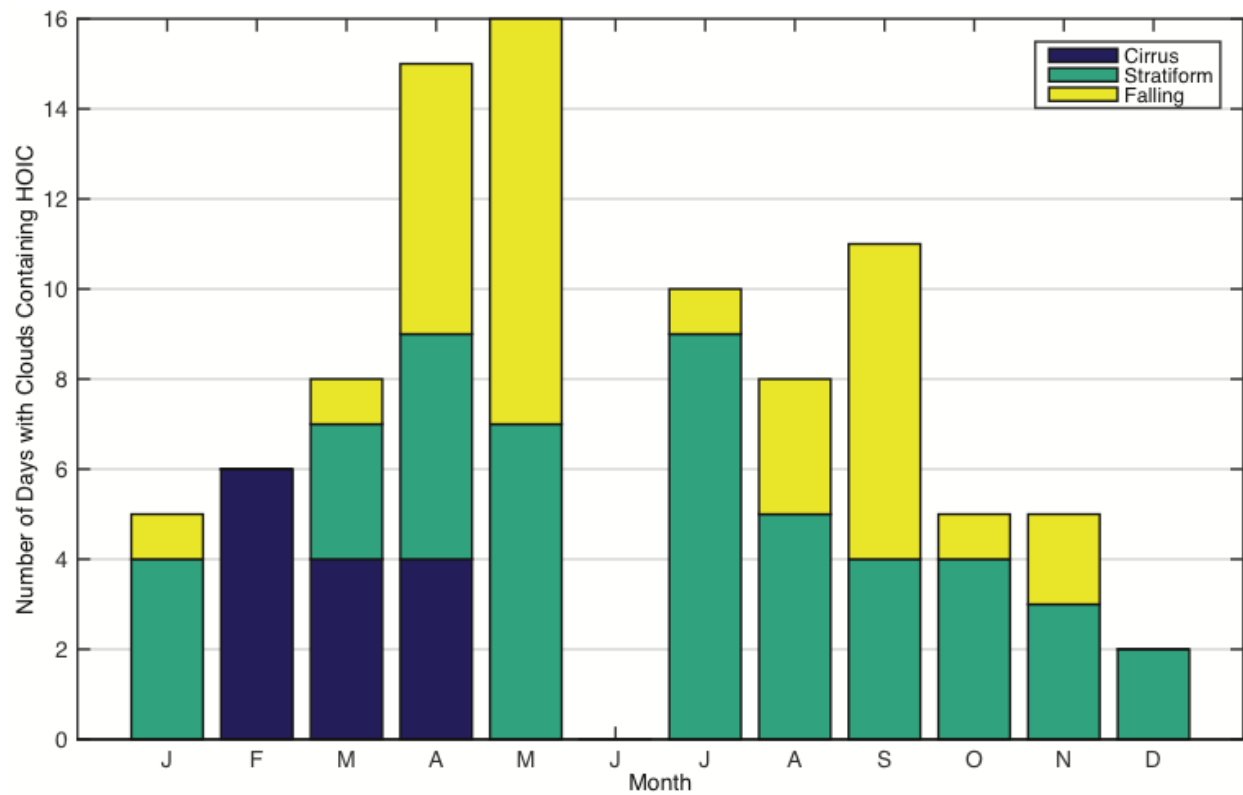
Figure 5.9: Monthly histogram of days on which HOIC occur parsed by the cloud type from July 2015 to May 2016 using the A voxel identifications from Cole et al. [127].
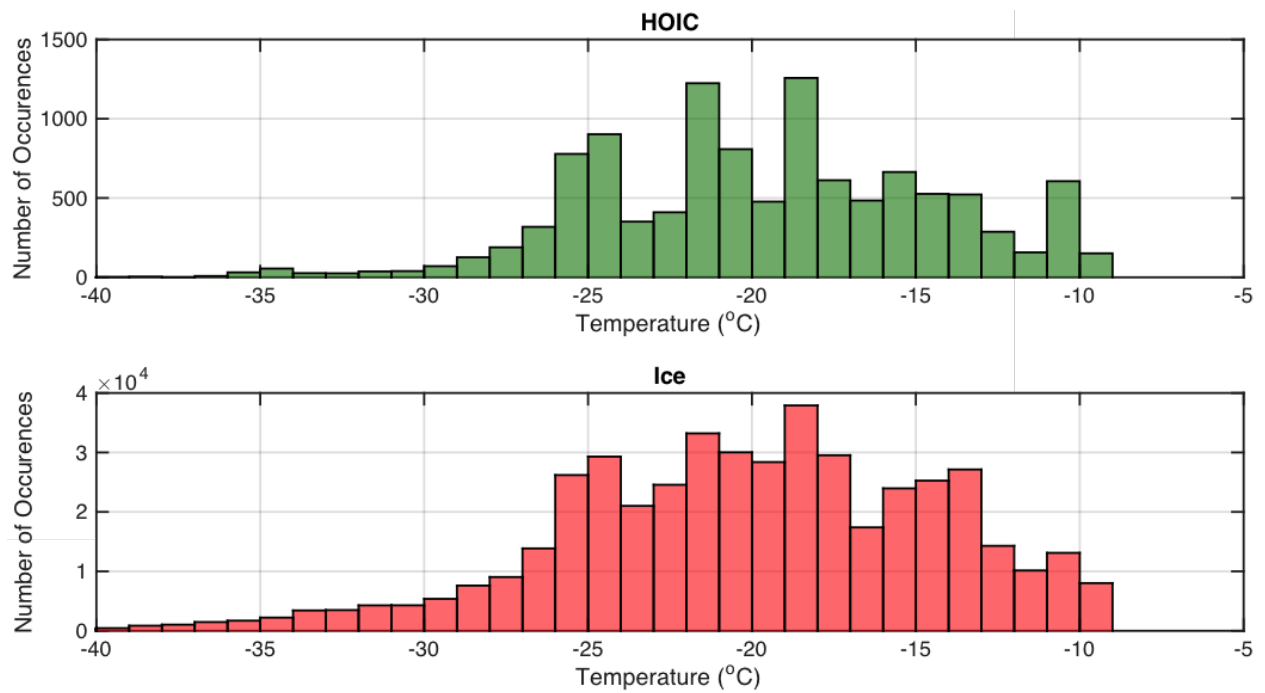
Figure 5.10: Histogram of the temperature of ROIC and HOIC events from July 2015 to May 2016 using the A voxel identifications from Cole et al. [127].
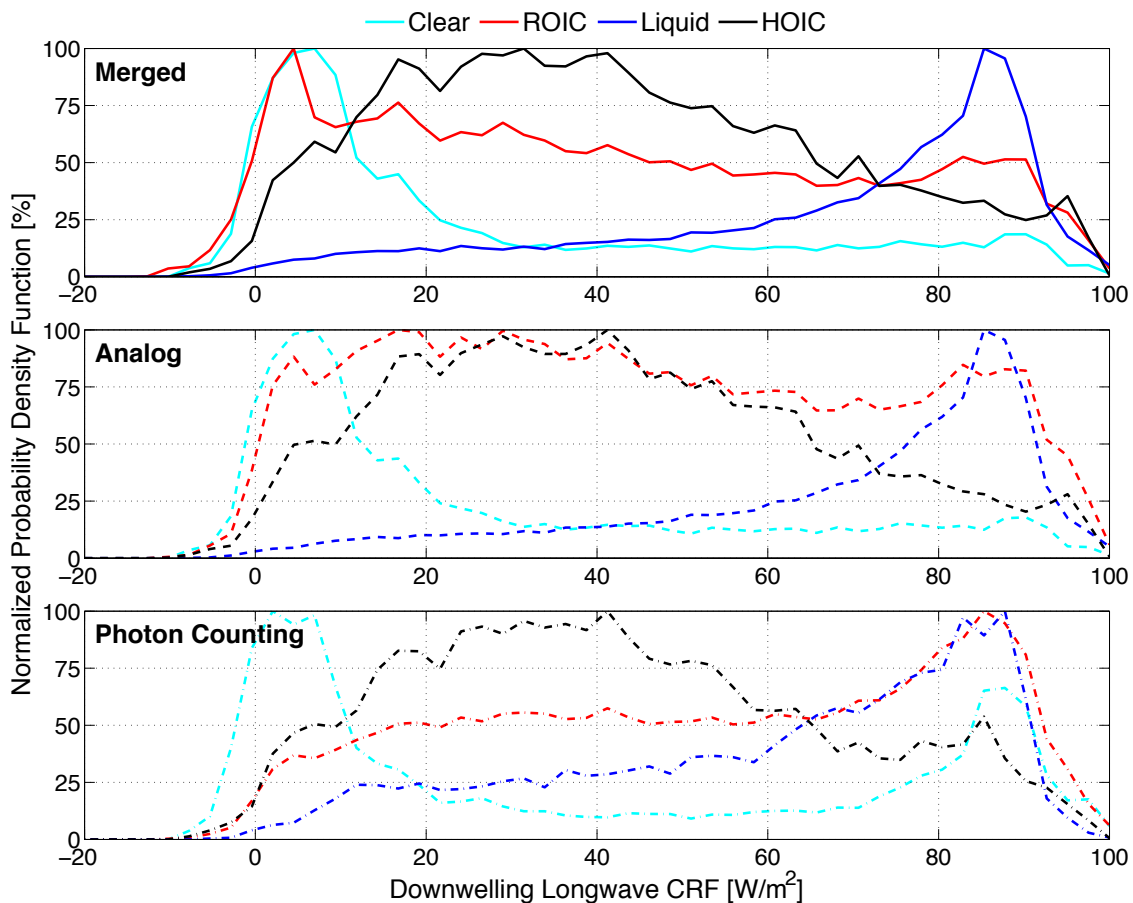
Figure 5.11: Normalized probability density functions of longwave CRE, NOAA downwelling long-wave radiation measurements minus RRTM calculated clear sky irradiance. The CRE spectrum is expected to be bimodal with liquid water composing one peak and clear air and ice composing the other. This is not observed in the PC voxels indicating liquid is mistaken for ice. The longwave effect of HOIC is of particular interest because it seems to exist distinctly between the two main modes.
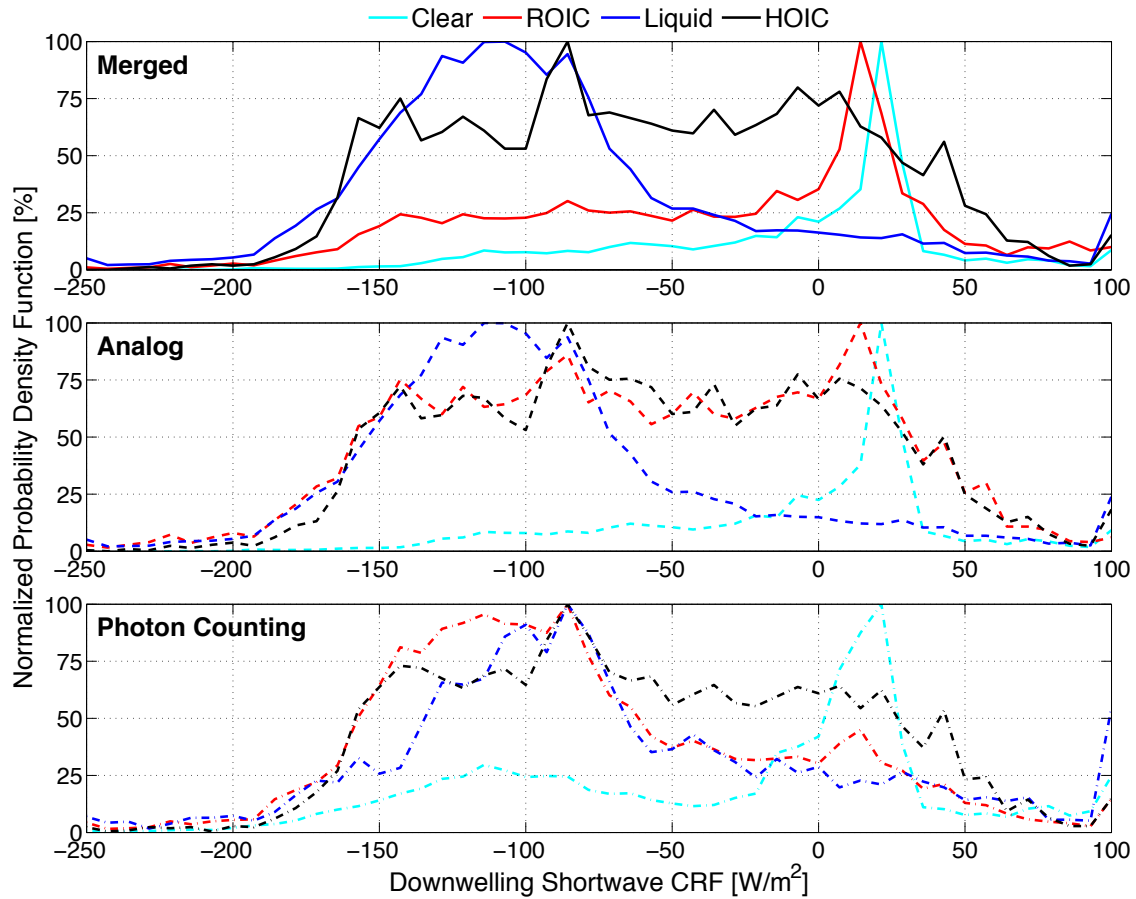
Figure 5.12: Normalized probability density functions of shortwave CRE, NOAA downwelling short-wave radiation measurements minus RRTM calculated clear sky irradiance. Liquid water dominates the shortwave effect indicating the greatest albedo and optical depth. HOIC have been shown to increase the albedo of clouds thus increasing the CRE in the shortwave [128, 129]. HOIC are observed here with a broader distribution than strictly ROIC.

and clear air/ice mode. The affect of HOIC on the SRB has not, to the author's knowledge, ever been reported. The median of the downwelling longwave probability density function for HOIC is shifted by 1.72 W/m^2 relative to ROIC. Interestingly the HOIC probability density function has a statistically different shape than ROIC, with HOIC have a narrower distribution than ROIC whose mode is shifted in magnitude by almost 20 W/m^2.

For the period of study, July to December 2016, it appears as if the longwave effect of ice columns containing HOIC is more pronounced than that of columns containing strictly ROIC. For the period of observation, HOIC compose only 1.5% of all ice voxel observations but are contained within 25.7% of ice columns. This overall small percentage of HOIC voxels is consistent with the findings of Cole et al. [127], who report 2.9% occurrence of HOIC during 11 months from July 2015 to May 2016 at Summit. In spite of the analysis presented in Section 4.2.2, which stated the radar reflectivity of ROIC is higher than HOIC, the longwave effect of HOIC seems to be stronger, i.e. more warming, than that of ROIC. It is unclear if the enhanced longwave CRE of columns containing HOIC is caused by the occurrence of HOIC or if the occurrence of HOIC is a result of the enhanced longwave effect. Given that HOIC are observed in approximately a quarter of all columns over this 6 month period, more study is required to elucidate this link.

The shortwave CRE effect of liquid and ice is also as seen by the simplified radiation approach of Section 5.1. Liquid dominates the shortwave CRE indicating higher reflectivity driven by higher optical depth. The clear air peak is slightly skewed indicating a bias in the removal of the clear air background which could be linked to the specification of absorbing gasses. However, it can be seen that the clear air has the lowest mode and median in the shortwave CRE as expected. Again, the behavior of HOIC is surprising. Figure 5.12 restricts solar zenith angle (SZA) to 80° or less forcing indicating that the enhanced CRE is due to enhanced reflection of clouds. The theoretical enhanced albedo of HOIC has been shown by Takano and Liou and Noel and Chepfer [128, 129] and is further indication that the CAPABL HOIC identification procedure is returning reasonable results. It is noted that the specification of the limit of the SZA in the analysis changes the location of the median of the HOIC peak. In particular, the peak moves towards zero by including higher

SZA values and moves more negative as the SZA values are restricted to lower values. For SZA less than $90°$, the shift in median from HOIC to ROIC is 8.58 W/m^2. For SZA less than $75°$, the shift in median from HOIC to ROIC jumps to 41.0 W/m^2. The median is always negative but its value is some non-trivial function of SZA. One possible mechanism for this change is related to single scattering off of ice clouds. Specular reflections off of ice crystals are expected. As ice clouds have lower optical depth in the Arctic than liquid clouds in general, the scattering regime is closer to single than multiple scattering. With strict single scattering, as the SZA is allowed to creep towards $90°$, the reflection from clouds is directed downwards instead of upwards. If the sun is observed above the horizon above clouds, sunlight will be reflected upwards, but if the sun is observed near the horizon between clouds and the ground, the sunlight hitting clouds is reflected downwards. The analysis presented here prompts more questions than it answers especially about the effect of HOIC on shortwave CRE, but is beyond the scope of this thesis to address. Note that no qualitative change is observed in longwave observations as a function of SZA as expected.

5.3   Contributions to Other Scientific Efforts

One other noteworthy study involving CAPABL and the author was an explanation of a serendipitous event. In the winter of 2016, specular reflections off of ice crystals in CAPABL's main beam were imaged by the onsite science technician at Summit. One example of the photos taken is given in Figure 5.13. Many interesting aspects of Figure 5.13 can be investigated in detail, but the interference patterns created by crystals in the beam path were of particular interest. The size, shape and orientation of crystals within the beam and the orientation of observation changes the interference pattern observed from the crystal faces. Using that fact, Goerke et al. attempted to create a new method of ice crystal identification by matching interference patterns to those calculated by modeled ice crystals.

Using models of crystals, like those given in Figure 5.14, modeled interference patterns were matched to observed interference patterns. The matches are given in Figure 5.15 where panels a, c, e, and g show the photographed interference pattern and panels b, d, f, and h the modeled
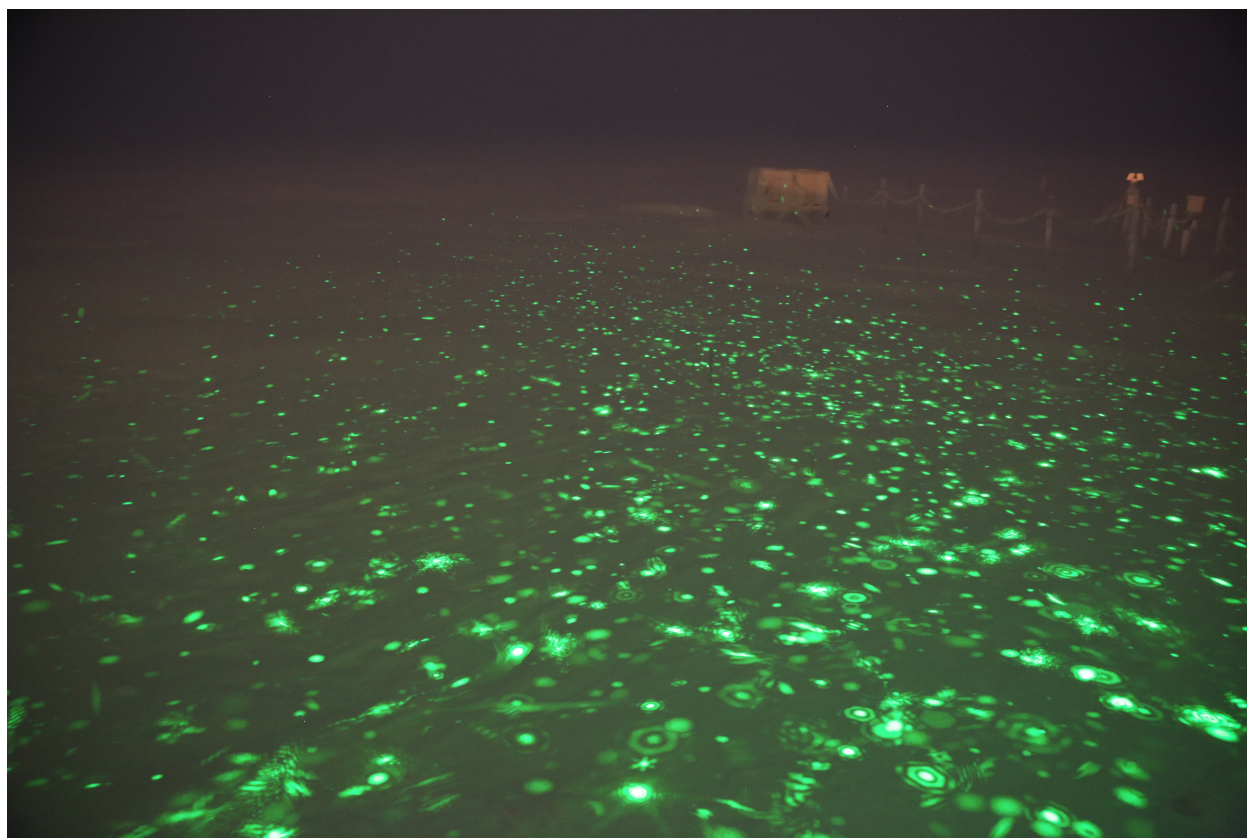
Figure 5.13: A photo of light scattering from CAPABL's beam in the polar winter taken on December 6, 2016. Many unique and identifiable interference patterns are observable, which were used by Goerke et al. to quantitatively describe the size and shape of the crystals aloft. Photo Credit: Mellissa Goerke.

interference patterns for crystals of shape given in panel a, b, c, and d respectively from Figure 5.14 respectively. While the method of matching patterns from Goerke et al. was not used in an operational manner, it could conceivably be made to run operationally with a large enough database of modeled crystals.

The ICECAPS data suite contributed to this study by providing context with which to understand the measurements made. For example, the relative humidity with respect to ice is near 100% as described by Goerke et al., but there are small areas where the saturation dips below 100% where sublimation and rounding of some ice crystals could have occurred. Additionally, as ice crystal growth habits are strong functions of temperature, temperature measurements via radiosonde provided useful information on crystal habit. While all the crystals shown in Figure 5.14 and Figure 5.15 are hexagonal, scalene plates were also observed at Summit. Crystals observed were in the range of 40 μm to 150 μm with widths from 0.5 μm to 4 μm.

5.4   Relevance to Posed Thesis Questions

The observations from the CAPABL system directly addresses two of the thesis questions posed. A bulleted summarizing list of relevant findings is given for each question.

(1) How to accurately identify and distinguish liquid and ice water in Arctic clouds using polarimetric lidar?

    (a) The SVLE developed by Hayman and Thayer [98] shows how instrument effects like diattenuation and retardance affect depolarization measurements. The results of the CAPABL system illustrate further how depolarization measurements can be affected by system dynamic range and cloud macrophysical properties. The results from CA-PABL include both effects to further identify and distinguish instrument and measurement related effects from cloud microphysical effects.

(2) What unique signatures about Arctic cloud microphysical properties can be revealed using polarimetric and Raman lidar?
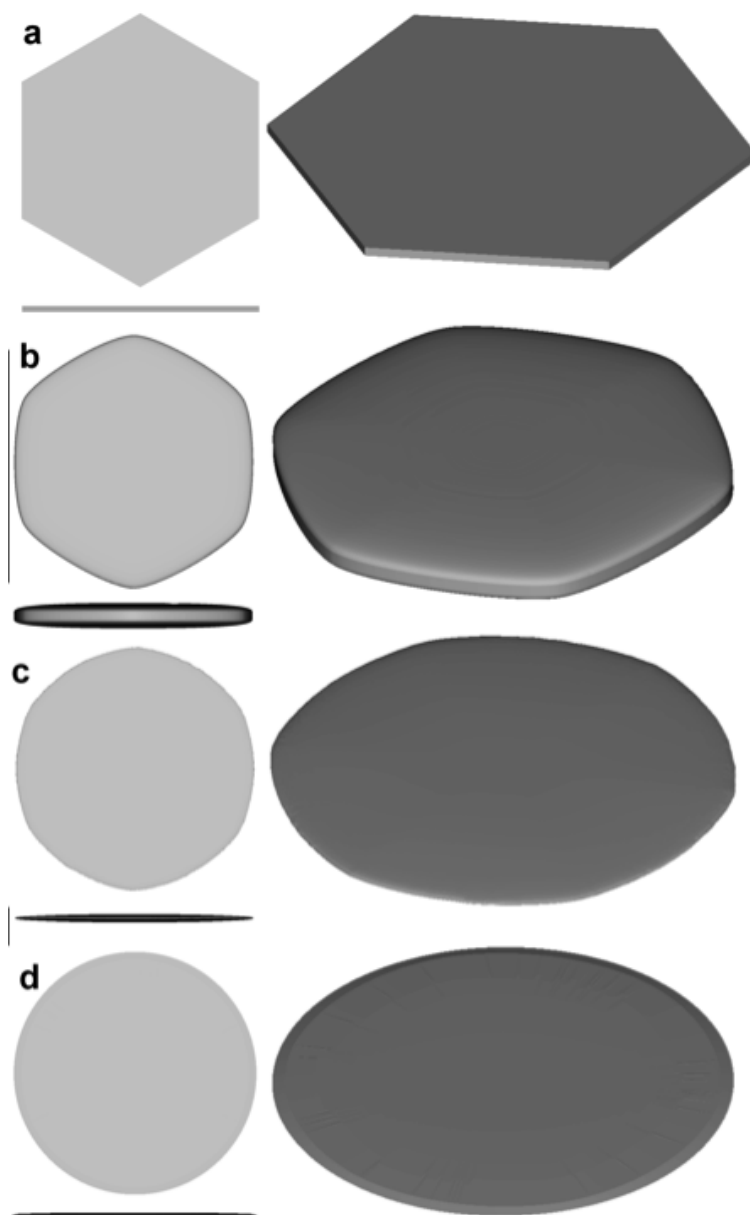
Figure 5.14: Ideal ice crystal shapes used to match photographed interference patterns [166]. Panel a, a 150 μm hexagonal plate with 1 μm thickness, corresponds to the photoed and modeled patterns in panel a and b of Figure 5.15. Panel b, a 130 μm slightly rounded hexagonal plate with 4 μm thickness, corresponds to the photoed and modeled patterns in panel c and d of Figure 5.15. Panel c, a 120 μm semi-rounded hexagonal plate with 1 μm thickness, corresponds to the photoed and modeled patterns in panel e and f of Figure 5.15. Panel d, a 40 μm spheroid with 0.5 μm thickness, corresponds to the photoed and modeled patterns in panel g and h of Figure 5.15.
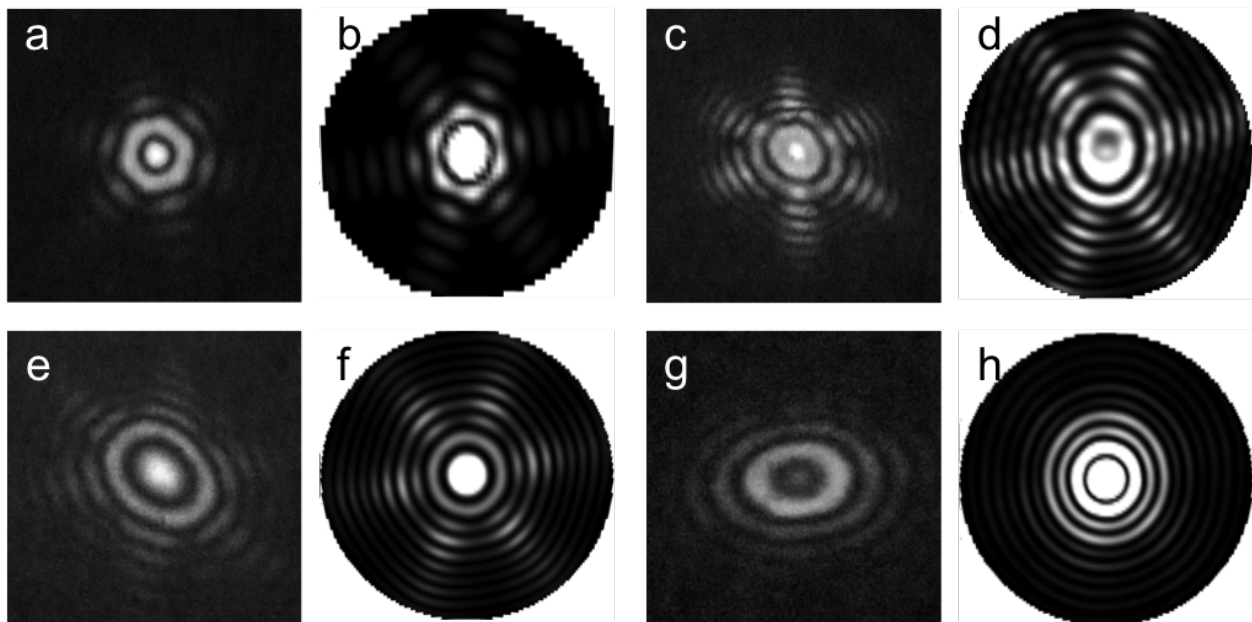
Figure 5.15: Photographed (panels a, c, e, and g) and modeled (panels b, d, f, and h) interference patterns from ice crystals, modified from Goerke et al. [166]. The size and shape of the corresponding crystals is given in Figure 5.14.

(a) The measurement of HOIC by polarization identification demonstrated by CAPABL is only possible by unique diattenuation signatures. This technique has lead to the longest continuous data set of HOIC known to the author.

(b) Using the CAPABL polarization identifications, the energy budget contribution of HOIC is now possible to evaluate. First results are provided showing HOIC have stronger longwave and shortwave CRE than ROIC.

(c) HOIC and ROIC are shown to have different mean Doppler velocities and radar reflectivity [165] as well as temperature and relative humidity [127].

Chapter 6

The Summit Polarized Raman Lidar

Addressing a lack of continuous high vertical and temporal resolution measurements of moisture and atmospheric thermodynamics in the Arctic was the main motivation for the proposal and creation of the Summit Polarized Raman (SuPR) lidar system. In addition to water vapor, temperature is a critical atmospheric variable because it controls atmospheric stability [92]. Radiosondes currently form the backbone of temperature and thermodynamic profiling throughout the world for operational weather forecasting, but many problems including dry biases and temporal performance variation are observed. Radiosondes standard temporal resolution is 12 hrs, however many high-impact meteorological events can occur on much shorter timescales. SuPR is designed to improve temporal resolution from 12 hrs to approximately 5 min to 15 min, which would be useful in increasing forecasting skill and in process studies of relevant events. In the Arctic due to the extremely sparse sampling, accurate profiles of moisture and temperature as well as cloud properties drove the creation of SuPR.

In addition to the operational measurements across the world, numerous field campaigns have described intensive radiosonde sampling efforts such as the recent Midlatitude Continental Convective Clouds Experiment (MC3E) and the Planes Elevated Convection At Night (PECAN) Experiment, which have been used to determine the atmospheric thermodynamic state during meteorological events [167, 168]. Such intensive efforts are exceptionally useful in understanding specific processes in short-term, high-impact weather events but require major efforts, infrastructure, and coordination. These campaigns thus occur infrequently and are not operationally viable. SuPR

offers an autonomous alternative to such intensive efforts via remote sensing easing the human time and coordination at the expense of infrastructure.

6.1 Requirements Specification and Systems Engineering

The SuPR lidar system was proposed as a next-generation Arctic lidar system that could enhance the observational capabilities of the Arctic Observing Network. The scientific requirements of the system are given in Table 6.1 resulting largely from the needs of the ICECAPS program and benefits of higher resolution atmospheric thermodynamic profiling. In particular, the 12 hr resolution of radiosonde measurements and the lack of vertical resolution in passive microwave and infrared retrievals drives the dramatic increase in resolution, which, combined with an instrument suite like ICECAPS, could provide a more complete picture of the atmosphere by providing more information.

Table 6.1: Description of SuPR's scientific measurement requirements. These requirements are specified in the SuPR NSF proposal and are related to the ICECAPS science requirements using the ICECAPS requirements tracability matrix given in Figure 4.1. The requirements that were found to be the most difficult to meet are highlighted in red.

Observation	Method	Vertical Resolution	Vertical Range	Temporal Resolution	Accuracy
Water Vapor Mixing Ratio	Vibrational Raman	30 m	0.3-8 km	15 min (Day) 5 min (Night)	< 10% (Day) < 5% (Night)
Temperature	Rotational Raman	30 m	0.3-25 km	5 min (Day)	< 10% (Day)
Cloud & Aerosol Abundance	Total Backscatter & Extinction	15 m	0-35 km	30 sec	< 10%
Cloud Phase	Polarization	15 m	0-15 km	30 sec	< 2 %

The most stringent requirements are highlighted in Table 6.1 in red. A vertical range from 0 km to 8 km for water vapor mixing ratio stretches the ability of SuPR largely due to the lack of water vapor in the Arctic atmosphere, especially in the winter time (night time). To meet the requirements stated in Table 6.1, it does not suffice to take the specifications of a Raman lidar designed for the mid-latitudes or tropics and simply deliver it to the Arctic due almost exclusively to the dry atmospheric conditions. Additionally, the temperature range of 25 km is exceptionally

difficult to meet based on the strength of the lidar signals and detector induced dynamic range caused by the solid angle term of the lidar equation and SVLE. Finally, as noted extensively in Chapter 4, accurate measurements of polarization properties are intimately linked to system design and are therefore unavoidably stringent. Figure 5.5 indicates possible fractional occurrence errors on the order of 30% observed by CAPABL; SuPR requires an error of no more than 2%. This set of requirements represented a system that could add water vapor mixing ratio and relative humidity measurements to the existing infrastructure at Summit for an all-in-one water observing system. The detailed requirements are not given in the interest of brevity, but were collected in a critical design document and used extensively to drive the design of SuPR using rigorous systems engineering principles.

An iterative process was adopted where a complete system optical design was specified and modeled using the SVLE and all available information about the optics and scattering. The ideal performance was tested against the science requirements given in Table 6.1 and the lower level system requirements, not shown, to determine what, if any, design modifications were required. Any design that met the science requirements for SuPR was then analyzed in the context of laser safety to meet the major system level requirement of safe continuous operation. The final system design of the SuPR lidar is presented in Section 6.2, the results of the safety analysis in Section 6.3, and the results of the system model developed are given in Section 6.4.

One point to emphasize is the selection of the Raman technique for measuring water vapor and temperature. At least theoretically, these measurements are possible via the differential absorption lidar (DIAL) technique [169]. Based on the lack of technical readiness of the DIAL temperature technique, a Raman system is specified as it is the only mature lidar technique with the ability to make the measurements.

6.2   SuPR System Design

The SuPR system was designed based on requirements specified for deployment to Summit, Greenland. Summit is a year round atmospheric observatory staffed with anywhere between 5

(September through April) and 50 (May - August) people at any time. The station is accessible mostly in the summer months with a year round technician for scientific equipment, who is a non-expert in laser technologies. As a result of limited skilled access and the harsh environments experienced in Greenland, the system requires a high level of autonomy, robustness, and redundancy. The requirements written for Summit, however, do not preclude other Arctic or Antarctic field sites or indeed midlatitude and tropical field sites, but rather represent a stringent set of guidelines required for instrument deployment. The designed temperature range extends from Arctic temperatures at -40° C to tropical 40° C to accommodate possible validation studies and testing as well as planned operations.

6.2.1   Instrument Overview

The SuPR lidar system represents a substantial increase in instrument complexity from CAPABL. It does however leverage much of the trials and successes of CAPABL. CAPABL uses a twin laser head and a single detector with 2 pen steering motors. SuPR uses a similar twin laser head but measures 6 channels with 7 motors. The measurement system and motors are made by the same manufacturers for both systems allowing for much of the infrastructure and software for SuPR to be tested via CAPABL. A block diagram of the SuPR lidar is given in Figure 6.1. More explanation of the systems and design are in this section. More detail about the optics and transmitter and receiver hardware can be found in Appendix 8.5 including descriptions, model numbers, manufacturers, and price.

Of particular need for the SuPR system is the designed reference channel, or alignment leg. There is a main receiver consisting of optics 1-41 to be used for operation. The alignment leg is included as optics 44-49. This alignment leg is used as the alignment reference for the transmit laser beam as well as the polarization reference for the entire system.
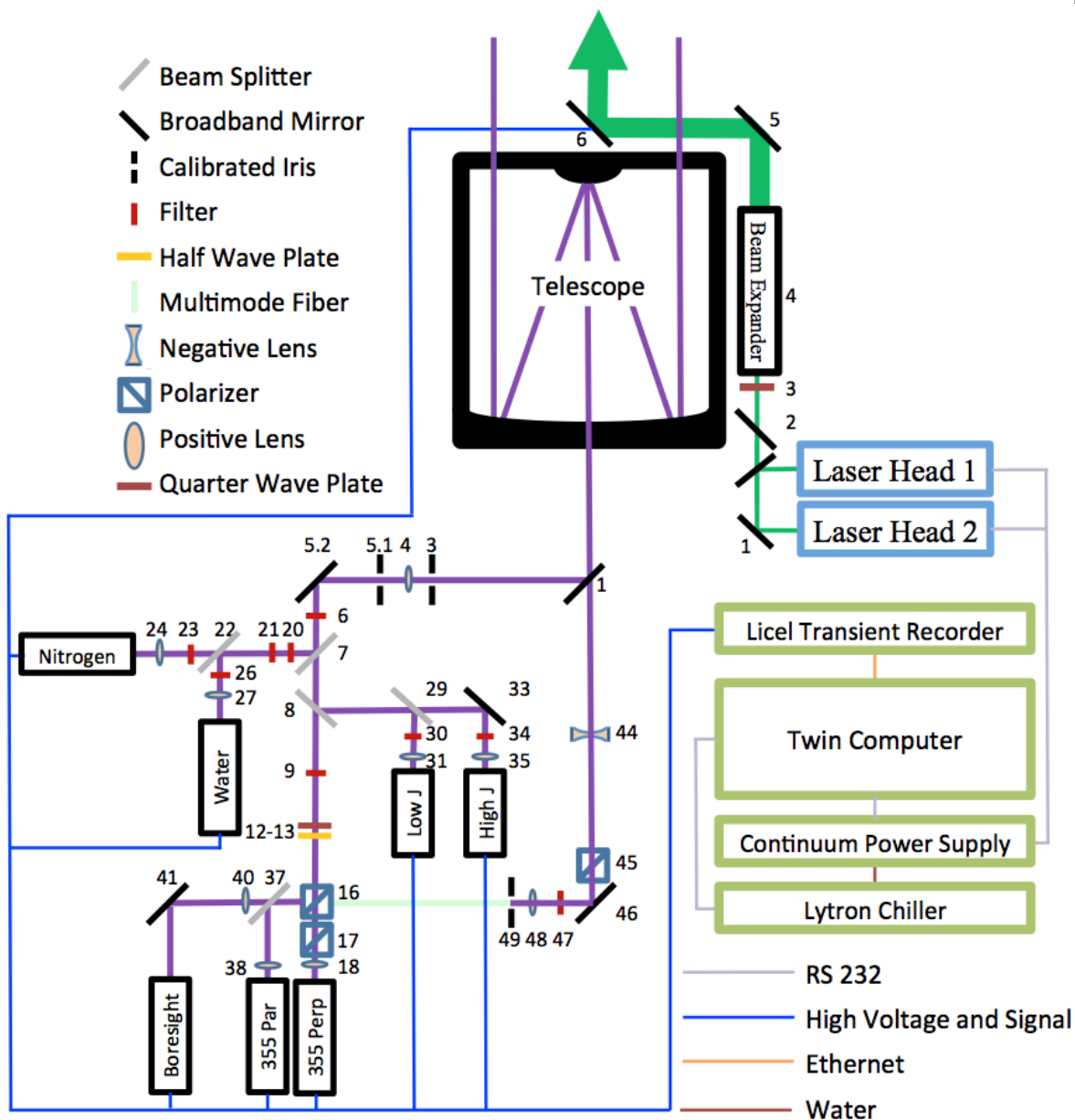
Figure 6.1: A system diagram of the SuPR lidar system with major measurement electronics and optics as well as some major electrical connections. The optics are numbered based on the mount in which they sit to correspond to the numbering in Appendix 8.5. Some numbers are skipped as the mounts are initially numbered then the optics are numbered based on their mount. The transmitter is co-aligned after the optic labeled 2 by a flip mount which moves in and out of the beam path.

6.2.2   Enclosure

SuPR is housed in a custom built 20 foot shipping container. The container consists of two main insulated compartments both with Arctic entry door and both individually heated and cooled.

The main room houses the optical components and laser while the secondary room houses the laser chiller and serves as an entry vestibule. The rooms are split in an effort to maintain a constant temperature in the optical room while the vestibule area is allowed to fluctuate more widely because of the insulation to the main optical room. A CAD rendering of the container is given in Figure 6.2 with the optical system shown in the main room.
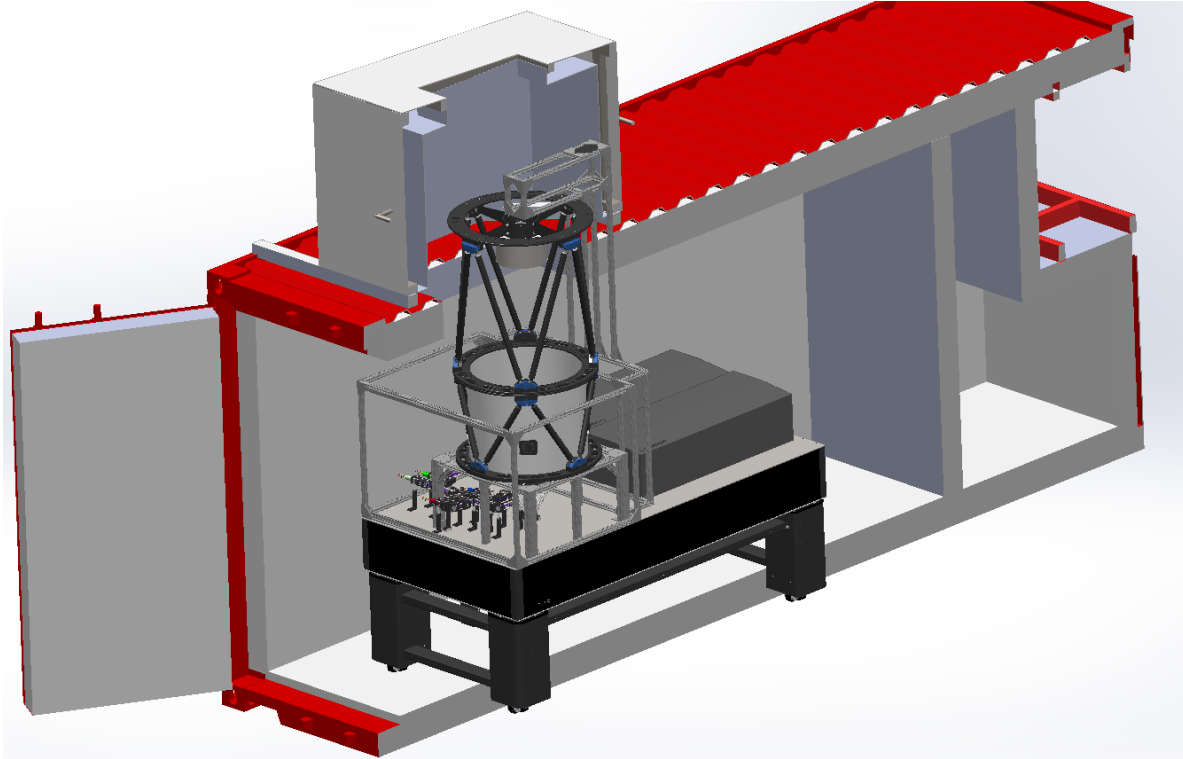
Figure 6.2: Solidworks drawing of the SuPR system in its shipping container. The interior and main entrance door are removed in this view but are in the upper right. The container is connected via a 440 volt Appleton plug and an ethernet internet cable. The hvac, main power and distribution, uninterruptible power supply, laser power supply, and chiller are contained within the container. This chiller is located on the opposite side of the demising wall to help maintain temperature control of the optical room. The system electronics are mounted under the table and are obscured from view in this projection.

Some relevant building specifications that are required based on the Arctic specification of the SuPR system are as follows. The insulation of the building is specified as $R \geq 48$. This is provided by 6 inch thick high density foam insulation around all walls, ceiling, floor, and entries. Heated Arctic entry doors are used to connect the vestibule to the optical room and as an entry

into the container. Connections between rooms or with the outside are done through narrow feedthrough ports, which have end caps to minimize airflow. The main heating and air conditioning is provided by two separate wall mounted temperature units, which share a common condenser. Current temperature control designs deployed to Summit as part of the ICECAPS program directly ventilate with outside air, but the temperature control of these rooms has shown shifts as much as $\pm 5^\circ$ C over a period of 10 min. As a result, air exchange was explicitly designed to minimize the shock of mixing cold outside air with warmer indoor air by preventing direct air exchange between outside and inside.

The laser exit port and main viewing window are tilted at an angle of 5° from the horizontal and can be rotated into the prevailing wind. This design has been tested extensively at Summit for CAPABL and MPL deployed there [35, 89, 105]. Fans are mounted within the building to slowly mix air along the length as well as up into the telescope head room to prevent window frosting, a design also proven reliable at Summit as part of ICECAPS. The laser window is based on a design originally built for the ARM Southern Great Planes Raman lidar, which has operated without lose of quality for nearly 20 years. A high energy plug made out of fused silica, which is anti-reflection coated at the laser wavelength, forms the center of the main window. The outer ring of the main window is composed of UV transparent Schott glass. The window is 27 in in diameter with a designed clear aperture of 25 in.

The building electrical system is connected to an uninterruptible power supply (UPS) which is capable of powering the system nominally for 15 min including all measurement and hvac systems. At Summit, and more generally at remote field sites, grounding and power are major design features. At Summit, the power grid is run off of several diesel generators, which are often serviced and power load is shifted off and on. Furthermore, Summit sits on approximately 3 km of ice meaning electrical grounding is a concern due to the lack of a true earth ground. Therefore, the UPS is also used to condition the power and as a ground reference as well as smooth power distribution to avoid data gaps based on interruptions and maintenance to the local electrical grid.

6.2.3   Transmitter

The laser transmitter for SuPR is specifically designed to be as simple and robust as possible to reduce the possibilities of single point failures. The design is a result of past experience with transmitters in extreme environments and especially experience with CAPABL's transmitter. There are a few design features of particular importance to SuPR's ability to complete the desired measurements primarily related to redundancy and continuity. Of note are the twin laser head design and the polarization design of the system.

The twin laser head, a flashlamp pumped Continuum model 9030 frequency tripled Nd:YAG, is designed to be compatible with a single power supply. The single power supply contains a water to water heat exchanger, which is connected to a water to air heat exchanger, referred to here as the chiller, which is capable of removing more than 6 kW of heat at low atmospheric pressure, critical for high altitude deployment sites like Summit. The vestibule air in the absence of more heat exchange has been observed to rise in excess of $60°$ C in 30 min to 45 min with the heat load from the laser and chiller. Two more air conditioning units described in Section 6.2.2 that cool building air with outside air using a closed condenser system. This general transmitter design has demonstrated robust longterm operation at the Southern Great Planes ARM site for approximately 20 years [73].

The transmitter optics are designed to co-align the beams such that the beams can be switched without requiring a system realignment. This is useful during times when flashlamps need to be changed to reduce system downtime as well as removing a single point failure, which is untenable in the high Arctic. An automatic flip mount, pen motors, and rotation stages can be software controlled to each individual laser. The pen motor design is based on that of CAPABL to compensate for slight changes in orientation of the laser heads and temperature fluctuations allowing for the beam to be well aligned in the receiver's far field. The temperature fluctuations are of particular concern based on the author's experience with the Kühlungsborn Rayleigh Mie Raman lidar system [108].

The polarization state of the transmitter is desired to be purely linear. However, because of the number of folding mirrors in the transmitter required to transmit the laser beam to the sky, retardance is of concern. As a result, a motorized quarter wave plate is included in the transmitter. The laser beam starts out linearly polarized but through several mirror reflections can retard into an elliptical polarization. The transmitter quarter wave is used to cancel the retardance induced by the mirrors. It is important to note however that this is used once the beams are co-aligned and results in a beam which is not linearly polarized after the wave plate but at the exit of the transmitter system. An example of the polarization states of the SuPR beam plotted in Poincaré space after interaction with the transmitter mirrors and quarter wave plate (QWP) is given in Figure 6.3. In Figure 6.3, some arbitrary linear polarization is retarded by interaction with each transmit mirror (using Equation 2.6 and assuming a simple 10° retradance angle). The nominal situation with the final two steering mirrors contributing more retardance and retarding the beam back to linear polarization is shown via the bold arrows. The cyan line indicates all the theoretical output polarization states of the SuPR transmitter.

The polarization purity of the nominal output state is verified via the alignment leg of the receiver, which uses as its first optic a polarization analyzer. By observing atmospheric scattering during a clear air period, linear output polarization will be indicated by minimizing the signal throughput to the receiver detector. Minimized receiver signal will occur only with a linear output polarization and a receiver polarizer cross polarized with the transmitter. Either a minimization procedure or a full map of the signal as a function of QWP and polarizer angles can be done. For SuPR, the latter is chosen.

6.2.4   Receiver

Great care has been taken with the SuPR receiver to mitigate hardware effects on signals and to optimize the system for the cold dry environment of the Arctic. An extensive instrument model was developed to simulate the dry atmosphere of the Arctic to analyze design decisions based on the most realistic approximation of the Arctic atmosphere possible. Data were included
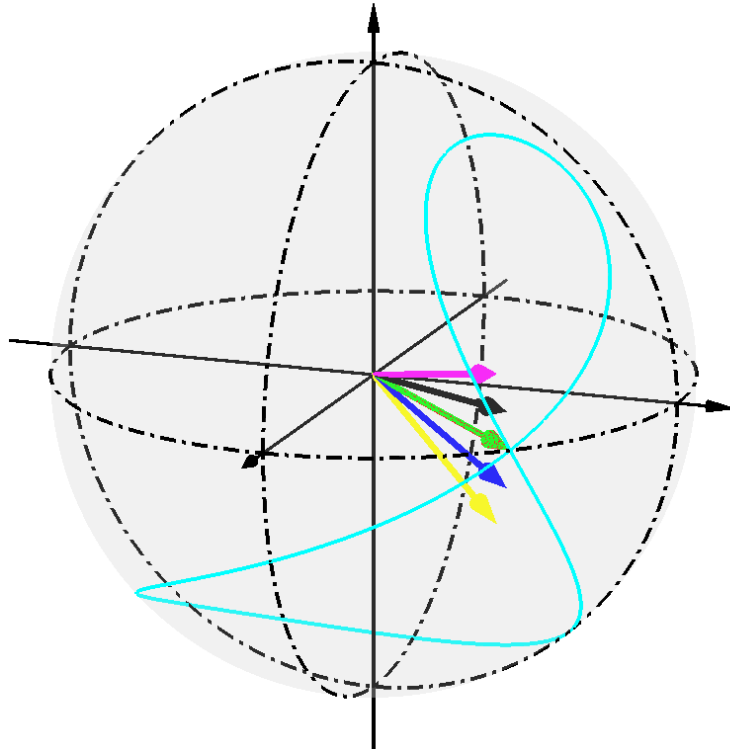
Figure 6.3: Possible output polarization states of the SuPR system projected onto the Poincaré sphere. In nominal operations, the red arrow (covered by green) is the output state of the laser. The blue and yellow arrows depict the polarization assuming 10% retardance from each of the two folding mirrors before the beam expander in the transmitter. The pink arrow depicts the compensation by the transmitter quarter wave plate and the black and green the polarization states after the final two steering mirrors. The output polarization is linear in nominal operations. The cyan line depicts the possible polarization states of the transmitter in alignment or off nominal operations assuming the same 4 mirror retardance values.

from the ICECAPS program. Specifically, radiosonde measurements of temperature and humidity were used in all seasons as well as estimates of solar background from both ICECAPS lidar data as well as shortwave spectrometer data courtesy of Germar Bernhard in all seasons. The results of this instrument modeling highlighted critical design elements including expected weak water vapor Raman signals and polarization purity requirements indicated in red in Table 6.1.

The SuPR receiver consists of 6 measurement channels measuring elastic and inelastic scattering phenomena. These channels are described in detail in Table 6.2. The channels included are two polarization channels measuring elastically backscattered light, two channels measuring Stokes

vibrational Raman signals from nitrogen and water vapor, and two channels measuring anti-Stokes rotational Raman signals from nitrogen and oxygen. A CAD rendering of the receiver is given in Figure 6.4. The beam path from the field stop through the receiver is given in purple. This beam slowly grows through the receiver, as a result of the conservation of etendue, which is specifically sized to avoid relay mirrors and vignetting in an attempt to reduce unwanted complexity and optical surfaces to maximize optical efficiency.

Table 6.2: Description of SuPR's optical channels. The central wavelength and bandpass are filter characteristics and the channel optical efficiency is the combined optical efficiency of all elements from the telescope to the detectors, including the detector quantum efficiency, for all elements. The center wavelength and bandpass are the requirements given to the narrowband filter manufacturer. As filters can be tilt tuned blueward, the nitrogen and water vapor filters are shifted by the tolerance redward.

Channel	Central Wavelength	Bandpass width (FWHM)	Channel Optical efficiency
Parallel	$354.71 \pm 0.03\,nm$	$0.3 \pm 0.05\,nm$	1.54%
Perpendicular	$354.71 \pm 0.03\,nm$	$0.3 \pm 0.05\,nm$	1.53%
Low J	$354.00 \pm 0.03\,nm$	$0.3 \pm 0.05\,nm$	7.10%
High J	$353.30 \pm 0.03\,nm$	$0.3 \pm 0.05\,nm$	6.06%
Nitrogen	$386.69 \pm 0.03\,nm$	$0.3 \pm 0.05\,nm$	24.0%
Water Vapor	$407.45 \pm 0.03\,nm$	$0.3 \pm 0.05\,nm$	25.1%

For the vibrational Raman channels, shown with the blue PMTs (cylindrical ends of the beam path with power and signal wires out the end), optical attenuation is provided by a shortpass filter, common for the entire receiver, and two Raman longpass filters used to block elastic scattering signals and sky noise from contaminating Raman signals. With the narrowband filters, the blocking from 425 nm to 700 nm is greater than optical depth (OD) 11 and the blocking at the Cabannes line is greater than OD 20. Narrow band filters, which are mounted on precision tilt tuning mounts, are then used to select the final bandpass wavelength of interest. The tilt sensitivity of the filters is specified to be 1 pm to 2 pm per 1°. Dichroic beam splitters are used to split the vibrational Raman signals from the other measured signals. The optical efficiency is maximized for the weakest signal, which is the water vapor channel.

The rotational Raman channels, shown with the red and pink PMTs are split from the main channel with a 90-10 beam splitter. Great care has been taken with this beam splitter,
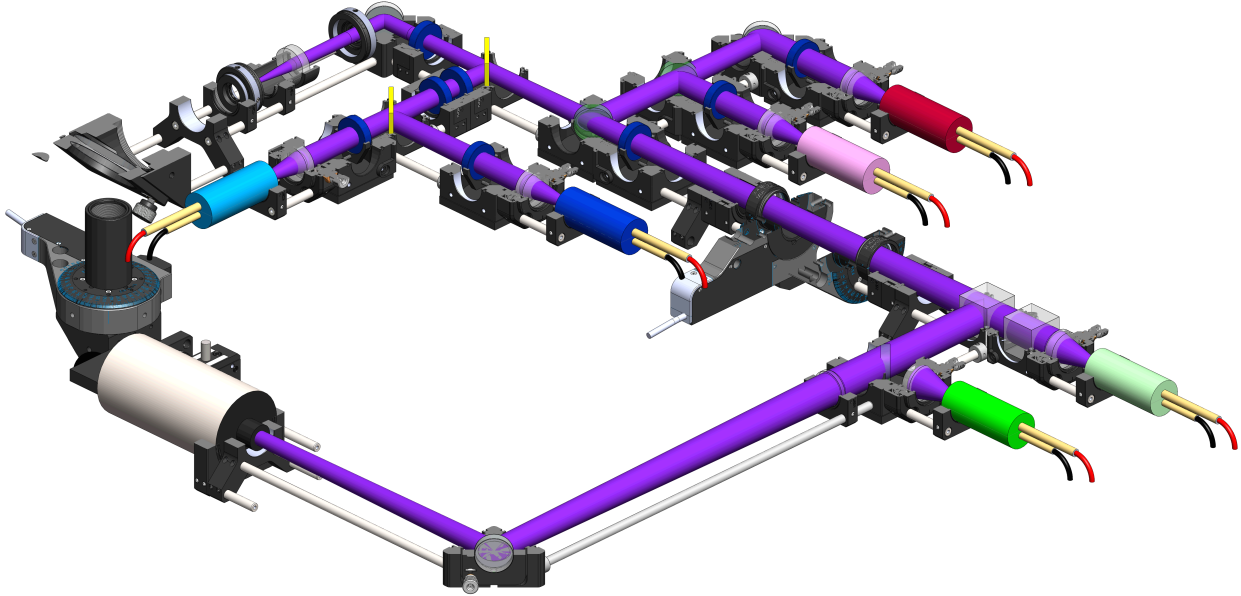
Figure 6.4: Solidworks drawing of the SuPR receiver. The top of the receiver is removed to show the beam paths. Yellow square optics are dichroic optics, blue round optics are optical filters, non-polarizing beam splitters are given as light green optics, polarizing beam splitters are clear white cubes, and lenses are clear white circles. The channels are indicated by different colored PMTs (cylindrical ends of the beam path with power and signal wires out the end) as follows: light blue = nitrogen, dark blue = water vapor, pink = high J, red = low J, dark green = parallel, light green = perpendicular, and gray = boresite camera. The telescope is coupled to the receiver using the kinematic mirror mount in the upper left. Note that the beam size changes through the receiver through the conservation of etendue.

which is nominally at 45° incidence to the beam path, to have reflectivity and transmission that are insensitive to the S or P polarization near the laser output wavelength. The transmission of the S and P polarizations are within 1% of each other from 352 nm to 359 nm. Because the rotational Raman lines show high depolarization, greater than 75%, a polarizing beam splitter is used to separate the high and low J signals instead of a traditional power beam splitter. The low J rotational channel, bandpass centered less than 1 nm from the Cabannes line, is set to observe at a polarization perpendicular to the transmitter. This has the effect of attenuating the elastic scattering signals in the low J channel, which is the most sensitive to light leakage due to its proximity to the Cabannes line.

The elastic PMT efficiency is intentionally reduced by optical design because of the expected

strong scattering observed. As mentioned with the rotational Raman 90-10 beam splitter, all optics before the elastic polarization analyzer are designed to be non-diattenuating. Retardance is controlled via QWP and half wave plate (HWP) mounted on motor controlled rotation stages. After verifying linear output of the transmitter using the alignment leg, receiver polarization effects can be mitigated by simply maximizing the difference between parallel and perpendicular voltages in clear sky.

The total optical efficiency of each of the 6 operational measurements and an included boresite camera used for operational fine alignment is given in Figure 6.5. The efficiency for S and P polarizations is explicitly given for the Raman channels. The efficiencies near the elastic scattering wavelengths being similar for S and P polarization minimizes any systematic diattenuating effects that typically arise from using optics at non-normal incidence.

6.3   Monte Carlo Laser Safety Analysis

For ground-based lidar systems that lack steering and are directed vertically like SuPR, direct and scattered laser beam exposure is a safety concern for aircraft/spacecraft as well as personnel working near the system. The American National Standards Institute (ANSI), in an attempt to standardize and regulate the vast array of laser systems, defines limits of exposure to which one can be safely subjected [170]. Careful attention must be paid to ensure that at no point can human exposure to laser light exceed the Maximum Permissible Exposure (MPE), which is a function of laser characteristics such as wavelength, peak power, pulse repetition rate, pulse width, and exposure time. Using the MPE and beam characteristics, the Nominal Ocular Hazard Distance (NOHD) and Nominal Hazard Zone (NHZ) can be calculated, which assume no scattering for the NOHD and complete Lambertian scattering for the NHZ. However atmospheric conditions can lead to indirect exposure through scattering that fits neither standard calculation type.

The ANSI standard definition of the propagation medium of laser beams leaves much to be desired for application to atmospheric lidar systems and especially for severe weather. The ANSI standards allow for attenuation of beam calculations for long propagation distances but only include
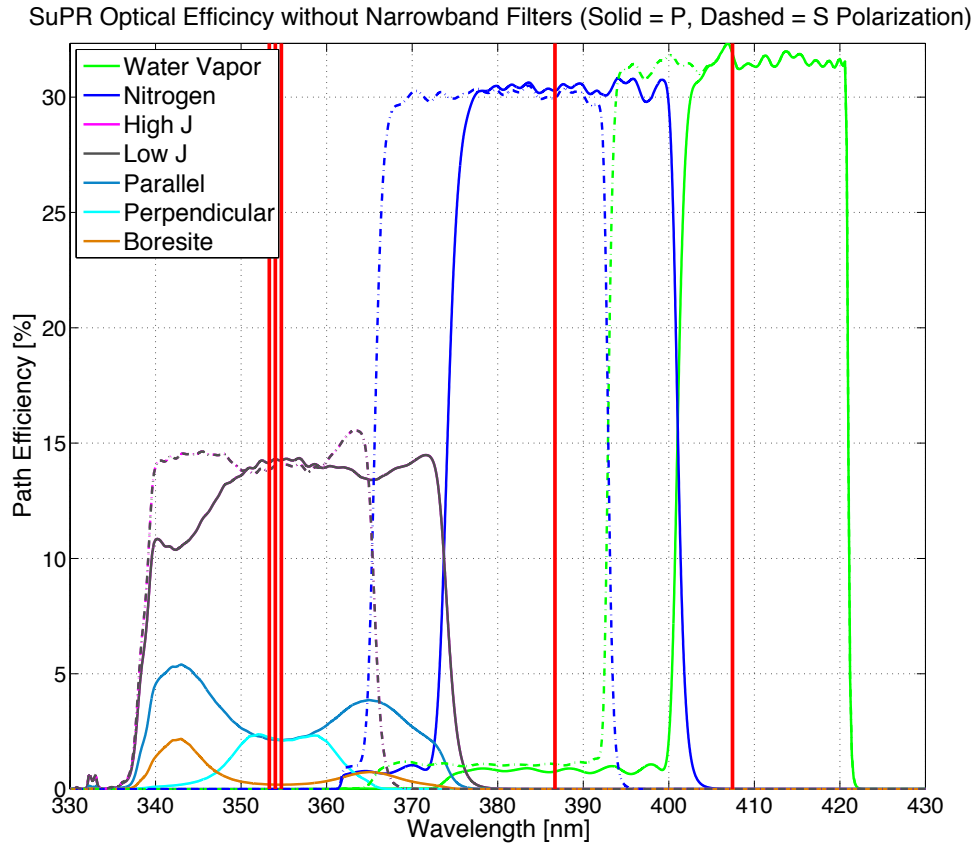
Figure 6.5: Optical path efficiencies for each of SuPR's 6 detection channels and its boresite channel. These efficiencies include all optics from the telescope to the detection including detector quantum efficiencies excluding the narrowband filters for each channel. In the measurement range of interest for each detection channel, efficiencies for the S and P polarization for each optic are given indicating no major polarization dependence for any channel. The wavelengths of the channels are indicated by vertical red lines.

absorption effects and not scattering phenomena. Additionally, the requirements specifically state that atmospheric attenuation is only a problem and should only be calculated for horizontally propagating beams relying on the false assumption that there is little significant scattering through a thinning atmosphere. Finally, any deviation to the nominal atmospheric condition of clean dry air is relegated to an appendix section in the ANSI outdoor standard, which states that deviations from nominal conditions might require more analysis techniques but fails to describe any techniques or provide any guidance of any kind to describe when further analysis might be required. In the

Arctic, this nominal picture of the atmosphere is rarely observed.

Ensuring laser safety for atmospheric lidar is thus uniquely challenging due to designs requiring high peak power, short pulses, and output wavelengths near the visible portion of the spectrum. Furthermore, for atmospheric lidar, the beam cannot be fully enclosed after it leaves the building meaning atmospheric characteristics must be considered. The beam is most readily accessible in the atmosphere, but the ANSI standard description of the propagation medium is over simplified by not accounting for scattering through the propagation medium [170, 171]. In light of the deficiencies of the ANSI standards, a new analysis method was developed during the design process of SuPR based on Monte Carlo simulations of laser light. Specifically, the change in the hazard zone definitions compared to the NOHD and NHZ as a function of common atmospheric scattering regimes like clear air, fog and blowing snow for the designed Arctic environment are performed.

Laser light is modeled via a Monte Carlo scattering scheme following the theory described in Section 3.4 to track the energy density of the directly transmitted and scattered laser light as a function of location. In all cases, the distances r and h are prescribed to determine the energy density caused by the beam at the boundary of the cylindrical region of interest. Simulations are run to determine where the beam exceeds the MPE; thus, r and h become the hazard zone and ocular hazard distance respectively when the energy density drops below the MPE. These can be compared to the ANSI standard NOHD and NHZ to determine the effect of scattering.

The laser parameters for SuPR that are important for the Monte Carlo scattering scheme are given in Table 6.3. The SuPR transmit beam specifications are important to accurately model the beam entrance into the propagation and scattering layer of interest. The pulse energy and pulse rate are used to scale the Monte Carlo results based on output beam power. Additionally, based on the given laser specifications, the ANSI standard calculations are given in Table 6.4. Here, the second and third harmonic wavelengths of the SuPR beam are calculated as during the design process both wavelengths were considered.

Table 6.3: Specifications of the Raman lidar system to be simulated using the Monte Carlo code developed. These specifications are based upon previously demonstrated Raman lidar systems designed for lower atmospheric monitoring and upon a Raman lidar system under development designed for polar deployment.

Specification	Value
Beam Diameter	$2.7\,cm$
Beam Divergence	$167\,\mu\text{rad}$
Beam Shape	Top Hat
Laser Energy	$0.400\,J$
Laser Rep Rate	$30\,Hz$
Laser Wavelength	$354.75\,nm$ and $532\,nm$
Pulse Width	$3\,ns$ to $7\,ns$

Table 6.4: ANSI standard range and energy density calculations based on the worst-case laser system specifications given in Table 6.3 and the standards specified in ANSI Z136.1 [170]. All simulations to be presented will have color bars scaled to the MPE values given here. Exposure duration of 10 *sec* is assumed using a factor of 2.5 reduction in MPE for exposure to such systems everyday for $355\,nm$. The extended source correction is applied to $532\,nm$ wavelength assuming a nominal flight altitude of $500\,m$ and scattering from anywhere within $4\,m$ of the exit port (the size of the regions for the simulations run). The direct pulse MPE is used for the NOHD calculation and the indirect for the NHZ calculation.

ANSI Standard Value	$\lambda = 355\,nm$	$\lambda = 532\,nm$
Direct Pulse MPE	$4.14\,mJ/cm^2$	$2.0 \times 10^{-4}\,mJ/cm^2$
Indirect Pulse MPE	$1.33\,mJ/cm^2$	$10.7 \times 10^{-4}\,mJ/cm^2$
NOHD	$0.645\,km$	$95.7\,km$
NHZ	$9.77\,cm$	$345\,cm$

6.3.1 Clear Air

A comparison between the simulation developed with the ANSI standards is used to compare and contrast the differences in the assumed standard scene and the weather observed at Summit. Reproducing the ANSI standards with the same scene and then replicating a more accurate system scene is necessary. The first step taken was to model clear air. Rayleigh scattering by diatomic nitrogen and oxygen is considered. The Rayleigh phase function given in Figure 3.8 is used. The optical depth is converted to distance using a simple scattering model that is a combination of a Rayleigh scattering model and an aerosol model [172]. This results in an average optical depth per meter of $3.67 \times 10^{-5}\,m^{-1}$ for the UV calculated over a range of pressures from the surface to 10

km above sea level. The atmospheric model from which the pressures are simulated is the MSIS model.

A set of simulations is run with cylindrical regions all of the same radius but with varying heights. A map of Monte Carlo photons per unit optical depth area is calculated, then converted to photons per area using the specified optical depth per meter. Finally, it is converted to energy density by converting the simulated photons to laser photons. This yields a map of energy density as a function of location for each trial. The top of each cylinder is given to demonstrate how energy density is scattered and directly transmitted. This is shown in Figure 6.6.

The side of each cylinder can be treated in the same manner as the tops. The radius varies from the ANSI calculated NHZ to $4\,m$ for $355\,nm$. This size is chosen to represent distances from the beam outward to the edge of a window which would cover a lidar telescope and on to the roof of a building where one of the onsite staff could potentially be working. This is shown in Figure 6.7. In both cases it can be seen that the only hazard is from the direct beam. Even at a wavelength of $355\,nm$ where one expects a significant amount of scattering due to diatomic nitrogen and oxygen, the simulation does not indicate the scattered light to be a hazard.

The laser safety analysis for $355\,nm$ is duplicated for $532\,nm$ based on an original system design that included both. It should be noted that the $532\,nm$ laser propagation analysis is only an exercise and does not represent the laser operations planned for SuPR, which is at $355\,nm$, based on these results. The Rayleigh phase function in the visible is nearly identical to that at $355\,nm$. The optical depth per meter is similar as well but slightly less for the longer wavelength. Both are calculated independently but only the results for $355\,nm$ are given in the interest of brevity. The energy density exiting the side of each cylinder for $532\,nm$ is shown in Figure 6.8. The results are not repeated for $532\,nm$ range-dependency because the beam is well in excess of the MPE and as such shows little structure.
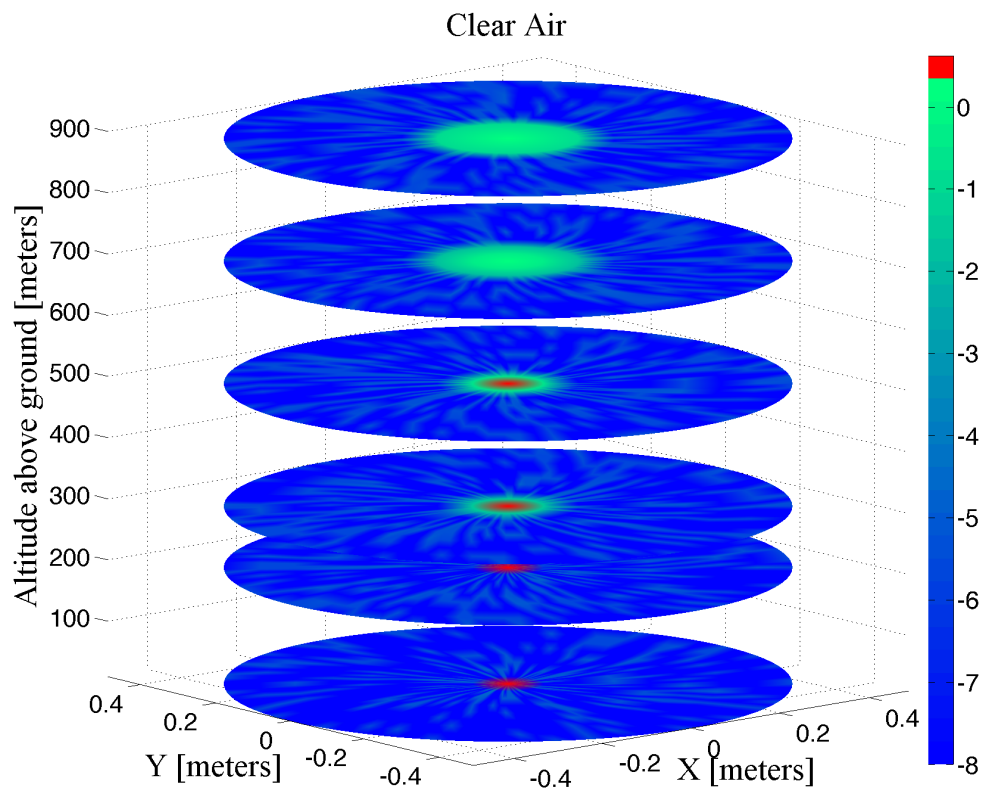
Figure 6.6: Energy density of all 355 nm laser radiation at the top of the layer of interest for 6 different altitudes: 10 m, 200 m, 300 m, 500 m, 700 m, 900 m. The color bar is given in log base 10 of the energy density with units of mJ/cm^2. Note that the red color indicates that the energy density for the hypothetical system with clear air would exceed the single pulse (direct) MPE for the system as modeled.
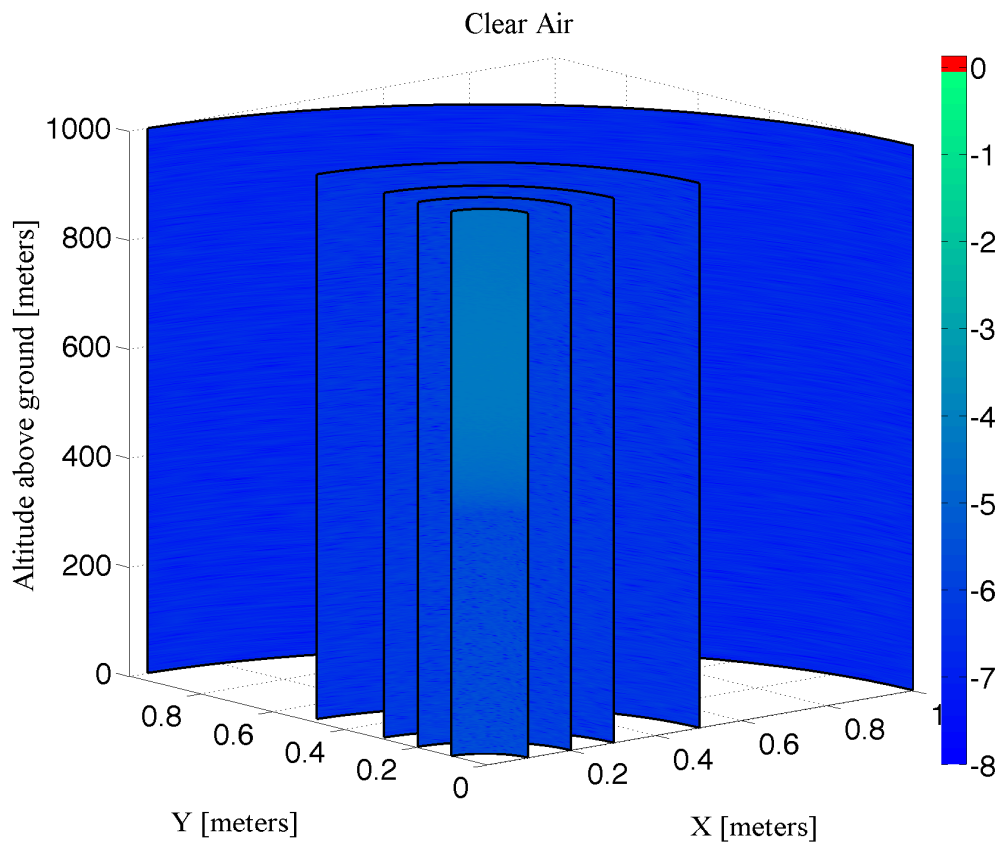
Figure 6.7: Clear-air scattered energy density of all $355\,nm$ laser radiation on the side of the layer of interest with 5 different radii: $10\,cm$, $20\,cm$, $30\,cm$, $50\,cm$, and $100\,cm$. The color bar is given in log base 10 of the energy density with units of mJ/cm^2. Note that the red color indicates that the energy density for the hypothetical system with clear air would exceed the indirect MPE for the system as modeled.
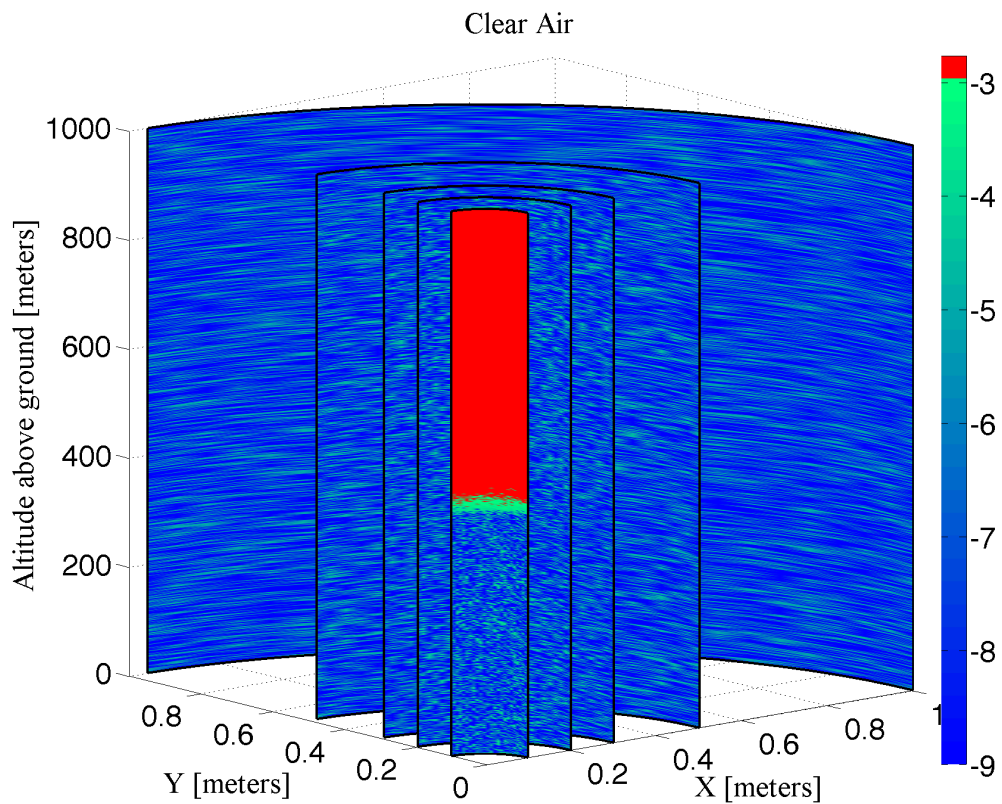
Figure 6.8: Clear-air scattered energy density of all $532\,nm$ laser radiation on the side of the layer of interest with 5 different radii which are the same as Figure 6.7. The color bar is given in log base 10 of the energy density with units of mJ/cm^2. Note that the red color indicates that the energy density for the hypothetical system with clear air would exceed the indirect MPE for the system as modeled. The MPE for $532\,nm$ is more than 3 orders of magnitude lower than for $355\,nm$.

6.3.2   Liquid Fog

Liquid fog near the start and end of the summer season is a regular occurrence observed at Summit. Low-level fog is frequently observed for several hours after the sun dips below the horizon resulting in relatively cold temperatures compared to the day. Furthermore, much atmospheric research is focused on understanding liquid and mixed phase clouds, both of which occur at Summit [35, 105]. In either case, liquid drops formed in supersaturated air but with few condensation nuclei are not converted directly to ice via the Wegener/Bergeron/Findeisen process. Although colloidally unstable, liquid water persists in the Arctic throughout the year [164].

This fog causes visibility to drop significantly and provides a good case study for determining laser safety. Here a fog with a liquid water path of $20\,g/m^2$ per every $500\,m$ and an effective radius, defined as the third moment of the size distribution divided by the second moment, of fog droplets of $15\,\mu m$ is assumed. The conversion of liquid water path to optical depth in Equation 6.1 gives optical thickness per meter [173]; here LWP is the liquid water path, R_e is the particle effective radius, τ is the optical depth, and ρ is the density of liquid water or ice. The assumed liquid water path is based on measurements of the ICECAPS Program. This fog is assumed to form at the ground but these assumptions could also be representative of a thin low-level liquid cloud.

$$LWP = \frac{2r_e\tau\rho}{3} \tag{6.1}$$

Similar to the clear air case, two sets of data runs are presented: one which holds radius fixed, Figure 6.9, and varies height while the second holds height fixed and varies radius, Figure 6.10.

In comparison to the clear air case, the effective NOHD decreases dramatically from that predicted by the ANSI standards, by a factor of approximately 2.3. However, this is not evident in the radial case because the scattered intensity is not near or in excess of the MPE. However, the same set of results at $532\,nm$ indicates that liquid water fog could present a serious safety risk within $2\,m$ to $3\,m$ of the beam. The results for $532\,nm$ are presented in Figure 6.11.
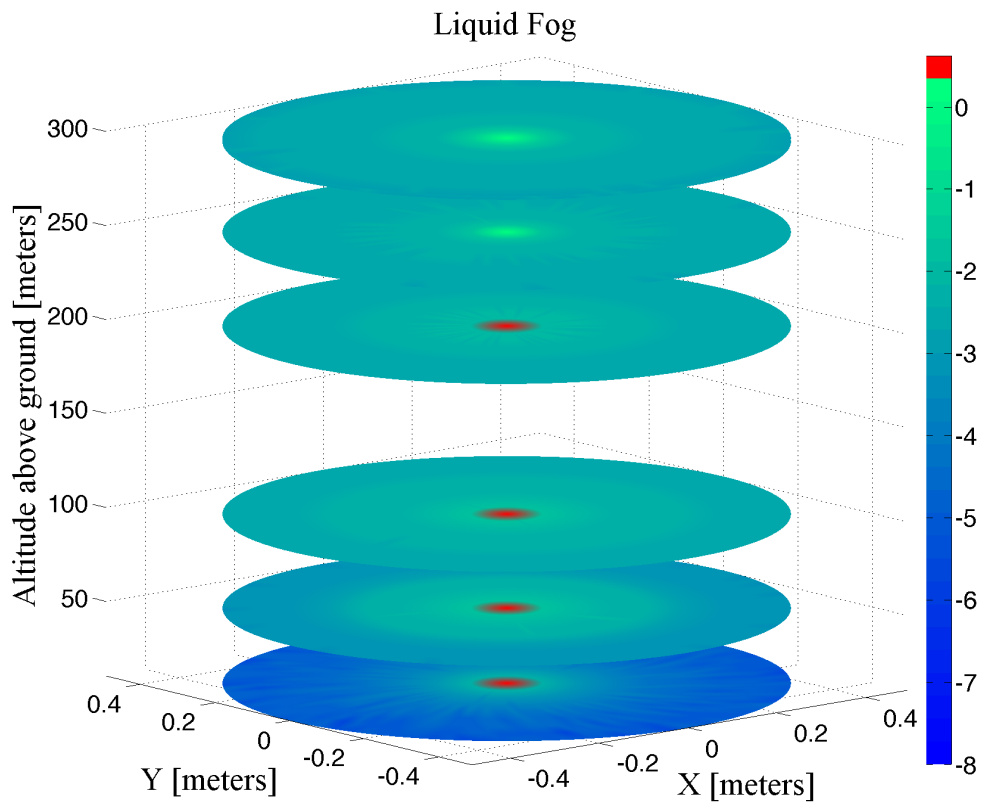
Figure 6.9: Fog-scattered energy density of all 355 nm laser radiation at the top of the layer of interest for 6 different altitudes: 10 m, 50 m, 100 m, 200 m, 250 m, 300 m. The color bar is given in log base 10 of the energy density with units of mJ/cm^2. Note that the red color indicates that the energy density for the hypothetical system with clear air would exceed the direct MPE for the system as modeled.
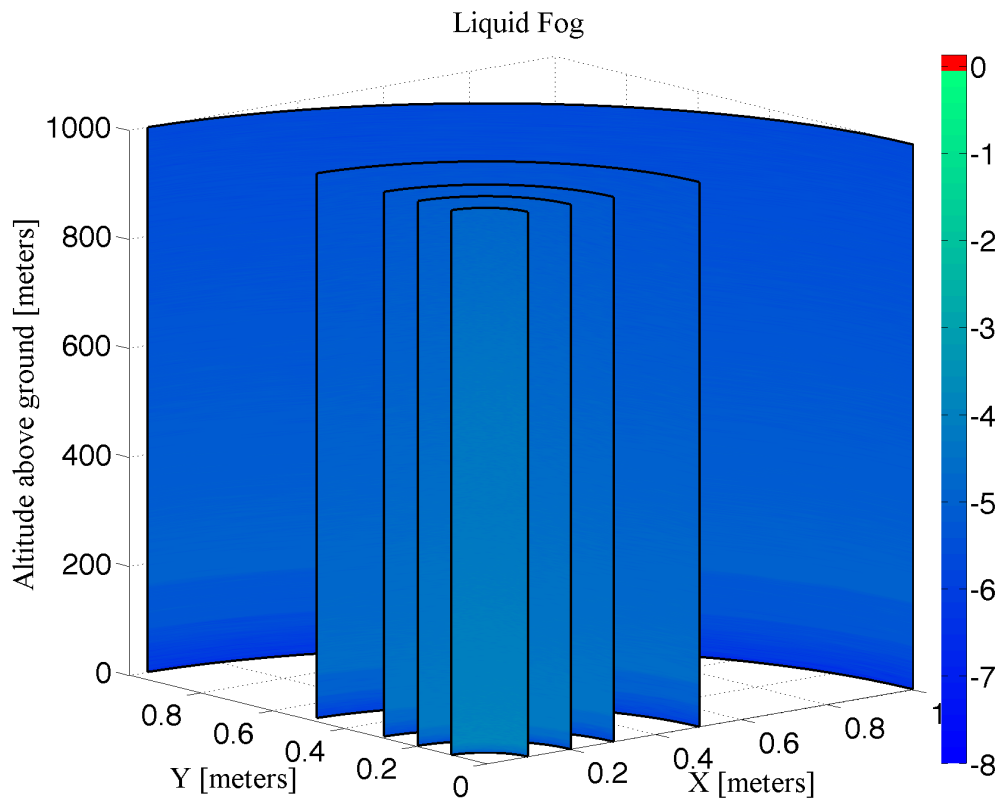
Figure 6.10: Energy density of all 355 nm laser radiation on the side of the layer of interest for foggy conditions at the same ranges as Figure 6.7 and 6.8. On the scale of the MPE, there is very little energy leaving the side of the layer of interest.
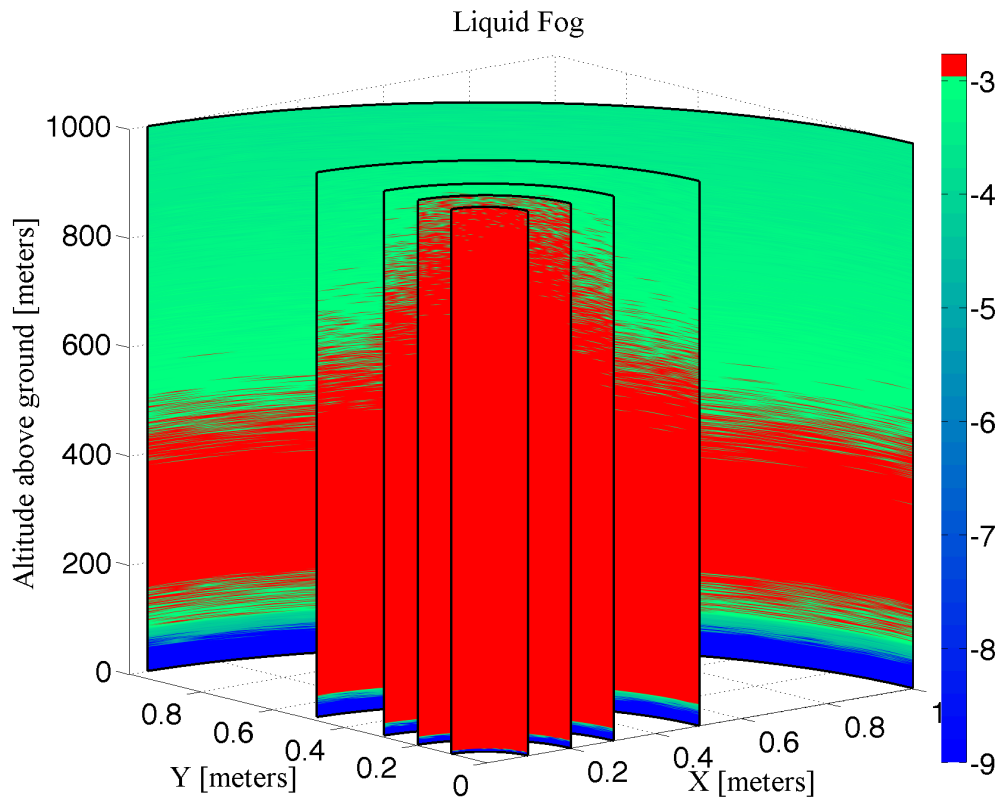
Figure 6.11: Fog-scattered energy density of all 532 nm laser radiation on the side of the layer of interest at the same ranges as Figure 6.7, 6.8, and 6.10.

The scattered radiative energy density out of the sides of the regions of interest exceeds the clear air case by at least 2 orders of magnitude. This is to be expected given the relatively large optical depth of fog versus clear air. One can observe that the scattered energy density out the side of the region of interest for fog also shows less uniformity near the ground. Considering that the phase function is sharply forward peaked for liquid water droplets, this is not surprising. For a photon to leave the layer near the ground, one would expect that scattering near 90° would be approximately 4 orders of magnitude less than that in the forward scattering direction.

6.3.3 Blowing Snow

Ice crystals exist suspended in the air above Summit for much of the year. Ice particles can either be precipitated out of clouds as snow or it can be lifted from the surface via wind. Precipitation events are observed throughout the year and occur most frequently during summer [35]. Furthermore, enhancements in precipitation caused by cloud systems, such as seeder feeder cloud systems where ice crystals from a higher cloud fall through and collect liquid water from a lower, have been observed by the ICECAPS program's polarization lidars. To model this system, the phase function used could be any mix of common ice crystal habits including but not limited to plates, columns, needles, or dendrites. To avoid the complication of having to choose a habit, a mixture of habits is assumed; it is also assumed that that the crystals have been roughened [120]. This choice, while limiting in its scope, allows for one to apply the simulations equally to entrained snow as well as that precipitated assuming some riming occurs during the crystals fall time.

Similar results to the case found for liquid water fog for $355\,nm$ were found for blowing snow, Figures 6.12 and 6.13. The effective radius of particles is assumed to be $20\,\mu m$ with the same LWP of $20\,g/m^2$ for consistency. With these parameters, one again sees a large difference of the NOHD between the blowing snow and ANSI standards. This is to be expected. The beam energy stays focused for longer due to a combination of slightly smaller optical depth and the more strongly forward peaked phase function.

Again, the scattering of radiation out the side is below the MPE when plotted for $355\,nm$.
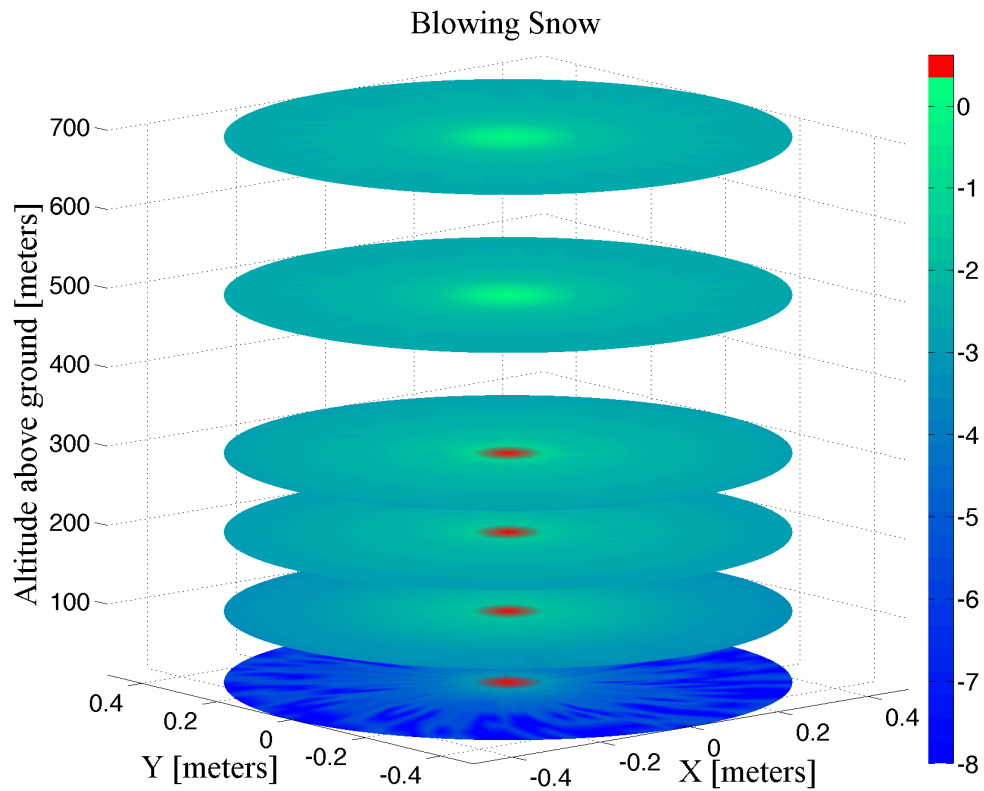
Figure 6.12: Snow-scattered energy density of all $355\ nm$ laser radiation at the top of the layer of interest for 6 different altitudes: $10\ m$, $100\ m$, $200\ m$, $300\ m$, $500\ m$, $700\ m$. The color bar is given in log base 10 of the energy density with units of mJ/cm^2.
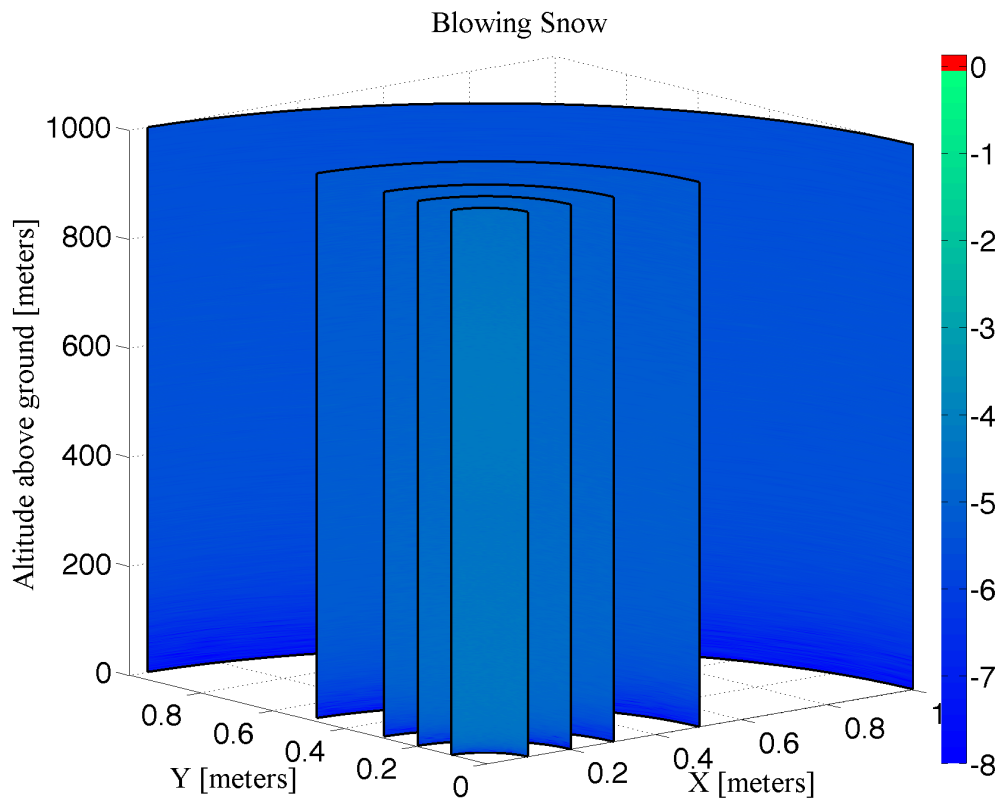
Figure 6.13: Snow-scattered energy density of all 355 nm laser radiation on the side of the layer of interest at the same ranges as Figure 6.7, 6.8, 6.10, and 6.11. The scattered energy at 355 nm is scaled relative to the MPE and shows no danger.

However, at $532\,nm$, the scattered radiation exceeds the MPE. This is shown in Figure 6.14.

Extending this work to other crystal habits is certainly possible. One simulation, which is interesting is the preferential orientation of ice crystals. This extension is interesting due to the specular reflections that characterize their scattering interaction (such as those shown in Figure 5.13) but is complicated due to the common assumption of random orientation in geometric optics and T-Matrix codes. To perform this simulation, the scattering regime would have to be represented but would be dependent on the angle of incidence of all scattered photons, which for multiply scattered photons would likely not be normal. As a result, the oriented ice crystal case is beyond the scope of this analysis.

6.3.4 Comparison of Monte Carlo and Standard ANSI Results

Considering the ANSI definitions of the NOHD and the NHZ, these standard distances are always overestimated. For example, the NOHD is defined in Equation 6.2 [170] in terms of the full divergence angle, ϕ, the beam energy Q, and the beam waist a. A simple rearrangement can help illuminate the underlying physical meaning of this equation, given in Equation 6.3. This equation is almost exactly the equation for the expansion of the circular beam area as it propagates in vacuum, assuming a small angle approximation for ϕ. The term $\phi NOHD$ represents the amount of growth of the beam assuming ϕ is sufficiently small such that $\tan \phi \approx \phi$.

$$NOHD = \frac{1}{\phi}\sqrt{\frac{4Q}{\pi MPE} - a^2} \tag{6.2}$$

$$\frac{\pi \left(\phi^2 NOHD^2 + a^2\right)}{4} = \frac{Q}{MPE} \tag{6.3}$$

The vacuum assumption is reasonable for short propagation distances but as the distance increases, the optical depth of the propagation medium grows. The probability of scattering increases with optical depth thus as propagation distance increases, so too does the probability that beam energy is scattered from the beam. Furthermore, the NOHD equation does not represent the
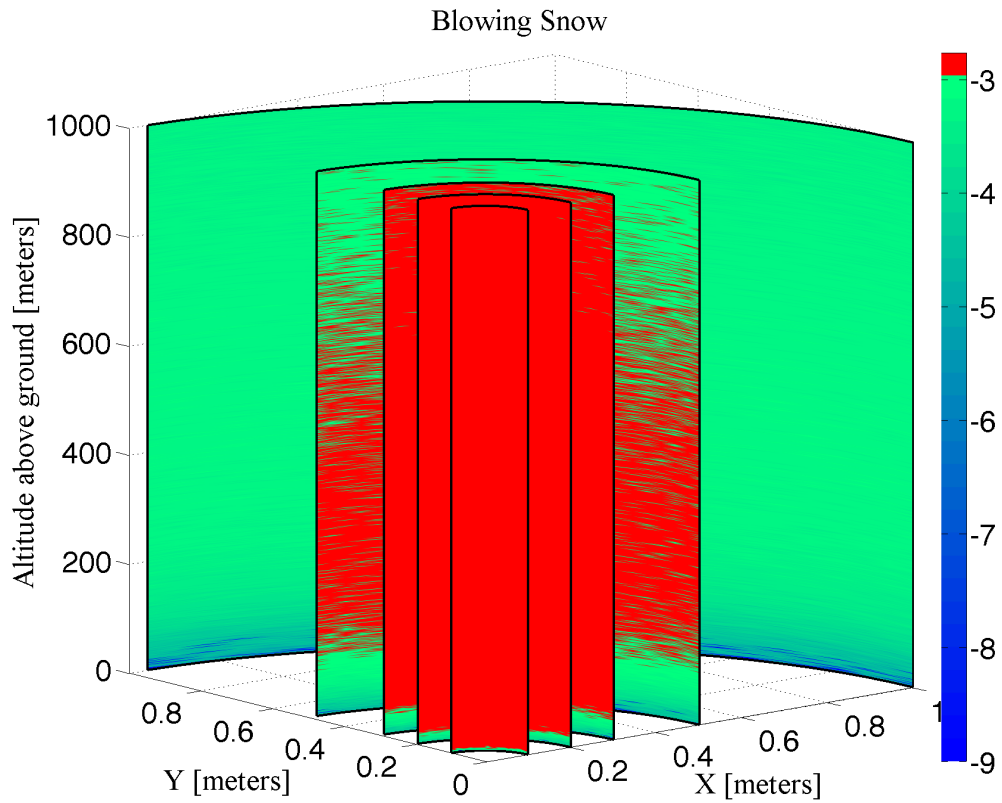
Figure 6.14: Snow-scattered energy density of all 532 nm laser radiation on the side of the layer of interest at the same ranges as Figure 6.7, 6.8, 6.10, 6.11, and 6.13. The scattered energy at $532\,nm$ is scaled relative to the MPE and shows much more danger than at $355\,nm$.

Table 6.5: The distances that a beam needs to travel through the medium of interest to show no more energy density in the forward direction which exceeds the MPE. These values are scaled to the MPE for 355 nm because the beam will become safe below airplane altitudes. The 532 nm beam shows little structure because its beam is always in excess of the MPE below aircraft altitudes. OHD stands for ocular hazard distance.

Case	OHD at 355 nm	NOHD Difference
ANSI NOHD	645 m	————
Blowing Snow	430 m	33.3%
Clear Air	626 m	2.95%
Liquid Fog	285 m	55.81%

physics of aerosol or cloud scattering. A summary of the propagation distances required for the beam energy density to fall below the MPE is given in Table 6.5.

The NHZ equation can still be used to define the safe radius about the beam but it too can be severely overestimated if the beam energy is attenuated. Here again, there is a problem that is poorly captured within the definition of the NHZ. A simple rearrangement of the definition of NHZ can also yield a form which is essentially an area equaling the laser energy divided by the MPE. This equation will always yield an overestimate of area as well, basically assuming energy is spread by a completely hard target Lambertian scatterer, an idealization which is not physical for atmospheric "soft target" scatterers. A summary of the calculated hazard zone radius to show when the energy density falls below the MPE is given in Table 6.6.

Table 6.6: The distance from the beam center that the Monte Carlo results show the energy density of at least one area is in excess of the MPE for 532 nm. This calculated distance is compared to the NHZ to determine how close a worker or plane could come to the beam without being exposed to a dangerous energy level. HZ stands for hazard zone.

Case	HZ at 532 nm	NHZ Difference
ANSI NHZ	345 cm	————
Blowing Snow	111 cm	67.8%
Clear Air	19 cm	94.5%
Liquid Fog	249 cm	27.8%

While over estimating the hazard will ensure that accidental access is not achieved, as laser systems become more mobile, powerful and capable, it is reasonable to question the scale to which

safety bounds are overestimated. For SuPR, the overestimate is calculable. For simple molecular scattering, the NOHD estimate is reasonable but for fog, the NOHD is overestimated by nearly a factor of 2.3 higher than observed in this simulation. For the NHZ, the fact that atmospheric scatterers, "soft targets", do not scatter all light and are not Lambertian yields a factor of approximately 18 difference between the NHZ calculated with the ANSI standards and those calculated assuming scattering.

The final point of emphasis to be considered is enhancements due to the definition of the region of interest. The results above assume that the region of interest bounds the scattering volume and when the photon leaves, its energy is imparted into that small section of space. This effectively assumes that each section on the exterior of the region of interest can encounter a person. If, however, this assumption is recast and it is assumed that only one person exists to interact with the beam, this assumption is unnecessarily restrictive. It is possible for a photon to leave the region of interest and then return and interact with a completely different region. As a result, enhancement in energy density can be observed. In this case, a photon only leaves the layer of interest out the top or bottom.

A simulation was written to accommodate this condition where the photon is allowed to propagate out the sides and return to the layer of interest. The stopping condition in this case is only when the photon leaves the top and bottom. Then enhancement of energy density of such a condition is considered. The enhancement for all of the cases presented was observed. For clear air, the maximum of the enhancement was less than a percent, 0.23% of the energy density, for liquid water it was 3.58% and for ice it was 3.73% all for a wavelength of 532 nm. This corresponds to an enhanced range of the hazard zone presented in Table 6.6 of 4 cm for clear air, 2 cm for liquid water, and 1 cm for blowing snow. As the enhancements for liquid water and blowing snow are spread over a greater surface area, it takes relatively more enhancement to cause changes in distance than does the smaller clear air hazard zone.

6.4   System Model and Ideal Performance

The final simulation developed based on the SVLE is shown to demonstrate the baseline performance of the SuPR system. A full range resolved version of the SVLE is modeled using scattering theory for Rayleigh and Raman scattering from Chapter 3. The wavelength dependent receiver and transmitter efficiencies are based on manufacturer measured or quoted specifications for the final optical design. The optical efficiency of each receiver element is given in Tables 6.7 and 6.8 where it is noted that numbers with 3 significant figures are manufacturer measured and numbers with 2 significant figures are estimates by the manufacturer but not measured. Atmospheric transmission is calculated based on total Rayleigh scattering from molecular nitrogen and oxygen scaled by pressure from ICECAPS radiosonde measurements and the MSIS model. The system overlap function is calculated from a ray tracing code developed by Matt Hayman for SuPR. The background is calculated from UV spectrometer measurements from Summit camp and using a wavelength of 355 nm.

Full simulation parameters are given in Appendix 8.6 and are not repeated here in the interest of brevity. Throughout the design process, it was found that an optical efficiency of approximately 25% was required for the water vapor channel given a 12 W laser and a 24 in telescope. This is achievable but required substantial accommodation in the optical design. For example, the maximum efficiency available for dichroic optics is in reflection meaning that all dichroic optics for SuPR are shortpass optics which are non-standard. Additionally, special UV optimization of the telescope coatings were required. These requirements, especially the shortpass nature of the dichroic optics are of concern based on their polarization properties.

Including all relevant manufacturer information about the components of the SuPR system, baseline counts can be modeled from the SVLE for each measurement channel. A set of modeled signals for 100 $shots$, 3.33 sec at 30 Hz, is given in Figure 6.15 and for 27,000 $shots$, 15 min at 30 Hz, in Figure 6.16 for Arctic wintertime conditions. These baseline signals clearly show the focus on the water vapor channel is warranted. The count number is between 0.5 and 3.5 orders of

Table 6.7: Path efficiencies as a function of wavelength. Note that channels given are for the center wavelengths: Water $= 407.45\,nm$, Nitrogen $= 386.69\,nm$, High J $= 353.3\,nm$, and Low J $= 354\,nm$. All wavelengths are given in air. Finally, optics at non-normal incidence have their S and P polarization efficiencies given separately.

Optic Name	Water Vapor	Nitrogen	High J	Low J
Telescope Primary	94.3%	94.5%	95.6%	95.6%
Telescope Secondary	94.3%	94.5%	95.6%	95.6%
Bench mirror				
Collimating lens	98.6%	98.3%	98.1%	98.1%
System mirror (P)	100.%	100.%	100.%	100.%
System mirror (S)	100.%	100.%	100.%	100.%
Short Pass filter	96.8 %	95.5 %	90.4%	91.2 %
Nitrogen dichroic	99.8% (R)	99.6% (R)	93.8% (T)	93.9% (T)
Raman Longpass	97.6%	97.0%	———	———
Raman Longpass	97.6%	97.0%	———	———
Water dichroic	99.5% (R)	95.8% (T)	———	———
90-10 BS (P)	———	———	91.5% (R)	91.6% (R)
90-10 BS (S)	———	———	90.0% (R)	90.4% (R)
50-50 BS	———	———	(R)	(T)
Steering mirror (P)	———	———	———	100.%
Steering mirror (S)	———	———	———	100.%
QWP	———	———	———	———
HWP	———	———	———	———
Polarizer	———	———	———	———
90-10 BS (P)	———	———	———	———
Polarizer	———	———	———	———
Filter	79.4%	80.9%	52.1%	47.9%
Focusing lens	98.6%	98.3%	98.1%	98.1%
PMT Quantum Efficiency	40%	40%	40%	40%
Total optical efficiency	25.1%	24.0%	7.10%	6.06%

magnitude smaller than the next smallest signal.

The results of this simulation indicate one counterintuitive conclusion, winter time conditions are harder to measure than summer time conditions. In the summer, background sunlight contributes to signal degradation, but in the winter low overall water vapor quantities contribute similarly. However, given excess signal in all other channels, receiver channels can be attenuated via receiver neutral density filters like CAPABL to improve summer time performance but no systematic or operational value of SuPR can compensate for water vapor abundance. Therefore, the driving condition is Arctic winter.
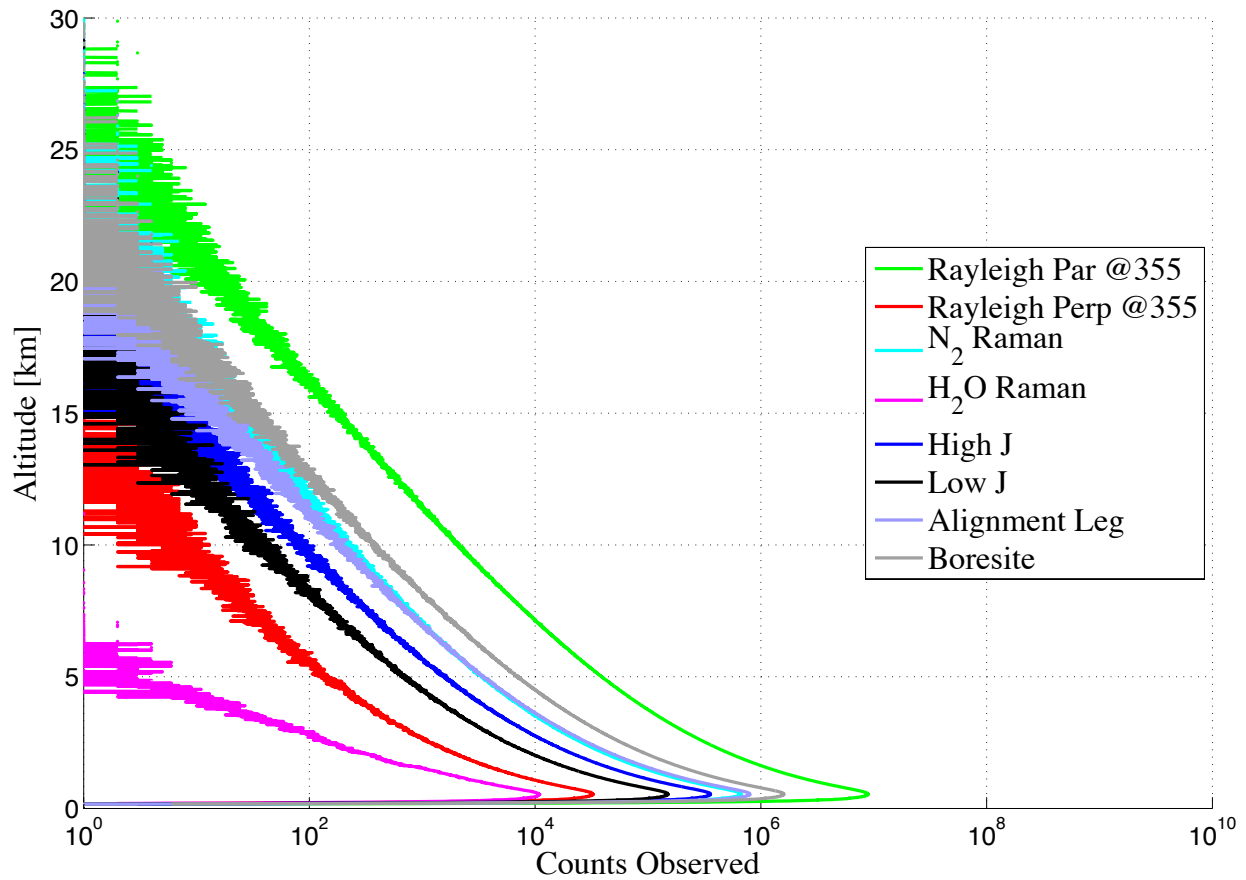
Figure 6.15: Photon counts modeled as a function of height for the count channels for SuPR. Background counts have been added and Poisson counting distribution has been imposed on the data. The integration time is 3.33 sec at 30 Hz using the Continuum 9030 laser and a 24 in telescope. The optical paths modeled follow from Tables 6.7 and 6.8. The background light level is low with a water vapor profile corresponding to winter.
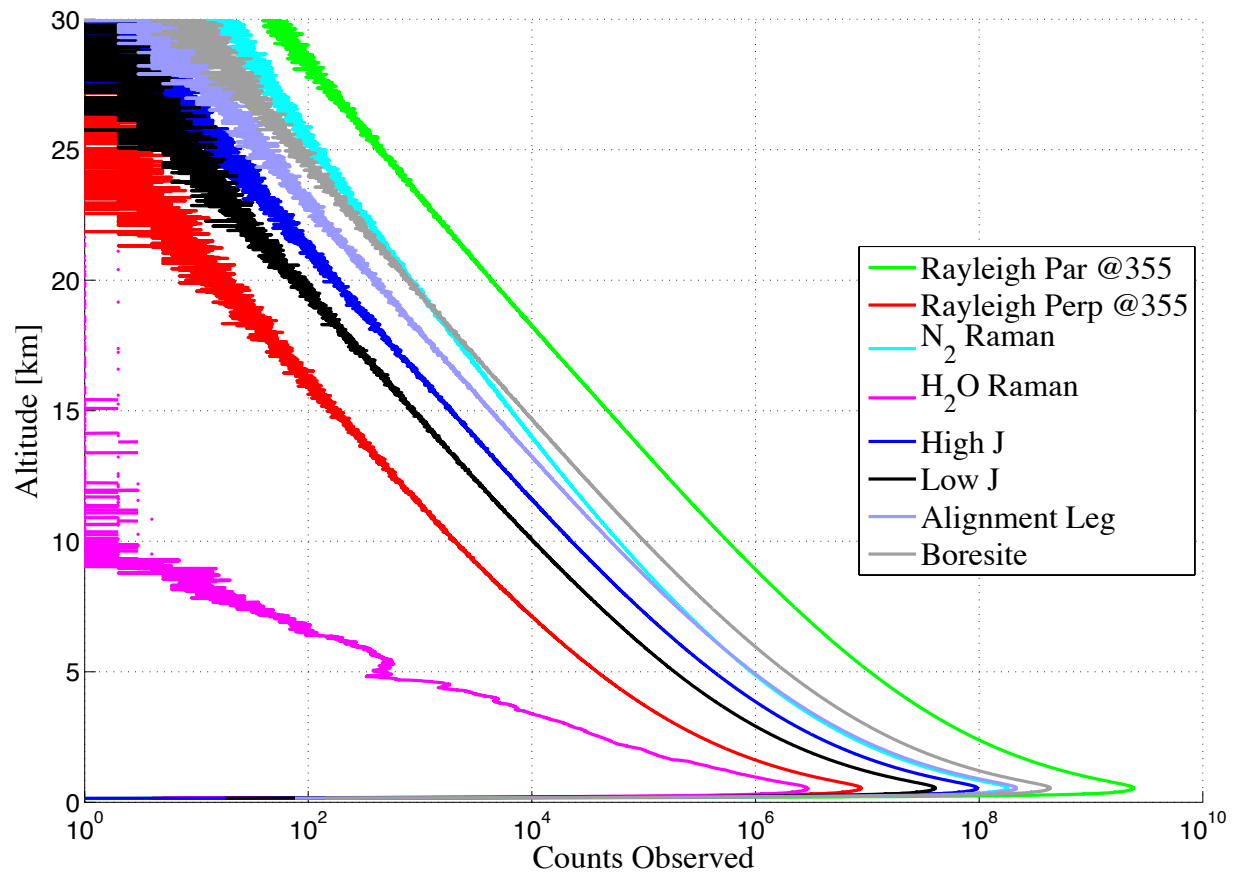
Figure 6.16: Photon counts modeled as a function of height for the count channels for SuPR. Background counts have been added and Poisson counting distribution has been imposed on the data. The integration time is 15 *min* at 30 *Hz* using the Continuum 9030 laser and a 24 *in* telescope. The optical paths modeled follow from Tables 6.7 and 6.8. The background light level is low with a water vapor profile corresponding to winter.

Table 6.8: Path efficiencies as a function of wavelength. Note that channels given are for the center wavelengths: Parallel/Perpendicular $= 354.71\,nm$. All wavelengths are given in air. Finally, optics at non-normal incidence have their S and P polarization efficiencies given separately.

Optic Name	Parallel	Perpendicular
Telescope Primary	95.5%	95.5%
Telescope Secondary	95.5%	95.5%
Bench mirror		
Collimating lens	98.1%	98.1%
System mirror (P)	100.%	100.%
System mirror (S)	100.%	100.%
Short Pass filter	90.8%	90.8%
Nitrogen dichroic	94.2% (T)	94.2% (T)
Raman Longpass	———	———
Raman Longpass	———	———
Water dichroic	———	———
90-10 BS (P)	8.34% (T)	8.34% (T)
90-10 BS (S)	9.41% (T)	9.41% (T)
50-50 BS	———	———
Steering mirror (P)	———	———
Steering mirror (S)	———	———
QWP		
HWP		
Polarizer	99% (R)	90% (T)
90-10 BS (P)	91.7% (R)	———
Polarizer	———	90%
Filter	74.8%	74.8%
Focusing lens	98.1%	98.1%
PMT Quantum Efficiency	40%	40%
Total optical efficiency	1.53%	1.54%

Using the baseline signals, retrievals of polarization parameters as well as Raman ratios of water vapor mixing ratio and temperature can be calculated. Retrievals for 100 $shots$, 3.33 sec at 30 Hz, is given in Figure 6.17 and for 27,000 $shots$, 15 min at 30 Hz, in Figure 6.18. These retrievals are given for water vapor mixing ratio derived from the lidar equation in Appendix 8.3.5, for temperature derived from the lidar equation in Appendix 8.3.6, and depolarization derived from the SVLE in Appendix 8.3.7. The percent error of the measured value is calculated by knowing the input value used to originally simulate the photon counts. This allows for direct analysis of the requirements specified in Table 6.1. It can be seen that only through extensive integration can

upper tropospheric moisture be measured to within the required value but that short integration times on the order of seconds can be used to define lower tropospheric water vapor concentration. Temperature is similarly so where only the troposphere can be accurately measured on the time scales of seconds and that the lower stratosphere requires longer integration. The single shot dynamic range required to make the measurements of interest is about 5-6 orders of magnitude, which is on the edge of possible for the Licel counting system specified for SuPR.

6.5   First Observations and Verification

SuPR has been under construction for approximately the last 9 months. The enclosure was delivered in May 2016, but delays were experienced related to water leaks and enclosure temperature control. First observations were taken with SuPR in the atmosphere on March 13th using its alignment leg. Using only 0.5 W of the available 12 W of transmit power and attenuating the receiver signals of the alignment leg by 3 orders of magnitude to match the optical efficiency of the whole receiver system, signals were measured off of the night sky to approximately 13 km. The system specifications used that morning were modeled by the simulation created for SuPR and compared favorably. The SuPR simulation suggested that in clear air, signal should be observed to approximately 15 km, but a layer of cirrus was clearly visible in the measurements making direct comparison impossible.

First vibrational Raman data was observed on March 22nd, 2017. Rough alignment of the elastic polarization channels and the vibrational Raman channels is demonstrated for a 6 hour time period on the night of March 29th, 2017 in Figure 6.19. These measurements are taken with all necessary optics placed for the described 4 channels with an additional neutral density filter (ND = 1) in the elastic channels. The night of the 29th was chosen due to the relatively clear air that was helpful to align the system overlap functions of the 4 channels. Data was taken at 7.5 m and 5 sec resolution for a 6 hr period and post processed to 30 m and 30 sec resolution. While the night was chosen for its stable and simple elastic signals, the water vapor field is constantly changing throughout the 6 hr test.
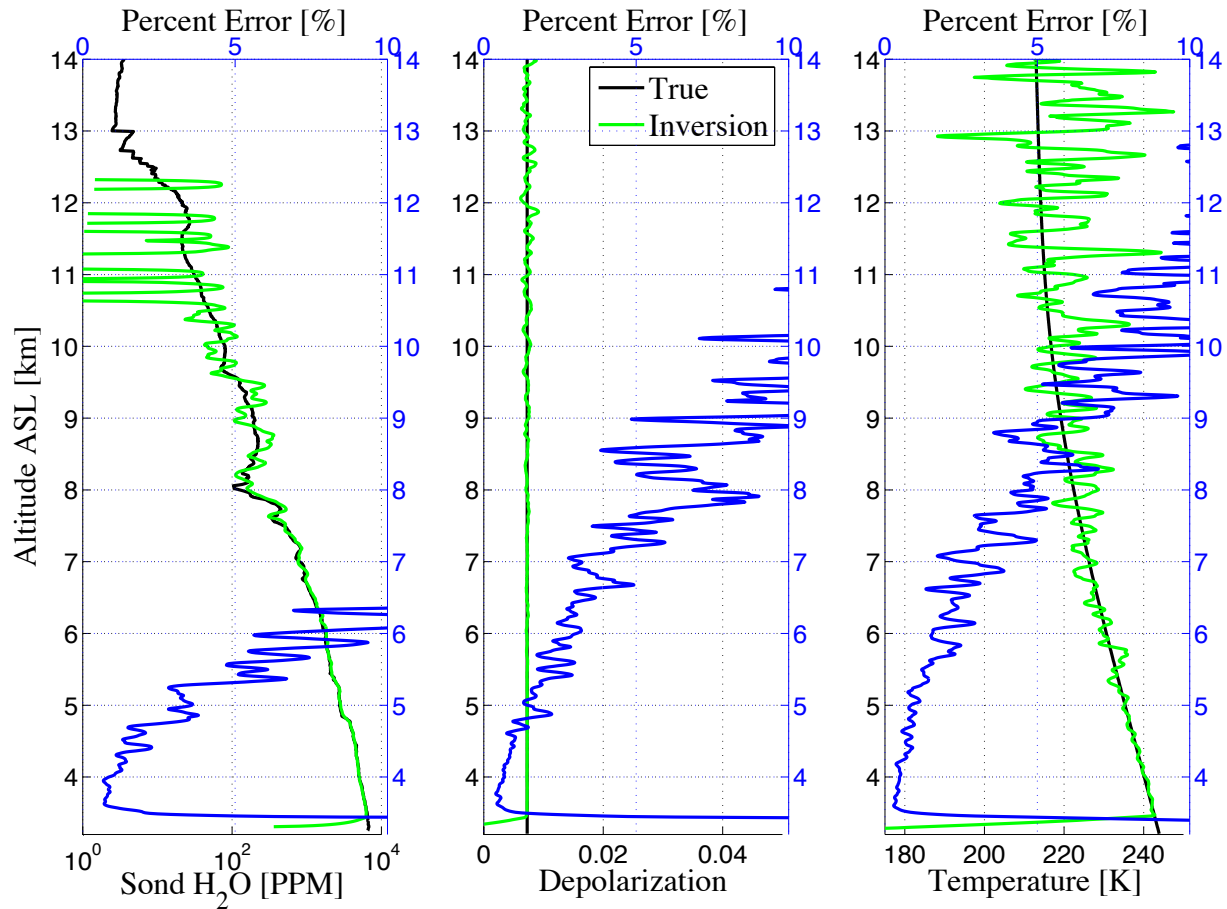
Figure 6.17: Retrieved values for three simulation input variables with low solar background. Water vapor concentration in parts per million are calculated as given in Appendix 8.3.5. Temperature inversions are calculated as in Appendix 8.3.6. Depolarization is calculated using the orthogonal data retrievals given explicitly in Appendix 8.3.7. The integration time is 3.33 *sec* with 30 *Hz* rep rate. The percent error is calculated assuming the input simulation value is truth.
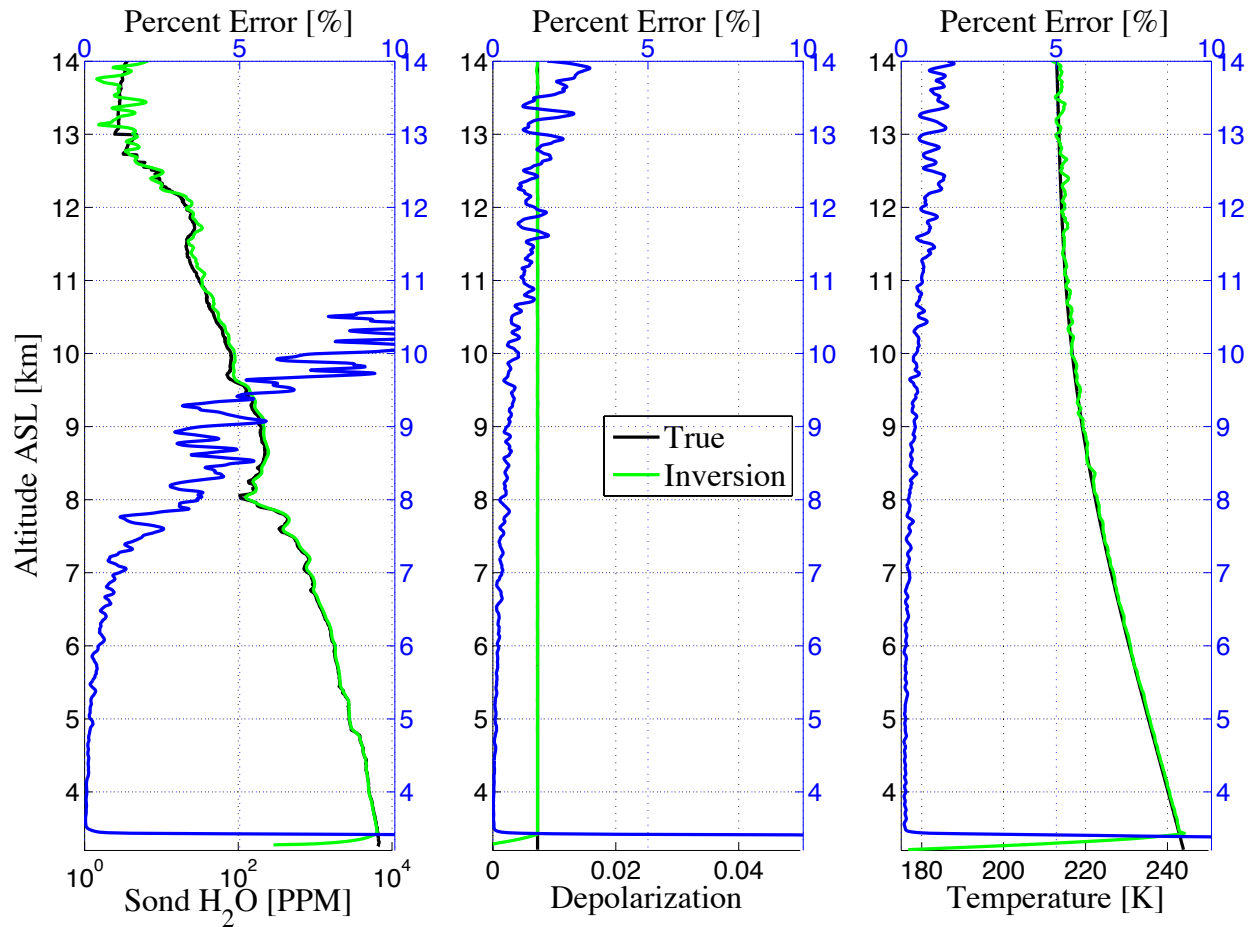
Figure 6.18: Retrieved values for three simulation input variables with low solar background. Water vapor concentration in parts per million are calculated as given in Appendix 8.3.5. Temperature inversions are calculated as in Appendix 8.3.6. Depolarization is calculated using the orthogonal data retrievals given explicitly in Appendix 8.3.7. The integration time is 15 min with 30 Hz rep rate. The percent error is calculated assuming the input simulation value is truth.

Total backscatter is calculated by adding the uncalibrated parallel and perpendicular channels together. Uncalibrated depolarization ratio is calculated by taking the ratio of parallel to perpendicular signals. Note here that uncalibrated refers to retardance calibrations in the transmitter and receiver that are not aligned for this test. Backscattering ratio is calculated as the ratio of total backscatter to the nitrogen signal. This ratio is calibrated for differential transmission of the nitrogen and elastic scattered signals but not for the differential overlap of the signals in the low altitude bins. Relative water vapor mixing ratio is likewise calculated as the ratio of the water vapor signal divided by the nitrogen signal. Again, differential transmission is calculated but absolute calibration is not performed as no nearby in-situ measurement of water vapor is available.

Comparison of the measured signals to the model developed based on the SVLE are useful to understand basic system performance. Data is integrated to 15 min resolution during the clear air period at 23 local time, background subtracted, and compared directly to the simulated results in Figure 6.20. The model indicates that the SuPR system performance can be ideally enhanced by approximately an order of magnitude for all data channels. Additionally, the model indicates that background light is a major problem to be solved. This is a known problem as the receiver is not fully light tight and can be improved. Finally, calibration for Signal Induced Noise (SIN) appears to be required. The shape of the profiles, especially for the parallel profile, changes slope at approximately 10 km. As a baseline measurement, the data from the 29th indicates that there is certainly major efficiency advances that can be made. However, as signal optimization is not yet done, provides a good benchmark from which to meet the stated requirements.

These observations show several enhancements over the CAPABL measurement capabilities. The increased power aperture product of the system increases the signal range of elastic signals such that error bounds on the order of the required 2% are observable throughout the column. Additionally, the decreased field of view of the receiver reduces the overall observation of multiple scattering signal that is shown to affect on the order of 5% of CAPABL voxels. The backscattering ratio does not require a Klett inversion, but rather directly samples the molecular backscattering. This for SuPR is critical especially as the Klett inversion for CAPABL is shown to miss the tops
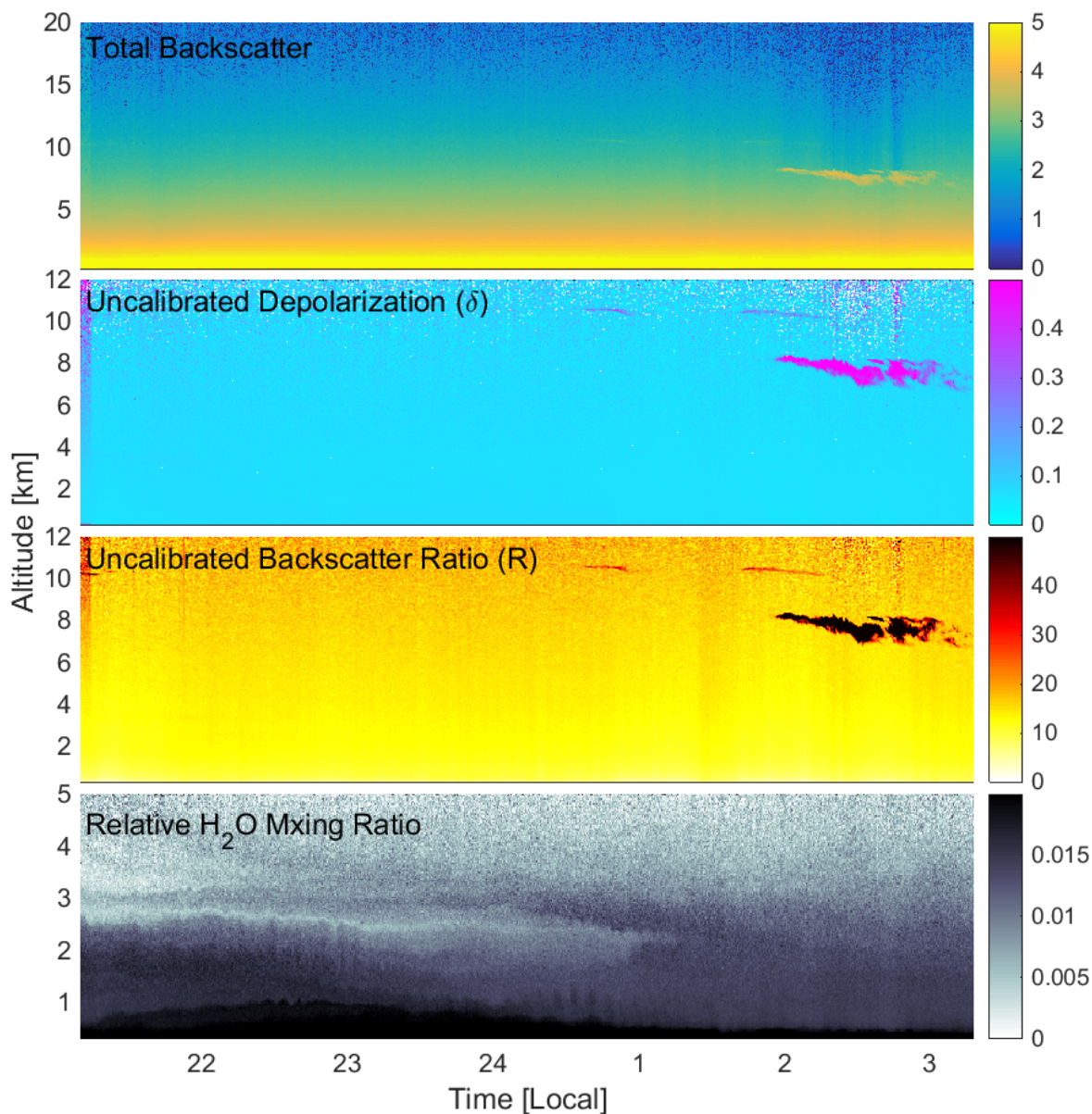
Figure 6.19: First measurements of elastic and vibrational Raman signals from SuPR taken during a mostly clear night on March 29/30, 2017. Total backscattering is simply the addition of signal from both polarization channels. Depolarization is calculated as $\delta = N_\perp / N_\parallel$ but is labeled as uncalibrated as the transmitter and receiver retardance is not canceled by placement of wave plates in the transmitter and receiver. Uncalibrated backscatter is calculated similarly to the water vapor mixing ratio but with nitrogen and total backscatter. It is uncalibrated as differential overlap is not yet characterized. Relative H_2O is not yet absolutely calibrated via radiosonde as is planned operationally leaving the calibration constant unity.
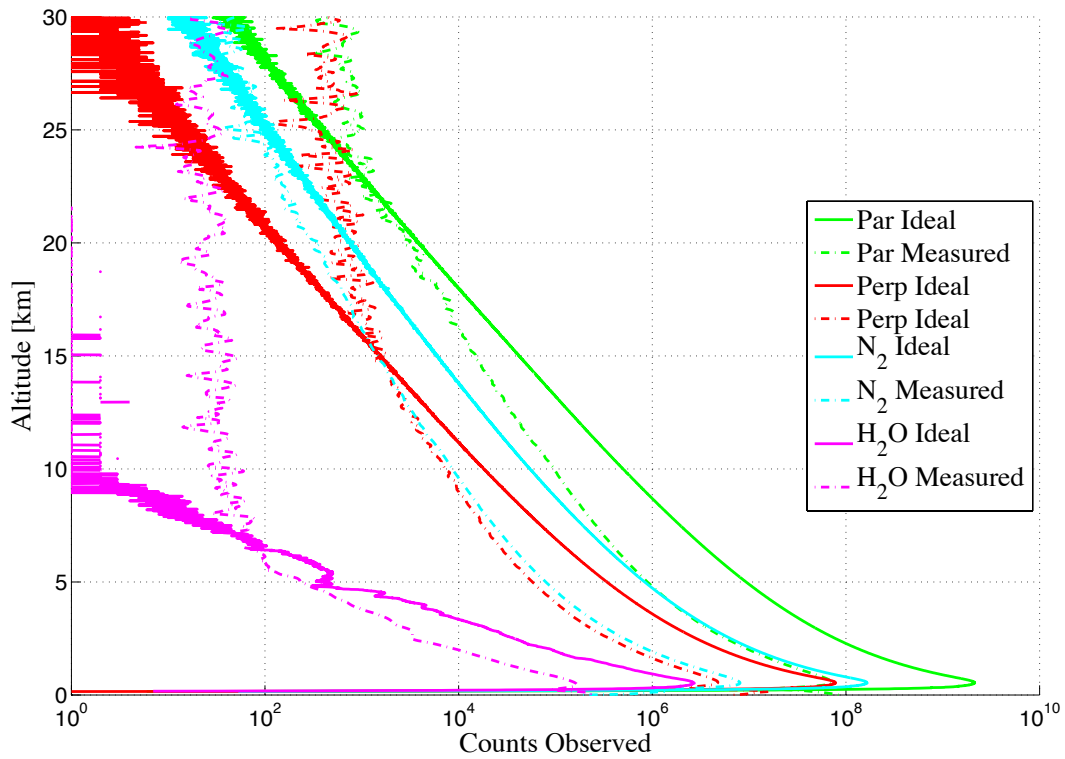
Figure 6.20: A comparison of the ideal SuPR photon counts with those observed on March 29th, 2017. The model indicates approximately an order of magnitude better signal intensity across all measurement channels. Additionally, the background light levels in the measured counts far exceed the modeled. Finally, the measured counts seem to suffer dramatically from signal induced noise.

of clouds due to the inaccuracy of initial guess values when integrating. Finally, with SuPR, all 3 phases of water can be observed simultaneously. For the Arctic, this provides a critical link for specifying atmospheric moisture and aerosol state for CRE calculations, allows for study of the links between relative humidity and cloud formation, and allows for the separation of diamond dust and aerosols contributions to lidar signals.

More work is needed to fully characterize the SuPR system's ability to measure water. Work to be completed in the summer of 2017 includes water vapor calibration with co-located radiosonde, calibration of receiver and transmitter retardance effects, inclusion of data housekeeping measures like active steering and laser power meter, and first observations with rotational Raman measurements. The provided measurements are a first attempt to classify SuPR's observational capabilities and verify the requirements specified during its design.

6.6   Meeting the Requirements of the SuPR System

To complete the systems engineering analysis of the SuPR system, verification of requirements should be performed. The requirements highlighted in Table 6.1 are worth noting for this thesis work. The first requirements to examine are the requirements related to the observation of water vapor. The range of observation was highlighted as a major area of concern especially for night time operations. Initial signal results indicate optimization is required to meet this requirement. Specifically, the author suggests that major gains can be made by optimizing receiver alignment and tilt tuning the water vapor filter. This filter is on a precision tuning mount and has been observed to cause signal changes by more than an order of magnitude by adjusting the mount by approximately 5°. The precision requirement is possible to meet based on simulation results only through further noise reduction of the system. As almost no attempt has been made to make the SuPR receiver light tight, this will be possible.

The temperature bound requirements are not yet analyzed. Observations of water in its 3 phases are the main focus of this thesis, so the polarization and water vapor Raman channels were attempted first. Based on the signal strength of the nitrogen Raman channels, the range

requirements are expected to be reasonably met.

The polarization requirements identified for SuPR are a stringent test of system design. The limiting factor of the polarization purity are the optics in the receiver. The manufacturers of the optics have measured and certified the relevant optics to have met their design criteria. As such, the practical limit of the SuPR system is the polarization purity of the lasers which is specified and certified at 100:1. This is in excess of the required 2% depolarization ratio, which requires purity on the order of 50:1.

6.7   Relevance to Posed Thesis Questions

The design and analysis of SuPR directly addresses all 2 of the 3 thesis questions posed. A bulleted summarizing list of relevant findings is given for each question.

(2) What unique signatures about Arctic cloud microphysical properties can be revealed using polarimetric and Raman lidar?

    (a) Unlike CAPABL, SuPR is able to profile water vapor through the troposphere. Incorporating Raman scattering into the results of CAPABL would allow for full characterization of the state of water in the polar regions, adding water vapor as the final piece to an all-in-one water observing system, with a keen awareness of systematic biases caused by system and measurement effects.

    (b) Unlike CAPABL, SuPR has the ability to directly measure molecular scattering which makes estimates of the scattering ratio more physically reasonable. Combined with the classification scheme of CAPABL, a study about the effect of aerosol abundance on cloud formation and phase would be possible with SuPR.

    (c) Combined with CAPABL, SuPR would clarify many of the findings about the temperature and relative humidity of HOIC particles reported by Cole et al. [127].

(3) How do we meet the needs of the next generation cloud and atmospheric state observations in the Arctic using lidar?

(a) The design analysis of SuPR has elucidated the design issues with deploying and quantitatively described the specifications of a Raman lidar to a remote and dry location such as the Arctic.

(b) A new Monte Carlo method for the analysis of atmospheric scattering was created for the analysis of SuPR. It highlights that the area of concern for laser safety is inextricably linked to scattering properties of the medium and quantitatively assesses the link for common atmospheric conditions.

(c) The ongoing construction of SuPR initiated for this thesis is the first tangible step to an autonomously deployable 3-phase water observing lidar system for the Greenland Ice Sheet.

Chapter 7

Concluding Remarks and The Path Forward

The hypothesis that this thesis examines is: ground-based, active optical remote sensing measurements can contribute to the knowledge of atmospheric state and cloud properties by providing unmatched data resolution and quality to help identify and elucidate key cloud microphysical and cloud state properties. To address this hypothesis, 3 specific questions were developed and posed:

(1) How to accurately identify and distinguish liquid and ice water in Arctic clouds using polarimetric lidar?

(2) What unique signatures about Arctic cloud microphysical properties can be revealed using polarimetric and Raman lidar?

(3) How do we meet the needs of the next generation cloud and atmospheric state observations in the Arctic using lidar?

The specific answers to these questions are collected and restated here. The main results from each system is summarized with an emphasis both on how it answers the thesis question and any new questions it raises that is the topic for further work for future students.

7.1   Observing Liquid and Ice Water in the Arctic

The deviation of polarization properties of non-spherical scatterers from Mie theory has been used since 1971 as the basis to distinguish the phase of hydrometeors. However, many systems have in that time suffered from confounding effects, both systematic and geophysical, that manifest

as non-zero depolarization. This thesis has theoretically described and demonstrated how system observable dynamic range affects hydrometeor retrievals especially in the Arctic where clouds occur primarily low in the atmosphere. This thesis has demonstrated that fractional occurrence of cloud phase type can be affected by as much as 30% due to lidar system effects coupled with cloud macrophysical properties, primarily base height and optical depth. Furthermore, this work introduces and validates a novel method for classifying raw data and combining raw data types into a single best estimate lidar hydrometeor phase identification product. This validated best estimate product deviates substantially from co-located observations collected by a micro-pulse lidar indicating sensitivity enhancements on the order of at least an order of magnitude, especially in the Arctic summer, but is shown to be consistent with ancillary instrumentation from scales of minutes to months.

Of particular importance is the acknowledgement that ice can exist with low depolarization when viewed in a zenith or nadiar direction if the ice is preferentially oriented. This work has built upon the theoretical work of Hayman and Thayer [98] and first demonstration of Neely et al. [89] to remove the confounding effects of orientation by adding a more descriptive polarization retrieval framework that can identify HOIC. Generalizations to the retrieval theory used by Neely et al. are derived for this thesis that enhances overall data availability in the region of scientific interest at Summit (0 km to 8 km) by 28%. This has resulted in the longest record of HOIC known to the author. This data set is ongoing with autonomous data streaming from raw signal measurements by CAPABL to basic polarization retrievals, and automated data voxel identifications and calculation of a best guess merged polarization product.

7.2   Unique Signatures of Cloud Microphysical Properties in the Arctic

Leveraging the automated retrievals of the CAPABL system and co-located ICECAPS sensor suite, several signatures of cloud microphysical properties at Summit are identified by this work. First, the nature of HOIC is identified for the first time. Specifically, the noise-like character of the occurrences highlighted by the automatic algorithm identifies many occurrences of HOIC that are

easily missed by manual data processing. Furthermore, the identification of HOIC in stratiform and precipitating ice are new findings especially within the context of previous HOIC measurements that suggested they exist primarily in cirrus clouds. In contrast to the case by case analysis of the original CAPABL processing, only with the work presented in this thesis is a climatology of HOIC possible to characterize, as first attempted by Cole et al. (on which the author is a co-author) [127].

The radiative impacts of ice and liquid in the Arctic have been published by many. However, this thesis work enables and reports the first estimates of CRE from HOIC and their differences from ROIC. The first estimates of longwave and shortwave CRE are contributed by identifying that, though HOIC are a minor sub-population of cloud crystals (approximately 1-3% at Summit), they contribute disproportionately to the downwelling longwave warming at the surface (enhancing the CRE by approximately 1.7 W/m^2 in the longwave) and downwelling shortwave cooling at the surface (enhancing the CRE by as much as 41 W/m^2 in the shortwave depending on the allowable solar zenith angle) . This work has enabled, for the first time, a full characterization of ice particle orientation on the surface radiation budget.

7.3   Meeting the Needs of the Next Generation Arctic Lidar System

The design and construction of the SuPR lidar for autonomous observation of the Arctic is one of a few designs in the world for automated Raman retrievals. This system, when operational will be the 6th such system in the world and 2nd for the Arctic [174], including the ARM program lidars at Okiktok Point, Oklahoma, the Azores, and two further lidars at Payerne, Switzerland, and Lindernerg, Germany. In contrast to the ARM lidar at Okiktok Point, SuPR was designed from the ground up to observe the Arctic. The design process, which leverages more that 6 years of observations from CAPABL, has highlighted several critical design features such as polarization purity and water vapor signal strength that are critical to enable full Arctic observing capability.

One major contribution to the ability to design such Arctic observing lidar systems is an analysis method for atmospheric effects on laser safety. The ANSI standards are often invoked but the deficiencies of the atmospheric description are described. Specifically the ANSI standards in-

correctly specify the major atmospheric contribution as absorption where the new method accounts for absorption and scattering. A new Monte Carlo analysis method is developed and analyzed in depth [134].

7.4   Studies Identified and Future Research Projects

In the process of completing this thesis and answering the hypothesis statement, new questions have arisen. Much of the data and analysis methods open questions that could not be previously addressed, especially those related to the nature of HOIC in the Arctic. In particular, a short list of topics that have come to light based on the results of this work are given below. Some questions raised by the CAPABL data set are:

(1) Can orthogonal and non-orthogonal polarization retrievals be further enhanced via optimal estimation to limit error to further expand lidar valid observations?

(2) What fraction of HOIC are missed via diattenuation measurements and what is the ideal diattenuation limit?

(3) Are there seasonal or diurnal changes in the occurrence frequency or properties of HOIC such as relative humidity and temperature?

(4) What are the total cloud radiative effects of HOIC on the surface and at the top of the atmosphere?

Some questions raised by the availability of SuPR are:

(1) What is the radiative effect in the Arctic of upper tropospheric and stratospheric aerosols?

(2) What is the dependence of ice crystal orientation on temperature and water vapor mixing ratio, and is it different than that first observed by Cole et al. using low resolution thermodynamic measurements?

(3) How are atmospheric thermodynamic variable affected by the synoptic conditions and topography of the Greenland Ice Sheet?

Bibliography

[1] C. Ahrens, <u>Essentials of Meteorology An Introduction to The Atmosphere</u>. Carnage Learning, 7 ed., 2015.

[2] A. M. Society, "Glossary of meteorology," September 2015.

[3] T. Schneider, P. A. O'Gorman, and X. J. Levine, "Water vapor and the dynamics of climate changes," <u>Reviews of Geophysics</u>, vol. 48, no. 3, 2010. RG3001.

[4] R. M. Rauber, J. E. Walsh, and D. Charlevoix, <u>Severe and Hazardous Weather An Introduction to High Impact Meteorology</u>. Kendal Hunt Publishing Company, 4 ed., 2012.

[5] S. C. Sherwood, R. Roca, T. M. Weckwerth, and N. G. Andronova, "Tropospheric water vapor, convection, and climate," <u>Reviews of Geophysics</u>, vol. 48, no. 2, pp. n/a–n/a, 2010. RG2001.

[6] N. Kaempfer, ed., <u>Monitoring Atmospheric Water Vapour</u>. No. 10 in ISSI Scientific Report Series, Springer, 2012.

[7] S. Bony, B. Stevens, D. M. W. Frierson, C. Jakob, M. Kageyama, R. Pincus, T. G. Shepherd, S. C. Sherwood, A. P. Siebesma, A. H. Sobel, M. Watanabe, and M. J. Webb, "Clouds, circulation and climate sensitivity," <u>Nature Geosci</u>, vol. 8, pp. 261–268, 04 2015.

[8] T. M. Weckwerth, D. B. Parsons, S. E. Koch, J. A. Moore, M. A. LeMone, B. B. Demoz, C. Flamant, B. Geerts, J. Wang, and W. F. Feltz, "An overview of the international h2o project (ihop_2002) and some preliminary highlights," <u>Bulletin of the American Meteorological Society</u>, vol. 85, no. 2, pp. 253–277, 2004.

[9] I. Tan, T. Storelvmo, and M. D. Zelinka, "Observational constraints on mixed-phase clouds imply higher climate sensitivity," <u>Science</u>, vol. 352, no. 6282, pp. 224–227, 2016.

[10] S. C. Sherwood, S. Bony, and J.-L. Dufresne, "Spread in model climate sensitivity traced to atmospheric convective mixing," <u>Nature</u>, vol. 505, pp. 37–42, 01 2014.

[11] B. Stevens and S. Bony, "Water in the atmosphere," <u>Physics Today</u>, pp. 29–34, 2013.

[12] G. L. Stephens, J. Li, M. Wild, C. A. Clayson, N. Loeb, S. Kato, T. L'Ecuyer, P. W. Stackhouse, M. Lebsock, and T. Andrews, "An update on earth's energy balance in light of the latest global observations," <u>Nature Geoscience</u>, vol. 5, pp. 691–696, 10 2012.

[13] M. R. Allen and W. J. Ingram, "Constraints on future changes in climate and the hydrologic cycle," Nature, vol. 419, pp. 224–232, 09 2002.

[14] J. Hansen, M. Sato, and R. Ruedy, "Radiative forcing and climate response," Journal of Geophysical Research: Atmospheres, vol. 102, no. D6, pp. 6831–6864, 1997.

[15] J. Hansen, M. Sato, P. Kharecha, and K. von Schuckmann, "Earth's energy imbalance and implications," Atmospheric Chemistry and Physics, vol. 11, no. 24, pp. 13421–13449, 2011.

[16] K. E. Trenberth, J. T. Fasullo, and J. Kiehl, "Earth's global energy budget," Bulletin of the American Meteorological Society, vol. 90, pp. 311–323, 2014/02/24 2009.

[17] K. E. Trenberth and J. T. Fasullo, "Tracking earth's energy," Science, vol. 328, no. 5976, pp. 316–317, 2010.

[18] R. Bennartz, M. D. Shupe, D. D. Turner, V. P. Walden, K. Steffen, C. J. Cox, M. S. Kulie, N. B. Miller, and C. Pettersen, "July 2012 greenland melt extent enhanced by low-level liquid clouds," Nature, vol. 496, pp. 83–86, 04 2013.

[19] B. Schrader, ed., Infrared and Raman Spectroscopy Methods and Applications. VCH Verlagsgesellschaft mbH, 1995.

[20] W. Demtroeder, Molecular Physics Theoretical Principles and Experimental Methods. WILEY-VCH Verlag GmbH and Co. KGaA, 2005.

[21] S. Solomon, Climate Change 2007 The Physical Science Basis. Cambridge University Press, 2007.

[22] T. Stocker, D. Qin, G.-K. Plattner, M. Tignor, S. Allen, J. Boschung, A. Nauels, Y. Xia, V. Bex, and P. Midgley, eds., IPCC, 2013: Climate Change 2013: The Physical Science Basis. Contribution of Working Group I to the Fifth Assessment Report of the Intergovernmental Panel on Climate Change. Cambridge University Press, Cambridge, United Kingdom and New York, NY, USA, 2013.

[23] J. M. Gregory, P. Huybrechts, and S. C. B. Raper, "Climatology: Threatened loss of the greenland ice-sheet," Nature, vol. 428, pp. 616–616, 04 2004.

[24] K. K. Kjeldsen, N. J. Korsgaard, A. A. Bjørk, S. A. Khan, J. E. Box, S. Funder, N. K. Larsen, J. L. Bamber, W. Colgan, M. van den Broeke, M.-L. Siggaard-Andersen, C. Nuth, A. Schomacker, C. S. Andresen, E. Willerslev, and K. H. Kjær, "Spatial and temporal distribution of mass loss from the greenland ice sheet since ad 1900," Nature, vol. 528, no. 7582, pp. 396–400, 2015.

[25] M. B. Lythe and D. G. Vaughan, "Bedmap: A new ice thickness and subglacial topographic model of antarctica," Journal of Geophysical Research: Solid Earth, vol. 106, no. B6, pp. 11335–11351, 2001.

[26] J. T. Overpeck, M. Sturm, J. A. Francis, D. K. Perovich, M. C. Serreze, R. Benner, E. C. Carmack, F. S. Chapin, S. C. Gerlach, L. C. Hamilton, L. D. Hinzman, M. Holland, H. P. Huntington, J. R. Key, A. H. Lloyd, G. M. McDonald, J. McFadden, D. Noone, T. D. Prowse, P. Schlosser, and C. Vörösmarty, "Arctic system on trajectory to new, seasonally ice-free state," Eos, Transactions American Geophysical Union, vol. 86, no. 34, pp. 309–313, 2005.

[27] J. A. Francis and E. Hunter, "New insight into the disappearing arctic sea ice," Eos, Transactions American Geophysical Union, vol. 87, no. 46, pp. 509–511, 2006.

[28] D. K. Perovich, J. A. Richter-Menge, K. F. Jones, and B. Light, "Sunlight, water, and ice: Extreme arctic sea ice melt during the summer of 2007," Geophysical Research Letters, vol. 35, no. 11, 2008. L11501.

[29] W. Maslowski, J. C. Kinney, M. Higgins, and A. Roberts, "The future of arctic sea ice," Annual Review of Earth and Planetary Sciences, vol. 40, no. 1, pp. 625–654, 2012.

[30] D. Notz, "How well must climate models agree with observations?," Philosophical Transactions of the Royal Society of London A: Mathematical, Physical and Engineering Sciences, vol. 373, no. 2052, 2015.

[31] K. R. Arrigo and G. L. van Dijken, "Continued increases in arctic ocean primary production," Progress in Oceanography, vol. 136, pp. 60–70, 8 2015.

[32] D. Lamb and J. Verlinde, Physics and Chemistry of Clouds. Cambridge University Press, 2011.

[33] J. A. Curry, J. L. Schramm, W. B. Rossow, and D. Randall, "Overview of arctic cloud and radiation characteristics," Journal of Climate, vol. 9, pp. 1731–1764, 2015/11/02 1996.

[34] M. D. Shupe and J. M. Intrieri, "Cloud radiative forcing of the arctic surface: The influence of cloud properties, surface albedo, and solar zenith angle," Journal of Climate, vol. 17, pp. 616–628, 2015/09/28 2004.

[35] M. D. Shupe, D. D. Turner, V. P. Walden, R. Bennartz, M. P. Cadeddu, B. B. Castellani, C. J. Cox, D. R. Hudak, M. S. Kulie, N. B. Miller, R. R. Neely, W. D. Neff, and P. M. Rowe, "High and dry: New observations of tropospheric and cloud properties above the greenland ice sheet," Bulletin of the American Meteorological Society, vol. 94, no. 2, pp. 169–186, 2013.

[36] F. Pithan, B. Medeiros, and T. Mauritsen, "Mixed-phase clouds cause climate model biases in arctic wintertime temperature inversions," Climate Dynamics, vol. 43, no. 1, pp. 289–303, 2014.

[37] J. E. Kay, L. Bourdages, N. B. Miller, A. Morrison, V. Yettella, H. Chepfer, and B. Eaton, "Evaluating and improving cloud phase in the community atmosphere model version 5 using spaceborne lidar observations," Journal of Geophysical Research: Atmospheres, vol. 121, no. 8, pp. 4162–4176, 2016. 2015JD024699.

[38] K. Van Tricht, S. Lhermitte, J. T. M. Lenaerts, I. V. Gorodetskaya, T. S. L'Ecuyer, B. Noel, M. R. van den Broeke, D. D. Turner, and N. P. M. van Lipzig, "Clouds enhance greenland ice sheet meltwater runoff," Nat Commun, vol. 7, 01 2016.

[39] M. Tedesco, T. Mote, X. Fettweis, E. Hanna, J. Jeyaratnam, J. F. Booth, R. Datta, and K. Briggs, "Arctic cut-off high drives the poleward shift of a new greenland melting record," Nat Commun, vol. 7, 06 2016.

[40] M. D. Shupe, "A ground-based multisensor cloud phase classifier," Geophysical Research Letters, vol. 34, no. 22, pp. n/a–n/a, 2007. L22809.

[41] M. D. Shupe, S. Y. Matrosov, and T. Uttal, "Arctic mixed-phase cloud properties derived from surface-based sensors at sheba," Journal of the Atmospheric Sciences, vol. 63, pp. 697–711, 2016/02/15 2006.

[42] J. Verlinde, B. D. Zak, M. D. Shupe, M. D. Ivey, and K. Stamnes, "The arm north slope of alaska (nsa) sites," Meteorological Monographs, vol. 57, pp. 8.1–8.13, 2016.

[43] E. A. G. Schuur, A. D. McGuire, C. Schadel, G. Grosse, J. W. Harden, D. J. Hayes, G. Hugelius, C. D. Koven, P. Kuhry, D. M. Lawrence, S. M. Natali, D. Olefeldt, V. E. Romanovsky, K. Schaefer, M. R. Turetsky, C. C. Treat, and J. E. Vonk, "Climate change and the permafrost carbon feedback," Nature, vol. 520, pp. 171–179, 04 2015.

[44] D. Rind, "Just add water vapor," Science, vol. 281, no. 5380, pp. 1152–1153, 1998.

[45] I. M. Held and B. J. Soden, "Robust responses of the hydrological cycle to global warming," Journal of Climate, vol. 19, no. 21, pp. 5686–5699, 2006.

[46] B. Stevens and S. Bony, "What are climate models missing?," Science, vol. 340, no. 6136, pp. 1053–1054, 2013.

[47] M. D. Shupe and J. M. Intrieri, "Cloud radiative forcing of the arctic surface: The influence of cloud properties, surface albedo, and solar zenith angle," Journal of Climate, vol. 17, pp. 616–628, 2015/09/28 2004.

[48] H. D. Curtis, Orbital Mechanics for Engineering Students. 30 Corporate Drive, Burlington, MA 01803: Elsevier Butterworth-Heinemann, 2010.

[49] D. Vallado, Fundamentals of Astrodynamics and Applications. Hawthorne, CA: Microcosm Press, 4 ed., 2013.

[50] C. Weitkamp, ed., Lidar Range-Resolved Optical Remote Sensing of the Atmosphere, vol. 102. Springer, 2005.

[51] T. Fujii and T. Fukuchi, eds., Laser Remote Sensing. Taylor and Francis Group, 2005.

[52] R. M. Measures, Laser Remote Sensing: Fundamentals and Applications. John Wiley and Sons, 1984.

[53] G. W. Petty, A First Course in Atmospheric Radiation. Sundog Pub., 2 ed., 2006.

[54] E. O. Hulburt, "Observations of a searchlight beam to an altitude of 28 kilometers," J. Opt. Soc. Am., vol. 27, pp. 377–382, Nov 1937.

[55] L. Elterman, "A series of stratospheric temperature profiles obtained with the searchlight technique," Journal of Geophysical Research, vol. 58, no. 4, pp. 519–530, 1953.

[56] L. Elterman, "Reply [to "comment on 'the measurement of the atmospheric density distribution by the searchlight technique' by edward v. ashburn and l. g. lamarca"]," Journal of Geophysical Research, vol. 60, no. 3, pp. 363–363, 1955.

[57] L. Elterman, "Aerosol measurements in the troposphere and stratosphere," Appl. Opt., vol. 5, pp. 1769–1776, Nov 1966.

[58] J. Hecht, "Short history of laser development," Optical Engineering, vol. 49, no. 9, pp. 091002–091002–23, 2010.

[59] T. H. Maiman, "Stimulated optical radiation in ruby," Nature, vol. 187, pp. 493–494, 08 1960.

[60] R. T. H. Collis, F. G. Fernald, and M. G. H. Ligda, "Laser radar echoes from a stratified clear atmosphere," Nature, vol. 203, pp. 1274–1275, 09 1964.

[61] G. Fiocco and G. Grams, "Observations of the aerosol layer at 20 km by optical radar," Journal of the Atmospheric Sciences, vol. 21, pp. 323–324, 2015/09/30 1964.

[62] J. A. Cooney, "Measurements on the raman component of laser atmospheric backscatter," Applied Physics Letters, vol. 12, pp. 40–42, 1968.

[63] J. Cooney, "Measurement of atmospheric temperature profiles by raman backscatter," Journal of Applied Meteorology, vol. 11, pp. 108–112, 2015/09/30 1972.

[64] D. H. Höhn, "Depolarization of a laser beam at 6328 å due to atmospheric transmission," Appl. Opt., vol. 8, pp. 367–369, Feb 1969.

[65] R. M. Schotland, K. Sassen, and R. Stone, "Observations by lidar of linear depolarization ratios for hydrometeors," Journal of Applied Meteorology, vol. 10, pp. 1011–1017, 2015/09/30 1971.

[66] R. D. Boudreau, "On the use of ultraviolet lidar for observing atmospheric constituents by raman scattering," Journal of Applied Meteorology, vol. 9, pp. 316–317, 2015/09/30 1970.

[67] Y. F. Arshinov, S. M. Bobrovnikov, V. E. Zuev, and V. M. Mitev, "Atmospheric temperature measurements using a pure rotational raman lidar," Appl. Opt., vol. 22, pp. 2984–2990, Oct 1983.

[68] D. N. Whiteman, S. H. Melfi, and R. A. Ferrare, "Raman lidar system for the measurement of water vapor and aerosols in the earth's atmosphere," Appl. Opt., vol. 31, pp. 3068–3082, Jun 1992.

[69] European Rocket and Balloon Programmes and Related Research, Status of the ALOMAR Rayleigh/Mie/Raman Lidar, 1997.

[70] J. P. Thayer, N. B. Nielson, R. E. Warren, and C. J. Heinselman, "Rayleigh lidar system for middle atmosphere research in the arctic," Optical Engineering, vol. 36, no. 7, pp. 2045–2061, 1997.

[71] U. von Zahn et al, "The alomar rayleigh/mie/raman lidar: objectives, configuration, and performance," Annales Geophysicae, pp. 815–833, 2000.

[72] D. M. Winker, M. A. Vaughan, A. Omar, Y. Hu, K. A. Powell, Z. Liu, W. H. Hunt, and S. A. Young, "Overview of the calipso mission and caliop data processing algorithms," Journal of Atmospheric and Oceanic Technology, vol. 26, no. 11, pp. 2310–2323, 2009.

[73] J. E. M. Goldsmith, F. H. Blair, S. E. Bisson, and D. D. Turner, "Turn-key raman lidar for profiling atmospheric water vapor, clouds, and aerosols," Appl. Opt., vol. 37, pp. 4979–4990, Jul 1998.

[74] J. D. Spinhirne, J. A. R. Rall, and V. S. Scott, "Compact eye safe lidar systems," The Review of Laser Engineering, 1995.

[75] A. Cohen, J. A. Cooney, and K. N. Geller, "Atmospheric temperature profiles from lidar measurements of rotational raman and elastic scattering.," Appl Opt, vol. 15, pp. 2896–2901, Nov 1976.

[76] P. Piironen and E. W. Eloranta, "Demonstration of a high-spectral-resolution lidar based on an iodine absorption filter," Opt. Lett., vol. 19, pp. 234–236, Feb 1994.

[77] G. S. Kent and G. M. Hansen, "Scanning lidar with a coupled radar safety system," Appl. Opt., vol. 38, pp. 6383–6387, Oct 1999.

[78] J. R. Campbell, D. L. Hlavka, E. J. Welton, C. J. Flynn, D. D. Turner, J. D. Spinhirne, V. S. S. III, and I. H. Hwang, "Full-time, eye-safe cloud and aerosol lidar observation at atmospheric radiation measurement program sites: Instruments and data processing," Journal of Atmospheric and Oceanic Technology, vol. 19, pp. 431–442, April 2002.

[79] S. D. Mayor and S. M. Spuler, "Raman-shifted eye-safe aerosol lidar," Appl. Opt., vol. 43, pp. 3915–3924, Jul 2004.

[80] P. Di Girolamo, R. Marchese, D. N. Whiteman, and B. B. Demoz, "Rotational raman lidar measurements of atmospheric temperature in the uv," Geophysical Research Letters, vol. 31, no. 1, 2004.

[81] M. Frioud, M. Gausa, G. Baumgarten, J. Kristjansson, and I. Fore, "New tropospheric lidar system in operation at alomar," in Reviewed and Revised Papers presented at the 23rd ILRC Conference Nara, Hapan, pp. 179–182, 2006.

[82] C. J. Flynn, A. Mendoza, Y. Zheng, and S. Mathur, "Novel polarization-sensitive micropulse lidar measurement technique," Opt. Express, vol. 15, pp. 2785–2790, Mar 2007.

[83] M. Radlach, A. Behrendt, and V. Wulfmeyer, "Scanning rotational raman lidar at 355 nm for the measurement of tropospheric temperature fields," Atmospheric Chemistry and Physics Discussions, vol. 7, pp. 7569–7602, May 2007.

[84] S. Mitchell, J. P. Thayer, and M. Hayman, "Polarization lidar for shallow water depth measurement," Appl. Opt., vol. 49, pp. 6995–7000, Dec 2010.

[85] M. Hayman and J. P. Thayer, "Lidar polarization measurements of {PMCs}," Journal of Atmospheric and Solar-Terrestrial Physics, vol. 73, no. 14–15, pp. 2110 – 2117, 2011. Layered Phenomena in the Mesopause Region.

[86] R. R. Neely and J. P. Thayer, "Raman lidar profiling of tropospheric water vapor over kangerlussuaq, greenland," Journal of Atmospheric and Oceanic Technology, vol. 28, pp. 1141–1148, 2013/12/04 2011.

[87] G. J. Nott, T. J. Duck, J. G. Doyle, M. E. W. Coffin, C. Perro, C. P. Thackray, J. R. Drummond, P. F. Fogal, E. McCullough, and R. J. Sica, "A remotely operated lidar for aerosol, temperature, and water vapor profiling in the high arctic," Journal of Atmospheric and Oceanic Technology, vol. 29, pp. 221–234, 2016/12/20 2011.

[88] J. Reichardt, U. Wandinger, V. Klein, I. Mattis, B. Hilber, and R. Begbie, "Ramses: German meteorological service autonomous raman lidar for water vapor, temperature, aerosol, and cloud measurements," Appl. Opt., vol. 51, pp. 8111–8131, Dec 2012.

[89] R. R. Neely, M. Hayman, R. A. Stillwell, J. P. Thayer, R. M. Hardesty, M. O'Neill, M. D. Shupe, and C. Alvarez, "Polarization lidar at summit, greenland for the detection of cloud phase and particle orientation," Journal of Atmospheric and Oceanic Technology, 2013/07/21 2013.

[90] Y. Zhao, Y. Li, L. Li, Y. Yu, C. Pan, C. Song, A. Boselli, G. Pisani, N. Spinelli, and X. Wang, "Implementation of high dynamic raman lidar system for 3d map of particulate optical properties and their time evolution," International Journal of Remote Sensing Applications, vol. 3, no. 4, pp. 240–244, 2013.

[91] S. M. Spuler, K. S. Repasky, B. Morley, D. Moen, M. Hayman, and A. R. Nehrir, "Field-deployable diode-laser-based differential absorption lidar (dial) for profiling water vapor," Atmospheric Measurement Techniques, vol. 8, no. 3, pp. 1073–1087, 2015.

[92] D. Wu, Z. Wang, P. Wechsler, N. Mahon, M. Deng, B. Glover, M. Burkhart, W. Kuestner, and B. Heesen, "Airborne compact rotational raman lidar for temperature measurement," Opt. Express, vol. 24, pp. A1210–A1223, Sep 2016.

[93] C. F. Bohren and E. E. Clothiaux, Fundamentals of Atmospheric Radiation. WILEY-VCH Verlag GmbH and Co. KGaA, 2005.

[94] E. W. Eloranta, "Practical model for the calculation of multiply scattered lidar returns," Appl. Opt., vol. 37, pp. 2464–2472, Apr 1998.

[95] M.J.Moran, H. Shapiro, B. Munson, and D. DeWitt, Introduction to Thermal Systems Engineering: Thermodynamics, Fluid Mechanics, and Heat Transfer. John Wiley and Sons, 2003.

[96] E. Hecht, Optics. Addison-Wesley, 4 ed., 2002.

[97] D. H. Goldstein, Polarized Light. 6000 Broken Sound Parkway NW, Suite 300, Boca Raton, FL 33487-2742: Taylor and Francis Group, 3 ed., 2011.

[98] M. Hayman and J. P. Thayer, "General description of polarization in lidar using stokes vectors and polar decomposition of mueller matrices," J Opt Soc Am A Opt Image Sci Vis, vol. 29, pp. 400–9, Apr 2012.

[99] S.-Y. Lu and R. A. Chipman, "Interpretation of mueller matrices based on polar decomposition," J. Opt. Soc. Am. A, vol. 13, pp. 1106–1113, May 1996.

[100] M. Hayman, Optical theory for the advancement of polarization lidar. PhD thesis, University of Colorado, 2011.

[101] M. Hayman and J. P. Thayer, "Explicit description of polarization coupling in lidar applications," Opt Lett, vol. 34, pp. 611–3, Mar 2009.

[102] H. Di, H. Hua, Y. Cui, D. Hua, B. Li, and Y. Song, "Correction technology of a polarization lidar with a complex optical system," J. Opt. Soc. Am. A, vol. 33, pp. 1488–1494, Aug 2016.

[103] J. Biele, G. Beyerle, and G. Baumgarten, "Polarization lidar: Correction of instrumental effects," Opt. Express, vol. 7, pp. 427–435, Dec 2000.

[104] V. Freudenthaler, M. Esselborn, M. Wiegner, B. Heese, M. Tesche, A. Ansmann, D. Mueller, D. Althausen, M. Wirth, A. Fix, G. Ehret, P. Knippertz, C. Toledano, J. Gasteiger, M. Garhammer, and M. Seefeldner, "Depolarization ratio profiling at several wavelengths in pure saharan dust during samum 2006," Tellus B, vol. 61, no. 1, pp. 165–179, 2009.

[105] R. A. Stillwell, R. R. N. III, J. P. Thayer, M. D. Shupe, and M. S. O'Neill, "Low-level, liquid-only and mixed-phase cloud identification by polarimetric lidar," Atmospheric Measurement Techniques Discussions, 2016.

[106] K. Sassen, "The polarization lidar technique for cloud research: A review and current assessment," Bulletin of the American Meteorological Society, vol. 72, no. 12, pp. 1848–1866, 1991.

[107] S. Groß, V. Freudenthaler, M. Wirth, and B. Weinzierl, "Towards an aerosol classification scheme for future earthcare lidar observations and implications for research needs," Atmospheric Science Letters, vol. 16, no. 1, pp. 77–82, 2015.

[108] R. Eixmann, M. Gerding, J. Höffner, and M. Kopp, "Lidars with narrow fov for daylight measurements," IEEE Transactions on Geoscience and Remote Sensing, vol. 53, pp. 4548–4553, August 2015.

[109] S. P. Burton, E. Chemyakin, X. Liu, K. Knobelspiesse, S. Stamnes, P. Sawamura, R. H. Moore, C. A. Hostetler, and R. A. Ferrare, "Information content and sensitivity of the 3+2lidar measurement system for aerosol microphysical retrievals," Atmos. Meas. Tech., vol. 9, pp. 5555–5574, 11 2016.

[110] B. V. Kaul, I. V. Samokhvalov, and S. N. Volkov, "Investigating particle orientation in cirrus clouds by measuring backscattering phase matrices with lidar," Appl. Opt., vol. 43, pp. 6620–6628, Dec 2004.

[111] M. Hayman, S. Spuler, B. Morley, and J. VanAndel, "Polarization lidar operation for measuring backscatter phase matrices of oriented scatterers," Opt. Express, vol. 20, pp. 29553–29567, Dec 2012.

[112] C. F. Bohren and D. R. Huffman, Absorption and Scattering of Light by Small Particles. WILEY-VCH Verlag GmbH and Co. KGaA, 1983.

[113] W. L. Eberhard, "Correct equations and common approximations for calculating rayleigh scatter in pure gases and mixtures and evaluation of differences," Appl. Opt., vol. 49, pp. 1116–1130, Mar 2010.

[114] D. A. Long, The Raman Effect: A Unified Treatment of the Theory of Raman Scattering by Molecules. John Wiley and Sons, Ltd, 2002.

[115] G. Placzek, "The rayleigh and raman scattering," in Handbuch der Radiologie, pp. 209–374, Akademische Verlagsgesellschaft, 1934.

[116] H. V. D. Hulst, Light Scattering By Small Particles. John Wiley and Sons, 1957.

[117] C.-Y. She, "Spectral structure of laser light scattering revisited: bandwidths of nonresonant scattering lidars," Applied Optics, vol. 40, no. 27, pp. 4875–4884, 2001.

[118] S. Asano and G. Yamamoto, "Light scattering by a spheroidal particle," Appl. Opt., Jan 1975.

[119] P. Yang, H. Wei, H.-L. Huang, B. A. Baum, Y. X. Hu, G. W. Kattawar, M. I. Mishchenko, and Q. Fu, "Scattering and absorption property database for nonspherical ice particles in the near- through far-infrared spectral region," Appl. Opt., vol. 44, pp. 5512–5523, Sep 2005.

[120] P. Yang, L. Bi, B. A. Baum, K.-N. Liou, G. W. Kattawar, M. I. Mishchenko, and B. Cole, "Spectrally consistent scattering, absorption, and polarization properties of atmospheric ice crystals at wavelengths from 0.2 to 100 m," Journal of the Atmospheric Sciences, vol. 70, pp. 330–347, 2015/03/21 2012.

[121] C. Mätzler, "Functions for mie scattering and absorption," tech. rep., Institut für Angewandte Physik, 2002.

[122] G. Avila, J. Fernández, B. Maté, G. Tejeda, and S. Montero, "Ro-vibrational raman cross sections of water vapor in the {OH} stretching region," Journal of Molecular Spectroscopy, vol. 196, no. 1, pp. 77 – 92, 1999.

[123] G. Avila, G. Tejeda, J. Fernández, and S. Montero, "The rotational raman spectra and cross sections of h2o, d2o, and {HDO}," Journal of Molecular Spectroscopy, vol. 220, no. 2, pp. 259 – 275, 2003.

[124] G. Avila, J. Fernández, G. Tejeda, and S. Montero, "The raman spectra and cross-sections of h2o, d2o, and {HDO} in the oh/od stretching regions," Journal of Molecular Spectroscopy, vol. 228, no. 1, pp. 38 – 65, 2004.

[125] G. G. Gimmestad, "Reexamination of depolarization in lidar measurements," Appl. Opt., vol. 47, pp. 3795–3802, Jul 2008.

[126] C. D. Westbrook, A. J. Illingworth, E. J. O'Connor, and R. J. Hogan, "Doppler lidar measurements of oriented planar ice crystals falling from supercooled and glaciated layer clouds," Quarterly Journal of the Royal Meteorological Society, vol. 136, no. 646, pp. 260–276, 2010.

[127] S. Cole, R. R. N. III, and R. A. Stillwell, "First look at the occurrence of horizontally oriented ice crystals over summit, greenland," Atmospheric Chemistry and Physics Discussions, 2017.

[128] Y. Takano and K.-N. Liou, "Solar radiative transfer in cirrus clouds. part i: Single-scattering and optical properties of hexagonal ice crystals," Journal of the Atmospheric Sciences, vol. 46, pp. 3–19, 2015/09/07 1989.

[129] V. Noel and H. Chepfer, "A global view of horizontally oriented crystals in ice clouds from cloud-aerosol lidar and infrared pathfinder satellite observation (calipso)," Journal of Geophysical Research: Atmospheres, vol. 115, no. D4, 2010.

[130] L. Thomas, J. C. Cartwright, and D. P. Wareing, "Lidar observations of the horizontal orientation of ice crystals in cirrus clouds," Tellus B, vol. 42, no. 2, pp. 211–216, 1990.

[131] R. Yoshida, H. Okamoto, Y. Hagihara, and H. Ishimoto, "Global analysis of cloud phase and ice crystal orientation from cloud-aerosol lidar and infrared pathfinder satellite observation (calipso) data using attenuated backscattering and depolarization ratio," Journal of Geophysical Research: Atmospheres, vol. 115, no. D4, 2010.

[132] C. Zhou, P. Yang, A. E. Dessler, Y. Hu, and B. A. Baum, "Study of horizontally oriented ice crystals with calipso observations and comparison with monte carlo radiative transfer simulations," Journal of Applied Meteorology and Climatology, vol. 51, pp. 1426–1439, 2014/02/24 2012.

[133] C. Zhou, P. Yang, A. Dessler, and F. Liang, "Statistical properties of horizontally oriented plates in optically thick clouds from satellite observations," Geoscience and Remote Sensing Letters, IEEE, vol. 10, no. 5, pp. 986–990, 2013.

[134] R. A. Stillwell, P. Pilewskie, J. P. Thayer, M. S. O'Neill, and R. R. N. III, "Monte carlo method for the analysis of laser safety for a high-powered lidar system under different atmospheric conditions," Journal of Laser Applications, vol. 29, May 2017.

[135] P. Bevington, Data Reduction and Error Analysis for the Physical Sciences. McGraw-Hill, 1992.

[136] J. N. Bixler, B. H. Hokr, A. Winblad, G. Elpers, B. Zollars, and R. J. Thomas, "Methods for variance reduction in monte carlo simulations," 2016.

[137] G. N. Plass and G. W. Kattawar, "Monte carlo calculations of light scattering from clouds," Appl. Opt., vol. 7, pp. 415–419, Mar 1968.

[138] G. N. Plass and G. W. Kattawar, "Reflection of light pulses from clouds," Appl. Opt., vol. 10, pp. 2304–2310, Oct 1971.

[139] S. A. Prahl, M. Keijzer, S. L. Jacques, and A. J. Welch, "A Monte Carlo model of light propagation in tissue," SPIE Proceedings of Dosimetry of Laser Radiation in Medicine and Biology, vol. IS 5, pp. 102–111, 1989.

[140] L. Wang, S. L. Jacques, and L. Zheng, "Mcml—monte carlo modeling of light transport in multi-layered tissues," Computer Methods and Programs in Biomedicine, vol. 47, no. 2, pp. 131 – 146, 1995.

[141] T. Binzoni, T. S. Leung, A. H. Gandjbakhche, D. Rüfenacht, and D. T. Delpy, "The use of the henyey–greenstein phase function in monte carlo simulations in biomedical optics," Physics in Medicine and Biology, vol. 51, no. 17, p. N313, 2006.

[142] W. M. Cornette and J. G. Shanks, "Physically reasonable analytic expression for the single-scattering phase function," Appl. Opt., vol. 31, pp. 3152–3160, Jun 1992.

[143] D. Toublanc, "Henyey-greenstein and mie phase functions in monte carlo radiative transfer computations," Appl. Opt., vol. 35, pp. 3270–3274, Jun 1996.

[144] P. J. Olver and C. Skakiban, Applied Linear Algebra. Prentice Hall, 2006.

[145] A. W. Gisler, Monte Carlo Simulations of Polarized Light Propagating Through Optically Dense Media with Applications for Lidar Systems. PhD thesis, University of Colorado, 2015.

[146] S. Warren, "Optical constants of ice from the ultraviolet to the microwave," Applied Optics, vol. 23, pp. 1206–1225, April 1984.

[147] D. D. Turner and R. G. Ellingson, eds., The Atmospheric Radiation Measurement (ARM) Program: The First 20 Years. AMS Meteorological Monographs, 2016.

[148] D. P. Donovan, J. A. Whiteway, and A. I. Carswell, "Correction for nonlinear photon-counting effects in lidar systems," Appl Opt, vol. 32, pp. 6742–53, Nov 1993.

[149] Z. Liu, Z. Li, B. Liu, and R. Li, "Analysis of saturation signal correction of the troposphere lidar," Chinese Optics Letters, pp. 1051–1054, 2009.

[150] R. K. Newsom, D. D. Turner, B. Mielke, M. Clayton, R. Ferrare, and C. Sivaraman, "Simultaneous analog and photon counting detection for raman lidar," Appl. Opt., vol. 48, pp. 3903–3914, Jul 2009.

[151] J. M. Intrieri, M. D. Shupe, T. Uttal, and B. J. McCarty, "An annual cycle of arctic cloud characteristics observed by radar and lidar at sheba," Journal of Geophysical Research: Oceans, vol. 107, no. C10, pp. SHE 5–1–SHE 5–15, 2002.

[152] J. D. Klett, "Stable analytical inversion solution for processing lidar returns," Appl. Opt., vol. 20, pp. 211–220, Jan 1981.

[153] D. N. Whiteman, "Examination of the traditional raman lidar technique. i. evaluating the temperature-dependent lidar equations," Appl. Opt., vol. 42, pp. 2571–2592, May 2003.

[154] G. J. Nott and T. J. Duck, "Lidar studies of the polar troposphere," Meteorological Applications, vol. 18, no. 3, pp. 383–405, 2011.

[155] G. Cesana and H. Chepfer, "Evaluation of the cloud thermodynamic phase in a climate model using calipso-goccp," Journal of Geophysical Research: Atmospheres, vol. 118, no. 14, pp. 7922–7937, 2013.

[156] K. P. Moran, B. E. Martner, M. J. Post, R. A. Kropfli, D. C. Welsh, and K. B. Widener, "An unattended cloud-profiling radar for use in climate research," Bulletin of the American Meteorological Society, vol. 79, pp. 443–455, 2016/12/20 1998.

[157] E. E. Clothiaux, K. P. Moran, B. E. Martner, T. P. Ackerman, G. G. Mace, T. Uttal, J. H. Mather, K. B. Widener, M. A. Miller, and D. J. Rodriguez, "The atmospheric radiation measurement program cloud radars: Operational modes," Journal of Atmospheric and Oceanic Technology, vol. 16, pp. 819–827, 2016/12/20 1999.

[158] M. P. Cadeddu, J. C. Liljegren, and D. D. Turner, "The atmospheric radiation measurement (arm) program network of microwave radiometers: instrumentation, data, and retrievals," Atmospheric Measurement Techniques, vol. 6, no. 9, pp. 2359–2372, 2013.

[159] N. B. Miller, M. D. Shupe, C. J. Cox, V. P. Walden, D. D. Turner, and K. Steffen, "Cloud radiative forcing at summit greenland," Journal of Climate, vol. 28, no. 15, pp. 6267–6280, 2015.

[160] B. Albrecht and S. K. Cox, "Procedures for improving pyrgeometer performance," Journal of Applied Meteorology, vol. 16, no. 2, pp. 188–197, 1977.

[161] N. B. Miller, M. D. Shupe, C. J. Cox, D. Noone, P. O. G. Persson, and K. Steffen, "Surface energy budget responses to radiative forcing at summit, greenland," The Cryosphere, vol. 11, pp. 497–516, 02 2017.

[162] E. J. Mlawer, S. J. Taubman, P. D. Brown, M. J. Iacono, and S. A. Clough, "Radiative transfer for inhomogeneous atmospheres: Rrtm, a validated correlated-k model for the longwave," Journal of Geophysical Research: Atmospheres, vol. 102, no. D14, pp. 16663–16682, 1997.

[163] D. D. Turner, "Arctic mixed-phase cloud properties from aeri lidar observations: Algorithm and results from sheba," Journal of Applied Meteorology, vol. 44, pp. 427–444, 2016/02/15 2005.

[164] H. Morrison, G. de Boer, G. Feingold, J. Harrington, M. D. Shupe, and K. Sulia, "Resilience of persistent arctic mixed-phase clouds," Nature Geoscience, vol. 5, pp. 11–17, 01 2012.

[165] R. A. Stillwell, R. R. N. III, J. P. Thayer, M. D. Shupe, and D. D. Turner, "Enhanced polarimetric lidar contained within a multi-sensor suite for observing arctic clouds and horizontally oriented ice crystals," Journal of Atmospheric and Oceanic Technology, 2017.

[166] M. Goerke, Z. Ulanowski, G. Ritter, E. Hesse, R. R. N. III, L. Taylor, R. A. Stillwell, and P. H. Kaye, "Characterizing ice particles using two-dimensional reflections of a lidar beam," Applied Optics, 2017.

[167] M. P. Jensen, W. A. Petersen, A. Bansemer, N. Bharadwaj, L. D. Carey, D. J. Cecil, S. M. Collis, A. D. D. Genio, B. Dolan, J. Gerlach, S. E. Giangrande, A. Heymsfield, G. Heymsfield, P. Kollias, T. J. Lang, S. W. Nesbitt, A. Neumann, M. Poellot, S. A. Rutledge, M. Schwaller, A. Tokay, C. R. Williams, D. B. Wolff, S. Xie, and E. J. Zipser, "The midlatitude continental convective clouds experiment (mc3e)," Bulletin of the American Meteorological Society, vol. 97, no. 9, pp. 1667–1686, 2016.

[168] B. Geerts, D. Parsons, C. L. Ziegler, T. M. Weckwerth, D. D. Turner, J. Wurman, K. Kosiba, R. M. Rauber, G. M. McFarquhar, M. D. Parker, R. S. Schumacher, M. C. Coniglio, K. Haghi, M. I. Biggerstaff, P. M. Klein, W. A. G. Jr., B. B. Demoz, K. R. Knupp, R. A. Ferrare, A. R. Nehrir, R. D. Clark, X. Wang, J. M. Hanesiak, J. O. Pinto, and J. A. Moore, "The 2015 plains elevated convection at night (pecan) field project," Bulletin of the American Meteorological Society, 2016.

[169] J. Bösenberg, "Ground-based differential absorption lidar for water-vapor and temperature profiling: methodology," Appl. Opt., vol. 37, pp. 3845–3860, Jun 1998.

[170] American National Standard for Safe Use of Lasers (ANSI Z136.1). Laser Institute of America, 2013.

[171] American National Standard for Safe Use of Lasers Outdoors (ANSI Z136.6). Laser Institute of America, 2013.

[172] R. J. Pressley, Handbook of Lasers. The Chemical Rubber Company, 1971.

[173] J. Bendix, "A satellite-based climatology of fog and low-level stratus in germany and adjacent areas," Atmospheric Research, vol. 64, no. 1–4, pp. 3 – 18, 2002. 2nd International Conference on Fog and Fog Collection.

[174] T. M. Weckwerth, K. J. Weber, D. D. Turner, and S. M. Spuler, "Validation of a water vapor micropulse differential absorption lidar (dial)," Journal of Atmospheric and Oceanic Technology, vol. 33, no. 11, pp. 2353–2372, 2016.

[175] G. Herzberg, The Spectra and Structures of Simple Free Radicals. Cornell University Press, 2012.

Chapter 8

Appendix

8.1   Nomenclature

Constants
c	$=$	Speed of light in vacuum	$c = 2.998 \times 10^8 \left[\frac{m}{s}\right]$
h	$=$	Planck's Constant	$h = 6.626 \times 10^{-34} \left[J \cdot s\right]$
$\hbar$	$=$	Reduced Planck's Constant	$\hbar = 1.055 \times 10^{-34} \left[J \cdot s\right]$
k_B	$=$	Boltzmann's constant	$k_B = 1.381 \times 10^{-23} \left[\frac{J}{K}\right]$
ϵ_o	$=$	Free space permittivity	$\epsilon_o = 8.854 \times 10^{-12} \left[\frac{s^4 A^2}{m^3 kg}\right]$

Letters
A	$=$	Telescope area	$\left[m^2\right]$
a	$=$	Depolarization of a general aligned depolarization	
		matrix for the horizontal-vertical polarization	$\left[unitless\right]$
a	$=$	Scattering particle diameter	$\left[m\right]$
a_n^s	$=$	Mie scattering a-coefficient	$\left[unitless\right]$
B_0	$=$	Ground diatomic rotational constant for a molecule	$\left[cm^{-1}\right]$
B_1	$=$	1st excited diatomic rotational constant for a molecule	$\left[cm^{-1}\right]$
b	$=$	Depolarization of a general aligned depolarization	

		matrix for the ± 45 polarization	$[unitless]$
b_n^s	$=$	Mie scattering b-coefficient	$[unitless]$
C	$=$	Separation constant for diatomic molecules	
c	$=$	Depolarization of a general aligned depolarization	
		matrix for the right-left circular polarization	$[unitless]$
D	$=$	Diattenuation magnitude	$[unitless]$
D_0	$=$	Ground diatomic rotational distortion for a molecule	$[cm^{-1}]$
d	$=$	Atmospheric depolarization	$[unitless]$
$d_{1,2,3}$	$=$	Depolarization about the 3 depolarization vector axes	$[unitless]$
E	$=$	Energy	$[J]$
E_i	$=$	Energy of the ith level	$[J]$
E_n^o	$=$	Potential energy function for diatomic molecules	$[J]$
$F_{\#\#}$	$=$	Scattering phase matrix element	$[unitless]$
G	$=$	Geometric overlap function	$[unitless]$
g_n	$=$	Nuclear spin statistical weight factor	$[unitless]$
$\hat{H}$	$=$	Hamiltonian operator	
h_n	$=$	Spherical Hankel function of order n	
I	$=$	Moment of inertia	$[kg \cdot m^2]$
i	$=$	Imaginary number	$i = \sqrt{-1}$
J	$=$	Rotational Quantum number	$[unitless]$
J_1	$=$	Starting Rotational Quantum number	$[unitless]$
J_2	$=$	Ending Rotational Quantum number	$[unitless]$
j_n	$=$	Spherical Bessel function of the first kind of order n	
K	$=$	Diatomic harmonic oscillator restoring force	$[N/m]$
M	$=$	Separation constant for rotating diatomic molecules	
m	$=$	Mass of a particle	$[kg]$
m	$=$	Complex index of refraction	$[unitless]$

$$m_1 \quad = \quad \text{Mass of a particle 1 used for a diatomic molecule} \qquad [kg]$$

$$m_2 \quad = \quad \text{Mass of a particle 2 used for a diatomic molecule} \qquad [kg]$$

$$N \quad = \quad \text{Function normalization constant}$$

$$N_B \quad = \quad \text{Background number of photons} \qquad [unitless]$$

$$N_D \quad = \quad \text{Number density of a particular species} \qquad [number/m^3]$$

$$N_{1,2,3} \quad = \quad \text{Number of photons in receiver polarization channels} \qquad [unitless]$$

$$P_L \quad = \quad \text{Laser power} \qquad [Watts]$$

$$p \quad = \quad \text{Degree of polarization} \qquad [unitless]$$

$$p_{i,j} \quad = \quad \text{Probability of being in state } i \text{ or } j \qquad [unitless]$$

$$p(\mu) \quad = \quad \text{Probability distribution function of variable } \mu \qquad [unitless]$$

$$R \quad = \quad \text{Range of observation} \qquad [m]$$

$$R \quad = \quad \text{Backscattering ratio} \qquad [unitless]$$

$$R \quad = \quad \text{Internuclear distance for a diatomic molecule} \qquad [m]$$

$$R_{i,j,k} \quad = \quad \text{Coordinates of the retardance vector} \qquad [unitless]$$

$$R_1 \quad = \quad \text{Location of particle 1 for a diatomic molecule} \qquad [m]$$

$$R_2 \quad = \quad \text{Location of particle 2 for a diatomic molecule} \qquad [m]$$

$$r_e \quad = \quad \text{Particle effective radius} \qquad [m]$$

$$S_{Obs} \quad = \quad \text{Observed signal count rate} \qquad [Hz]$$

$$S_O \quad = \quad \text{Ideal signal count rate} \qquad [Hz]$$

$$S_{PP} \quad = \quad \text{Shots per profile} \qquad [unitless]$$

$$S_{0-3} \quad = \quad \text{Stokes parameters} \qquad [unitless]$$

$$S_{1,2}(\Theta) \quad = \quad \text{Mie theory angular functions}$$

$$S_{\#\#} \quad = \quad \text{Mie theory Mueller matrix components} \qquad [unitless]$$

$$s \quad = \quad \text{Separation of variables radius dependent function}$$

$$T \quad = \quad \text{Temperature} \qquad [K]$$

$$T \quad = \quad \text{Separation of variables time dependent function}$$

$$\hat{T} \quad = \quad \text{Kinetic energy operator}$$

T_{R_x}	=	Transmission of received wavelength	$[unitless]$
T_{T_x}	=	Transmission of transmitted wavelength	$[unitless]$
t	=	Time	$[s]$
u	=	Separation of variables space dependent function	
$\hat{V}$	=	Potential energy operator	
v	=	Vibrational Quantum number	$[unitless]$
x	=	Size parameter of a scatterer	$[unitless]$
$\bar{x}$	=	Location of a particle/wave in Cartesian coordinates	$[m]$
Y	=	Separation of variables angular dependent function	

Matrix

$\bar{D}$	=	Diattenuation vector	$[unitless]$
$\bar{\bar{F}}$	=	Scattering phase Mueller matrix	$[unitless]$
$\bar{\bar{F}}_j$	=	Scattering phase Mueller matrix multiple scattering	$[unitless]$
$\bar{k}_i$	=	Incident wave vector	$[m^{-1}]$
$\bar{k}_s$	=	Scattered wave vector	$[m^{-1}]$
$\bar{\bar{M}}$	=	General Mueller matrix	$[unitless]$
$\bar{\bar{M}}_D$	=	General Diattenuator Mueller matrix	$[unitless]$
$\bar{\bar{M}}_i$	=	Monte Carlo rotation matrix	$[unitless]$
$\bar{\bar{M}}_{Mie}$	=	General Mueller matrix predicted by Mie theory	$[unitless]$
$\bar{\bar{M}}_R$	=	General Retarder Mueller matrix	$[unitless]$
$\bar{\bar{M}}_{R_x}$	=	Receiver Mueller matrix	$[unitless]$
$\bar{\bar{M}}_{T_x}$	=	Transmitter Mueller matrix	$[unitless]$
$\bar{\bar{M}}_\Delta$	=	General Depolarizer Mueller matrix	$[unitless]$
$\bar{\bar{m}}_d$	=	General Diattenuator sub-matrix	$[unitless]$
$\bar{\bar{m}}_r$	=	General Retardance sub-matrix	$[unitless]$
$\bar{\bar{m}}_\delta$	=	General depolarization sub-matrix	$[unitless]$

$\bar{N}$	$=$	Observation vector	[$unitless$]
$\bar{\bar{O}}$	$=$	Observation matrix	[$unitless$]
$\bar{P}$	$=$	Polarizance vector	[$unitless$]
$\bar{R}$	$=$	Retardance vector	[$unitless$]
$\bar{\bar{R}}_y$	$=$	Rotation matrix about the Cartesean y-axis	[$unitless$]
$\bar{\bar{R}}_z$	$=$	Rotation matrix about the Cartesean z-axis	[$unitless$]
$\bar{S}$	$=$	General Stokes Vector	[$unitless$]
$\bar{S}_B$	$=$	Background Stokes Vector	[$unitless$]
$\bar{S}_{T_x}$	$=$	Transmitted Stokes Vector	[$unitless$]
$\bar{\bar{T}}$	$=$	rotation matrix between the conventional Poincar?e coordinates S1, S2, and S3 to the eigen polarization states of the depolarizer	[$unitless$]
$\bar{\bar{T}}_{atm}$	$=$	Atmospheric transmission Mueller matrix	[$unitless$]
$\bar{\bar{T}}_{j_{atm}}$	$=$	$\bar{\bar{T}}_{atm}$ for multiple scattering	[$unitless$]
$\bar{\Omega}$	$=$	Direction of Monte Carlo photon	[m]
$\bar{\tau}$	$=$	Location of Monte Carlo photon	[m]

Greek

α	$=$	Mean polarizability	[$unitless$]
α'	$=$	Derivative of the mean polarizability	[$unitless$]
β	$=$	Backscattering coefficient	[$meters^{-1}$]
β_a	$=$	Aerosol backscattering coefficient	[$meters^{-1}$]
β_m	$=$	Molecular backscattering coefficient	[$meters^{-1}$]
χ	$=$	Particle wave function in spherical coordinates	
χ_{PC}	$=$	Azimuth angle of the Stokes vector in Poincaré space	
ΔE	$=$	Change in energy during Raman scattering	[J]

ΔJ	$=$	Change in rotational quantum number	$[unitless]$
ΔR	$=$	Range resolution in the lidar equation	$[m]$
Δt	$=$	Time of the laser pulse	$[seconds]$
$\Delta \tilde{\nu}$	$=$	Frequency change during scattering	$[Hz]$
δ	$=$	Atmospheric depolarization ratio	$[unitless]$
ϵ_{ijk}	$=$	Levi-Civitá permutation symbol	$[unitless]$
η_b	$=$	Mie backscattering efficiency	$[unitless]$
η_{R_x}	$=$	Optical efficiency of the receiver	$[unitless]$
η_s	$=$	Mie total scattering efficiency	$[unitless]$
η_{T_x}	$=$	Optical efficiency of the transmitter	$[unitless]$
Γ	$=$	Angle of retardance about the retardance vector	$[unitless]$
γ	$=$	Anisotropy of the polarizability	$[unitless]$
γ'	$=$	Derivative of the anisotropy of the polarizability	$[unitless]$
λ	$=$	General wavelength	$[m]$
λ_{R_x}	$=$	Receiver wavelength	$[m]$
λ_{T_x}	$=$	Transmitter wavelength	$[m]$
μ	$=$	Reduced mass of a molecule	$\mu = \frac{m_1 m_2}{m_1 + m_2}$
$\tilde{\nu}$	$=$	Incident frequency	$[Hz]$
$\tilde{\nu}_{vib}$	$=$	Ground diatomic vibration constant for a molecule	$\left[cm^{-1}\right]$
$\pi_{1,2,...,n}$	$=$	Legendre polynomial	
Φ	$=$	Separation of variables azimuth dependent function	
Φ_J	$=$	Placzek-Teller factor and geometry weight	$[unitless]$
ϕ	$=$	Azimuth angle in spherical coordinates	$[rad]$
ϕ	$=$	Transmitter linear polarization rotation angle	$[rad]$
ϕ_i	$=$	ϕ of the ith propagation segment	$[rad]$
ψ	$=$	Particle wave function in Cartesian coordinates	
ψ_{PC}	$=$	Elevation angle of the Stokes vector in Poincaré space	

ρ	$=$	Density of a substance	$\left[kg/m^3\right]$
σ	$=$	Scattering cross section	$\left[m^2\right]$
$\sigma_{B_{J_1}}$	$=$	Backscattering cross section of rotational level J_1	$\left[m^2\right]$
σ_D	$=$	Error estimate of non-orthogonal diattenuation	$[unitless]$
σ_{Ray}	$=$	Rayleigh backscattering cross section	$\left[m^2\right]$
σ_b	$=$	Mie backscattering cross section	$\left[m^2\right]$
σ_d	$=$	Error estimate of non-orthogonal depolarization	$[unitless]$
σ_{ext}	$=$	Extinction cross section	$\left[m^2\right]$
σ_s	$=$	Mie total scattering cross section	$\left[m^2\right]$
τ	$=$	Optical depth	$[unitless]$
τ_i	$=$	Optical depth of the ith segment	$[unitless]$
τ_{NP}	$=$	Nonparalyzable dead time	$[sec]$
τ_P	$=$	Paralyzable dead time	$[sec]$
$\tau_{1,2,...,n}$	$=$	Derivatives of the Legendre polynomial	
Θ	$=$	Separation of variables elevation dependent function	
θ	$=$	Elevation angle in spherical coordinates	$[rad]$
θ	$=$	Linear polarization rotation angle	$[rad]$
θ_i	$=$	θ of the ith propagation segment	$[rad]$
υ	$=$	General rotation angle	$[rad]$
ξ	$=$	Number taken from a uniform prob. distribution	$[unitless]$
ξ	$=$	Simplifying variable for lidar inversions	$[unitless]$
ζ	$=$	General rotation angle	$[rad]$
ζ	$=$	Location of a photon in a Monte Carlo layer	$[m]$
ζ	$=$	Simplifying variable for lidar inversions	$[unitless]$

8.2   Acronyms

ADC	=	Analog-To-Digital
ANSI	=	American National Standards Institute
ARM	=	Atmospheric Radiation Measurement Program
AS	=	Anti-Stokes
CAD	=	Computer-Aided Design
CALIOP	=	Cloud-Aerosol Lidar with Orthogonal Polarization
CAPABL	=	Clouds Aerosols Polarization and Backscatter Lidar
CRE	=	Cloud Radiative Effect
DIAL	=	Differential Absorption Lidar
EM	=	Electro-Magnetic
FO	=	Fractional Occurence
FWHM	=	Full Width at Half Maximum
GrIS	=	Greenland Ice Sheet
HATPRO	=	Humidity and Temperature Profiler
High J	=	Branch designation for Raman branch using high rotational numbers
HOIC	=	Horizontally Oriented Ice Crystals
HVAC	=	Heating Ventilation and Air Conditioning
HWP	=	Half Wave Plate
ICECAPS	=	Integrated Characterization of Energy Clouds and Atmospheric State and Precipitation at Summit
IR	=	Infra-red
Laser	=	Light Amplification by the Stimulated Emission of Radiation
LCVR	=	Liquid Crystal Variable Retarder
Lidar	=	Light Detection And Ranging
Low J	=	Branch designation for Raman branch using low rotational numbers
LWP	=	Liquid Water Path
Maser	=	Microwave Amplification by the Stimulated Emission of Radiation

MC3E	=	Midlatitude Continental Convective Clouds Experiment
MMCR	=	Millimeter Cloud Radar
MPE	=	Maximum Permissible Exposure
MPL	=	Micro-Pulse Lidar
MSIS	=	United States Naval Research Laboratory Mass Spectrometer and Incoherent Scatter Radar Exosphere
MWR	=	Microwave Radiometer
NASA	=	National Aeronautics and Space Administration
Nd:YAG	=	Neodymium-doped Yttrium Aluminium Garnet ($Nd:Y_3Al_5O_{12}$)
Nd:YLF	=	Neodymium-doped Yttrium Lithium Fluoride ($Nd:LiYF_4$)
NHZ	=	Nominal Hazard Zone
NO	=	Non Orthogonal
NOAA PSD	=	National Oceanic and Atmospheric Administration Physical Science Division
NOHD	=	Nominal Ocular Hazard Distance
NSF	=	National Science Foundation
O Branch	=	Raman scattering branch with rotational selection rule $\Delta J = -2$
OD	=	Optical Depth
P Polarization	=	Parallel polarization to the plane of incidence
PC	=	Photon Counting
PECAN	=	Planes Elevated Convection At Night
PIR	=	Precision Infrared Radiometers
PMT	=	Photo Multiplier Tube
Q Branch	=	Raman scattering branch with rotational selection rule $\Delta J = 0$
QWP	=	Quarter Wave Plate
ROIC	=	Randomly Oriented Ice Crystals
RRTM	=	Rapid Radiative Transfer Model

S Branch	=	Raman scattering branch with rotational selection rule $\Delta J = 2$
S Polarization	=	Senkrecht (german for Perpendicular) polarization to the plane of incidence
SAW	=	Standard Arctic Winter
SHEBA	=	Surface Heat Budget of the Arctic
SIN	=	Signal Induced Noise
Sodar	=	Sound Detection And Ranging
SNR	=	Signal to Noise Ratio
SRB	=	Surface Radiation Budget
SuPR	=	Summit Polarized Raman Lidar
SVLE	=	Stokes Vector Lidar Equation
SZA	=	Solar Zenith Angle
UPS	=	Uninterruptible Power Supply
UTC	=	Universal Time Coordinated
UV	=	Ultraviolet
UVA	=	Ultraviolet A $320 - 400\ [nm]$

8.3   Derivations

8.3.1   Seperating Schrödinger's Equation For Diatomic Molecules

Schrödinger's equation is the starting point of this derivation that will use separation of variables to first separate the equation in the the time-dependent and time-independent Schrödinger equation. From that point, a diatomic molecule will be assumed. Switching the coordinate basis from Cartesian space for each molecule to a set of equations which rely on the internuclear distance of the system, the equation can be converted into an analog of the separation and exact solution for the hydrogen atom. Again performing separation of variables into radial and angular components,

vibration and rotation quantization can be retrieved. Vibration is retrieved from the radial solution and rotation is retrieved from the angular dependance. Schrödinger's equation is given in Equation 8.1. Note that this section simply reproduces derivations for completeness, which were originally provided by Demtroeder and Herzberg [20, 175].

$$i\hbar\frac{\partial}{\partial t}\psi\left(\bar{x},t\right)=\hat{H}\psi\left(\bar{x},t\right) \tag{8.1}$$

Using the separation of variables technique, a solution of the form $\psi\left(\bar{x},t\right)=u\left(\bar{x}\right)T\left(t\right)$ is assumed. Inserting this assumed form into Equation 8.1 is given in Equation 8.2.

$$i\hbar\frac{\partial}{\partial t}\left[u\left(\bar{x}\right)T\left(t\right)\right]=\hat{H}\left[u\left(\bar{x}\right)T\left(t\right)\right] \tag{8.2}$$

The Hamiltonian operator in Cartesian coordinates is given in Equation 8.3 and is inserted into Equation 8.2 given in Equation 8.4.

$$\hat{H}=\hat{T}+\hat{V}=-\frac{\hbar^2}{2m}\nabla^2+\hat{V} \tag{8.3}$$

$$i\hbar\frac{\partial}{\partial t}\left[u\left(\bar{x}\right)T\left(t\right)\right]=\left[-\frac{\hbar^2}{2m}\nabla^2+\hat{V}\right]\left[u\left(\bar{x}\right)T\left(t\right)\right] \tag{8.4}$$

Separating the variables into time-dependent and non-time-dependent terms is demonstrated with the final answer given in Equation 8.7.

$$i\hbar u\left(\bar{x}\right)\frac{\partial}{\partial t}\left[T\left(t\right)\right]=\left[-\frac{\hbar^2}{2m}\nabla^2 u\left(\bar{x}\right)+\hat{V}u\left(\bar{x}\right)\right]T\left(t\right) \tag{8.5}$$

$$\frac{i\hbar}{T\left(t\right)}\frac{\partial T\left(t\right)}{\partial t}=\frac{1}{u\left(\bar{x}\right)}\left[-\frac{\hbar^2}{2m}\nabla^2 u\left(\bar{x}\right)+\hat{V}u\left(\bar{x}\right)\right] \tag{8.6}$$

Because the left side of the above equation is purely a function of time and the right is purely a function of space, the two must equal a constant. That constant is the energy of the system.

$$\frac{i\hbar}{T\left(t\right)}\frac{\partial T\left(t\right)}{\partial t} = \frac{1}{u\left(\bar{x}\right)}\left[-\frac{\hbar^2}{2m}\nabla^2 u\left(\bar{x}\right) + \hat{V}u\left(\bar{x}\right)\right] = Const. = E \tag{8.7}$$

Thus, the time-dependent and time-independent Schrdinger equations are given in Equation 8.8 and Equation 8.9, respectively.

$$\frac{i\hbar}{T\left(t\right)}\frac{\partial T\left(t\right)}{\partial t} = E \tag{8.8}$$

$$\hat{H}u\left(\bar{x}\right) = Eu\left(\bar{x}\right) \tag{8.9}$$

For a diatomic molecule, the location of each molecule can be inserted into the Hamiltonian assuming a potential function of $\hat{V} = E_n^0\left(\bar{R}_1, \bar{R}_2\right)$ and letting the wave function be ψ_{nm} where n is the ro-vibrational state and m is the nuclear state.

$$\left[-\frac{\hbar^2}{2m_1}\nabla_1^2 - \frac{\hbar^2}{2m_2}\nabla_2^2 + E_n^0\left(\bar{R}_1, \bar{R}_2\right)\right]\psi_{nm}\left(\bar{R}_1, \bar{R}_2\right) = E\psi_{nm}\left(\bar{R}_1, \bar{R}_2\right) \tag{8.10}$$

Multiplying the kinetic terms by one can help combine the terms later.

$$\left[-\frac{\hbar^2 m_2}{2m_1 m_2}\nabla_1^2 - \frac{\hbar^2 m_1}{2m_1 m_2}\nabla_2^2 + E_n^0\left(\bar{R}_1, \bar{R}_2\right)\right]\psi_{nm}\left(\bar{R}_1, \bar{R}_2\right) = E\psi_{nm}\left(\bar{R}_1, \bar{R}_2\right) \tag{8.11}$$

Now, redefining the location coordinates not in terms of the Cartesian locations relative to some arbitrary origin but rather relative to the center of mass and thus redefining the location in terms of the internuclear distance, $R = \left|\bar{R}_1 - \bar{R}_2\right|$ yields a vast simplification of Equation 8.10. This simplifications requires the definition of the reduced mass, $\mu = \frac{m_1 m_2}{m_1 + m_2}$. Several steps are shown with the final answer given in Equation 8.15.

$$\left[-\frac{\hbar^2 m_2}{2m_1 m_2}\nabla^2 - \frac{\hbar^2 m_1}{2m_1 m_2}\nabla^2 + E_n^0\left(R\right)\right]\psi_{nm}\left(\bar{R}_1, \bar{R}_2\right) = E\psi_{nm}\left(\bar{R}_1, \bar{R}_2\right) \tag{8.12}$$

$$\left[\left(-\frac{\hbar^2 m_2}{2m_1 m_2} - \frac{\hbar^2 m_1}{2m_1 m_2}\right)\nabla^2 + E_n^0\left(R\right)\right]\psi_{nm}\left(\bar{R}_1, \bar{R}_2\right) = E\psi_{nm}\left(\bar{R}_1, \bar{R}_2\right) \tag{8.13}$$

$$\left[\left(-\frac{\hbar^2}{2\frac{m_1 m_2}{m_1+m_2}}\right)\nabla^2 + E_n^0(R)\right]\psi_{nm}\left(\bar{R}_1, \bar{R}_2\right) = E\psi_{nm}\left(\bar{R}_1, \bar{R}_2\right) \tag{8.14}$$

$$\left[-\frac{\hbar^2}{2\mu}\nabla^2 + E_n^0(R)\right]\psi_{nm}\left(\bar{R}_1, \bar{R}_2\right) = E\psi_{nm}\left(\bar{R}_1, \bar{R}_2\right) \tag{8.15}$$

Equation 8.15 looks almost exactly like the equation for the hydrogen atom, but the potential is not the Coulomb potential. As a result, the solution to this equation can be again attained through the separation of variables. As with hydrogen, a change from Cartesian coordinates to spherical coordinates yields a seperatable form. The form of the solution will be to separate radial and angular components by assuming a solution of the form $\chi(R, \theta, \phi) = S(R)Y(\theta, \phi)$. Note that the wave function $\chi(R, \theta, \phi)$ is used to clarify that the dependancies are in spherical coordinates.

One piece needed to convert Equation 8.15 to spherical coordinates is a representation of the Laplacian in spherical coordinates. This is given in Equation 8.16.

$$\nabla^2 = \frac{1}{R^2}\frac{\partial}{\partial R}\left(R^2\frac{\partial}{\partial R}\right) + \frac{1}{R^2\sin(\theta)}\frac{\partial}{\partial\theta}\left(\sin(\theta)\frac{\partial}{\partial\theta}\right) + \frac{1}{R^2\sin^2(\theta)}\frac{\partial^2}{\partial\phi^2} \tag{8.16}$$

Inserting Equation 8.16 into Equation 8.15 and inserting the new wave function in terms of spherical coordinates yields:

$$\left[-\frac{\hbar^2}{2\mu}\left[\frac{1}{R^2}\frac{\partial}{\partial R}\left(R^2\frac{\partial}{\partial R}\right) + \frac{1}{R^2\sin(\theta)}\frac{\partial}{\partial\theta}\left(\sin(\theta)\frac{\partial}{\partial\theta}\right) + \frac{1}{R^2\sin^2(\theta)}\frac{\partial^2}{\partial\phi^2}\right] + E_n^0(R)\right]\chi(R, \theta, \phi)$$
$$= E\chi(R, \theta, \phi)$$
$$\tag{8.17}$$

Finally, inserting the separation of variables solution, which will be assumed, is given in Equation 8.18. This equation is the one that we seek to separate, to represent vibrations and rotations of diatomic molecules.

$$\left[-\frac{\hbar^2}{2\mu}\left[\frac{1}{R^2}\frac{\partial}{\partial R}\left(R^2\frac{\partial}{\partial R}\right)+\frac{1}{R^2\sin(\theta)}\frac{\partial}{\partial\theta}\left(\sin(\theta)\frac{\partial}{\partial\theta}\right)+\frac{1}{R^2\sin^2(\theta)}\frac{\partial^2}{\partial\phi^2}\right]+E_n^0(R)\right]$$
$$S(R)Y(\theta,\phi)=ES(R)Y(\theta,\phi)$$

$$(8.18)$$

Distributing the wave function and expanding yields:

$$-\frac{\hbar^2}{2\mu}\left[\frac{1}{R^2}\frac{\partial}{\partial R}\left(R^2\frac{\partial}{\partial R}\right)S(R)Y(\theta,\phi)+\right.$$
$$\frac{1}{R^2\sin(\theta)}\frac{\partial}{\partial\theta}\left(\sin(\theta)\frac{\partial}{\partial\theta}\right)S(R)Y(\theta,\phi)+$$
$$\left.\frac{1}{R^2\sin^2(\theta)}\frac{\partial^2}{\partial\phi^2}S(R)Y(\theta,\phi)\right]+E_n^0(R)S(R)Y(\theta,\phi)\quad=\quad ES(R)Y(\theta,\phi)$$

$$(8.19)$$

$$-\frac{\hbar^2}{2\mu R^2}\left[Y(\theta,\phi)\frac{\partial}{\partial R}\left(R^2\frac{\partial S(R)}{\partial R}\right)+\right.$$
$$\frac{S(R)}{\sin(\theta)}\frac{\partial}{\partial\theta}\left(\sin(\theta)\frac{\partial Y(\theta,\phi)}{\partial\theta}\right)+$$
$$\left.\frac{S(R)}{\sin^2(\theta)}\frac{\partial^2 Y(\theta,\phi)}{\partial\phi^2}\right]+E_n^0(R)S(R)Y(\theta,\phi)\quad=\quad ES(R)Y(\theta,\phi)$$

$$(8.20)$$

$$\left[Y(\theta,\phi)\frac{\partial}{\partial R}\left(R^2\frac{\partial S(R)}{\partial R}\right)+\right.$$
$$\frac{S(R)}{\sin(\theta)}\frac{\partial}{\partial\theta}\left(\sin(\theta)\frac{\partial Y(\theta,\phi)}{\partial\theta}\right)+$$
$$\left.\frac{S(R)}{\sin^2(\theta)}\frac{\partial^2 Y(\theta,\phi)}{\partial\phi^2}\right]\quad=\quad-\frac{2\mu R^2}{\hbar^2}\left(E-E_n^0\right)S(R)Y(\theta,\phi)$$

$$(8.21)$$

Dividing both sides by the angular dependent wave function, $Y(\theta,\phi)$ yields:

$$\frac{1}{Y(\theta,\phi)}\left[Y(\theta,\phi)\frac{\partial}{\partial R}\left(R^2\frac{\partial S(R)}{\partial R}\right)+\right.$$
$$\frac{S(R)}{\sin(\theta)}\frac{\partial}{\partial\theta}\left(\sin(\theta)\frac{\partial Y(\theta,\phi)}{\partial\theta}\right)+$$
$$\left.\frac{S(R)}{\sin^2(\theta)}\frac{\partial^2 Y(\theta,\phi)}{\partial\phi^2}\right]=-\frac{2\mu R^2}{\hbar^2}\left(E-E_n^0\right)S(R)$$

$$(8.22)$$

$$\frac{S(R)}{Y(\theta,\phi)}\left[\begin{array}{c}\frac{\partial}{\partial R}\left(R^2\frac{\partial S(R)}{\partial R}\right)+\\[2mm]\frac{1}{\sin(\theta)}\frac{\partial}{\partial\theta}\left(\sin(\theta)\frac{\partial Y(\theta,\phi)}{\partial\theta}\right)+\\[2mm]\frac{1}{\sin^2(\theta)}\frac{\partial^2 Y(\theta,\phi)}{\partial\phi^2}\end{array}\right]=-\frac{2\mu R^2}{\hbar^2}\left(E-E_n^0\right)S(R)$$

$$(8.23)$$

$$\frac{\partial}{\partial R}\left(R^2\frac{\partial S(R)}{\partial R}\right)+\frac{2\mu R^2}{\hbar^2}\left(E-E_n^0\right)S(R)=-\frac{S(R)}{Y(\theta,\phi)}\left[\frac{1}{\sin(\theta)}\frac{\partial}{\partial\theta}\left(\sin(\theta)\frac{\partial Y(\theta,\phi)}{\partial\theta}\right)+\right.$$
$$\left.\frac{1}{\sin^2(\theta)}\frac{\partial^2 Y(\theta,\phi)}{\partial\phi^2}\right]$$

$$(8.24)$$

Finally, separating out the Y and S dependancies is given in Equation 8.25.

$$\frac{1}{S(R)}\frac{\partial}{\partial R}\left(R^2\frac{\partial S(R)}{\partial R}\right)+\frac{2\mu R^2}{\hbar^2}\left(E-E_n^0\right)=-\frac{1}{Y(\theta,\phi)}\left[\frac{1}{\sin(\theta)}\frac{\partial}{\partial\theta}\left(\sin(\theta)\frac{\partial Y(\theta,\phi)}{\partial\theta}\right)+\right.$$
$$\left.\frac{1}{\sin^2(\theta)}\frac{\partial^2 Y(\theta,\phi)}{\partial\phi^2}\right]$$

$$(8.25)$$

As before, each side of Equation 8.25 is separated by functional dependance, radial on the left and angular on the right. The only way to make this true is if the above is also equal to a

constant factor, C. One can solve for the separated equations to yield the dependance of vibration and rotation, Equation 8.28.

$$\frac{1}{S(R)}\frac{\partial}{\partial R}\left(R^2\frac{\partial S(R)}{\partial R}\right) + \frac{2\mu R^2}{\hbar^2}\left(E - E_n^0\right) = C \tag{8.26}$$

$$\frac{\partial}{\partial R}\left(R^2\frac{\partial S(R)}{\partial R}\right) + \frac{2\mu R^2}{\hbar^2}\left(E - E_n^0\right)S(R) - CS(R) = 0 \tag{8.27}$$

$$\boxed{\frac{1}{R^2}\frac{\partial}{\partial R}\left(R^2\frac{\partial S(R)}{\partial R}\right) + \frac{2\mu}{\hbar^2}\left(E - E_n^0 - \frac{C\hbar^2}{2\mu R^2}\right)S(R) = 0} \tag{8.28}$$

Performing the same steps for rotation, one can simplify to the finalized form in Equation 8.31.

$$-\frac{1}{Y(\theta,\phi)}\left[\frac{1}{\sin(\theta)}\frac{\partial}{\partial\theta}\left(\sin(\theta)\frac{\partial Y(\theta,\phi)}{\partial\theta}\right) + \frac{1}{\sin^2(\theta)}\frac{\partial^2 Y(\theta,\phi)}{\partial\phi^2}\right] = C \tag{8.29}$$

$$C + \frac{1}{Y(\theta,\phi)}\left[\frac{1}{\sin(\theta)}\frac{\partial}{\partial\theta}\left(\sin(\theta)\frac{\partial Y(\theta,\phi)}{\partial\theta}\right) + \frac{1}{\sin^2(\theta)}\frac{\partial^2 Y(\theta,\phi)}{\partial\phi^2}\right] = 0 \tag{8.30}$$

$$\boxed{CY(\theta,\phi) + \frac{1}{\sin(\theta)}\frac{\partial}{\partial\theta}\left(\sin(\theta)\frac{\partial Y(\theta,\phi)}{\partial\theta}\right) + \frac{1}{\sin^2(\theta)}\frac{\partial^2 Y(\theta,\phi)}{\partial\phi^2} = 0} \tag{8.31}$$

8.3.2 Solving the Seperated Schrödinger's Equation For A Rigid Rotor

To solve Equation 8.31 for a rigid rotor and determine the energy quantization, it is necessary to perform a few more steps. The goal is to perform a separation of variables one more time into azimuth and elevation functions then use the separated functions to determine the quantization. The azimuth equation will yield a constraint on the elevation equation that can be transformed to look like the general Legendre equation, which has canonical solutions. The requirement to make the elevation equation exactly equal to the general Legendre equation will ultimately yield the rotational quantization for a rigid rotor that we seek.

Assuming a form of the solution of Equation 8.31 which is $Y(\theta,\phi) = \Theta(\theta)\Phi(\phi)$.

$$C\Theta\left(\theta\right)\Phi\left(\phi\right)+\frac{1}{\sin\left(\theta\right)}\frac{\partial}{\partial\theta}\left(\sin\left(\theta\right)\frac{\partial\Theta\left(\theta\right)\Phi\left(\phi\right)}{\partial\theta}\right)+\frac{1}{\sin^2\left(\theta\right)}\frac{\partial^2\Theta\left(\theta\right)\Phi\left(\phi\right)}{\partial\phi^2}=0 \tag{8.32}$$

This equation can be slightly modified to separate the dependancies as follows.

$$C\sin^2\left(\theta\right)\Theta\left(\theta\right)\Phi\left(\phi\right)+\sin\left(\theta\right)\frac{\partial}{\partial\theta}\left(\sin\left(\theta\right)\frac{\partial\Theta\left(\theta\right)\Phi\left(\phi\right)}{\partial\theta}\right)+\frac{\partial^2\Theta\left(\theta\right)\Phi\left(\phi\right)}{\partial\phi^2}=0 \tag{8.33}$$

Removing the pieces of the original $Y\left(\theta,\phi\right)$ function from the partial derivatives that do not depend upon the variable of differentiation yields:

$$C\sin^2\left(\theta\right)\Theta\left(\theta\right)\Phi\left(\phi\right)+\Phi\left(\phi\right)\sin\left(\theta\right)\frac{\partial}{\partial\theta}\left(\sin\left(\theta\right)\frac{\partial\Theta\left(\theta\right)}{\partial\theta}\right)+\Theta\left(\theta\right)\frac{\partial^2\Phi\left(\phi\right)}{\partial\phi^2}=0 \tag{8.34}$$

$$C\sin^2\left(\theta\right)+\frac{1}{\Theta\left(\theta\right)}\sin\left(\theta\right)\frac{\partial}{\partial\theta}\left(\sin\left(\theta\right)\frac{\partial\Theta\left(\theta\right)}{\partial\theta}\right)+\frac{1}{\Phi\left(\phi\right)}\frac{\partial^2\Phi\left(\phi\right)}{\partial\phi^2}=0 \tag{8.35}$$

$$\frac{1}{\Theta\left(\theta\right)}\left[\sin\left(\theta\right)\frac{\partial}{\partial\theta}\left(\sin\left(\theta\right)\frac{\partial\Theta\left(\theta\right)}{\partial\theta}\right)+C\sin^2\left(\theta\right)\Theta\left(\theta\right)\right]=-\frac{1}{\Phi\left(\phi\right)}\frac{\partial^2\Phi\left(\phi\right)}{\partial\phi^2} \tag{8.36}$$

This completely separated equation can be related again to a separation constant, which will be called M^2. Note that the constant is squared because the second derivative of the conical solution given yields a squared term; this simply avoids needing to have a square root. Looking first at the azimuthal equation, we see that its solutions are readily known. They are given in Equation 8.37.

$$\frac{\partial^2\Phi\left(\phi\right)}{\partial\phi^2}+M^2\Phi\left(\phi\right)=0\rightarrow\Phi\left(\phi\right)=Ne^{iM\phi} \tag{8.37}$$

To have a normalized wave function, the value of N is subject to the condition that the integral over one period is: $\int_0^{2\pi}\Phi^*\left(\phi\right)\Phi\left(\phi\right),d\phi=1$. This means that $N=2\pi-\frac{1}{2}$. Finally, M can be solved by applying a cyclic boundary condition that $e^{iM\phi}=e^{iM\left(\phi+2\pi\right)}$. Separating the boundary condition yields:

$$e^{iM\phi}=e^{iM\left(\phi+2\pi\right)}=e^{iM\phi}e^{iM2\pi}\rightarrow e^{iM2\pi}=1 \tag{8.38}$$

This means that $M \in \mathbb{Z}$. This forms a constraint on the elevation equation which is given again for clarity.

$$\frac{1}{\Theta(\theta)} \left[\sin(\theta) \frac{\partial}{\partial \theta} \left(\sin(\theta) \frac{\partial \Theta(\theta)}{\partial \theta} \right) + C \sin^2(\theta) \Theta(\theta) \right] = M^2 \tag{8.39}$$

Simplifying and combining terms yields:

$$\frac{\partial}{\partial \theta} \left(\sin(\theta) \frac{\partial \Theta(\theta)}{\partial \theta} \right) + \left[C \sin(\theta) - \frac{M^2}{\sin(\theta)} \right] \Theta(\theta) = 0 \tag{8.40}$$

This equation is in the form of the general Legendre equation assuming that M is an integer, which was just proved, and that the constant $C = J(J+1)$ where $J \geq |M|$. Thus, the rotational energy levels which satisfy Schrödinger's Equation must have a $J(J+1)$ quantization. Furthermore, the wave functions that correspond to those energy values are the associated Legendre polynomials. To relate these results to the energy levels used in the main body of this paper, one must simply set $C = \frac{2IE}{\hbar}$ where I is the moment of inertia of the rigid rotor and E is the energy level of interest. Solving for E explicitly, in Equation 8.41, yields the energy for a rigid rotor.

$$\boxed{E = hc \frac{\hbar}{2I} J(J+1) = hcB_o J(J+1)} \tag{8.41}$$

8.3.3 Solving the Seperated Schrödinger's Equation For A Harmonic Oscillator

As with the rotational quantization procedure, a few more steps are needed to solve Equation 8.28. This will be performed after the first separation constant, C, is carefully considered. First the coordinates used will be redefined to be displacement from equilibrium instead of internuclear distance. Next a definition of the potential energy function for a harmonic oscillator will be given, which is a function of the spring constant and the distance from equilibrium. This will yield a conical form of the equation from which a solution can be guessed with the quantization chosen to force the guessed solution to fit all cases.

The first thing to consider is the separation constant, C, which results from the separation of variables into radial and angular wave function. As a harmonic oscillator has no angular component,

it is reasonable to set the value of the separation constant to zero. By doing so, no rotational quantum numbers exist that can satisfy the rigid rotor solutions. Therefore, Equation 8.28 can be recast as:

$$\frac{1}{R^2}\frac{\partial}{\partial R}\left(R^2\frac{\partial S(R)}{\partial R}\right) + \frac{2\mu}{\hbar^2}\left(E - E_n^0\right)S(R) = 0 \tag{8.42}$$

A redefinition of coordinates for a harmonic oscillator are reasonable because the radial distance, R, is always positive, but the forces acting on the atoms change about the equilibrium distance, Q. Thus, equilibrium distance is a more reasonable physical variable to use. Thus, Equation 8.28 can be recast as given in Equation 8.43.

$$\frac{\partial^2}{\partial Q^2}S(Q) + \frac{2\mu}{\hbar^2}\left(E - E_n^0\right)S(Q) = 0 \tag{8.43}$$

The harmonic oscillator is defined with a clear potential function that is simply a function of the spring constant, K, and the squared separation of the atoms in the oscillator. Therefore, Equation 8.43 can be slightly modified to:

$$\frac{\partial^2}{\partial Q^2}S(Q) + \frac{2\mu}{\hbar^2}\left(E - \frac{K}{2}Q^2\right)S(Q) = 0 \tag{8.44}$$

A constant, $\beta^2 = \frac{\hbar}{\sqrt{\mu K}}$, can be defined, which will help simplify the above equation. Furthermore, a reduced distance variable, $\tilde{Q}$, is introduced such that $\tilde{Q} = \frac{Q}{\beta}$. The second partial of this equation is given as $\frac{\partial^2}{\partial Q^2} = \frac{1}{\beta^2}\frac{\partial^2}{\partial \tilde{Q}^2}$. Substituting in these definitions yields a final form given in Equation 8.47.

$$\frac{1}{\beta^2}\frac{\partial^2}{\partial \tilde{Q}^2}S\left(\tilde{Q}\right) + \frac{2\mu}{\hbar^2}\left(E - \frac{K}{2}\left(\tilde{Q}\beta\right)^2\right)S\left(\tilde{Q}\right) = 0 \tag{8.45}$$

$$\frac{\partial^2}{\partial \tilde{Q}^2}S\left(\tilde{Q}\right) + \left(\frac{2\mu\beta^2}{\hbar^2}E - \frac{2\mu\beta^2}{\hbar^2}\frac{K}{2}\left(\tilde{Q}\beta\right)^2\right)S\left(\tilde{Q}\right) = \frac{\partial^2}{\partial \tilde{Q}^2}S\left(\tilde{Q}\right) + \left(\frac{2\mu\beta^2}{\hbar^2}E - \frac{\beta^4}{\frac{\hbar^2}{\mu K}}\tilde{Q}^2\right)S\left(\tilde{Q}\right) = 0 \tag{8.46}$$

$$\frac{\partial^2}{\partial \tilde{Q}^2} S\left(\tilde{Q}\right) + \left(\frac{2\mu\beta^2}{\hbar^2}E - \tilde{Q}^2\right) S\left(\tilde{Q}\right) = 0 \tag{8.47}$$

The Hermite polynomials can be used to solve the above equation. The wave function can be calculated as given in Equation 8.48 where H_v is the vth Hermite polynomial and N_v is the normalization of that function.

$$S\left(\tilde{Q}\right) = N_v H_v \exp\left(-\frac{\tilde{Q}^2}{2}\right) = \left[\frac{1}{\sqrt{2^v v! \sqrt{\pi}}}\right]\left[(-1)^{-1}\exp\left(\tilde{Q}^2\right)\frac{\partial^v}{\partial \tilde{Q}^v}\exp\left(-\tilde{Q}^2\right)\right]\left[\exp\left(-\frac{\tilde{Q}^2}{2}\right)\right]$$

$$\tag{8.48}$$

The wave function given in Equation 8.48 is inherently quantized because the Hermite polynomials are defined for $v \in \mathbb{Z}$. Plugging this function back into Schrödinger's Equation yields an energy quantization given in Equation 8.49.

$$\boxed{E = \left(v + \frac{1}{2}\right)\hbar\sqrt{\frac{K}{\mu}}} \tag{8.49}$$

8.3.4 Expression and Derivation of Inversion Properties by Klett

Starting with the scalar lidar equation, because polarization is ignored, and assuming that the observed and transmitted wavelength are the same, one can derive an expression for the total backscattering efficiency as a function of range and measurements near the current measurement.

$$N = \left[\frac{P_L\left(\lambda_{T_x}\right)\Delta t}{\frac{hc}{\lambda_{T_x}}}\right][\sigma(\lambda_{T_x}, \lambda_{R_x})N_D(R)\Delta R]\left[\frac{A}{R^2}\right][T_{T_x}\left(\lambda_{T_x}R\right)T_{R_x}\left(\lambda_{R_x}R\right)][\eta_{T_x}\eta_{R_x}G(R)] + N_B\left(\lambda_{R_x}\right)$$

$$\tag{8.50}$$

The derivation of the Klett inversion as originally performed by Klett [152] begins by converting the lidar equation for count number to power as given in Equation 8.51.

$$P - P_B\left(\lambda\right) = [P_L\left(\lambda\right)\eta_{T_x}][\beta(R, \lambda)\Delta R]\left[\frac{A\eta_{R_x}}{R^2}\right]\left[T^2\left(\lambda, R\right)\right][G(R)] \tag{8.51}$$

The transmission integral in Equation 8.51 is cast into its explicit form in Equation 8.52.

$$P_{BS}\left(\lambda\right) = P_L\left(\lambda\right)\eta_{T_x}\beta(R, \lambda)\Delta R\left[\frac{A\eta_{R_x}}{R^2}\right]\exp\left[-2\int_0^R \sigma\left(R'\right)dR'\right]G(R) \tag{8.52}$$

Further removing dependancies from Equation 8.52 by range and overlap correcting correcting is given in Equation 8.53.

$$\frac{R^2 P_{BS}(\lambda)}{G(R)} = P_L(\lambda)\,\eta_{T_x}\beta(R,\lambda)\Delta RA\eta_{R_x}\exp\left[-2\int_0^R \sigma\left(R'\right)dR'\right] \tag{8.53}$$

Taking the natural logarithm of the Equation 8.53 to remove the exponential element of transmission is given in Equation 8.54.

$$\ln\left(\frac{R^2 P_{BS}(\lambda)}{G(R)}\right) = \ln\left(P_L(\lambda)\,\eta_{T_x}\beta(R,\lambda)\Delta RA\eta_{R_x}\exp\left[-2\int_0^R \sigma\left(R'\right)dR'\right]\right) \tag{8.54}$$

On can redefine the logarithm of the range and overlap corrected signal measured power as $Z(R,\lambda)$, which is given in Equation 8.54.

$$Z(R,\lambda) = \ln\left(P_L(\lambda)\,\eta_{T_x}\beta(R,\lambda)\Delta RA\eta_{R_x}\exp\left[-2\int_0^R \sigma\left(R'\right)dR'\right]\right) \tag{8.55}$$

Performing back integration is akin to subtracting two $Z(R,\lambda)$ values at different range. This is shown in Equation 8.56.

$$Z(R_2,\lambda) - Z(R_1,\lambda) = \ln\left(\frac{P_L(\lambda)\,\eta_{T_x}\beta(R,\lambda)\Delta RA\eta_{R_x}\exp\left[-2\int_0^{R_2}\sigma\left(R'\right)dR'\right]}{P_L(\lambda)\,\eta_{T_x}\beta(R,\lambda)\Delta RA\eta_{R_x}\exp\left[-2\int_0^{R_1}\sigma\left(R'\right)dR'\right]}\right) \tag{8.56}$$

Canceling out common terms yields a simplified expression for Equation 8.56 given in Equation 8.57 and with its terms parsed in Equation 8.58.

$$Z(R_2,\lambda) - Z(R_1,\lambda) = \ln\left(\frac{\beta(R_2,\lambda)\exp\left[-2\int_0^{R_2}\sigma\left(R'\right)dR'\right]}{\beta(R_1,\lambda)\exp\left[-2\int_0^{R_1}\sigma\left(R'\right)dR'\right]}\right) \tag{8.57}$$

$$Z(R_2,\lambda) - Z(R_1,\lambda) = \ln\left(\frac{\beta(R_2,\lambda)}{\beta(R_1,\lambda)}\right) - 2\int_{R_1}^{R_2}\sigma\left(R'\right)dR' \tag{8.58}$$

The differential form of Equation 8.58 is given in Equation 8.59 assuming the constitutive relationship $\beta = c_o\sigma^K$

$$\frac{\partial Z}{\partial R} = \frac{1}{\beta}\frac{\partial\beta}{\partial R} - 2\sigma \tag{8.59}$$

Equation 8.59 is exactly how it is formulated by Klett in his initial inversion except the Z term also contains the overlap function [152].

8.3.5   Extracting Water Vapor Mixing Ratio From Raman Measurement

The derivation of the extraction of water vapor mixing ratio for Raman signals starts with the scalar lidar equation given in Equation 2.1 and reproduced in Equation 8.60 for reference.

$$N = \left[\frac{P_L\left(\lambda_{T_x}\right)\Delta t}{\frac{hc}{\lambda_{T_x}}} \right] \left[\sigma(\lambda_{T_x}, \lambda_{R_x})N_D(R)\Delta R\right] \left[\frac{A}{R^2}\right] \left[T_{T_x}\left(\lambda_{T_x}, R\right)T_{R_x}\left(\lambda_{R_x}, R\right)\right] \left[\eta_{T_x}\eta_{R_x}G(R)\right]$$
$$+ N_B\left(\lambda_{R_x}\right)$$

(8.60)

By taking the ratio of two background subtracted signals, vibrational Raman scattering of water vapor and vibrational Raman scattering of nitrogen, the mixing ratio can be calculated. This ratio is given in Equation 8.61, where the blue terms will directly cancel because they are common to both channels.

$$\frac{N_W - N_{B_W}}{N_{N_2} - N_{B_{N_2}}} =$$

$$\frac{\left[\frac{P_L(\lambda_{T_x})\Delta t}{\frac{hc}{\lambda_{T_x}}}\right]\left[\sigma(\lambda_{T_x}, \lambda_{R_x})N_{D_{water}}(R)\Delta R\right]\left[\frac{A}{R^2}\right]\left[T_{T_x}\left(\lambda_{T_x}R\right)T_{R_x}\left(\lambda_{R_x}R\right)\right]\left[\eta_{T_x}\eta_{R_x}G(R)\right]}{\left[\frac{P_L(\lambda_{T_x})\Delta t}{\frac{hc}{\lambda_{T_x}}}\right]\left[\sigma(\lambda_{T_x}, \lambda_{R_x})N_{D_{N_2}}(R)\Delta R\right]\left[\frac{A}{R^2}\right]\left[T_{T_x}\left(\lambda_{T_x}R\right)T_{R_x}\left(\lambda_{R_x}R\right)\right]\left[\eta_{T_x}\eta_{R_x}G(R)\right]}$$

(8.61)

Equation 8.61 can be simplified as given below in Equation 8.62. In this equation, note that the green terms will form a non-range dependent calibration term and the red terms will form a range dependent calibration term. This is given explicitly in Equation 8.63.

$$\frac{N_W - N_{B_W}}{N_{N_2} - N_{B_{N_2}}} = \frac{\sigma(355[nm], 408[nm])N_{D_{water}}(R)T_{R_x}\left(408[nm], R\right)\eta_{R_x}\left(408[nm]\right)G(R)}{\sigma(355[nm], 387[nm])N_{D_{N_2}}(R)T_{R_x}\left(387[nm], R\right)\eta_{R_x}\left(387[nm]\right)G(R)}$$

(8.62)

$$\frac{N_W - N_{B_W}}{N_{N_2} - N_{B_{N_2}}} = \tilde{C}_1 C_2(R)\frac{N_{D_{water}}(R)}{N_{D_{N_2}}(R)}$$

(8.63)

One can then note that the water vapor mixing ratio can be given as a function of the number density of each species and the molecular weight of that species. This is given in Equation 8.64.

$$w = \frac{Mass_{Water}}{Mass_{Air}} = \frac{N_{D_{Water}}M_{Water}}{N_{D_{Air}}M_{Air}}$$

(8.64)

Assuming that air consists of 79% nitrogen, Equation 8.64 can be recast as given in Equation 8.65.

$$w = \frac{N_{D_{Water}} M_{Water}}{\frac{N_{D_{N_2}}}{0.79} M_{Air}} \tag{8.65}$$

Finally, inserting the ratio of number densities defined in Equation 8.63 yields an equation for the calculation of water vapor mixing ratio given in Equation 8.66.

$$\boxed{w(R) = \frac{0.79}{\tilde{C}_1 C_2(R)} \frac{M_{water}}{M_{N_2}} \frac{N_W - N_{B_W}}{N_{N_2} - N_{B_{N_2}}} = \frac{C_1}{C_2(R)} \frac{N_W - N_{B_W}}{N_{N_2} - N_{B_{N_2}}}} \tag{8.66}$$

Here the final range independent calibration constant is given as:

$$C_1 = \frac{0.79}{\tilde{C}_1} \frac{M_{water}}{M_{N_2}} \tag{8.67}$$

Here Equation 8.66 is equal to the equation given by Wandinger (Equation 9.24 from [50] for reference) with the exception that the range dependent calibration term also includes possible mismatches in the overlap function. This term cancels exactly assuming the fields of view of the two Raman channels are coincident which is not necessarily true.

8.3.6   Extracting Temperature From Raman Measurement

The temperature of the atmosphere can be measured by measuring the Stokes or anti-Stokes rotational Raman component of one of the major atmospheric constituents. In this case, both bands are chosen on the anti-Stokes side and due to the small energy separation of the rotational levels, it is not possible to remove the nitrogen and oxygen portions. Therefore, the scattering will be from both. In this case, a ratio of the two are given below in Equation 8.68 where again the blue terms will directly cancel.

$$\frac{N_{H_j} - N_{B_{H_j}}}{N_{L_j} - N_{B_{L_j}}} =$$

$$\frac{\left[\frac{P_L(\lambda_{T_x})\Delta t}{\frac{hc}{\lambda_{T_x}}}\right] \left[\sigma(\lambda_{T_x}, \lambda_{R_x}) N_{D_{N_2/O_2}}(R)\Delta R\right] \left[\frac{A}{R^2}\right] \left[T_{T_x}(\lambda_{T_x} R) T_{R_x}(\lambda_{R_x} R)\right] \left[\eta_{T_x} \eta_{R_x} G(R)\right]}{\left[\frac{P_L(\lambda_{T_x})\Delta t}{\frac{hc}{\lambda_{T_x}}}\right] \left[\sigma(\lambda_{T_x}, \lambda_{R_x}) N_{D_{N_2/O_2}}(R)\Delta R\right] \left[\frac{A}{R^2}\right] \left[T_{T_x}(\lambda_{T_x} R) T_{R_x}(\lambda_{R_x} R)\right] \left[\eta_{T_x} \eta_{R_x} G(R)\right]}$$

$$\tag{8.68}$$

Equation 8.68 can be simplified as given below in Equation 8.69. In this equation, note that the green terms will form a non-range dependent calibration term and the red terms will form a range dependent calibration term. This is given explicitly in Equation 8.70.

$$\frac{N_{H_j} - N_{B_{H_j}}}{N_{L_j} - N_{B_{L_j}}} = \frac{\sigma(355[nm], 353[nm]) T_{R_x}(353[nm], R) \, \eta_{R_x}(353[nm]) \, G(R)}{\sigma(355[nm], 354[nm]) T_{R_x}(354[nm], R) \, \eta_{R_x}(354[nm]) \, G(R)} \tag{8.69}$$

$$\frac{N_{H_j} - N_{B_{H_j}}}{N_{L_j} - N_{B_{L_j}}} = C_3 C_4(R) \frac{\sigma(355[nm], 353[nm])}{\sigma(355[nm], 354[nm])} \tag{8.70}$$

Finally, the ratio of scattering coefficients is temperature dependent. Thus, the temperature is proportional to that ratio as show in Equation 8.71. The temperature dependence of several wavelength bands for nitrogen is given below in Figure 8.1 and the ratio of two of those bands is given in Figure 8.2. Note that this assumes a rectangular filter function and infinitely sharp Raman lines. Both are weaknesses of the model that should be improved for publication.

$$T \propto \frac{\sigma(355[nm], 353[nm])}{\sigma(355[nm], 354[nm])} = \frac{1}{C_3 C_4(R)} \frac{N_{H_j} - N_{B_{H_j}}}{N_{L_j} - N_{B_{L_j}}} \tag{8.71}$$

Many techniques exist to leverage this proportionality shown here which have different accuracies. They are well discussed by Behrendt [50]. Note that this derivation's goal is simply to discuss the proportionality of the temperature to the Raman signal intensities.

Figure 8.1 can be expanded to include more wavelength bands. This will help in selecting adequate bands with enough signal. A line by line simulation was run where the first 50 Raman lines were calculated for the anti-Stokes rotational transition. A 0.3 nm bandpass filter with a rectangular filter function was then assumed and run through many different central wavelengths and temperatures. All the transition lines that existed within that band were then summed to yield an overall backscattering cross section as a function of center wavelength and location. Figure 8.3 shows the results of that simulation. Note that the exact transmitted wavelength was 354.7 nm and that the lines are assumed infinitely sharp.
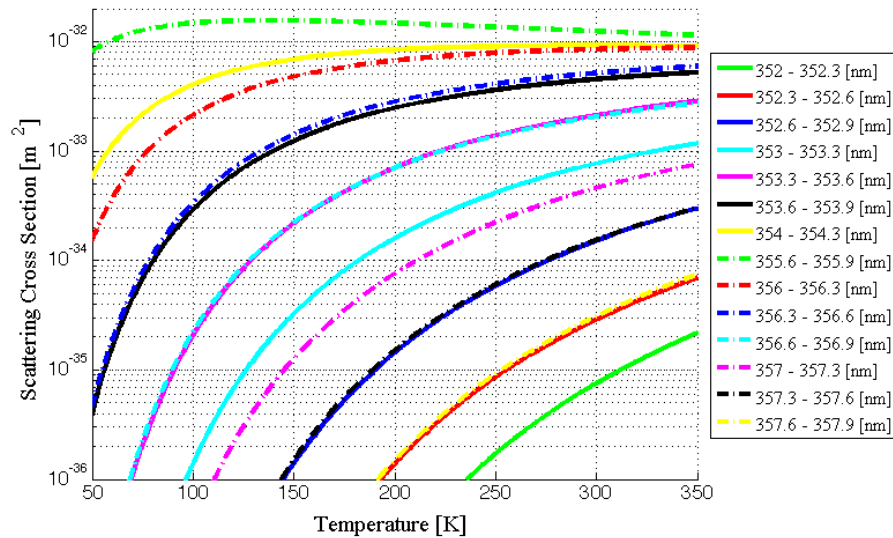
Figure 8.1: Scattering cross section of nitrogen as a function of temperature for several different wavelength bands.
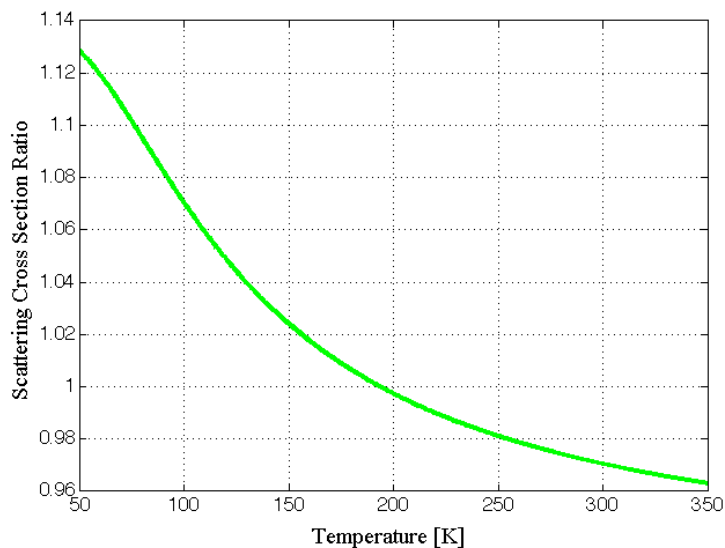
Figure 8.2: The ratio of two different wavelength bands cross sections as s function of temperature. In this case the two bands of interest are 352.6-352.9 nm and 353.6-353.9 nm. In the given calculations the former is rounded up and called 353 nm and the latter 354 nm or High J and Low J respectively.

8.3.7   Orthogonal Depolarization Measurement

To measure the polarization properties of a medium, one simply needs to specify the terms of the Stokes vector lidar equation given in Equation 2.9. Each term is split out and the assumptions
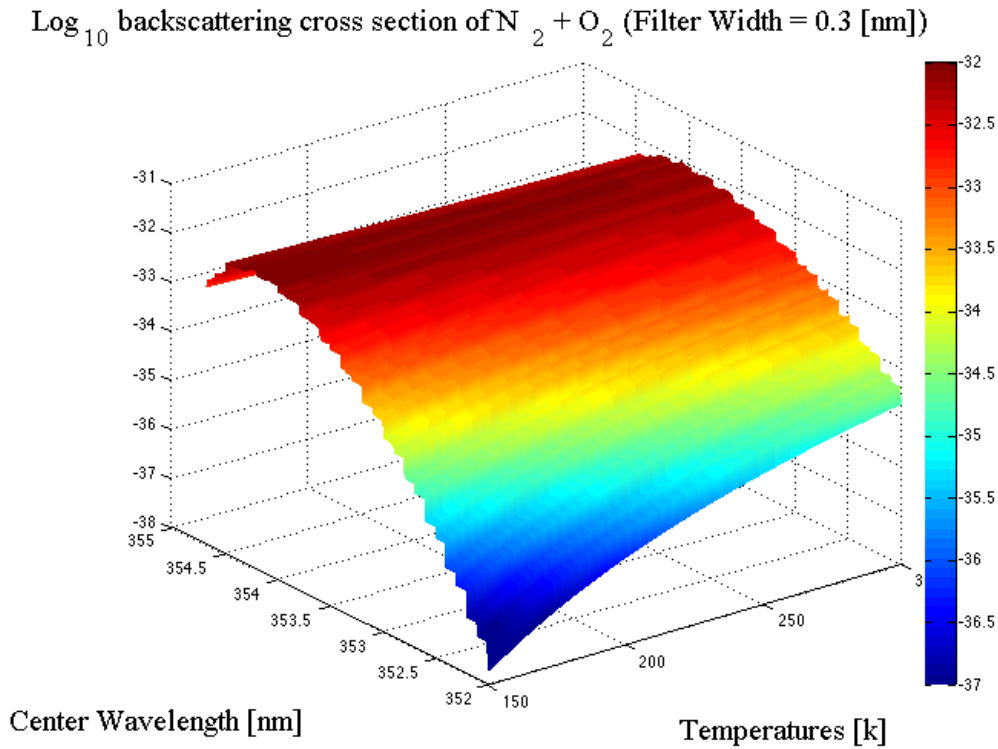
Figure 8.3: A surface illustrating the backscattering cross sections of many possible center wavelength filters at many relevant temperatures.

used to define the terms are given. First, it is assumed that the transmit system is designed in such a way that it is an identity matrix and that the polarization leaving the system is the definition of the parallel axis. This is given in Equation 8.72.

$$\bar{\bar{M}}_{T_x} \bar{S}_{T_x} = \left[\frac{P_L\left(\lambda_{T_x}\right) \Delta t}{\frac{hc}{\lambda_{T_x}}} \right] \begin{bmatrix} 1 \\ 1 \\ 0 \\ 0 \end{bmatrix} \tag{8.72}$$

Next it is assumed that only single scattering occurs and that the transmission is not polarization dependent. Therefore, the transmission matrix can be simplified to a range only dependent term and the identity matrix. This is the case for both the transmit beam, given in Equation 8.73, and

the received beam, given in Equation 8.74.

$$\bar{\bar{T}}_{atm}\left(\bar{k}_i, R\right) = T_{atm}\left(\lambda_{T_x}, R\right) \begin{bmatrix} 1 & 0 & 0 & 0 \\ 0 & 1 & 0 & 0 \\ 0 & 0 & 1 & 0 \\ 0 & 0 & 0 & 1 \end{bmatrix} \tag{8.73}$$

$$\bar{\bar{T}}_{atm}\left(\bar{k}_s, R\right) = T_{atm}\left(\lambda_{R_x}, R\right) \begin{bmatrix} 1 & 0 & 0 & 0 \\ 0 & 1 & 0 & 0 \\ 0 & 0 & 1 & 0 \\ 0 & 0 & 0 & 1 \end{bmatrix} \tag{8.74}$$

Next, the strictly randomly oriented matrix will be assumed. This is given below in Equation 8.75 and is a function of two variables: the backscattering coefficient β and the depolarization, d [100].

$$\bar{\bar{F}}\left(\bar{k}_i, \bar{k}_s, R\right) = \beta \begin{bmatrix} 1 & 0 & 0 & 0 \\ 0 & 1-d & 0 & 0 \\ 0 & 0 & d-1 & 0 \\ 0 & 0 & 0 & 2d-1 \end{bmatrix} \tag{8.75}$$

Next, the receiver system has a polarization compensator so it will be assumed that the matrix defining the system is just a rotating polarizer [96].

$$\bar{\bar{M}}_{R_x}\left(\theta\right) = \begin{bmatrix} 1 & 0 & 0 & 0 \\ 0 & cos\left(2\theta\right) & -\sin\left(2\theta\right) & 0 \\ 0 & \sin\left(2\theta\right) & cos\left(2\theta\right) & 0 \\ 0 & 0 & 0 & 1 \end{bmatrix} \begin{bmatrix} 1 & 1 & 0 & 0 \\ 1 & 1 & 0 & 0 \\ 0 & 0 & 0 & 0 \\ 0 & 0 & 0 & 0 \end{bmatrix} \begin{bmatrix} 1 & 0 & 0 & 0 \\ 0 & cos\left(-2\theta\right) & -\sin\left(-2\theta\right) & 0 \\ 0 & \sin\left(-2\theta\right) & cos\left(-2\theta\right) & 0 \\ 0 & 0 & 0 & 1 \end{bmatrix} \tag{8.76}$$

Finally, the background is assumed to be non-polarized. Thus, it is given in Equation 8.77 where it is a non-polarized Stokes vector multiplied by the number of photon counts.

$$\bar{S}_B(\lambda_{R_x}) = N_B \begin{bmatrix} 1 \\ 0 \\ 0 \\ 0 \end{bmatrix} \tag{8.77}$$

If we insert all of these matrices into Equation 2.9 a form of the number of photons received as a function of observation angle can be derived. This is given in Equation 8.78.

$$N\left(\theta\right) \propto \beta\left(1 - d\right)\cos\left(2\theta\right) \tag{8.78}$$

Depolarization can be measured simply by any two angles. In this case, the canonical parallel and perpendicular channels are assumed. This is given in Equation 8.79. Note that the proportionality sign falls out because all of the constants that are neglected in Equation 8.78 like the laser power, overlap function, solid angle, integration range, and integration time cancel directly. $N_\perp$ and $N_\parallel$ must be given as background subtracted signal.

$$\boxed{d = \frac{2N_\perp}{N_\parallel + N_\perp}} \tag{8.79}$$

8.3.8   Orthogonal Diattenuation Measurement

To measure preferential orientation in the atmosphere, one needs to do one of two things. One can either look for strong specular reflections at normal incidence as was done by Thomas [130] or one can measure multiple terms of the backscattering phase matrix with an off-zenith pointing system [89, 98, 100, 111]. First, it is assumed that the transmit system is designed in such a way that it is an identity matrix and that the polarization leaving the system is the definition of the 45 degree axis. This is given in Equation 8.80. This angle is referenced to the tilt angle of the system and is chosen to avoid interogating the phase scattering matrix and removing more than

three unknown terms.

$$\bar{\bar{M}}_{T_x} \bar{S}_{T_x} = \left[\frac{P_L\left(\lambda_{T_x}\right)\Delta t}{\frac{hc}{\lambda_{T_x}}} \right] \begin{bmatrix} 1 \\ 0 \\ 1 \\ 0 \end{bmatrix} \tag{8.80}$$

The transmission matrices are as before with the depolarization derivation and are given in Equation 8.73 for the transmitted beam and the received beam, given in Equation 8.74.

The scattering matrix is again as given in Equation 3.27 in the main text but restated here in Equation 8.81.

$$\bar{\bar{F}}\left(\bar{k}_i, \bar{k}_s, R\right) = \begin{bmatrix} f_{11}\left(\Theta,\Phi\right) & f_{12}\left(\Theta,\Phi\right) & 0 & 0 \\ f_{12}\left(\Theta,\Phi\right) & f_{22}\left(\Theta,\Phi\right) & 0 & 0 \\ 0 & 0 & f_{33}\left(\Theta,\Phi\right) & f_{34}\left(\Theta,\Phi\right) \\ 0 & 0 & -f_{34}\left(\Theta,\Phi\right) & f_{44}\left(\Theta,\Phi\right) \end{bmatrix} \tag{8.81}$$

The receiver system is again as given in Equation 8.76 and the background is as given in Equation 8.77. When inserted in to the Stokes vector lidar equation, Equation 2.9, with the multiplication carried out, an equation of the following form results:

$$N\left(\theta, \Theta = \pi, \Phi = 0\right) \propto f_{11} + \cos\left(2\theta\right) f_{12} + \sin\left(2\theta\right) f_{33}. \tag{8.82}$$

If we select out three measurements such that channels 2 and 3 are parallel and orthogonal to the outgoing beam respectively and channel 3 is 45 degrees from both yields a set of three equations and three unknowns. Solving this set for f_{12} is given in Equation 8.83.

$$\boxed{f_{12} = \frac{2N_3}{N_1 + N_2} - 1} \tag{8.83}$$

8.4   Modified Equations

The original equations used by Wandinger which are replaced by Equation 3.25 in the main text are given in Equation 8.84.

$$
\Phi_j = \begin{cases}
\dfrac{\left(\frac{h}{8\pi^2 c\tilde{\nu}_{vib}}\right)^2}{1-\exp\left[\frac{-hc\tilde{\nu}_{vib}}{k_B T}\right]} \dfrac{7J(J-1)}{30(2J-1)} \gamma'^2 & \Delta J = -2 \\[2em]
\dfrac{\left(\frac{h}{8\pi^2 c\tilde{\nu}_{vib}}\right)^2 (2J+1)}{1-\exp\left[\frac{-hc\tilde{\nu}_{vib}}{k_B T}\right]} \left[a'^2 + \dfrac{7J(J+1)}{45(2J+3)(2J-1)} \gamma'^2 \right] & \Delta J = 0 \\[2em]
\dfrac{\left(\frac{h}{8\pi^2 c\tilde{\nu}_{vib}}\right)^2}{1-\exp\left[\frac{-hc\tilde{\nu}_{vib}}{k_B T}\right]} \dfrac{7(J+1)(J+2)}{30(2J+3)} \gamma'^2 & \Delta J = 2
\end{cases}
\tag{8.84}
$$

8.5   More Summit Polarized Raman Lidar Detail

Lists of the optics and mounts that compose the the transmitter and receiver can be found here. The transmitter optics and mounts are given in Tables 8.4 and 8.5 respectively and receiver optics and mounts are given in Tables 8.6 and 8.7/8.8 respectively.

Table 8.4: Transmitter optic description. The numbers correspond to the numbers given in Figure 6.1. Note that the numbering nomenclature below has a single path after optic 2. #.L1 corresponds to the path from laser 1 to the common path and #.L2 corresponds to the path from laser 2 to the common path. The O.T simply stands for Optic.Transmitter.

Number	Description	Maker	Model Number	Price
O.T.1.L1	1" High Energy Nd:YAG Laser Mirror	CVI	Y3-1025-45	$135.00
O.T.1.L2	1" High Energy Nd:YAG Laser Mirror	CVI	Y3-1025-45	$135.00
O.T.2	1" High Energy Nd:YAG Laser Mirror	CVI	Y3-1025-45	$135.00
O.T.3	1" High Energy Nd:YAG Laser Mirror	CVI	Y3-1025-45	$135.00
O.T.4	1" Quarter Wave Plate	CVI	QWPM-355-10-4	$332.00
O.T.5	3x Beam Expander	CVI	BXUV-10.0-3X-355	$1,745.00
O.T.6	2" High Energy Nd:YAG Laser Mirror	CVI	Y3-2037-45	$225.00
O.T.7	3" High Energy Nd:YAG Laser Mirror	CVI	Y3-3050-45	$670.00
O.T.8	27" high energy lidar window	Orca		$6,976.00
			Sub Total	$10,488.00
			10% Discount	———
			Total	$10,488.00

Table 8.5: Transmitter mounting description. The numbers correspond to the numbers given in Figure 6.1 and to the optics listed in Table 8.4. Note that the numbering nomenclature below has a single path after optic 2. #.L1 corresponds to the path from laser 1 to the common path and #.L2 corresponds to the path from laser 2 to the common path. The M.T. simply stands for Mount.Transmitter.

Number	Description	Maker	Model Number	Price
M.T.1.L1	Polaris 1" Kinematic Mirror Mounts	Thor	POLARIS-K1	$129.00
M.T.1.L2	Motorized Flip Mount	Thor	MFF101	$619.50
M.T.2	Polaris 1" Kinematic Mirror Mounts	Thor	POLARIS-K1	$129.00
M.T.3	Polaris 1" Kinematic Mirror Mounts	Thor	POLARIS-K1	$129.00
M.T.4	Motorized Rotation Stage and Controller	Thor	PRM1Z8E	$1,301.50
M.T.5	3x Beam Expander			$
M.T.6	2" Precision Kinematic Mirror Mount	Thor	KS2	$124.00
M.T.7	3" Precision Kinematic Mirror Mount	Thor	KS3	$179.50
M.T.7.2	DC Servo Motor Actuators, 12 mm Travel	Thor	Z812	$1,180.00
M.T.7.3	DC Servo Motor Actuators, 12 mm Travel	Thor	Z812	$1,180.00
M.T.8	Transmit window cell	NCAR		$6,731.00
			Sub Total	$11,701.50
			10% Discount	$497.05
			Total	$11,204.45

Table 8.6: Receiver optic description. The numbers correspond to the numbers given in Figure 6.1. The O.R. in the numbering simply stands for Optic.Receiver. Note that there are numbers missing, which is acceptable because there are more mounts than optics. To force the number to align such that the optic that resides in a certain mount have the same number, optical numbering must skip empty mounts.

Number	Description	Maker	Model Number	Price
O.R.00	24" Dall-Kirkham Telescope	Planewave	DK24	$62850.00
O.R.01	2" UV Dielectric Mirror	Newport	5120	$389.00
O.R.03	Ring-Activated Threaded Iris	Thor	SM1D12C	$96.60
O.R.04	1" Near UV Achromat, 50mm EFL	Edmunds	65-975	$107.50
O.R.05.1	Ring-Activated Threaded Iris	Thor	SM1D12C	$96.60
O.R.05.2	1" Broadband Dielectric Mirror	ATF	MI1000-VIS	$230.00
O.R.06	1" 424 nm Shortpass Filter	Semrock	FF01-424/SP-25	$349.00
O.R.07	Nitrogen Dichroic	Materion	F-DB-0013750	$3990.00
O.R.08	1" Power Beam Splittter (90R-10T)	RMI	NPP90-10 355	$765.00
O.R.09	1" Elastic Filter	Materion	F-NB-0013744	$2280.00
O.R.12	1" Multi-Order Quarter-Wave Plate	Thor	WPMQ10M-355	$310.08
O.R.13	1" Multi-Order Half-Wave Plate	Thor	WPMH10M-355	$310.08
O.R.16	1" UV Laser Line Cube Polarizer	CVI	UPBS-355-100	$582.00
O.R.17	1" UV Laser Line Cube Polarizer	CVI	UPBS-355-100	$582.00
O.R.18	1" Near UV Achromat, 50mm EFL	Edmunds	65-975	$107.50
O.R.20	1" Raman Longpass Filter	Semrock	BLP01-335R-25	$349.00
O.R.21	1" Raman Longpass Filter	Semrock	BLP01-335R-25	$349.00
O.R.22	Water Dichroic	Materion	F-DB-0013749	$4980.00
O.R.23	1" Nitrogen Filter	Materion	F-NB-0013745	$3840.00
O.R.24	1" Near UV Achromat, 50mm EFL	Edmunds	65-975	$107.50
O.R.26	1" Water Filter	Materion	F-NB-0013746	$3990.00
O.R.27	1" Near UV Achromat, 50mm EFL	Edmunds	65-975	$107.50
O.R.29	Power Beam Splitter (50R/50T)			$
O.R.30	1" High J Filter	Materion	F-NB-0013748	$7110.00
O.R.31	1" Near UV Achromat, 50mm EFL	Edmunds	65-975	$107.50
O.R.33	1" Broadband Dielectric Mirror	ATF	MI1000-VIS	$230.00
O.R.34	1" Low J Filter	Materion	F-NB-0013747	$8940.00
O.R.35	1" Near UV Achromat, 50mm EFL	Edmunds	65-975	$107.50
O.R.37	1" Power Beam Splittter (90R-10T)	RMI	NPP90-10 355	$765.00
O.R.38	1" Near UV Achromat, 50mm EFL	Edmunds	65-975	$107.50
O.R.40	1" Double-Convex Lens, 500mm FL	Edmunds	48-314	$110.00
O.R.41	1" Broadband Dielectric Mirror	ATF	MI1000-VIS	$230.00
O.R.44	10 mm Glan-Thompson Polarizer	Thor	GTH10M-A	$572.78
O.R.44	1" Broadband Dielectric Mirror	ATF	MI1000-VIS	$230.00
O.R.46	1" Near UV Achromat, 50mm EFL	Edmunds	65-975	$107.50
O.R.47	Elastic Filter	Materion	F-NB-0013744	$2280.00
O.R.48	Near UV Achromat, 50mm EFL	Edmunds	65-975	$107.50
O.R.49	Zero Aperture Iris	Thor	D25SZ	$51.60
			Sub Total	$106,815.96
			10% Discount	$143.85
			Total	$106,672.11

Table 8.7: Part 1 of 2 of the receiver mounting description. Part 2 is given in Table 8.8. The numbers correspond to the numbers given in Figure 6.1. The M.R. simply stands for Mount.Receiver.

Number	Description	Maker	Model Number	Price
M.R.01	Right Angle 60 mm Cage Kinematic Mount	Thor	KCB2	$155.40
M.R.02	30mm to 60mm Cage Plate Adapter	Thor	LCP02	$38.00
M.R.03	SM1-Threaded 30 mm Cage Plate, 0.35"	Thor	CP02	$16.00
M.R.04.1	SM1-Threaded 30 mm Cage Plate, 0.35"	Thor	CP02	$16.00
M.R.04.2	1" SM1 Lens Tube, 1" Long External Threads	Thor	SM1V10	$32.60
M.R.05	Right Angle 30 mm Cage Kinematic Mount	Thor	KCB1	$144.00
M.R.06	30 mm Cage System Removable Filter Holder	Thor	CFH2	$100.98
M.R.07	Dichroic Cage Cube	Thor	CM1-DCH	$153.00
M.R.08	Beam Splitter Cube (see Table 8.9)	Thor	————	$ 381.40
M.R.09	Precision Filtering (see Table 8.9)	Thor	————	$ 381.40
M.R.10	30mm to 60mm Cage Plate Adapter	Thor	LCP02	$38.00
M.R.11	30mm Rotating Cage Plate Segment	Thor	CPR1	$150.00
M.R.12	Motorized Cage Rotation Mount	Thor	PRM1Z8E	$1326.50
M.R.13	Motorized Cage Rotation Mount	Thor	PRM1Z8E	$1326.50
M.R.14	30mm Rotating Cage Plate Segment	Thor	CPR1	$150.00
M.R.15	30mm to 60mm Cage Plate Adapter	Thor	LCP02	$38.00
M.R.16	30 mm Cage Cube For Beamsplitters	Thor	CM1-4ER	$127.50
M.R.17	30 mm Cage Cube For Beamsplitters	Thor	CM1-4ER	$127.50
M.R.18	30 mm Cage XY Translator for 1" Optics	Thor	CXY1	$169.05
M.R.19	SM1-Threaded 30 mm Cage Plate, 0.35"	Thor	CP02	$16.00
M.R.20	30 mm Cage System Removable Filter Holder	Thor	CFH2	$100.98
M.R.21	30 mm Cage System Removable Filter Holder	Thor	CFH2	$100.98
M.R.22	Dichroic Cage Cube	Thor	CM1-DCH	$153.00
M.R.23	Precision Filtering (see Table 8.9)	Thor	————	$ 381.40
M.R.24	30 mm Cage XY Translator for 1" Optics	Thor	CXY1	$169.05
M.R.25	SM1-Threaded 30 mm Cage Plate, 0.35"	Thor	CP02	$16.00
M.R.26	Precision Filtering (see Table 8.9)	Thor	————	$ 381.40
M.R.27	30 mm Cage XY Translator for 1" Optics	Thor	CXY1	$169.05
M.R.28	SM1-Threaded 30 mm Cage Plate, 0.35"	Thor	CP02	$16.00
M.R.29	Beam Splitter Cube (see Table 8.10)	Thor	————	$ 198.10
M.R.30	Precision Filtering (see Table 8.9)	Thor	————	$ 381.40
M.R.31	30 mm Cage XY Translator for 1" Optics	Thor	CXY1	$169.05
M.R.32	SM1-Threaded 30 mm Cage Plate, 0.35"	Thor	CP02	$16.00
M.R.33	Right Angle 30 mm Cage Kinematic Mount	Thor	KCB1	$144.00
M.R.34	Precision Filtering (see Table 8.9)	Thor	————	$ 381.40
M.R.35	30 mm Cage XY Translator for 1" Optics	Thor	CXY1	$169.05
M.R.36	SM1-Threaded 30 mm Cage Plate, 0.35"	Thor	CP02	$16.00
M.R.37	Beam Splitter Cube (see Table 8.10)	Thor	————	$ 198.10
M.R.38	30 mm Cage XY Translator for 1" Optics	Thor	CXY1	$169.05
M.R.39	SM1-Threaded 30 mm Cage Plate, 0.35"	Thor	CP02	$16.00
M.R.40	SM1-Threaded 30 mm Cage Plate, 0.35"	Thor	CP02	$16.00
M.R.41	Right Angle 30 mm Cage Kinematic Mount	Thor	KCB1	$144.00
M.R.42	30mm to 60mm Cage Plate Adapter	Thor	LCP02	$38.00
M.R.43	SM1-Threaded 60 mm Cage Plate, 0.50"	Thor	LCP01	$36.00

Table 8.8: Part 2 of 2 of the receiver mounting description. Part 1 is given in Table 8.7. The numbers correspond to the numbers given in Figure 6.1. The M.R. simply stands for Mount.Receiver.

Number	Description	Maker	Model Number	Price
M.R.45	Motorized Cage Rotation Mount	Thor	PRM1Z8E	$1326.50
M.R.46	Right Angle 30 mm Cage Kinematic Mount	Thor	KCB1	$144.00
M.R.47	30 mm Cage Removable Filter Holder	Thor	CFH2	$100.98
M.R.48	SM1-Threaded 30 mm Cage Plate, 0.35"	Thor	CP02	$16.00
M.R.49	SM1-Threaded 30 mm Cage Plate, 0.35"	Thor	CP02	$16.00
			Sub Total	$10,110.32
			10% Discount	$1,011.03
			Total	$9,099.29

Table 8.9: Description of the parts required to assemble the precision filtering cage cubes for SuPR's receiver.

Description	Maker	Model Number	Price
Precision Kinematic Rotating Cage Cube Platform	Thor	B4CRP	$275.00
30 mm Cage Cube	Thor	C4W	$57.90
Blank Cover Plate with Rubber O-Ring for C4W	Thor	B1C	$18.00
Cage Cube Optic Mount	Thor	B5C	$30.50
		Total	$381.40

Table 8.10: Description of the parts required to assemble the rotational cage cubes for SuPR's receiver.

Description	Maker	Model Number	Price
Kinematic Cage Cube Platform for C4W	Thor	B3CR	$91.70
30 mm Cage Cube	Thor	C4W	$57.90
Blank Cover Plate with Rubber O-Ring for C4W	Thor	B1C	$18.00
Cage Cube Optic Mount	Thor	B5C	$30.50
		Total	$198.10

8.6   More Summit Polarized Raman Lidar Simulation Detail

Simulation parameters used in the SuPR ideal performance calculations for the transmitter and receiver are listed in this section. The receiver optical efficiencies for the Raman channels are given in Table 8.11 and for the elastic scattering channels in Table 8.12. Transmitter data is given in Table 8.13 and for the specification of atmospheric parameters in Table 8.14.

Table 8.11: Path efficiencies as a function of wavelength for each optic in the SuPR receiver for the Raman channels. The channels given are for the center wavelengths: Water $= 407.45\,nm$, Nitrogen $= 386.69\,nm$, High J $= 353.3\,nm$, and Low J $= 354\,nm$. All wavelengths are given in air. Finally, optics at non-normal incidence have their S and P polarization efficiencies given separately. The distinction (R) indicates reflection efficiency and (T) transmission efficiency.

Optic Name	H_2O	N_2	High J	Low J
Telescope Primary	94.3%	94.5%	95.6%	95.6%
Telescope Secondary	94.3%	94.5%	95.6%	95.6%
Bench mirror				
Collimating lens	98.6%	98.3%	98.1%	98.1%
System mirror (P)	100.%	100.%	100.%	100.%
System mirror (S)	100.%	100.%	100.%	100.%
Short Pass filter	96.8 %	95.5 %	90.4%	91.2 %
Nitrogen dichroic	99.8% (R)	99.6% (R)	93.8% (T)	93.9% (T)
Raman Longpass	97.6%	97.0%	———	———
Raman Longpass	97.6%	97.0%	———	———
Water dichroic	99.5% (R)	95.8% (T)	———	———
90-10 BS (P)	———	———	91.5% (R)	91.6% (R)
90-10 BS (S)	———	———	90.0% (R)	90.4% (R)
50-50 BS	———	———	50.0% (R)	50.0% (T)
Steering mirror (P)	———	———	———	100.%
Steering mirror (S)	———	———	———	100.%
QWP	———	———	———	———
HWP	———	———	———	———
Polarizer	———	———	———	———
90-10 BS (P)	———	———	———	———
Polarizer	———	———	———	———
Filter	79.4%	80.9%	52.1%	47.9%
Focusing lens	98.6%	98.3%	98.1%	98.1%
PMT QE	40%	40%	40%	40%
Total efficiency	25.1%	24.0%	7.10%	6.06%

Table 8.12: Path efficiencies as a function of wavelength for each optic in the SuPR receiver for the elastic channels. The channels given are for the center wavelengths: Parallel/Perpendicular = 354.71 nm. All wavelengths are given in air. Finally, optics at non-normal incidence have their S and P polarization efficiencies given separately. The distinction (R) indicates reflection efficiency and (T) transmission efficiency.

Optic Name	Parallel	Perpendicular
Telescope Primary	95.5%	95.5%
Telescope Secondary	95.5%	95.5%
Bench mirror		
Collimating lens	98.1%	98.1%
System mirror (P)	100.%	100.%
System mirror (S)	100.%	100.%
Short Pass filter	90.8%	90.8%
Nitrogen dichroic	94.2% (T)	94.2% (T)
Raman Longpass	———	———
Raman Longpass	———	———
Water dichroic	———	———
90-10 BS (P)	8.34% (T)	8.34% (T)
90-10 BS (S)	9.41% (T)	9.41% (T)
50-50 BS	———	———
Steering mirror (P)	———	———
Steering mirror (S)	———	———
QWP		
HWP		
Polarizer	99% (R)	90% (T)
90-10 BS (P)	91.7% (R)	———
Polarizer	———	90%
Filter	74.8%	74.8%
Focusing lens	98.1%	98.1%
PMT QE	40%	40%
Total efficiency	1.53%	1.54%

Table 8.13: SuPR Hardware Simulation Parameters.

Transmitter Parameter	Value	Receiver Parameter	Value
Base Altitude	3.2 km	Diameter Primary	24 in
Base Latitude	72.596 N	Filter Width	0.3 nm
Base Longitude	38.422 W	Field of View	252 μrad
Divergence (from laser head)	500 μrad	Polarization Par	0°
Expansion	3x	Polarization Perp	90°
Polarization Transmit	0°	Range Bin Number	3072
Pulse Energy	400 mJ	Range Bin Width	7.5 m
Pulse Rate	30 Hz	PMT Quantum Efficiency	38%
η_{Trans}	0.2736		

Table 8.14: SuPR Atmospheric Simulation Parameters

Parameter	Value
Aerosol Layer Altitude	$3.2\ km$ to $8\ km$
Background Level (med)	$5 \times 10^{-9}\ W/cm^2$
Background Level (high)	$80 \times 10^{-6}\ W/cm^2$
Depolarization δ (Air)	0.00365
Depolarization d (Air)	0.00727